CRANFIELD UNIVERSITY

SCHOOL OF MECHANICAL ENGINEERING

PhD THESIS

Academic Year 2003-2007

Ahmad Badarudin Bin Mohamad Badry

Synthetic Turbulence Generation for LES on Unstructured Cartesian Grids

PhD

Supervised by

Dr P A Rubini

This thesis is submitted in partial fulfilment of the requirements for the degree of Doctor of Philosophy

Abstract

A parallel CFD code to solve incompressible fluid flow on unstructured Cartesian meshes has been developed almost from ground up. Turbulence statistics have been computed using the Large Eddy Simulation technique. The new code was subjected to some validation where results are compared to available reference data. An analysis on the iteration and discretisation errors was carried out.

This code was then applied to predict the lid driven cubical cavity flow in at a bulk Reynolds number of 10,000. Three different mesh sizes were used to investigate independence of results on grid size. Amongst others, turbulence statistics were checked against Kolmogorov -5/3 law.

A detailed study of synthetic turbulence methods was carried out and applied to the prediction of flow in a duct with square cross section using an inlet and outflow boundaries. Three different turbulence generation methods were investigated namely the artificial turbulence generation method, random perturbation method and a novel hybrid particle-wave method also termed as the enhanced vortex particle method in this study. The mean and instantaneous field variables together with the turbulence statistics from each method were compared and analysed.

Finally, the code was used to solve turbulent flow over arrays of wall-mounted obstacles with mesh densities comparable to previous studies. The velocity profiles and vector fields at various locations in the domain were compared to data obtained from recent LES simulations. The artificial turbulence generation case was applied for the first time to produce turbulence at the inlet. The turbulence kinetic energy spectrum distribution agrees well with reference data.

Important findings from this study are clarified and some suggestions for future work are given in the conclusions section.

Acknowledgements

I am greatly indebted to my supervisor, Dr. Philip Rubini for his guidance and advice in completing the thesis.

I survived student life at Cranfield thanks to my wife Nuryana Idris.

The moral support from my parents, Sabariah Yusoff and Mohamad Badry Jaafar is most appreciated.

Table of Contents

List of Figures

List of Tables

Nomenclature

a	Element of coefficient matrix
a_{ij}	Amplitude tensor (m/s)
A	Cell face area (m^2)
A^+	van Driest damping coefficient
$\vec{A}$	Surface vector
A_c	Square, sparse coefficient matrix
A_P	Coefficient of cell with node P
A_m	Coefficients of cells with nodes neighbouring node P
b_j	Filter coefficients
$\tilde{b}_j$	Approximate filter coefficients
B	Empirical constant related to the thickness of the viscous sublayer
C	Convective terms in the momentum equation
C_r	Random turbulent fluctuation amplitude regulator
C_K	Kolmogorov constant
C_S	Smagorinsky constant
C_{SD}	Smagorinsky constant with van Driest damping
C_{ij}	Cross-terms stress tensor (kg/ms^2)
C_μ	Empirical constant, $\left(u_\tau / \sqrt{k}\right)^4$
D	Diffusive terms in the momentum equation
$E(\kappa)$	Kinetic energy per unit mass per unit wavenumber (m^2/s^2)
f	Instantaneous field variable
$\bar{f}$	Resolvable-scale filtered field variable
g	Filter function
G	Free space Green's function
H	Domain length (m)
H	Convective term
k	Kinetic energy of turbulent fluctuations per unit mass
K	Number of subdomains from mesh partitioning
$\vec{K}$	Biot-Savart kernel
$\vec{K}_\varepsilon$	Mollified Biot-Savart kernel
L_{ij}	Leonard stress tensor (kg/ms^2)

M	Preconditioning matrix
n	Time level
n_r	Random number
$\vec{n}$	Unit normal vector
N	Number of vortex particles, number of filter support points
p	Instantaneous static pressure (kg/ms^2)
$\overline{p}$	Resolved static pressure (kg/ms^2)
P	Modified pressure in the filtered momentum equations (kg/ms^2)
Q_{ij}	LES stress tensor, $C_{ij} + R_{ij}$ (kg/ms^2)
Q_P	Source term
R_{ij}	Subgrid scale Reynolds stress tensor (kg/ms^2)
r_m	Random number series with zero mean and unity variance
$\vec{r}$	Displacement vector (m)
R	Random number field with zero mean and unity variance
S	Surface are encompassing a volume of fluid (m^2)
S_{ij}	Mean strain-rate tensor (1/s)
S_p	Scalar variable dependent source term
S_u	Independent source term
t	Time (s)
u, v, w	Instantaneous velocity components in x, y, z directions (m/s)
u_i	Instantaneous velocity in tensor notation (m/s)
u_i'	Fluctuating velocity in tensor notation (m/s)
$\overline{u}_i, \overline{u}_j$	Resolved velocity, mean velocity in tensor notation (m/s)
$\overline{u}_t$	Mean velocity parallel to a wall (m/s)
u_τ	Friction velocity (m/s)
$\vec{u}_\infty$	Free-stream velocity vector (m/s)
U_j	Spatially correlated fluctuating velocity in tensor notation (m/s)
V	Volume of fluid (m^3)
x, y, z	Rectangular Cartesian coordinates (m)
x', y'	Position displacement in rectangular Cartesian coordinates (m)
x_i	Position vector in tensor notation (m)
$\vec{x}$	Position vector (m)

$\vec{x}'$	Position displacement vector (m)
y^+	Sublayer-scaled dimensionless distance

Greek

α_p	Estimate of the initial circulation around the particle p (m^2/s)
δ	Boundary layer thickness (m), Dirac delta function
δ_{ij}	Kronecker delta
Δ	LES filter width (m), cell edge length (m)
Δx	Incremental change in length (m)
$\Delta\Omega$	Incremental change in volume (m^3)
ε	Dissipation per unit mass (m^2/kgs^2)
η	Cut-off function for the Biot-Savart kernel $\vec{K}$
κ	von Karman constant, wave number
Γ	Heat conductivity (kgm/s^3K), circulation (m^2/s)
μ	Dynamic molecular viscosity (kg/ms)
ν	Kinematic molecular viscosity (kg/ms)
ν_T	Smagorinsky eddy viscosity (kg/ms)
$\vec{\xi}$	Position vector in vector notation (m)
ρ	Mass density (kg/m^3)
σ	Parameter controlling the size of mollified vortex particles
τ_{ij}	Subgrid scale stress tensor (kg/ms^2)
τ_W	Wall shear stress (kg/ms^2)
ϕ	Scalar field variable
ψ	Streamfunction (kg/ms)
ω	Vorticity vector (1/s)
Ω	Cell volume (m^3)

Superscripts

*,**	Temporal intermediate values of a field variable
h	Smooth approximation with discrete vortex particles
n	Time level

Subscripts

b	Bottom face of grid cell
B	Bottom cell centre
e	East face of grid cell
E	East cell centre
n	North face of grid cell
N	North cell centre
p	Discrete vortex particle
P	Cell centre enclosed by the *e*, *w*, *n*, *s*, *t*, *b* faces
s	South face of grid cell
S	South cell centre
t	Top face of grid cell
T	Top cell centre
w	West face of grid cell
W	West cell centre

Abbreviatons

CFD	Computational fluid dynamics
CFL	Courant-Friedrichs-Levy
CPU	Central processing unit
DES	Detached eddy simulation
DNS	Direct numerical simulation
ENO	Essentially non-oscillatory
HVAC	Heating, ventilation, air-conditioning and cooling
LES	Large eddy simulation
MISD	Multiple instructions, single data
MIMD	Multiple instructions, multiple data
MPI	Message passing interface
MRSB	Multiple recursive spectral bisection
MUSCL	Monotone, upstream-centered schemes for conservation laws
PDE	Partial differential equation
PIM	Parallel iterative method

PISO	Pressure implicit with splitting pf operators
PVM	Parallel virtual machine
RANS	Reynolds averaged Navier-Stokes
RGMRES	Restarted generalised minimum residual
RMS	Root-mean-square
SGS	Subgrid scale
SIMD	Single instructions, multiple data
SIMPLE	Semi implicit method for pressure linked equations
SISD	Single instructions, single data
TVD	Total variation diminishing

CHAPTER 1

Introduction

1.1 Background

Engineering flows which are completely laminar is rare. One way of computing turbulent flow is by using Direct Numerical Simulation which may not very practical considering the amount of computing power of present computers to solve engineering flows which is proportional to $Re^{9/4}$ where Re is the Reynolds number that characterises the flow. Reynolds Averaged Navier-Stokes (RANS) models are much more economical but they are not universally accurate. For example, Wilcox (2002) pointed out that for boundary layer flows with adverse pressure gradient, the value of skin friction coefficient c_f, is over predicted in a number of cases, when using the low Reynolds number version of the k-ε turbulence model proposed by Jones and Launder (1972). In between these two extremes, a technique for simulating large eddies and modelling smaller ones which is called Large Eddy Simulation (LES), is available. The rationale behind this technique is, firstly, large eddies are the ones carrying most of the turbulent stresses or energy and they are largely responsible for the transport of conserved properties such as momentum and mass and secondly, small scale motions are more isotropic and are thus more suitable for modelling.

A hybrid LES-RANS technique also known as Detached Eddy Simulation (DES) has gained considerable research interest from the Computational Fluid Dynamics (CFD) community in the past few years. Squires (2004) provides an overview of the application

of DES for the flows around military strike aircraft. According to him, the accuracy of DES solutions was considerably better than those of RANS. An issue with this method is the difficulty in matching turbulence properties produced by LES to those predicted by RANS at the interface where the two zones meet. Chalot et al. (2007) performed LES and DES simulations on geometries related to aircraft design. To overcome the mismatch at the interface of the LES model and the RANS model, near-wall treatments were applied to correct the values of eddy viscosity in the near wall region. Quéméré and Sagaut (2002) proposed a different approach to DES by dividing the domain into zones solved by either RANS or LES but different from DES. The latter is used in zones where an accurate description of the flow field is required, which may include a boundary layer region. Even though this geometric division is dissimilar to DES, the issue encountered is the same in that the discontinuity at the interface still persists. They suggested the use of an interface variable, extrapolated from the LES subdomain to overcome this issue. An advantage of LES over DES is the higher accuracy in the results obtained for the boundary layer region by the former. In DES the boundary layer region, solved by RANS, loses a lot of information on turbulence when ensemble averaging is carried out on the Navier-Stokes equations. Gosman (1999) concluded that LES provides sufficient level of accuracy for some purposes in the wind engineering of built environments albeit there are quite a few weaknesses discovered in its modelling.

In LES, the most frequently encountered boundary type, especially in early simulations, is the periodic boundary condition. For example, Xie and Castro (2006) used periodic boundaries in the streamwise and spanwise directions to perform Large Eddy Simulation of turbulent flow over arrays of wall-mounted cubes. The type of flow and geometry are obviously limited by the use of this boundary type. Flows over non-repeating geometries and flows which are in a development stage (such as the developing boundary layer flow) require the use of inlet and outlet boundaries in the streamwise direction. In order to extend the application of LES to more complex geometries of industrial flows, the use of inlet and outlet boundaries is inevitable.

The time and space taken for turbulence to develop downstream of an inlet boundary with

a mean velocity profile superimposed may increase the cost of computation considerably. To improve this situation a suitable turbulence generation method at the inlet needs to be selected for LES. This requires a detailed study of turbulence generation method currently available, such as the vortex particle method by Mathey et al. (2003) and the artificial turbulence method of Klein, Sadiki and Janicka (2003) among others. Selection of a suitable method can then be made so that it can be used to solve practical flow problems.

Designing a mesh for a computational fluid dynamics (CFD) application is an important and critical issue which has far reaching consequences for computation cost (in terms of man-hour requirements, hardware and software capabilities and wall clock time to name a few) as well as the quality of results. In many instances, an optimum mesh delivering results within the specified accuracy limit and minimising cost is sought by the users.

Tetrahedral and non-orthogonal hexahedral cells frequently used in CFD with face normals, not aligned in the direction of the primary axes of a Cartesian coordinate system incur extra cost resulting from the computation of the flux components normal to these faces. Numerical difficulties may arise if the quality of the non-orthogonal cells is mediocre. Chalasani et al. (2005) stated that highly skewed and non-orthogonal anisotropic cells near convex and concave regions may result in a poor quality transition from the extruded mesh in the boundary layer and the void filling tetrahedral. A uniform hexahedral mesh does not have to face these issues. In contrast, it offers an advantage over non-orthogonal meshes with regards to the computation cost and also the quality of results in circumstances where the use of a non-orthogonal mesh is not necessary.

Current development in automatic meshing by major CFD suite vendors focuses on the cut or trimmed hexahedral and polyhedral meshers and flow solvers. These are applied to solve fluid flow problems in very complex geometries. However, more research should be carried out in order to quantify the effects of the general polyhedral cells on the results of simulation. An example of the use of polyhedral cells is provided by Dubief et al. (2005) studying the characteristics of aeroacoustic noise in a heating, ventilation, air-

conditioning and cooling (HVAC) submodule that monitored the pressure fluctuations on a monitoring plane. Their results are in good agreement with experimental data. In such a case, the construction of structured multi-block hexahedral cells would be too time consuming while employing tetrahedral cells would produce cells of deplorable quality. Wang et al. (2004) employed polyhedral cells in the viscous layer region and adaptive Cartesian grids that are far away from walls in order to predict the aerodynamic effects of surface roughness related to gas turbine components. Kim (2004) carried out validation studies of a commercial flow solver employing test cases such as vortex-shedding behind a square cylinder and also flows around a sphere, utilising polyhedral cells. Another example is given by Jasak, Weller and Nordin (2004) in which case polyhedral cells were used to perform simulations of in-cylinder fluid flow, heat transfer, fuel injection and combustion in internal combustion engines. Cannon et al. (2004) performed detailed validation of their LES code tailored for combustion using unstructured polyhedral cells. An alternative way to handle complex geometries is to use an overset chimera grid framework. Cheng, Koomullil and Noack (2005) and Morton, Tomaro and Noack (2006) used this type of grid to solve fluid flow around bodies in relative motion, alleviating the difficulty in the transfer of information across grids by the use of libraries and application programming interface.

Although the use of polyhedral or overlapping meshes is in fashion, this is not always required. An instance is given by Stoesser et al. (2003) wherein the geometry consists of a number of blocks mounted on a wall. The use of unstructured Cartesian hexahedral mesh consisting of cubic cells with edges aligned in the direction of the primary axes of a Cartesian coordinate system would be ideal for this type of application. An example of the application of a Cartesian mesh to solve fluid flow in a complex geometry is provided by Kamatsuchi (2007). In his study, Kamatsuchi employed the Immersed Boundary method to cells lying next to solid boundaries; he also used a tree-structured Building-Cube method for cell refinement, while neighbour cells were found using the tree-traversing technique. The immersed boundary method modifies the governing conservation equations by introducing source terms or forcing functions that reproduces the effect of the boundary. This is explained in more detail by Mittal and Iaccarino

(2005).

The size and computing intensity of the cases involved in this work necessitates the use of high-performance parallel machines. The computing capability of a single processor machine is limited by the speed at which data travels through hardware. In addition to this, the cost increases more rapidly for a given increase in floating point operations per second for a single processor machine. When dealing with large engineering problems requiring reasonable turnaround times, the only way forward is to use multiple processors so that computation can be divided optimally and carried out simultaneously in a coordinated manner. Strohmaier (2005) observed that every decade for the last six decades researchers experienced a two orders of magnitude increase in high-performance computer systems. Moore's law which states that chip performance should double approximately every 18 months is still valid. In the field of CFD, the use of high-performance computing will definitely increase. Although the bulk Reynolds numbers of flows computed so far using LES is relatively low, continuous development in highly parallel codes will definitely help in expanding the envelope of LES.

1.2 Objective

From the above discussion, it is obvious that there is a need to develop an LES flow solver on a high-performance computing system using simple yet flexible meshes to study flows of engineering interest.

In this study, the type of flow of interest refers to Newtonian (constant viscosity), incompressible class. This involves flows of liquids with negligible change in density and also gases with Mach numbers less than 0.3. Many flows of interest fall into this category, some practical applications include naval architecture, car aerodynamics and hydraulics.

The initial objective of this study was to develop a parallel code to solve incompressible, Newtonian fluid flows using unstructured hexahedral Cartesian mesh. This was followed by an evaluation of current turbulence generation methods applied to an inlet boundary of

a wall bounded flow. The most suitable inlet boundary turbulence synthesiser will be selected and incorporated into the code to solve a flow of practical interest.

1.3 Thesis Layout

The arrangement of this thesis mainly follows the chronological order of the tasks and is as follows. Chapter 2 describes current trend and state of the art LES simulation techniques related to the type of simulations carried out in later chapters. A considerable amount of material is invested in describing the implementation of three different synthetic turbulent inlet flow generation methods for a wall bounded flow inside a duct with square cross sections.

Chapter 3 gives an explanation on the theory of LES, governing equations and numerical schemes used in all the test cases. These include:

- the governing partial differential equations employed in LES
- the filter used in this study
- finite volume discretisation
- numerical differencing scheme
- treatment of no-slip wall boundaries

Chapter 3 also documents the step-by-step development of the flow solver and includes some validation results for the new code. Chapter 4 deals with the turbulent lid driven cavity flow case. An extensive discussion on the results such as energy spectrum, velocity profiles and time trace of velocities is also carried out in the chapter.

Chapter 5 describes the implementation and analysis of three different turbulent inlet flow generation methods for a wall bounded flow inside a duct with square cross sections. It also discusses the results based on the mean flow parameters and turbulence statistics. In this chapter, three turbulence generation techniques were studied in order to determine the method that gives the most rapid and accurate instantaneous and statistical results in contrast to some available reference data. Chapter 6 elucidates the application

of LES to a flow over geometries resembling simple buildings by incorporating a turbulent inlet flow generator studied in the previous chapter. Chapter 7 ends this thesis by discussing the conclusions and future works in view of the results obtained from the test cases.

CHAPTER 2

Aspects of Simulation

Prior to embarking on the task of programming the parallel LES flow solver, a survey of current numerical methods and also the present state of LES was carried out in order to find a direction in designing and developing the code. This overview gives an idea about existing studies on LES which might be improved and investigated further in order to expand the envelope of LES.

2.1 Approximate Expressions

There are four approximation schemes commonly used for LES, which are finite difference, finite element, finite volume and spectral methods. These are described in some detail by Hirsch (1988) among others.

The finite volume approximation scheme modifies the partial differential equations (PDE) by integrating each term with respect to the cell volume. This is normally implemented by applying Gauss' divergence theorem to the volume integrals, expressing the integrals as surface integrals. Surface fluxes are then calculated by using a suitable differencing scheme through the interpolation of field variable values at the node of neighbouring cells.

For relatively complex geometries, finite element and finite volume are two of the most popular approximation methods used by researchers. The weighted integral of the conservation law for finite element and integral form of conservation equations for finite

volume make these two methods suitable to handle complex geometries. Another advantage of the finite volume method is that it conserves mass, momentum and energy, which is important for LES applications. The finite difference and spectral methods have only been used for simple geometries such as straight rectangular ducts and square cavities as in Mittal, Simmons and Udaykumar (2001). Another example is provided by Lenormand, Sagaut and Ta Phuoc (2000), solving subsonic and supersonic channel flows at a bulk Reynolds number of 3,000 with the use of fourth-order accuracy in space discretisation scheme.

Rollet-Miet, Laurence and Ferziger (1999) used the finite element approximation to investigate flow in a tube bundle. They obtained good statistical agreement with experimental data when using a collocated finite element scheme combined with linear approximating function. Uchiyama (1998) also used the finite element method. The author obtained good results, but only for streamwise stress components in a homogeneous (i.e. turbulence has the same structure regardless of the location in a flow field), geometrically simple domain.

Benhamadouch, Mahesh and Constantinescu (2002) used the finite volume method in their code which was originally designed for RANS. They found that the numerical methods are not suitable for LES, and subsequently, changed them into those which conserve global kinetic energy. A conservative, hybrid, finite difference, finite element scheme was proposed by Lê et al. (1997). The finite difference method was used to handle discretisation near the boundaries while the finite element method was assigned to the task of discretising the pressure gradient term and the non-linear convection term.

The study conducted by Haworth and Jansen (2000) investigated the flow inside a simplified reciprocating internal combustion engine. They obtained better results (for computed mean and root-mean-square velocity profiles) than RANS while using a simple SGS turbulence model, and maintaining the same mesh size typical in RANS calculation.

Fröhlich et al. (1998) performed a comparison between a structured finite volume code and an unstructured finite element code. They discovered that both unstructured and structured methods incur similar computational cost. For the unstructured case, the use of a less efficient algorithm is compensated by using fewer nodes in the computation. The finite volume code performed better than its finite element counterpart when predicting the drag coefficient.

Camarri et al. (2004) used a hybrid finite volume and finite element approximation for their study of LES performance using a low diffusion spatial discretisation scheme. They claimed that the method was able to produce accurate results with relatively coarse meshes.

2.2 Flow Solver

Any flow solver for the Navier-Stokes equation can be used though some are more efficient than others. For example, Rollet-Miet, Laurence and Ferziger (1999) used the Adams-Bashforth Crank-Nicolson scheme though some discrepancies were encountered in the prediction of the normal stress budget. This was attributed to the second order accuracy with respect to time (Peyret and Taylor (1983)) of this method. Haworth and Jansen (2000) used the Semi Implicit Method for Pressure Linked Equations (SIMPLE) algorithm to predict the flow inside a reciprocating internal combustion engine. Okong'o and Knight (1998) and Simons and Pletcher (1998) used the fourth order Martinelli, Jameson and Grasso (1986) Runge-Kutta method for the prediction of compressible turbulent flows. Bijl, Carpenter and Vatsa (2001) emphasised that the fourth-order Runge-Kutta method was more efficient than the Backward Differencing Formulations by at least a factor of 2.5 for all error tolerance levels. Park (2006) compared the performance of the Adams-Bashforth Crank-Nicolson predictor step in a PISO transient flow solver over the fractional step method, and he concluded that the former performed equally as the latter in predicting turbulent channel flows.

Due to the presence of inner iteration loops, the SIMPLE family of algorithms is not likely to be more efficient than other algorithms listed above since in transient

simulations such as those required by LES, the pressure-correction equation must be solved accurately at each time step meaning that the momentum and pressure-correction equations must be solved more than once per time step.

A question that needs to be asked is how large a time step can be taken by the flow solver when predicting turbulence using LES? Obviously, small time steps would give accurate results regardless of whether the flow solver is explicit or implicit with respect to time but computational costs could be reduced if large time steps are possible. Furthermore, in Direct Numerical Simulation (DNS), even the smallest time scales of eddies are larger than the time step for stability requirement, implying that, for LES, larger time steps (than explicit methods) can be utilised in the solution algorithm. However, Fröhlich and Rodi (2002) warned that using excessively large time steps would result in oscillations and distortions of eddies with sizes comparable to the local grid size, influencing the accuracy of results.

One example of such an investigation was conducted by Choi and Moin (1994) using DNS for turbulent flow over riblets. They used a fully implicit technique, combining fractional step method and Newton-iterative scheme to solve the nonlinear momentum equations as described by Kim and Moin (1985). Semi-implicit method was not used due to the limit on the time step size imposed by such methods. The main finding was, larger time steps than those of explicit and semi-implicit methods could be used to achieve statistical accuracy, but it has to be less than the Kolmogorov time scale to maintain realistic turbulence properties. When large eddies are simulated, the time step size can be made even larger than DNS since the smallest simulated eddies are within the inertial subrange region.

Miller (1971) analysed the stability conditions of time discretisation schemes for the heat equation in partial differential form namely the Leapfrog scheme, the Dufort-Frankel scheme and Richardson's scheme amongst others, while using a reductive approach. Using this approach, from $det(G - \lambda I) = 0$ the zeros λ of a polynomial $f(\lambda)$ with real or complex coefficients

$$f(\lambda) = a_0 + a_1\lambda + ... + a_n\lambda^n \qquad (2.1)$$

where G^1 is the amplification matrix, I is the identity matrix, λ are the eigenvalues of G, are reduced to the zeros of a polynomial of a lower degree having the same properties as those of the higher order polynomial. By repeated application of this method, the degree of the polynomial can be reduced until the polynomial is simple enough for the criterion of stability to be determined analytically.

The degree of the polynomial $f(\lambda)$ may be sufficiently large to render an analytical approach too complicated and time consuming. An alternative approach is to carry out numerical calculations. Peyret and Taylor (1983) computed the eigenvalues of G directly and constructed a graph of the results.

Wesseling (1995) performed a von Neumann stability analysis for the second order Adams-Bashforth Crank-Nicolson scheme with second order central differencing for the convective terms. The steps are as follows. The characteristic polynomial was obtained from $det(G-\lambda I)$ as described in Equation (2.1). The eigenvalue λ was assumed to be of the form $e^{i\mu}$. By varying or changing the values of wavenumber and the parameter μ, values of the real and imaginary part of the polynomial coefficients were calculated to obtain the stability domain S. By choosing suitable values for two parameters, a and b (that defines the simple shapes to fit S, explained below), together with the known values of Courant and diffusion numbers, the correct shapes to fit S was found. In the case of the second order Adams-Bashforth Crank-Nicolson scheme with second order central differencing, a parabola with b set to $2\sqrt{3}$ and an oval with a was set to 1/2 and b to a value of $(3/4)^{1/4}$ were employed to get a good fit to the bounds of S. A useful stability condition was obtained by requiring parabola $\cup$ oval $\subseteq S$ for the second order Adams-Bashforth Crank-Nicolson scheme with second order central differencing. This establishes the von

[1] The amplification matrix G is reduced to the amplification factor g if a scalar field variable is involved and two-time level discretisation schemes are used (e.g. the Courant number of a hyperbolic equation for a scalar, using the explicit Euler and central schemes for the temporal and spatial derivatives, respectively).

Neumann stability condition for this method:

$$\sum_{\alpha} \sigma_{\alpha}^{2} / d_{\alpha} \leq 2/3 \tag{2.2}$$

where σ and d are the Courant and diffusion numbers respectively. The summation is over all Cartesian coordinate directions.

2.3 Discretisation Scheme

The order of the approximation or discretisation scheme for the integral terms is important in the attempt to achieve acceptable accuracy levels when performing LES. This is even more so when complex geometries and non-orthogonal grids are involved.

An example of the importance of the order of approximation or discretisation was highlighted by Haworth and Jansen (2000) who discovered that the energy spectrum distribution did not compare very well with experimental data. This was mainly due to numerical dissipation than the physics of SGS models since superior results have been obtained using higher order spatial discretisations with the same number of nodes. Other factors include lack of rigorous analysis with regards to the effect and consequences of applying implicit filters when using relatively coarse mesh.

Benhamadouch, Mahesh and Constantinescu (2002) found that, for the convective terms, second-order upwinding is dissipative and consequently changed the scheme to a symmetric, central one. This was also the case with Simons and Pletcher (1998) who reiterated that upwind scheme is dissipative and should be avoided but sometimes it is needed to enhance stability for example when using tetrahedral cells.

To explain monotone schemes such as Monotone Upstream-Centered Schemes for Conservation Laws (MUSCL) and Total Variation Diminishing (TVD) briefly, and the reason for using this scheme, consider the first and second order upwind differencing schemes. First order upwinding schemes are dissipative while second order discretisation

schemes, although oscillate at discontinuities, are more accurate. In order to achieve a physical (non oscillatory) numerical solution, in other words, to get the best of both worlds, TVD conditions can be used. Typically when using TVD, a second order upwind scheme is used, with the second order terms multiplied by (non linear) flux limiters which satisfy the TVD condition, ensuring that the sum of all maxima minus the sum of all minima does not grow (Hirsch 1990). Okong'o and Knight (1998) used the solution to the Riemann problem in combination with third order Essentially Non-Oscillatory (ENO), which is a generalisation of TVD reconstruction scheme that calculates the convective fluxes at cell faces. Camarri et al. (2004) proposed a separation of sub-grid damping and numerical damping by using a low-diffusion MUSCL scheme for the former. The reason for doing so was the excessive numerical damping effect when the SGS term was used for both sub-grid and numerical dampings. Berglund and Fureby (2007) applied a second-order TVD scheme to handle convective fluxes in the LES simulation of supersonic flow and combustion in a model scramjet combustor, and both the non-reacting and reacting flowfields were reasonably well predicted. In their study, Mary and Sagaut (2002) carried out an LES of flow around a nearly stalled airfoil whereby the turbulent kinetic energy transfer was performed using an implicit Monotone Integrated LES (MILES) method and an explicit selective mixed scale SGS model.

2.4 Inlet Boundary Conditions

The periodic boundary has been used since the early days of LES. The main reason for applying this boundary is to avoid using large computational domains in order to capture the evolution of eddies. However, the use of periodic boundaries means that only flows in simple geometries and turbulence that are fully developed can be computed. Employing the inlet and outlet boundaries, these restrictions can be removed and this enables LES to be applied to flows of engineering interest.

To avoid simulating laminar and transitional region near a leading edge (of a solid wall surface for example) when utilising the inlet and outlet boundaries, a realistic fully turbulent inflow condition is needed to reflect the three-dimensional and unsteady flow inside the computational domain. Ideally, the synthetic turbulence generator has to be

capable of producing anisotropic, inhomogeneous turbulence with a controllable degree of auto and cross-correlations of velocities with respect to time and space as well as satisfy mass conservation.

Liu and Pletcher (2006) developed a fully turbulent inflow condition for boundary layer flows by rescaling instantaneous profiles at a dynamically positioned downstream location based on the law of the wall and also the defect law followed by the recycling of the instantaneous profiles to the inlet plane. The method was successful in reducing the startup transient and shortening the inlet buffer zone.

Smirnov, Shi and Celik (2001) generated a non-homogeneous, anisotropic flow field by synthesising divergence-free vector fields from a sample of Fourier harmonics; the technique was applied to study the character of ship wakes. In this study, synthetic turbulence was generated by producing a continuous flow-field from the superposition of harmonic functions. Using an anisotropic velocity correlation tensor as an input (form RANS calculations), an orthogonal transformation tensor[2] diagonalising the velocity correlation tensor and coefficients representing turbulent fluctuating velocities were also obtained. The continuous flow-field was then subjected to a scaling and an orthogonal transformation, which used the coefficients that represented turbulent fluctuating velocities and the orthogonal transformation tensor in order to obtain a new flow-field.

Another synthetic turbulence generation technique was proposed by Davidson (2005) based on an earlier work by Billson, Eriksson and Davidson (2003). In this study, a prescribed length scale and an energy spectrum were used to produce turbulence fluctuations at the inlet. This was validated for hybrid LES-RANS of a channel flow. The method generates synthetic turbulence by making use of superimposed Fourier modes with random phase and directions. A prescribed energy spectrum was used to compute the amplitude of fluctuations. The method requires a turbulence length scale as input. The mean velocity profile for a channel flow was then added to the fluctuations which were

[2] An orthogonal transformation is a linear transformation preserving the lengths of vectors and also angle between vectors. The tensor is called an orthogonal matrix (or unitary matrix if dealing with real numbers).

correlated in time and space.

Glaze and Frankel (2003) compared two inlet generation techniques namely the Gaussian random forcing and a version of the weighted amplitude wave superposition spectral representation method. They concluded that the latter method was successful in producing self sustaining turbulence unlike the Gaussian random forcing method. di Mare et al. (2006) developed a synthetic turbulence generation method by applying digital filters to random data. In this method, the complete two point correlation functions in time and space can be specified locally for each coordinate direction. The method was found to be suitable for use with wall bounded flows.

A different approach to generating turbulence at inlet boundaries was proposed by Mathey et al. (2003) exploiting the Lagrangian vortex method. The method does not employ ad-hoc parameters while maintaining efficiency and accuracy. It is claimed that the results agree well with available data and reference simulations for channel flow, fully developed pipe flow and separated hill flow. Cottet and Koumoutsakos (2000) provide an apt introduction to the simulation of fluid flow using vortex method. An important development in this method was carried out by Krasny (1986a) confirming the existence of a singularity in the Green's function solution of the Poisson equation with periodic boundary conditions; the study suggested a simple solution to this problem in Krasny (1986b) by modifying the denominator of the kernel involved in the solution of the Poisson equation.

By running an auxiliary simulation in conjunction with the main computation presenting a developing boundary layer flow, Lund, Wu and Squires (1998) extracted velocity data; the data was used to generate inflow conditions at the inlet boundary of the primary computation domain. Also, a pair of inflow and outflow boundaries was used for the auxiliary simulation. The velocity field from a plane near this outflow boundary was rescaled according to two laws: the defect law and the law of the wall. The modified data was then reintroduced to the inlet plane. This method is more expensive compared to the other methods described here and it can only be used for cases with simple geometries.

For instance, the varying cross-sections moving in the streamwise direction in a gas turbine flow prohibits the use of this method. Sagaut et al. (2003) extended the capability of this recycling procedure to handle supersonic wall bounded flows. Liu and Pletcher (2006) proposed a modification to this method by locating the recycling plane dynamically so that the plane is located in a region where the flow is turbulent at all time marching levels of the simulation.

A method similar to Mathey et al. (2003) for the generation of turbulence at the inlet was used by Jarrin, Benhamadouche and Laurence (2005). The study was based on the use of a two-dimensional discrete Lagrangian particle method to simulate vortices in the lateral directions at the inlet.

Wang, Jiang and Zhang (2005) superimposed a time averaged velocity profile with a randomly fluctuating velocity components resembling white noise on the inlet boundary and performed LES simulations in indoor environments. This obviously does not represent real turbulence behaviour since motions of large eddies are correlated in time and space. In their study, Tutar, Celik and Yavuz (2007) performed LES around a circular cylinder and applied a random flow generation algorithm at the inlet boundary of the finite element flow solver. This algorithm is based on the generation of Fourier harmonics and the act of synthesising the divergence free vector field from the superimposed harmonics. On the other hand, McMullan, Gao and Coats (2007) utilised a hyperbolic tangent function whereby the data was derived from boundary layer simulations to generate turbulent inflow conditions for the simulation of spatially developing mixing layers with LES.

The following sub-section describes these techniques in more detail. These methods were applied to a developing square cross section duct flow in Chapter 5. The performance criterion of these methods was based on the downstream distance taken to achieve a fully developed flow profile.

Specific background and implementation details on each individual turbulence generation

method at the inlet are described below.

2.4.1 Random Perturbation Method

In this method, the inlet is subjected to a uniform inlet velocity in the streamwise direction. A random fluctuation in velocity is superimposed on the uniform inlet velocity:

$$u_i = \overline{u}_i + C_r u_i' n_r \tag{2.3}$$

where u_i is the resultant instantaneous velocity component, $\overline{u}_i$ is the uniform inlet velocity component (non-zero only in the streamwise direction), u_i' denotes the square root of turbulence intensity and n_r is a random number with magnitude less than unity and acting in the direction of the velocity component. C_r is a parameter which relates the amplitude of the fluctuations to the location of the inlet boundary relative to the wall. C_r might be related to some geometrically related parameters such as the non dimensional distance from the wall y^+, to reflect the increase in eddy sizes moving away from the wall region. As suggested by Ferziger and Peric (2002) u_i' is given by:

$$u_i' = \sqrt{\frac{2}{3}k} \tag{2.4}$$

where k is the turbulence kinetic energy per unit mass. This implies an isotropic turbulence generated at the inlet, which is not very realistic for real engineering flows typically containing inhomogeneous anisotropic eddies; but this method has the virtue of being simple to code. k is an average value at the inlet, meaning that, the turbulence intensity, in any given coordinate direction is invariant anywhere on the inlet boundary. In this instance, the turbulence kinetic energy was approximated by:

$$k = 10^{-4}\overline{u}^2 \tag{2.5}$$

where $\overline{u}$ is the uniform velocity component at the inlet. Besides, applied to the flow

inside a duct with a square cross section test case, the parameter C_r was set to a constant value of one for the sake of simplicity.

To avoid obtaining the same set of random numbers at the inlet, the timer function of MPI (see Chapter 3) which returns a double-precision floating point number is added to the random number seed every time the simulation is restarted.

2.4.2 Enhanced Discrete Vortex Particle Method

An inviscid fluid in two dimensions on unbounded domains was considered for this study. The general idea was to assign vorticity in the domain to discrete particles. Helmholtz's and Kelvin's laws are followed this method. Helmholtz law when applied to a vortex tube of an inviscid fluid, states that, the strength of the vortex tube is the same at all cross sections and this gives:

$$|\omega_1| A_1 = |\omega_2| A_2 \tag{2.6}$$

where A_1 and A_2 and ω_1 and ω_2 are two cross sections, and vorticity of the vortex tube, respectively. Kelvin's law states that the substantial derivative of circulation Γ does not vary with time for an inviscid fluid:

$$\frac{D\Gamma}{Dt} = 0 \tag{2.7}$$

where D/Dt is the rate of change of a quantity in a Lagrangian frame or the substantial derivative. Here the circulation Γ is given by:

$$\Gamma = \int_V \nabla \cdot \omega \, dV = \int_S \omega \cdot \vec{n} \, dS \tag{2.8}$$

where the surface S encompasses the volume of the fluid V. The relationship between vorticity and velocity is realised through the application of Biot-Savart law relating the

velocity to a vortex line:

$$\vec{u} = \vec{u}_\infty + \vec{K} * \omega \tag{2.9}$$

where $*$ denotes a convolution process and $\vec{u}_\infty$ is the free-stream velocity vector. *K* is the velocity kernel which is the rotational counterpart of Green's function *G*, for the Laplacian operator in two dimensions. The convolution or running integral operation is to be expected here since this is the inverse of the curl operation in $\vec{\omega} \equiv \nabla \times \vec{u}$.

G is related to *K* via:

$$\vec{K}(\vec{x};\vec{x}') = \nabla_{\vec{x}} \times G(\vec{x};\vec{x}')\hat{z}. \tag{2.10}$$

The kernel *G* is associated with the solution of the Poisson equation (with no boundaries) relating streamfunction and vorticity:

$$\psi(\vec{x},t) = G * \omega \tag{2.11}$$

which is the solution of the Poisson equation:

$$\nabla^2 \vec{\psi} = -\omega\,. \tag{2.12}$$

The streamfunction is related to the velocity vector by the relationship:

$$\vec{u} = \nabla \times \psi \hat{z}\,. \tag{2.13}$$

Through this relationship, Equation (2.9) is recovered.

Hence, $\vec{K}$ takes the form:

$$\vec{K}(\vec{x};\vec{x}') = \frac{1}{2\pi|\vec{x}-\vec{x}'|^2}\begin{bmatrix} y-y' \\ x'-x \end{bmatrix}. \tag{2.14}$$

To avoid numerical difficulties (such as unbounded velocity fields) during the close proximity of particles, adding a small positive constant to the denominator, helps, in removing the singularity of $\vec{K}$. A better approach is to modify $\vec{K}$ by convolving it with a cut-off function η yielding the mollification kernel $\vec{K}_\varepsilon$. As per Cottet and Koumoutsakos (2000), the form of cut-off function employed for this case is:

$$\eta(\vec{x}) = 1 + \left(\left(|\vec{x}-\vec{x}'|^2/2\sigma^2\right)-1\right)\exp\left(-|\vec{x}-\vec{x}'|^2/2\sigma^2\right) \tag{2.15}$$

where the parameter σ provides control over the size of the mollified particles. This parameter is approximated as:

$$\sigma = \frac{ck^{3/2}}{2\varepsilon} \tag{2.16}$$

where k is the turbulence kinetic energy per unit mass, ε is the dissipation, whereby the constant c is set to a value of 0.16 following Mathey et al. (2003).

The mollified kernel $\vec{K}_\varepsilon$ is then given by

$$\vec{K}_\varepsilon(\vec{x};\vec{x}') = \frac{1}{2\pi|\vec{x}-\vec{x}'|^2}\begin{bmatrix} y-y' \\ x'-x \end{bmatrix}\left(1-\left(\left(|\vec{x}-\vec{x}'|^2/2\sigma^2\right)-1\right)\exp\left(-|\vec{x}-\vec{x}'|^2/2\sigma^2\right)\right). \tag{2.17}$$

The vortex method deals with point vortices in which case each discrete fluid particle has a value of initial circulation (around that particle) assigned to it. By dividing the computational domain into cells and assigning a particle to the centre of each cell, in relation to Equation (2.8) the vorticity distribution becomes:

$$\omega(\vec{x},t) \approx \omega^h(\vec{x},t) = \sum_p \alpha_p \delta\left(\vec{x} - \vec{x}_p^h(t)\right) \tag{2.18}$$

where the superscript h indicates a smooth approximation with fluid particles, α_p is an estimate of the initial circulation around the particle p and δ is the Dirac delta function. This approximation increases in accuracy with of vortex particles (decreasing area of cells) increasing in number. The formal proof of this approximation was given by Cottet and Koumoutsakos (2000) by utilising the principle of weak solutions to advection equations.

The initial vortex strength or circulation in this case is given by:

$$\alpha_p(\vec{x}) = 4\sqrt{\frac{\pi A k(x,y)}{3N\left[2\ln(3) - 3\ln(2)\right]}}\,. \tag{2.19}$$

To set the values of turbulence kinetic energy, Equation (2.5) is used again and dissipation for this particular instance is set to $k^{3/2}/l$, where l is a length scale set, in this case, to ten percent of the inflow plane length. Initially, the particles were set to occupy random positions on the inflow plane and during computation all the particles were subjected to a random convective velocity parallel to the inflow plane.

The fourth order Runge-Kutta method is brought to task to determine the location of each particle at every time step during the simulation:

$$\begin{aligned} x_{n+1/2}^{*} &= x^n + \frac{\Delta t}{2} u\left(t_n, x^n\right) \\ x_{n+1/2}^{**} &= x^n + \frac{\Delta t}{2} u\left(t_{n+1/2}, x_{n+1/2}^{*}\right) \\ x_{n+1}^{*} &= x^n + \Delta t\, u\left(t_{n+1/2}, x_{n+1/2}^{**}\right) \end{aligned} \tag{2.20}$$

$$x^{n+1} = x^n + \frac{\Delta t}{6}\left[u\left(t_n, x^n\right) + 2u\left(t_{n+1/2}, x^*_{n+1/2}\right) + 2u\left(t_{n+1/2}, x^{**}_{n+1/2}\right) + u\left(t_{n+1}, x^*_{n+1}\right)\right]$$

where the superscript * indicates intermediate values of the solution, not the final values at time levels of n and $n+1$. A similar set of equations was used to obtain the y-coordinate of the particles. If a boundary face contains vortex particles, the fluctuating velocity components for that boundary face are set to the average velocity components of the particles residing on that boundary face. By interpolating fluctuating velocity components from boundary faces containing vortex particles in comparison to those with no vortex particles, an approximately smooth fluctuating velocity component is obtained on the inflow plane.

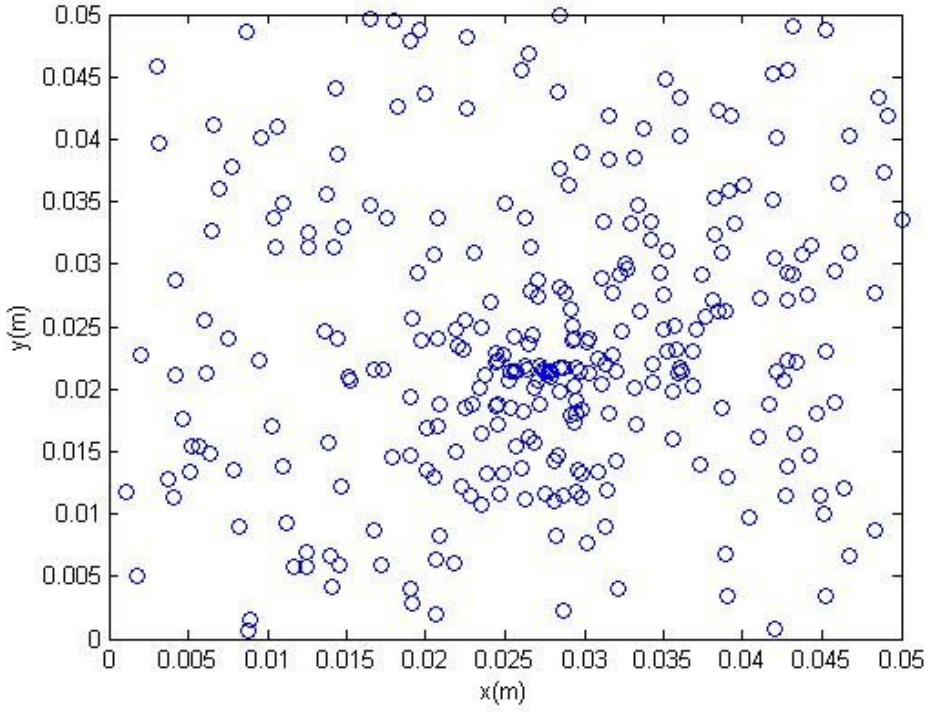

Figure 2.1 Vortex particles on the inflow plane at t=0.0010s.

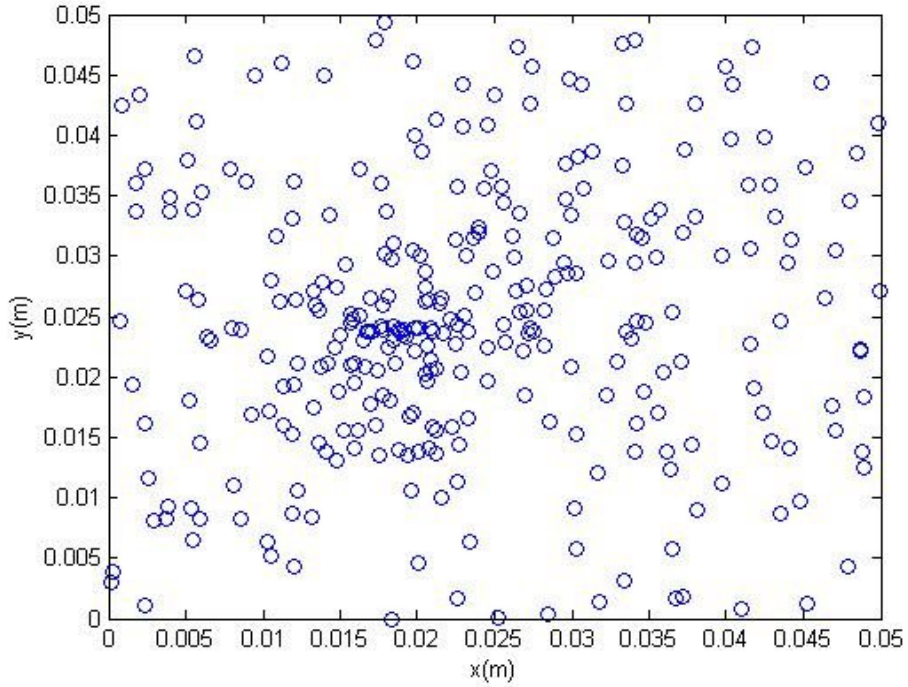

Figure 2.2 Vortex particles on the inflow plane at t=0.0100s.

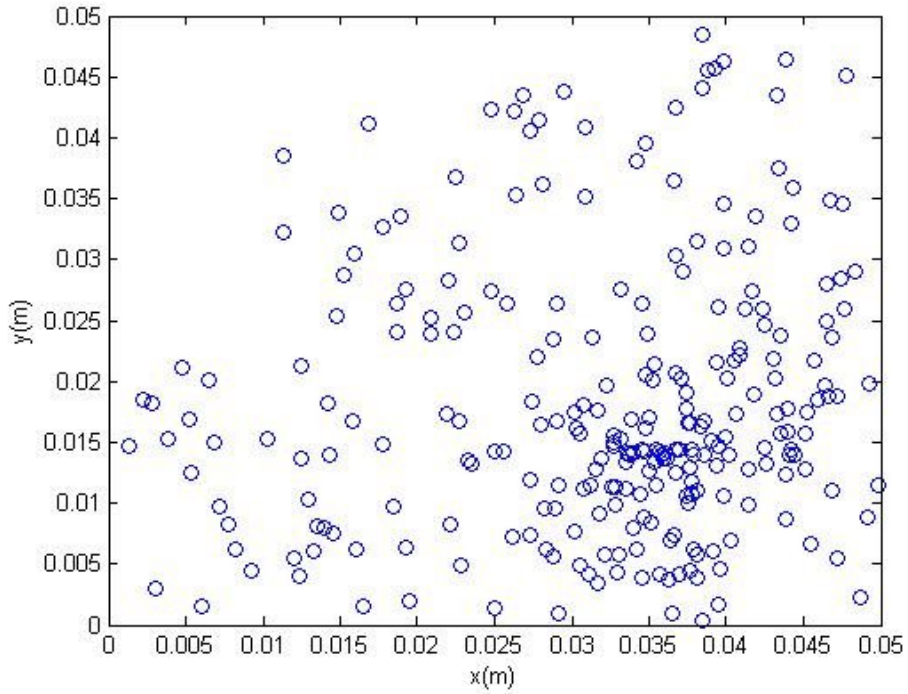

Figure 2.3 Vortex particles on the inflow plane at t=0.1000s.

To illustrate the motion of the particles on the inflow plane using this method of turbulence generation, plots of the location of particles at three different times are shown in Figures 2.1 to 2.3.

Up to this point, only the velocity components in the transverse direction of the flow have been taken care of. In order to supply fluctuations of velocity in the streamwise direction, the energy spectrum obtained by Huser and Biringen (1993) is used to provide sinusoidal fluctuations at three different frequencies corresponding to the three turbulence zones in the energy spectrum plot namely the energy containing range, the inertial sub-range and the dissipative range. The frequencies selected are 0.5Hz, 10Hz and 1000Hz with an amplitude of the lowest frequency fluctuation set based on Equations (2.4) and (2.5) by making use of the uniform inlet velocity at inlet. For the other two components of fluctuations, the turbulence kinetic energy spectrum result from Huser and Biringen (1993) is used as a rough guide to fix the values of amplitude. With these approximations, the amplitudes (units in m/s) were then set to 1.8E-3, 1.8E-4 and 1.0E-6 respectively. The phases for each of these fluctuations were subjected to a uniform random deviation arbitrarily chosen, between values of 0.0 and 1.0 radians (0.0° and 57.3°) at each inlet boundary face and time step. A more elaborate way to impose the fluctuations in the *z*-direction is, to apply the inverse Fast Fourier Transform to the magnitude and phase (as functions of frequency) data, related to the turbulence kinetic energy spectrum, from a similar flow, at the required points on the inflow plane. To obtain some degree of two point velocity cross-correlation, the amplitude can be varied depending on the local magnitude of the velocity on the plane.

2.4.3 Artificial Turbulence Method

This method was based on the directive proposed by Klein, Sadiki and Janicka (2003), di Mare et al. (2006) and Lund, Wu and Squires (1998). Basically, three random fields of fluctuating signals with average values of zero and unity variance were filtered here. The purpose of carrying out the filtering operation is to correlate the data in space and time (Equation (2.33)). At the inflow plane, the correlated data were transformed by an amplitude tensor related to the Reynolds stress tensor to give the correct amplitude to the

fluctuations. This result was superimposed on the mean velocity components.

The filter coefficients were derived from a presumed correlation function of the form

$$\frac{\overline{u_m u_{m+k}}}{\overline{u_m u_m}} = \exp\left(-\frac{\pi(k\Delta)^2}{4(n\Delta)^2}\right) \tag{2.21}$$

where Δ is the cell edge length and $k\Delta$ is the spacing between points m and $m+k$. $n\Delta$ is the prescribed length scale and u_m is the value of a fluctuating velocity component at point m, from a realisation of a filtering operation:

$$u_m = \sum_{n=-N}^{N} b_n r_{m+n} \tag{2.22}$$

where r_m is a series of random data with zero mean and unity variance, b_n are the filter coefficients and N is the support of the filter. The auto-correlation function is related to the filter coefficients by noting that $\overline{r_m r_n} = 0$ for $m \neq n$ and $\overline{r_m r_n} = 1$ for $m = n$:

$$\frac{\overline{u_m u_{m+k}}}{\overline{u_m u_m}} = \frac{\sum_{j=-N+k}^{N} b_j b_{j-k}}{\sum_{j=-N}^{N} b_j^2}. \tag{2.23}$$

The approximate value for the filter coefficient b_k was derived by Kempf, Klein and Janicka (2005). They showed that a normalised autocorrelation function can be obtained from the convolution of a random signal with zero mean and unit variance with a Gauss filter. The normalised autocorrelation function takes an approximate form below:

$$\frac{\sum_{j=-N+k}^{N} b_j b_{j-k}}{\sum_{j=-N}^{N} b_j^2} = \exp\left(-\frac{\pi k^2}{4n^2}\right). \tag{2.24}$$

The approximate filter coefficient $\tilde{b}_k$ takes the form below:

$$\tilde{b}_k = \exp\left(-\frac{\pi k^2}{2n^2}\right). \tag{2.25}$$

The steps taken to generate the artificial turbulence for the test case described in Chapter 5 are as follows:

1. A length scale $n\Delta$ is chosen based on the dimension of the edges of the domain at the inlet.

2. Three random fields R_α, α=x, y, z representing fluctuating signals with an average value of zero and unity variance are generated to occupy a three dimensional space. The inlet plane in Figure 2.1 is viewed in the negative z-direction The x, y and z-directions in this instance correspond to the -z, y and x-directions shown in Figure 2.1. The dimensions of R_α are [-N_x : N_x , -N_y+1 : M_y+N_y , -N_z+1 : M_z+N_z]. The support of the filter N_x, N_y and N_z was set to a value of 8 which is large enough to capture twice the length scale of integral eddies, based on, the dimensions of the inflow boundary. M_x and M_y are the number of cells in the x and y-directions on the inflow plane.

3. Filter coefficients based on Equation (2.25) are calculated.

4. The random signals are filtered using the filter coefficients from Step 3 above to obtain the spatially correlated data U_α for α=x,y,z:

$$U_\alpha(j,k) = \sum_{i'=-N_x}^{N_x} \sum_{j'=-N_y}^{N_y} \sum_{k'=-N_z}^{N_z} b(i',j',k') R_\alpha(i', j+j', k+k'). \tag{2.26}$$

5. The transformation $u_i = \bar{u}_i + a_{ij}U_j$ (changing the sub script of U from α to j) is

performed. $\overline{u}_i$ is the average (not resolved) value of the velocity component on the inlet plane. u_i can be regarded as the filtered or resolved velocity component on the inlet plane and a_{ij} is the amplitude tensor.

6. Data from Step 5 are copied to the inflow plane.

7. Data on the first *yz*-plane of R_α (on the inlet plane) are eliminated and the rest of the data in R_α are shifted forward (moved towards the inlet plane):

$$R_\alpha(i,j,k) = R_\alpha(i+1,j,k) \ . \tag{2.27}$$

8. New random numbers are assigned to the $R_\alpha(N_x,j,k)$ plane.

9. For each time step, Step 4 to Step 8 is repeated.

The amplitude tensor is related to the Reynolds stress tensor via:

$$\begin{aligned} a_{11} &= \sqrt{R_{11}} \\ a_{21} &= R_{21}/a_{11} \\ a_{22} &= \sqrt{R_{22} - a_{21}^2} \\ a_{31} &= R_{31}/a_{11} \\ a_{32} &= \left(R_{32} - a_{21}a_{31}\right)/a_{22} \\ a_{33} &= \sqrt{R_{33} - a_{31}^2 - a_{32}^2} \end{aligned} \ . \tag{2.28}$$

providing the required amplitude of fluctuations and cross-correlation of velocity. Other elements not listed above are zero.

The Reynolds stress tensor was obtained using the specified value of turbulence kinetic energy at the inlet as suggested by Ferziger and Peric (2002) via:

$$R_{11} = \frac{2}{3}\left(10^{-4}\bar{u}^2\right) \tag{2.29}$$

where the term in the bracket is the approximate turbulence kinetic energy. A $\bar{u}$ was taken as the uniform velocity component at the inlet. R_{22} and R_{33} were set equal to R_{11} assuming isotropic turbulence. Other non-zero Reynolds stress tensor entries were set to a value equal to 10% of R_{11}.

Based on the studies mentioned above, it can be said that it is more economical to use an accurate and efficient turbulence generator at the inlet as opposed to computing the laminar and transitional regions from a leading edge.

2.5 Applications with Unstructured Cartesian Meshes

There is a wide niche market demanding the use of Cartesian hexahedral meshes and the range of physical phenomenas simulated with this type of grid spans a wide spectrum. An example is provided by Hostikka and McGrattan (2001) where LES is coupled with a one-dimensional pyrolysis model, wherein spreading of full-scale flame was predicted in a room with wood linings. Chlond (1998) applied LES to trace the evolution of contrails for a half-hour period. He utilised a detailed microphysical model to resolve the size distribution of ice particles and studied the evolution of the size distribution. A related application was carried out by Emmerich and McGrattan (1998). In their case, LES was applied to study ventilating airflow in an enclosure. They reported that the Smagorinsky model gave good agreement with measured values and an LES with a dynamic sub-grid scale model, except, near the floor and ceiling. Sergent, Joubert and Le Quéré (2003) developed a local subgrid-scale diffusivity model to reproduce the turbulent-like behaviour of the local heat transfer in a square, differentially heated cavity. An analysis on the breakdown of spanwise vortices convected downstream form the leading edge corner of an open cavity was undertaken by Chang, Constantinescu and Park (2006). Yuan, Vanka and Thomas (2001) applied LES to predict continuous casting of steel in a rectangular cross-section geometry with inlet and outlet boundaries. Stoesser et al. (2003) predicted the flow around multiple cubes with two different channel height values with

uniform cube height arranged in a regular manner using LES while Rehm et al. (1999) performed LES on a single block representing simple buildings with multiple heights.

Combined with the relatively simple geometry and relatively low bulk Reynolds number involved in electronic component cooling (as opposed to that of an airliner or a power generation boiler) it makes an attractive candidate for the application of LES. Furthermore, Rodgers and Eveloy (2003) reported that the use of k-ε turbulence model did not satisfy the accuracy requirement in the prediction of a single component printed circuit board operating temperature. Roknaldin and Panigrahy (2004) analysed the heat transfer properties of a typical air-cooled electronic board with three chips in a row and a heat-sink problem by using LES.

Rembold (2003) computed the flow development in the near nozzle region and went further to predict the flow-induced acoustic radiation from a rectangular non-axisymmetric jet. By resolving noise-generating eddies aft of the trailing edge of a lifting surface, Wang and Moin (2000) predicted the far field acoustics with the help of an integral solution to the Lighthill equation. Related to this type of geometry are the backward and forward facing steps. Addad et al. (2003) used a commercial CFD code and discovered that acoustic sources of a forward-backward facing step originates from the vortical structures generated at the front edge of the obstacle. Wang, Zhang and Wang (2006) investigated the response, concentration and dispersion of particles by combining LES to predict the turbulent gas phase and Lagrangian method for the particle phase. The amplitude, frequency and streamwise evolution of the pressure field in the vicinity of the blunt trailing edge of a thick flat plate from LES simulations were used to provide data for the computation of radiated noise based on Lighthill's acoustic analogy, by Manoha, Trauff and Sagaut (2000).

An important issue to be noted is, when unstructured grids with non-regular variation (with respect to space) in cell sizes are used, the filter length varies as the mesh density changes. A desirable feature of the filter is its commutative property with the differentiation operator in the filtered Navier-Stokes equations. The same issue is

encountered when dealing with inhomogeneous turbulent flows wherein the resolved eddy sizes change within the computational domain and the filter length needs to be adjusted with respect to the change in size of the resolved eddies.

Marsden, Vasilyev and Moin (2002) constructed an interpolation based, two-dimensional filter via a polynomial function. The value of the field variable at a point in space is the weighted sum of three neighbouring field values which form a triangle enclosing the point where the filtered field variable is to be calculated. The weights involved in this interpolating polynomial are treated as filter coefficients and are found by the matrix inversion of the three linear algebraic equations forming the polynomial interpolating function. Constraints are imposed on the filter coefficient moments to achieve the desired order of the commutation error. This yields filters that commute with the differential operator up to the degree of the polynomial preserving the original form of the unfiltered Navier-Stokes equations.

2.6 Parallelisation

This sub-section provides some background information on the important aspects of parallelisation.

2.6.1 Domain Decomposition

The goal of mesh or graph partitioning is, to divide the mesh into K equal sized parts with balanced workload and minimize the interprocessor communication overhead. K is a positive integer, typically, the power of two.

Some state of the art unstructured mesh partitioning software include METIS (Karypis and Kumar (1998)), JOSTLE, SCOTCH and CHACO. Walshaw, Cross and Everett (1997) compared the parallel dynamic graph partitioning performance of JOSTLE-MD to that of METIS, GREEDY and MRSB (Multiple Recursive Spectral Bisection). The authors claimed that their parallel, dynamic partitioning package, JOSTLE-MD, provides best-in-class partitions (minimum number of edge cuts) very rapidly for a wide range of processor sizes. Pellegrini and Roman (1996) compared their static mapping package,

SCOTCH with METIS and CHACO. They obtained comparable performance with the latter two partitioning packages.

METIS was chosen in this study because it was readily available, and installed easily. It is also very popular with many CFD researchers such as Zhao et al. (2003) and Parikh (2001). It was also claimed by Karypis and Kumar (1998) to be 10% to 50% better than those produced by spectral partitioning algorithms. Having mentioned the positive points, the package is still not perfect, for example, Hendrickson and Kolda (2000), for instance, pointed out that the standard graph partitioning approach minimizes a less than ideal objective function and METIS "suffers from limitations due to the lack of expressibility in the graph model".

2.6.2 Hardware and Software

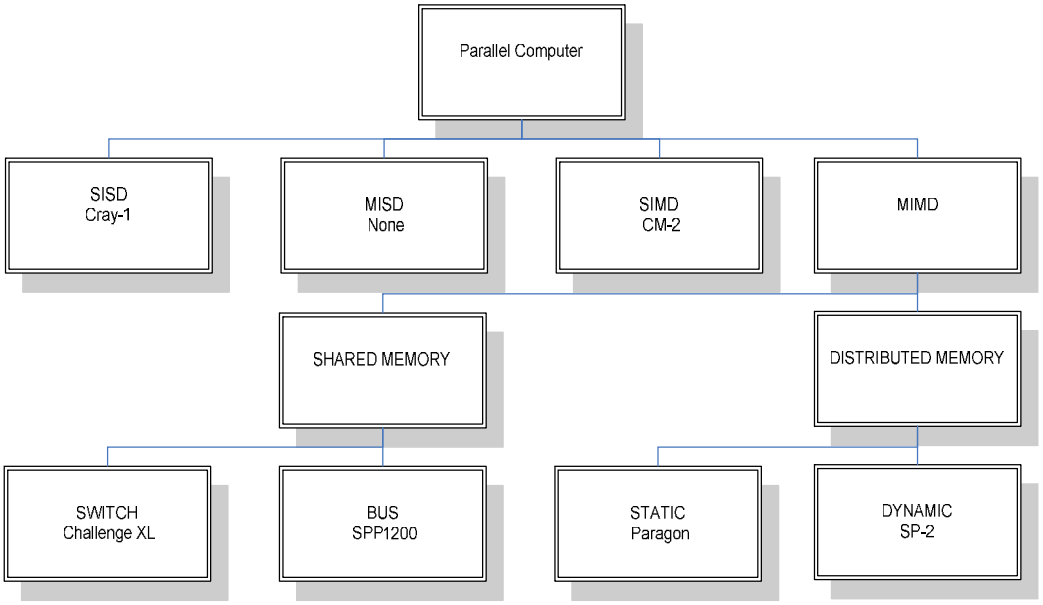

Figure 2.4 Classification of parallel computers.

A characterisation of existing parallel computing architecture is given in the tree diagram above (Figure 2.4). Modern machines tend to utilise more than one specific architecture, and as a result, arguments on classification of a machine persists. One of the challenges of parallel computing is posed by the hardware, specifically the network interconnect where there is a need for the communication to balance the computation. The hardware

can also be customised to deal with specific problems. An example is given by Taiji et al. (2003) on the petaflops MDGrape3 supercomputer, equipped with special purpose processors to simulate *N*-body problems and molecular dynamics simulation. They reported that the petaflops performance is achieved through solving the memory bandwidth bottleneck and lessening the heat dissipation problem.

In this study, a Sun Fire 15K server (an MIMD shared memory parallel machine) with 72x1.2GHz processors and 288GB of memory was used to run the jobs submitted by the user. The CPU/Memory board and I/O board are connected by the proprietary Sun Fireplane interconnect with a peak bandwidth of 172.8 GB/sec. Program development was carried out using the v880s front end servers. Each of the machines has 8x900MHz processors and 16GB shared memory on each machine. All servers are connected to the campus network.

When using a shared memory machine, OpenMP is considered a suitable tool that can be used for the development of parallel application. The Message Passing Interface (MPI) and Parallel Virtual Machine (PVM) libraries can also be used for the same purpose. These two packages can also be used for distributed memory machines. Jost et al. (2003) compared the performance of three programming paradigm on a shared memory parallel computer while Geist et al. (1996) compared the features of PVM with MPI. On the other hand, LeBeau et al. (2005) evaluated the performance of two CFD codes on commodity clusters using MPI.

2.6.3 Performance

The most important rule governing the speed-up of a parallel program is Amdahl's law which states that the speed-up of a parallel program is determined by the fraction of serial part contained inside the code assuming that the problem size is fixed. The speed-up of a parallel program is given by:

$$S = \frac{N}{(B * N) + (1 - B)} \tag{2.30}$$

where B is the fraction of the code which is strictly serial and N is the number of processes. The total efficiency E is defined as:

$$E = \frac{S}{N} \tag{2.31}$$

The fraction of the code which is strictly serial must be kept low in order to maintain the speed-up and total efficiency of that code as N is increased. In other words, the perfectly parallel part of the code must be maximised to reach the same goal.

In order to achieve favourable speed-up, detrimental effects such as blocking communications and worse still, deadlocking must be eliminated by the use of coupled or buffered send and receives. Algorithms which are inherently serial such as the Gaussian elimination and the Incomplete Lower-Upper methods should also be avoided.

Overlapping computation and communication may significantly improve total efficiency but this depends to some extent on the computer architecture available to run the parallel codes. Liu et al. (2003) compared the performance of MPI implementation with overlapping computation and communication over three low latency (less than 10μs) and high bandwidth (multiple gigabytes per second) network interconnects (protocol) for commodity clusters. They stated that better performing network interconnects for overlapping computation and communication avoid using message passing protocol that involves host intervention during handshake.

In order to understand the 'behaviour' of a parallel program, scalability calculations are needed. 'Behaviour' in this context means the change in requirements for computing and communication resources as the problem size is changed or the number of processes is increased. This task can be carried out analytically and experimentally. Davis et al. (2004) analysed the scalability of the BlueGene/L supercomputer using low-order as well as application level benchmark measured data. Results were compared against predictive

performance model and those from the ASCI Q machine with the conclusion that the performance of the new 131,072 processor machine is promising.

2.7 Turbulence

Turbulence is a highly irregular motion of fluid flow (both in time and space) with a wide range of time and length that can be described in a statistical manner. Turbulence is different from molecular motion of ideal gases in that the latter is completely random whereas the former contains repeating patterns of motion, more widely known as, coherent structures.

One of the most important features of turbulence is the increase in diffusivity which promotes the transfer of energy, momentum and mass. High velocity gradients result in the production of turbulence kinetic energy and extra stresses due to turbulence.

2.7.1 Kolmogorov -5/3 Law

The universal equilibrium theory describes the cascade process in which turbulence kinetic energy is transferred from larger eddies to smaller eddies. The smallest scales or Kolmogorov scales dissipate this energy as heat. The length, time and velocity scale or statistics of the smallest eddies can be described in terms of the dissipation rate ε (with units of length^2/time^3) and kinematic viscosity ν (with units of length^2/time) while the large or integral scales are L and U, the characteristic length and time respectively, belonging to the large scale motions. Unlike small-scale eddies, energy-bearing eddies provide the most effective mechanism for the transfer of mass, momentum in the flow domain (Hinze (1975)). Furthermore, the small-scale turbulent motions are more isotropic meaning that the normal turbulent stresses are all equal. It is therefore reasonable to simulate large-eddies and model smaller ones.

The hypothesis of similarity for incompressible viscous fluid with very large Reynolds number by Kolmogorov (1991) divides eddies into the energy containing range, inertial sub-range and dissipative range. The last two ranges are associated with small scales of motion whose statistical properties do not depend on the dynamics of the energy-bearing

range. The inertial sub-range is dependent on the rate of dissipation of turbulence kinetic energy ε and wave number κ (the reciprocal may be thought of as the eddy size or length scale) as shown in Equation (2.32) which is a physically meaningful equation obtainable from dimensional analysis by noting that the dissipation ε is proportional to v_l^3/l (again by dimensional analysis) where l is the length scale and v_l is the velocity scale of the inertial sub-range eddies. The energy spectrum function is then:

$$E(\kappa) = C_K \varepsilon^{2/3} \kappa^{-5/3}, \qquad 1/L << \kappa << 1/\eta \tag{2.32}$$

where C_K is the Kolmogorov constant, L is the integral length scale and η is the Kolmogorov length scale. *E(κ)* is defined as kinetic energy per unit mass per unit wavenumber (the reciprocal of wavelength). One of the most sought after results in LES is the evidence of existence of the inertial sub-range as shown in Figure 2.5. This will indicate that eddy sizes down to the inertial-sub-range scale have been succesfully simulated.

It is worth noting that the Kolmogorov constant C_K is not universal (meaning that it is dependent on the statistics of the energy containing eddies) if spatial fluctuations of the dissipation rate of turbulence kinetic energy per unit mass ε depends on flow structures associated with the integral length scale, known as intermittency. This was put forward by Landau and Lifshitz (1987).

Nevertheless, the deep physical insight provided by Kolmogorov makes the -5/3 law an indispensable guide in developing LES codes. Worthy (2003) provides a precise classification of different length and time scales as well as eddy ranges frequently encountered when dealing with turbulent flows.

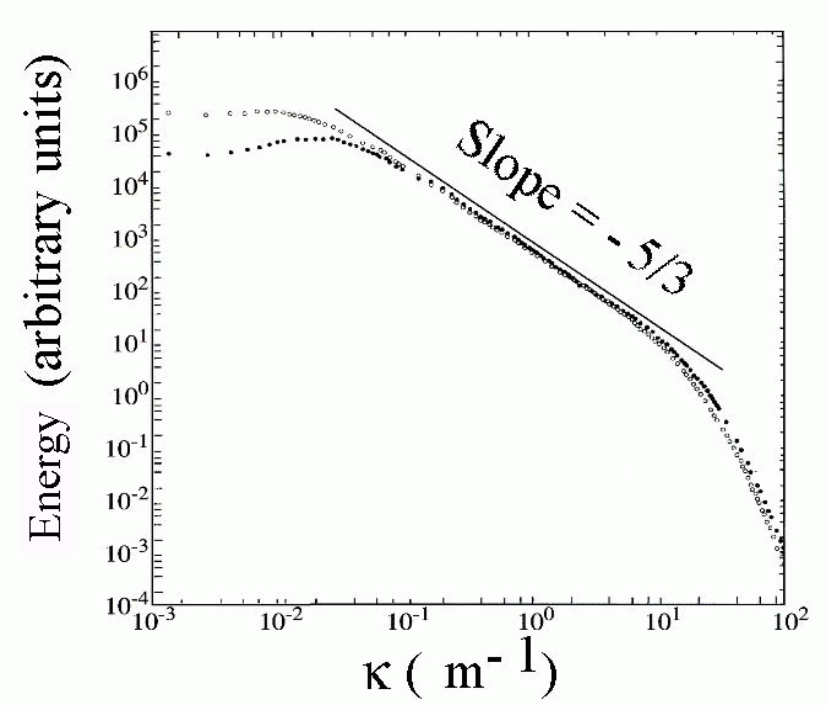

Figure 2.5 Typical energy spectrum for a turbulent flow.

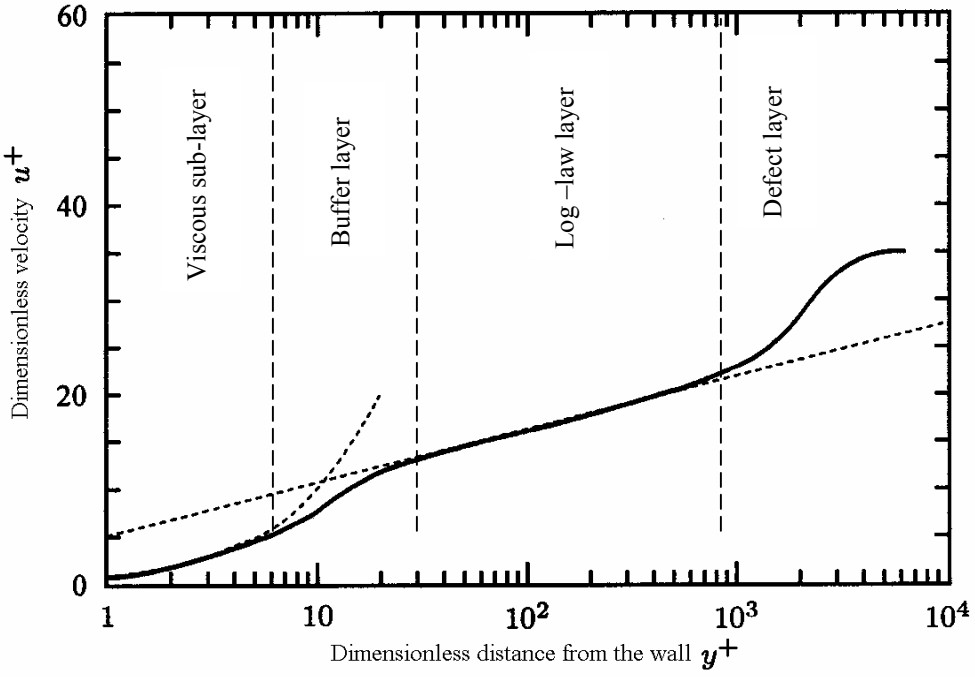

Figure 2.6 A typical turbulent boundary layer velocity profile.

2.7.2 Turbulent Boundary Layer

Since this study involves the use of no-slip impermeable wall boundaries, there is a need to gain some understanding of the physics of the turbulent flow in the region of these boundaries. The turbulent boundary layer is visualised by a layer of fluid located next to a solid boundary with an average velocity value of a certain fraction of the relative free-stream velocity value. It can be divided into an inner region and an outer region. In the former, the shear stress is approximately constant and is normally equated to the wall shear stress.

The turbulent boundary layer velocity profile is shown in Figure 2.6. y^+ is the non-dimensional distance normal to the wall, u^+ is the dimensionless velocity and δ is taken as the boundary layer thickness. The inner region of a turbulent boundary layer can be divided into the viscous sub-layer ($y^+<5$), the buffer layer ($5<y^+<30$) and the log-law layer ($30<y^+$ and $y/\delta<0.2$). In the log-law layer, eddy viscosity dominates over molecular viscosity. In the viscous sub-layer, the opposite is true while in the buffer layer the eddy viscosity is of the same order as the molecular viscosity. Next to the inner region exists the defect layer ($0.2<y/\delta<1$). In this region, inertia forces dominate over viscosity. Within the boundary layer, turbulence, including the small scales is anisotropic.

Starting from the Reynolds averaged momentum equation, the non-dimensional velocity profile of a turbulent flat plate boundary layer (two-dimensional, fully developed, parallel to the flat plate with zero pressure gradient) as shown in Figure 2.6, for each region, can be described in terms of the non-dimensional distance from the wall. This is explained in more detail in the following sub-chapters.

2.7.3 Two-Point Velocity Correlations

To investigate the length and time scales of turbulence, two point velocity correlations can be used. A two point correlation in time (at a given location in space) can be related to a two point correlation in space (at a given time) via Taylor's hypothesis:

$$\frac{\overline{u(\vec{x},t)u(\vec{u},t+t')}}{\overline{u^2(\vec{x},t)}} \approx \frac{\overline{u(\vec{x},t)u(\vec{x}+\vec{r},t)}}{\overline{u^2(\vec{x},t)}} \tag{2.33}$$

where u is the streamwise component of velocity, normally used in experimental flow with stationary turbulence, $\vec{x}$ is the vector determining the location in space of the measuring points, $\vec{r}$ is the displacement vector joining two points in the flow domain and t' is a time displacement. When periodic boundaries are used, the space correlation data can be utilised to determine the lengths of a computational domain to avoid spurious results. This length must be at least twice as large as the distance for negligible correlation between two points.

2.8 Closure

This chapter has described current development in LES involving a number of different aspects such as areas of application, boundary conditions and computing requirements. This may serve as a guide to focus on a specific area of research with an aim to expand the current knowledge in LES. The following chapter discusses the development of the flow solver.

CHAPTER 3

Numerical Schemes

This chapter introduces background information on turbulence first since the approach to tackle turbulence determines the type of flow solver and the class of numerical schemes employed in the simulations. This is followed by a description of the governing equations pertinent to Large Eddy Simulation (LES) relevant to the type of fluid and flow defined in Chapter 1. Only the impermeable solid wall boundary is discussed here, since this is the boundary type which is used in all test cases described in later chapters. Treatments of other boundary types applied to specific cases are discussed in relevant chapters.

The theory progresses to description of the step-by-step process (mainly in increasing functionality or capability) in developing a three-dimensional, unstructured Cartesian mesh, parallel LES code after evaluating numerical factors and available options carried out earlier. Validation of the code is also included in this chapter.

3.1 Governing Equations and Filtering

This study predicts turbulent incompressible flow using the LES technique. In LES, the instantaneous field variable f, is divided into the resolved part (denoted by an overbar symbol) and the modelled or filtered part (denoted by a prime symbol):

$$f = \bar{f} + f'. \tag{3.1}$$

The resolved part is obtained through the process of filtering which is in fact a convolution process. The general form of a filter is a convolution process:

$$\bar{f}(\vec{x},t) = \iiint f(\vec{\xi},t)g(\vec{x}-\vec{\xi};\Delta)d^3\vec{\xi} \tag{3.2}$$

where Δ is the filter width and g is the filter function. It is important to note that, when using a filter with the above form and applying the derivative theorem (Bracewell 1965), the differential operation and convolution operation commute, thanks to the uniform cell edge lengths of the meshes used in the computations of the test cases described in superceding chapters. If a non-uniform orthogonal mesh is used, the value of Δ can be found from $(\Delta_1\Delta_2\Delta_3)^{1/3}$ where the subscripts indicate the Cartesian coordinate directions, maintaining commutivity.

To separate the large and small scale components of the flow, filtering must be carried out. One of the earliest filters used in Large Eddy Simulation is the volume-average box filter by Deardorff (1970). Filtering can be implemented either explicitly in the physical space or implicitly in the spectral space. An example is given by Bouffanais et al. (2006) where both nodal and modal filters were used to study flow in a cubic cavity. On the other hand, the monograph by Sagaut (2001) provides a formal and comprehensive introduction to filtering. When filtering is performed in spectral space, the fluctuations of the field variables as a function of coordinate position is transformed into the frequency domain by the use of efficient transform algorithms such as the Fast Fourier Transform. The product of the filter function and fluctuating field variable spectrum is then carried out in the frequency domain. Consequently, the inverse transform to the physical space domain is performed on the filtered fluctuating field variable. Specific details regarding this technique can be found in Brigham (1974) and Oppenheim (1983).

The dependency of the temporal commutation error on a time-varying filter width was investigated by Leonard, Terracol and Sagaut (2007). This study was motivated by the need to couple LES with dynamic grids such as adaptive mesh refinement. They concluded that with a Gaussian filter, undesirable commutative error appear if the filter

cut-off length varies rapidly with time. Sagaut and Grohens (1999) defined a number of equivalence classes for multiple discrete filters. Besides, they investigated the sensitivity of several SGS models to these filters on a freely decaying homogeneous isotropic turbulence. In contrast, Sagaut, Comte and Ducross (2000) derived filtered SGS models with reduced sensitivity on the low frequency modes.

In this study, filtering was introduced explicitly through the action of central differencing scheme, for a given location in the computational domain:

$$\frac{\partial \overline{u}}{\partial x} \approx \frac{u(x+\Delta, y, z, t) - u(x-\Delta, y, z, t)}{2\Delta}. \tag{3.3}$$

Equation (3.3) can be written as:

$$\frac{\partial \overline{u}}{\partial x} = \frac{d}{dx}\left[\frac{1}{2\Delta}\int_{x-\Delta}^{x+\Delta} u(\xi, t) d\xi\right] \tag{3.4}$$

which may be interpreted as a filtering operation. The term in the parentheses can be generalised as:

$$\overline{u}(x,t) = \frac{1}{2\Delta}\int_{x-\Delta}^{x+\Delta} u(\xi,t) g(x-\xi;\Delta) d\xi \tag{3.5}$$

which is essentially Equation (3.2) applied to a one dimensional instance. Filtering the incompressible Navier-Stokes equations with constant fluid properties thus produce:

$$\frac{\partial \overline{u}_i}{\partial x_i} = 0 \tag{3.6}$$

$$\frac{\partial \overline{u}_i}{\partial t} + \frac{\partial}{\partial x_j}\left(\overline{u_i u_j}\right) = -\frac{1}{\rho}\frac{\partial \overline{p}}{\partial x_i} + \nu \frac{\partial^2 \overline{u}_i}{\partial x_j \partial x_j} \tag{3.7}$$

or

$$\frac{\partial \overline{u}_i}{\partial t} + \frac{\partial}{\partial x_j}\left(\overline{u}_i \overline{u}_j\right) = -\frac{1}{\rho}\frac{\partial \overline{p}}{\partial x_i} + \nu \frac{\partial^2 \overline{u}_i}{\partial x_j \partial x_j} + \frac{\partial \tau_{ij}}{\partial x_j} \tag{3.8}$$

where ρ is the density and ν is the kinematic viscosity. The subgrid scale stress τ_{ij} can be written as:

$$\tau_{ij} = \overline{u}_i \overline{u}_j - \overline{u_i u_j} \tag{3.9}$$

From Equation (3.1), by rearranging terms:

$$\overline{u}_i = u_i - u_i'. \tag{3.10}$$

By substituting Equations (3.10) and (3.1) for Equation (3.9),

$$\tau_{ij} = \overline{u}_i \overline{u}_j - \overline{\overline{u}_i \overline{u}_j} - \overline{\overline{u}_i u_j'} - \overline{u_j' \overline{u}_i} - \overline{u_i' u_j'} \tag{3.11}$$

or:

$$\overline{u_i u_j} = \overline{u}_i \overline{u}_j + L_{ij} + C_{ij} + R_{ij} \tag{3.12}$$

where:

$$\begin{aligned} L_{ij} &= \overline{\overline{u}_i \overline{u}_j} - \overline{u}_i \overline{u}_j \\ C_{ij} &= \overline{\overline{u}_i u_j'} + \overline{\overline{u}_j u_i'} \\ R_{ij} &= \overline{u_i' u_j'}. \end{aligned} \tag{3.13}$$

L_{ij}, C_{ij}, R_{ij} in Equation (3.13) are the Leonard stress, cross-term stress and subgrid scale Reynolds stress tensors respectively. Rearranging equation (3.11), the filtered momentum equation is written as:

$$\frac{\partial \overline{u}_i}{\partial t} + \frac{\partial}{\partial x_j}\left(\overline{u}_i \overline{u}_j\right) = -\frac{1}{\rho}\frac{\partial P}{\partial x_i} + \frac{\partial}{\partial x_j}\left[\nu \frac{\partial \overline{u}_i}{\partial x_j} + \tau_{ij}\right] \tag{3.14}$$

where:

$$\begin{aligned} \tau_{ij} &= -\left(Q_{ij} - \frac{1}{3}Q_{kk}\delta_{ij}\right) \\ P &= \overline{p} + \frac{1}{3}\rho Q_{kk}\delta_{ij} \\ Q_{ij} &= R_{ij} + C_{ij}. \end{aligned} \tag{3.15}$$

Similar to the RANS case, there are multiple subgrid scale models for LES. Since high wave number eddies are more isotropic than the energy bearing eddies, the latter can be modelled more accurately. The simplest model is an algebraic one which relates the subgrid Scale (SGS) stresses τ_{ij} to the resolved strain rate tensor S_{ij}:

$$\tau_{ij} = 2\nu_T S_{ij} \tag{3.16}$$

where ν_T is the Smagorinsky eddy viscosity:

$$\nu_T = \left(C_S \Delta\right)^2 \sqrt{S_{ij} S_{ij}}. \tag{3.17}$$

The expression for the resolved strain rate tensor S_{ij} is:

$$S_{ij} = \frac{1}{2}\left(\frac{\partial \overline{u}_i}{\partial x_j} + \frac{\partial \overline{u}_j}{\partial x_i}\right) \tag{3.18}$$

and the scalar product of the resolved strain rate tensor S_{ij} is:

$$S_{ij}S_{ij} = S_{11}S_{11} + S_{12}S_{12} + S_{13}S_{13} + S_{21}S_{21} + S_{22}S_{22} + S_{23}S_{23} + S_{31}S_{31} + S_{32}S_{32} + S_{33}S_{33}. \quad (3.19)$$

C_S in Equation (3.17) is the Smagorinsky coefficient and Δ is the grid scale. In this study Δ takes the value of the cell edge length. The grid scale Δ represents the largest characteristic size of the unresolved scales. $C_S\Delta$ can be regarded as an analogue to the mixing length in Prandtl's classic mixing length model. Kim and Moin (1982) noted that the value of v_T must decrease with decreasing cell size or resolution since "v_T represent the action of the unresolved scales of motion on those that are resolved". Lilly (1967) gave an explanation of the determination of the parameter C_S for an isotropic, homogeneous and stationary turbulent flow in the absence of body forces, whereby a value of 0.01 is typically used. Isotropic here means that the statistical properties of turbulent motions are independent of direction while homogeneous implies that turbulence structure is quantitatively similar anywhere in the flow field. A stationary turbulence has average properties that are invariant with time. Meyers and Sagaut (2006) carried out a theoretical analysis on the behaviour of the standard Smagorinsky model with constant model coefficients. Results were compared to those using coefficients which vary with the ratio of the LES filter width to the Kolmogorov scale and the ratio of the integral length scale to the LES filter width. It was found that the model coefficient should vary strongly with the ratio of the former.

C_S is a dimensionless parameter which varies with space inside the computation domain and it should also vary from flow to flow. For example, in the near-wall region, C_S needs to be increased with increasing normal distance to the wall. To overcome this difficulty, the method of van Driest (1956) could be utilised. This method was based on the analogy with Stokes flow near an oscillating plate in a stationary fluid. The effect of this modification is to reduce the value of the characteristic length for cells next to walls. The form of the modified Smagorinsky coefficient C_{SD} is:

$$C_{SD} = C_S\left(1 - e^{-y^+/A^+}\right) \tag{3.20}$$

with the constant A^+ set to 25. y^+ in Equation (3.20) is the dimensionless distance from the wall in viscous wall units:

$$y^+ = \frac{\rho u_\tau y}{\mu} \tag{3.21}$$

where u_τ is the shear or friction velocity. By assuming that the flow in this region is in local equilibrium (production and dissipation nearly equal):

$$u_\tau = C_\mu^{1/4}\sqrt{k}\ . \tag{3.22}$$

where C_μ is an empirical constant and k is the turbulence kinetic energy per unit mass.

The Smagorinsky model can be related to Prandtl's mixing-length hypothesis, which makes use of the gradient-diffusion process relating to the molecular transfer of momentum to lumps of fluid particles that stick and move together.

Another difficulty encountered at solid boundaries is the extremely thin viscous sublayer which relatively decreases in thickness as the bulk Reynolds number is increased. In this region, viscous stresses overcome turbulent stresses making the turbulence model inapplicable. Furthermore, resolving this layer is prohibitively expensive. To tackle this issue, the 'law of the wall' can be used. The validity of this approximation depends on how closely the real flow corresponds to the assumptions such as those given by Launder and Spalding (1974). Strictly speaking, this method is valid for the average but not the instantaneous profile. In the log-law layer of a turbulent boundary layer, the dimensionless velocity profile is:

$$u^+ = \frac{\overline{u}_t}{u_\tau} = \frac{1}{\kappa}\ln\left(y^+\right) + B, \qquad 30 < y^+, y/\delta < 0.2 \tag{3.23}$$

where $\overline{u}_t$ is the mean velocity parallel to the wall, κ is the von Karman constant, B is an empirical constant related to the thickness of the viscous sublayer and δ is the boundary layer thickness. In addition, κ is set to 0.41 and B is equal to 5.2 for the cases described in Chapters 4, 5 and 6. From Equations (3.22) and (3.23) the wall shear stress can be related to the velocity at the first grid point above the wall through:

$$\tau_W = \rho u_\tau^2 = \rho C_\mu^{1/4} \kappa \sqrt{k} \frac{\overline{u}_t}{\ln\left(y^+ E\right)} \tag{3.24}$$

where $E=e^{\kappa B}$. The law of the wall must be utilised with care when the boundary layer is not well behaved such as, in separated flows. A safer way to deal with separated flows is to increase mesh density in the separation region and also ensure that the value of y^+ is less than one, resolving the viscous region next to the wall.

3.2 Flow Solver

The flow solver used in this study is the second order accurate in time Adams-Bashforth Crank-Nicolson scheme. The method described here is similar to the one by Peyret and Taylor (1983). Other variants of this method are described by Ferziger and Peric (2002) and Kim and Moin (1985).

The reasons for using this algorithm are, firstly it allows the use of larger time steps than explicit schemes and secondly, the order of temporal accuracy delivered strikes a balance between computing cost and the quality of results. It is also favourable to other popular algorithm such as SIMPLE because it has no internal loops. This algorithm is also very popular with LES researchers and is quite straightforward to program.

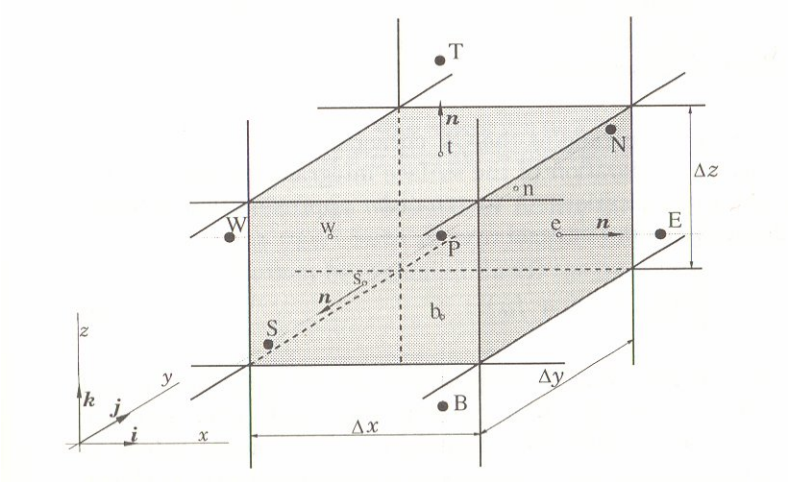

Figure 3.1 A typical cell in three dimensions with the notation used for a Cartesian grid following Ferziger and Peric (2002).

A typical cell (not located next to physical or sub-domain boundaries) is shown in Figure 3.1 as an aid in the explanation of finite volume discretisation in this chapter. In three dimensions, there are six plane faces belonging to a cell. These are marked as *e*, *w*, *n*, *s*, *t* and *b* indicating the orientation of cell faces according to compass direction. This typical cell has a volumetric centre at node *P* while *E*, *W*, *N*, *S*, *T* and *B* indicate the nodes of neighbouring cells according to compass direction. The cell edge length is denoted by Δ while the unit vector normal to a face is $\vec{n}$.

To derive the mass conservation equation, the mass balance inside a control volume must be considered. This can be explicitly stated as follows. The rate of increase of mass in a fluid volume must be equal to the net rate of flow of mass into the fluid volume. The mass conservation equation in integral form dropping the overbars for the resolved quantities is then:

$$\int_S \rho \vec{v} \cdot \vec{n} d\vec{S} = 0. \tag{3.25}$$

The starting point for the derivation of the momentum equations is Newton's second law which states that the rate of change of momentum of a fluid particle must be equal to the sum of forces on the particle. The forces acting on a fluid particle can be divided into two

groups. The first one is called surface forces, typically originating from pressure and also viscous forces. The second type of force is called body forces; for instance, gravitational force acting on the mass of the fluid particle. The momentum equation with no body force can be written as:

$$\frac{\partial}{\partial t}\int_{\Omega}\rho u_i d\Omega + \frac{3C^n - C^{n-1}}{2} - \frac{D^{n+1} + D^n}{2} + \int_{\Omega}\frac{\partial P^{n+1/2}}{\partial x_i}d\Omega = 0 \tag{3.26}$$

where C and D are the convective and diffusive terms respectively. Ω is the volume of a cell. Finite volume discretisation of the first term on the left hand side of Equation (3.26) yields:

$$\frac{\partial}{\partial t}\int_{\Omega}\rho u_i d\Omega \approx \rho\Delta\Omega\frac{u_i^{n+1} - u_i^n}{\Delta t}. \tag{3.27}$$

Using discretisation result from Equation (3.27), Equation (3.26) is split into an explicit second order (in time) Adams-Bashforth predictor step:

$$\rho\Delta\Omega\frac{u_i^* - u_i^n}{\Delta t} + \frac{3C^n - C^{n-1}}{2} - \frac{D^n}{2} = 0 \tag{3.28}$$

and an implicit second order (in time) Crank-Nicolson corrector step:

$$\rho\Delta\Omega\frac{u_i^{n+1} - u_i^*}{\Delta t} - \frac{D^{n+1}}{2} + \int_{\Omega}\frac{\partial P^{n+1/2}}{\partial x_i}d\Omega = 0. \tag{3.29}$$

Applying divergence operator and enforcing mass conservation to Equation (3.29), it yields the Poisson equation for modified pressure in integral form:

$$\int_{\Omega}\frac{\partial^2 P^{n+1/2}}{\partial x_i^2}d\Omega = \frac{\rho\Delta\Omega}{\Delta t}\frac{\partial u_i^*}{\partial x_i} \tag{3.30}$$

and by the application of Gauss' divergence theorem[3]:

$$\int_S grad\ P \cdot \vec{n} d\vec{S} = \frac{\rho \Delta \Omega}{\Delta t} \frac{\partial u_i^*}{\partial x_i}. \tag{3.31}$$

Approximating the convective term C in the u momentum equation on a uniform Cartesian mesh gives:

$$\int_S \rho u_i \vec{v} \cdot \vec{n} d\vec{S} \approx (\rho u_e A) u_e - (\rho u_w A) u_w + (\rho v_n A) u_n - (\rho v_s A) u_s + (\rho w_t A) u_t - (\rho w_b A) u_b. \tag{3.32}$$

The terms in parentheses in Equation (3.32) are the mass flow rates across each face of the cell. To avoid oscillation of pressure, a correction term is added to the interpolated velocity in the calculation of mass flow rates. This technique is described in more detail by Ferziger and Peric (2002). Essentially this correction term experiences an increase in absolute value when pressure oscillates rapidly and consequently, however, the pressure field is expected to be smoothed out. Approximating the diffusive term D for an incompressible, Newtonian fluid in the u momentum equation on a uniform Cartesian mesh gives:

$$\int_S \mu grad u_i \cdot \vec{n} d\vec{S} \approx \mu A \left(\frac{\partial u}{\partial x}\right)_e - \mu A \left(\frac{\partial u}{\partial x}\right)_w + \mu A \left(\frac{\partial u}{\partial y}\right)_n - \mu A \left(\frac{\partial u}{\partial y}\right)_s + \mu A \left(\frac{\partial u}{\partial z}\right)_t - \mu A \left(\frac{\partial u}{\partial z}\right)_b \tag{3.33}$$

where μ is the effective viscosity. A secondary contribution to the diffusive term resulting from the spatial variation of viscosity is given by:

[3] Gauss divergence theorem relates the integral of the divergence of a vector $\vec{v}$ over a volume Ω to the integral of the component of $\vec{v}$ normal to the surface which encloses the volume over the entire surface.

$$\int_S \left(\mu \frac{\partial u_j}{\partial x_i} i_j \right) \cdot \vec{n}\, d\vec{S} \,. \tag{3.34}$$

The magnitude of this term is assumed to be small compared to the term in Equation (3.33).

The diffusive term associated with a cell face that lies on an impermeable wall is the shear stress at the wall which is suggested in Equation (3.24).

The pressure gradient term in Equation (3.31) is approximated as follows:

$$\begin{aligned} \int_S grad\ P \cdot \vec{n} d\vec{S} \approx A\left(\frac{\partial P}{\partial x}\right)_e - A\left(\frac{\partial P}{\partial x}\right)_w + A\left(\frac{\partial P}{\partial x}\right)_n - A\left(\frac{\partial P}{\partial x}\right)_s + A\left(\frac{\partial P}{\partial x}\right)_t \\ - A\left(\frac{\partial P}{\partial x}\right)_b . \end{aligned} \tag{3.35}$$

At this point, the steps involved in the numerical solution of the flow solver algorithm is summarised in the following manner. Equation (3.28) is solved first to yield the provisional velocity components u_i^*. These values are then used in Equation (3.31) to give modified pressure *P* at an intermediate time level *n+1/2*. The last step is the solution of Equation (3.29) to obtain the velocity components u_i at the new time level *n+1*. This process is repeated until the required number of time steps is achieved.

This scheme can be categorised as a projection scheme because the provisional velocities obtained from the explicit step do not, in non trivial cases, satisfy mass conservation. The role of pressure is to correct the velocities by projecting out the divergence that produces part of the velocity field.

3.3 Discretisation Scheme

As pointed out in Chapter 3, the dissipative nature of second order upwind schemes favour the use of a second order central differencing scheme. While this scheme satisfies

conservativeness, there is an upper limit on the cell size since for the solution to be bounded, the Peclet number for any cell must be less than two. It is also worth mentioning that a second order central differencing scheme does not possess the transportiveness property. Another option is to use an upwind scheme with flux limiters.

With the central differencing scheme, the velocity component at a cell face (in this case the east face is considered) can be approximated as:

$$u_e \approx \frac{\left(u_E + u_P\right)}{2}. \tag{3.36}$$

and the discretisation of a diffusive term in Equation (3.33) can be written as:

$$\mu A\left(\frac{\partial u}{\partial x}\right)_e \approx \mu A \frac{\left(u_e - u_p\right)}{\Delta}. \tag{3.37}$$

and similarly for the pressure gradient term in Equation (3.35):

$$A\left(\frac{\partial P}{\partial x}\right)_e \approx A \frac{\left(P_e - P_p\right)}{\Delta} \tag{3.38}$$

The notations used in Equations (3.36), (3.37) and (3.38) follow that of Figure 3.1. Calculation of the shear stresses at a solid wall in Equations (3.28) and (3.29) involves first derivatives of the resolved velocity components tangential to the wall. This is discretised using two inner nodes and a parabolic fit to the boundary, resulting in a second order accurate approximation. This is described in more detail in Ferziger and Peric (2002). In this method, the normal stress at a solid wall is set to zero. The pressure at a solid boundary required in the solution of pressure through Equation (3.31) is approximated by projecting Equation (3.29) onto the unit normal $\vec{n}$ to the boundary, further details can be found in Peyret and Taylor (1983).

Rearrangement of terms in Equations (3.29) and (3.31) results in four sets of linear algebraic equations, i.e., one, for each field variable. The generic form of this equation is:

$$A_P \phi_P = \sum_m A_m \phi_m + Q_P \tag{3.39}$$

where the subscript P indicates the cell node at which the finite volume discretisation is carried out. Q_P contains all the terms with known variable values and ϕ is the field variable to be solved, in this case they are u, v, w and modified pressure P. The summation in Equation (3.39) is over all neighbouring nodes. For the filtered momentum equation, A_m in Equation (3.39) represents the effects of convection and diffusion while for the modified pressure equation, A_m contains the coefficients for the modified pressure P as written in Equation (3.38). Combining A_P and A_m will give the square sparse coefficient matrix A_c. Equation (3.39) is suitably modified to include boundary conditions. A suitable technique for the solution of a set of linear algebraic equations in the form of Equation (3.39) for an unstructured mesh is based on the Krylov subspace class of methods, described in Trefethen and Bau (1997) as well as Golub and van Loan (1996). Becker (2006) provides a thorough overview of linear algebraic equation solvers.

In this study, the set of linear algebraic equations are solved by the Restarted Generalised Minimum Residual (RGMRES) method. Essentially, this method works on minimising the norm of the residual. At every iteration step, an Arnoldi iteration is performed followed by the solution of a matrix least squares problem which may be solved using QR factorisation. To improve the rate of convergence of this method, the coefficient matrix needs to be preconditioned.

$$M^{-1} A_c \phi = M^{-1} Q_P \tag{3.40}$$

where M^{-1} is a left preconditioner. An example of this type of preconditioning is the diagonal (or Jacobi) left-preconditioner:

$$M = diag(A) \tag{3.41}$$

The Adams-Bashforth predictor step of Equation (3.28) can be calculated explicitly without further iteration since the only unknown value at the provisional time level is the value of the field variable at that particular node.

3.4 Stages of Development

The philosophy underlying the code development stage is to start from simpler units or routines which make up the flow solver and build on these developed units until a satisfactory working flow solver is obtained. In this case, the point of embarkation was the Poisson solver. Details of the stages are as follows:

3.4.1 Unstructured, Three-Dimensional Poisson Solver

This task was carried out to develop subroutines that would build lists for the unstructured grid. By using the cell and vertex partition data as well as a list of cell vertices, ghost or halo cells (cells surrounding the internal cells of the sub-domain) are obtained for a process. After determining the ghost cells of a process, subroutines inside this program build lists for the linear algebraic equations solver. Important lists include a face list for the calculation of fluxes at cell faces and a mapping list to transfer the correct data from neighbouring processes and storing them in the correct location. To ease the different tasks of data communication, computation and storage, three indexing systems for cells were used. Data were stored using the Harwell-Boeing format described in Duff, Grimes and Lewis (1992). In all the cases described below, one process owns only one sub-domain. The transfer of field variable data for the ghost cells was carried out by the Message Passing Interface (MPI) library.

Figures 3.2 and 3.3 show the data transfer routines to pass field variables from one process (internal cells) to another (ghost cells). Both methods use non-blocking communications. No data transfer takes place between two processes if one process has no ghost cells belonging to the other process.

The first successful (non-deadlocking) message passing routine is shown in Figure 3.2. The sequence of message passing is as follows. The first pass involves data transfer from one process to the next (higher ranking) process as shown in Figure 3.2. On the second pass, Process 1 transfers data to Process 3 and Process 2 transfers data to Process 4. On the third pass, Process 1 transfers data to Process 4, while the other two processes are idle. These steps are repeated in the reverse direction.

The second method of data transfer sends and receives messages in a cyclic manner. The first pass is shown in Figure 3.3. The second pass involves data transfer from Process 1 to Process 3, Process 2 to Process 4 and so on. The last pass transfers data from Process 1 to Process 4, Process 2 to Process 1 and so on.

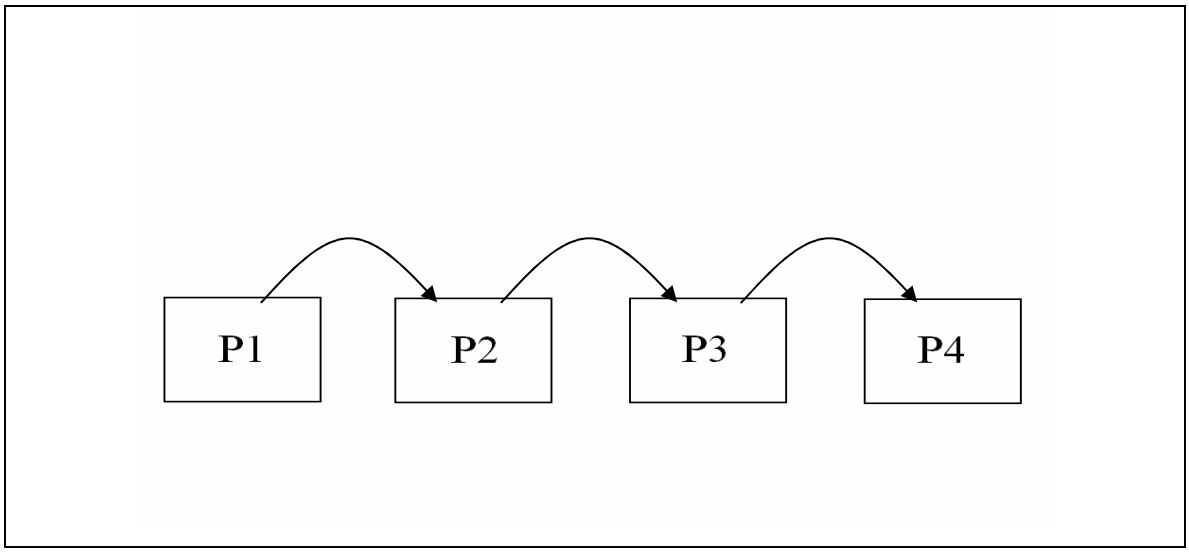

Figure 3.2 Linear message-passing.

The details of message passing for the second method can be described as follows:

Step 1. The number of cells involved in data transfer between two sub-domains is determined independently by both processes.

Step 2. Cells containing the data to be transferred (required by the ghost cells in the neighbouring sub-domain) are pinpointed by the use of a mapping list and these data are stored in an array.

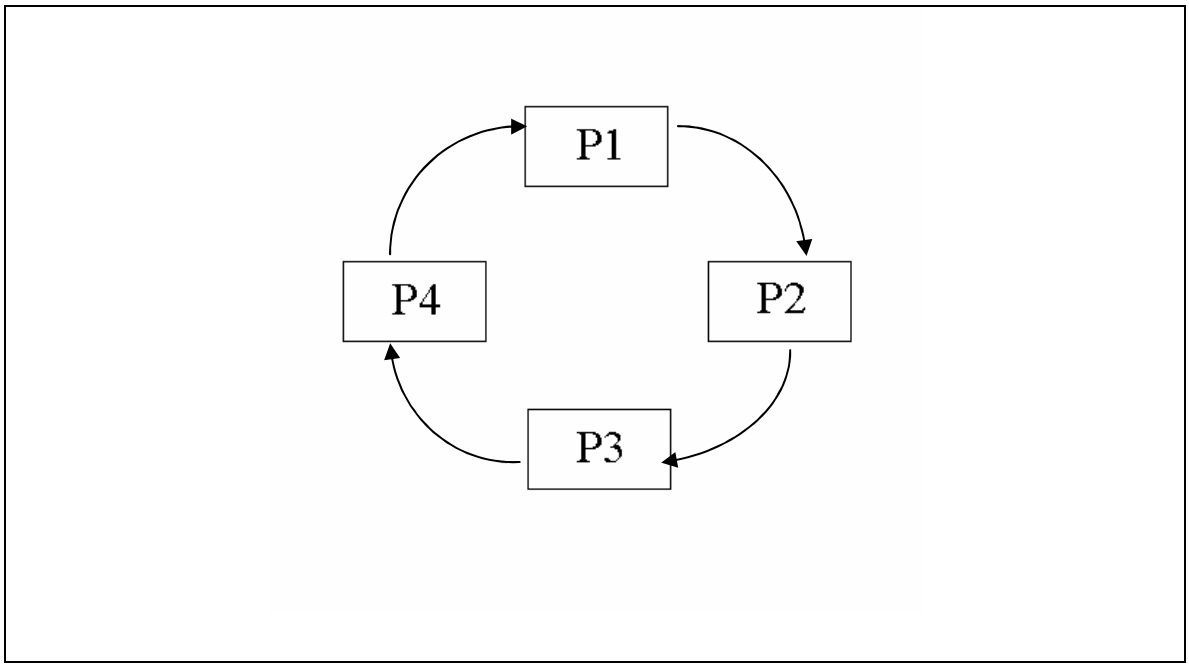

Figure 3.3 Cyclic message-passing.

Step 3. Data are passed to the neighbouring sub-domain using the MPI_ISEND and MPI_IRECV non-blocking subroutines every time the call to the message passing routine is executed in the flow solver.

Step 4. The receiving sub-domain inserts the received data into the list of field variable for the ghost cells after the call to the message passing routine has been executed in the flow solver.

This process is then repeated for all neighbouring sub-domains. It can be seen that to send a set of data, only one pair of send and receive is required. This cuts down communication time during the time integration loop by avoiding multiple sends and receives to transfer data. The Poisson solver is used (with some modification) in the third step, to solve the pressure equation.

Test runs were made using simple geometries to verify results from the code at each stage of the development. The outcome of these test runs are presented here.

Test runs were made to ensure that lists have been built correctly and inter-process data transfer has been carried out correctly. This should cut down development time for the unstructured Navier-Stokes solver.

The test case resembles a heat conduction problem. The domain is a cube with an edge length of one metre in all three directions. The number of cells used is ten in each coordinate direction. Heat conductivity was set to 1 W/mK. South, west and bottom boundaries were set to 100K while the north, east and top boundaries were set to 200K. The number of processors used was two. Another test run was also made with eight processors and 64 cells but results are not shown here.

Domain decomposition was done using METIS, a freely available package by Karypis and Kumar (1998). To obtain equal partitions (in terms of the number of cells in each partition), the mesh file is converted to its dual graph file. This graph file is then partitioned.

To solve the linear algebraic equations, the Restarted Generalised Minimum Residual (RGMRES) subroutine of PIM by da Cunha and Hopkins (1994) was used. The tolerance for stopping the RGMRES iteration was set to 10^{-10} based on the 2-norm residual values, whereby the diagonal (or Jacobi) left-preconditioning was used.

It can be seen in Figure 3.4 that the sub-domain edge-cuts performed by METIS are not straight. Results are compared to a structured grid code with a conjugate gradient Poisson solver by Mohamad Badry (2004).

From Figures 3.5 and 3.6 the code under investigation gave results which are in agreement with the reference data; this gives some confidence that the message passing routine is working as it was intended. Results are compared to a structured grid code with a conjugate gradient Poisson solver by Mohamad Badry (2004).

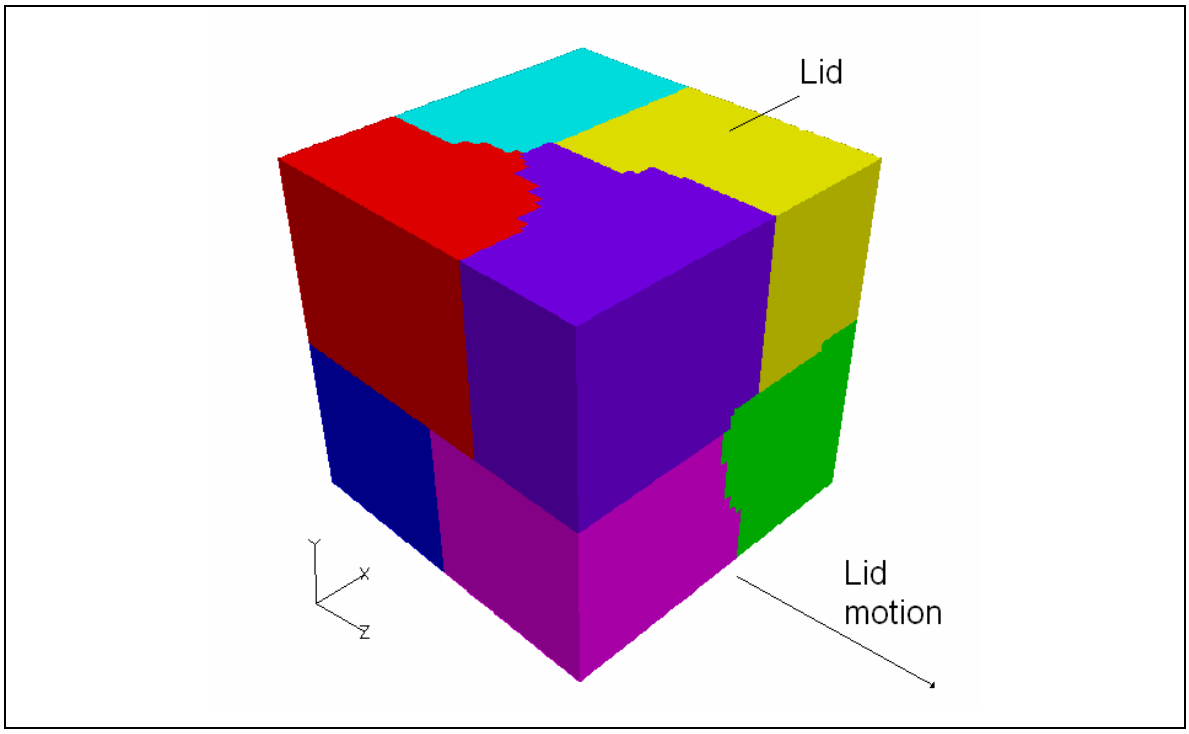

Figure 3.4 Computational domain partitioning by METIS.

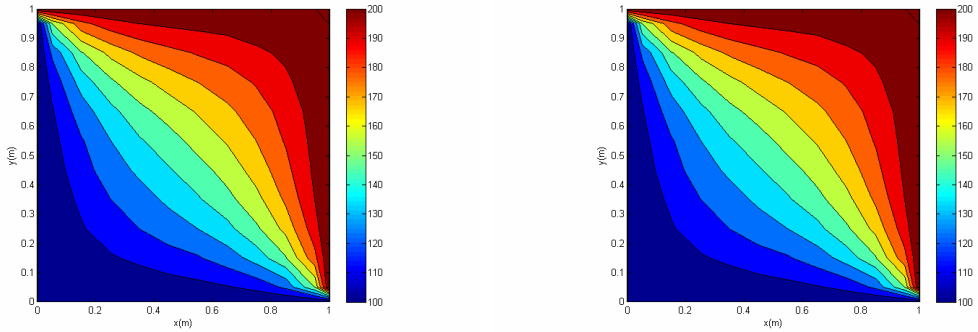

Figure 3.5 Comparison of scalar distribution with reference data (left) and developed code (right) with units in Kelvin.

The speed-up obtained from the Poisson solver is shown in Figure 3.7. For a fixed problem size, the speed-up decreases with increasing number of processes. This can be explained by applying Amdahl's law. The fraction of the serial part of the code must be reduced in order to improve speed-up. A practical way to achieve this is to increase the mesh size but this is not a universal rule since some algorithms have a ratio of communication to computation cost independent of the mesh size.

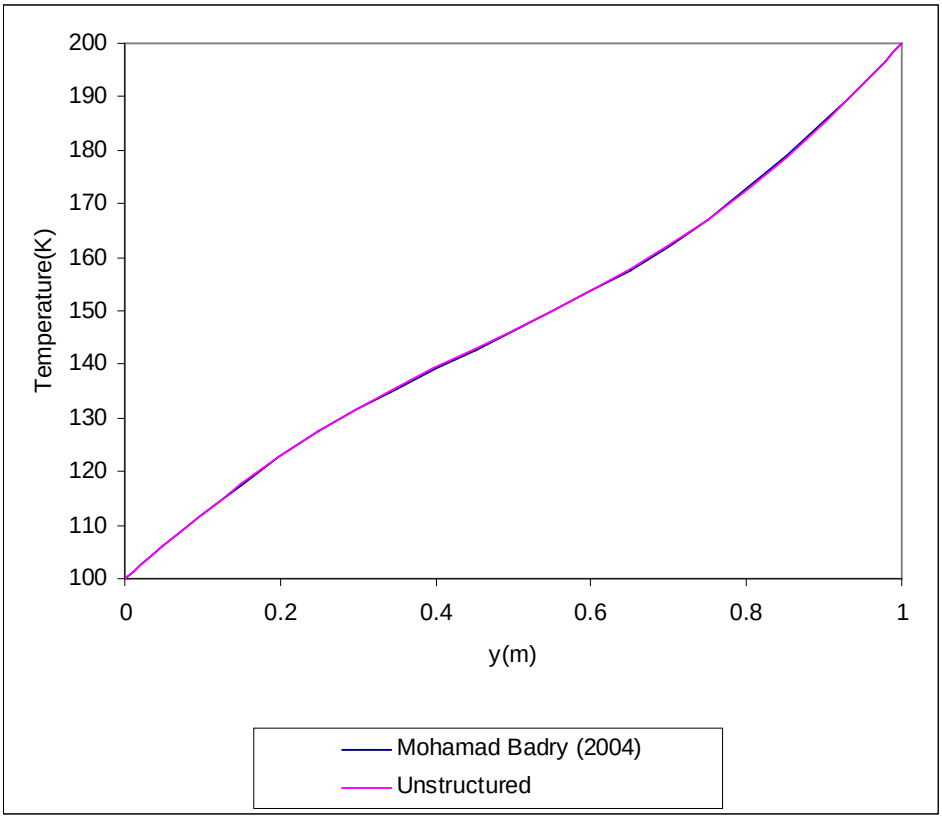

Figure 3.6 Plot of temperature against distance in the *Y* direction at x=0.5, y= 0.45.

The loop time for three different mesh sizes is shown in Figure 3.8. Loop time is the total time for running the simulation minus the initialisation time. The number of processors used is fixed at eight in this case. The line obtained is close to linear. This is to be expected as the amount of computation increases as the number of cells is increased. The slight increase in gradient with the number of cells increased could be due to the growing communication time as the size of data transferred gets larger. The slope of the line can be reduced by cutting down the number of repeated computations, by increasing cache hits. Performing more efficient communication, such as carrying out collective communication only once for multiple time steps, will also have a beneficial effect on the loop time.

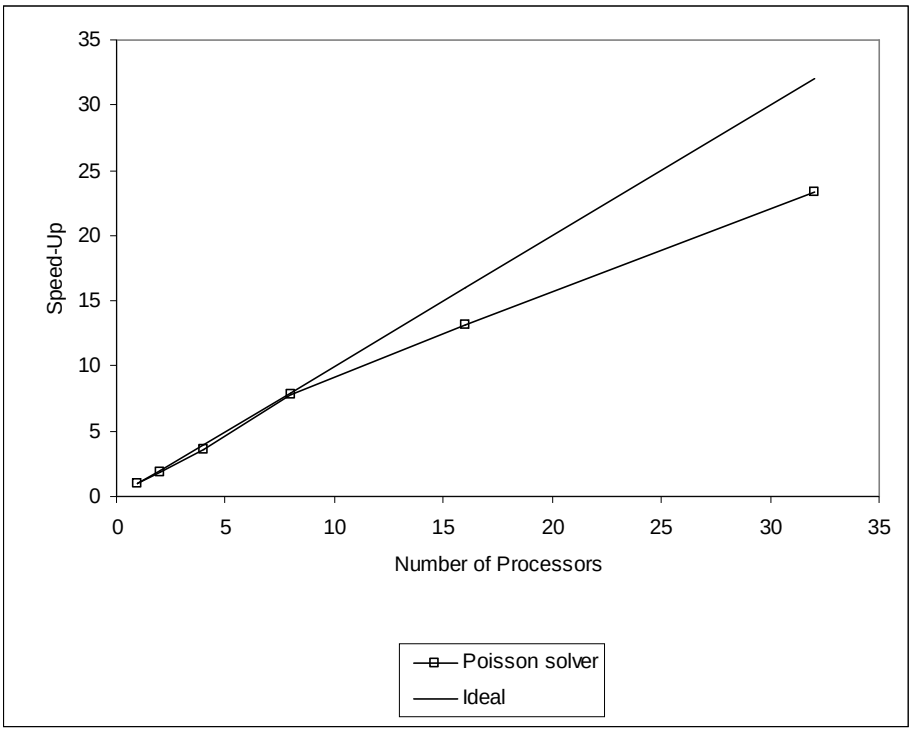

Figure 3.7 Speed-up of the parallel Poisson solver compared to the ideal slope.

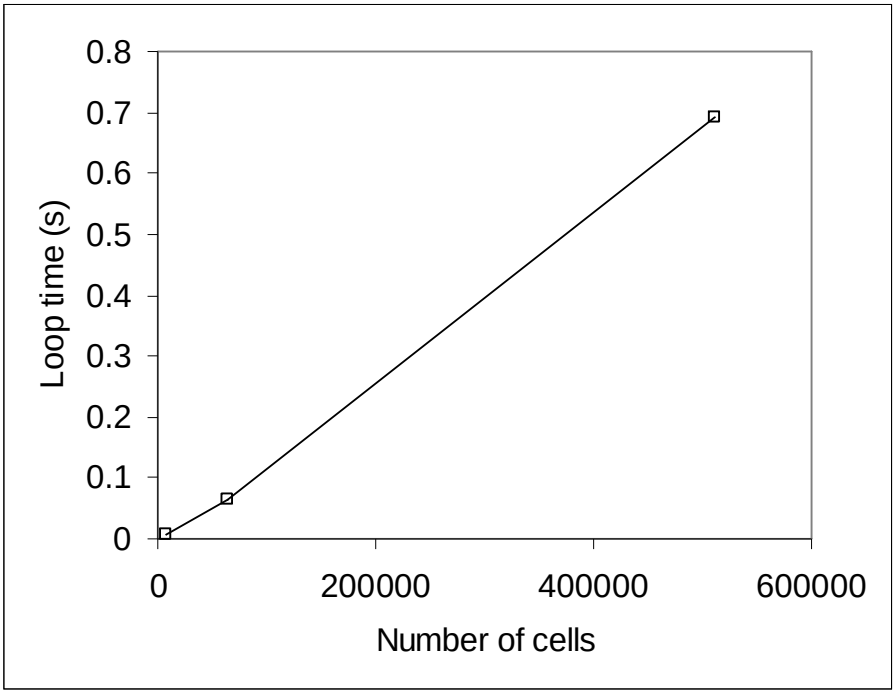

Figure 3.8 Variation of loop time with increasing number of cells.

3.4.2 Structured, Two-Dimensional Flow Solver

The main reason for developing a structured, two-dimensional flow solver is to have a functional, working Adams-Bashforth Crank-Nicolson solver. This program ensures that the algorithm and numerical schemes have been implemented correctly before the unstructured version is developed. The test case considered was a driven cavity flow at a bulk Reynolds number of 1,000. The geometry for this case is similar to that of the Poisson solver case, described in Figure 3.4.

The diffusive and convective terms were treated using central differencing scheme. All flow variables were initialised to zero. A ramp input to the speed of the lid was then applied for one second to avoid numerical difficulties during start-up. The steady-state lid speed was set to give a Reynolds number of one thousand based on the edge length of the cube. Time integration was carried out for seventy lid cycle time (the time taken for the lid to travel a distance equal to the edge length of the domain) given that the difference in field variable values at the monitoring location between two successive time steps is less than 10^{-4}.

Figure 3.9 shows the presence of the well known primary vortex and a sequence of secondary vortices at the lower corners of the domain. At this stage it can be stated that qualitatively correct results are produced by the code.

To check the order of accuracy of the Adams-Bashforth Crank-Nicolson scheme numerically, runs involving four different mesh sizes (20^2, 40^2, 80^2 and 160^2) were carried out. The strength of the primary vortex which is the mass flow rate from the primary vortex centre and the boundary was used to determine the spatial order of accuracy. The percentage error in circulation is shown in Figure 3.10. Basically, this error is the difference between the computed value and the value obtained by Erturk, Corke and Gökçöl (2005) using three different grid sizes, and Richardson extrapolation, in order to achieve a grid independent solution. It can be seen that the numerically obtained slope tends to the ideal slope for a second order method as the mesh is refined. In order to move towards the ideal slope as the cell size reduces, the time step size must also be

decreased. Another reason why the time step size needs to be reduced is due to transportiveness constraint in which case the Peclet number of a cell must not be larger than two. The time step size was set to 0.01s for the three coarsest grids and decreased to 0.001s for the finest mesh.

The order of accuracy of a method describes the rate of error reduction either spatially or temporally, but it does not state absolute magnitude of the error. Ferziger and Peric (2002) gave a formal derivation of an equation to approximate the order of the scheme by using values of a field variable on systematically refined grid.

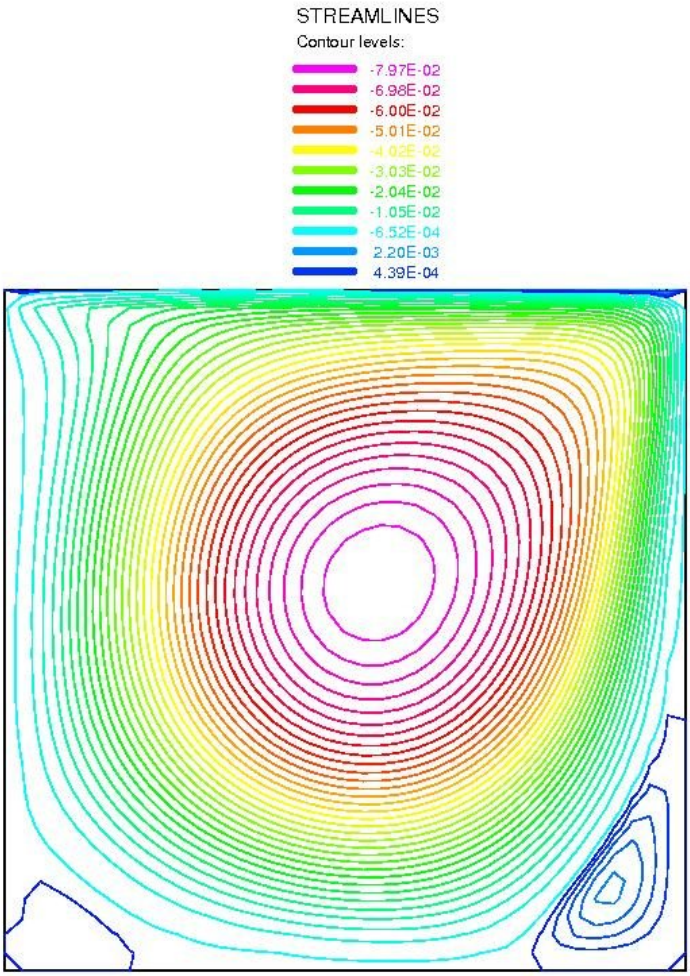

Figure 3.9 Streamlines of the driven cavity flow with units of streamfunction in kgm/s.

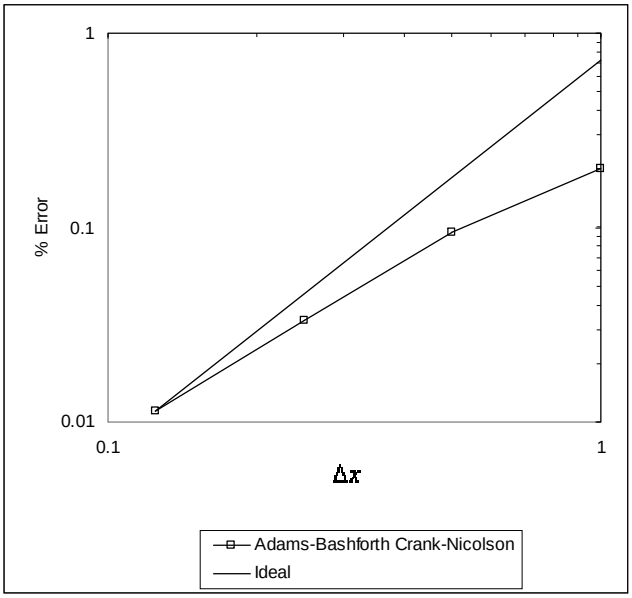

Figure 3.10 Strength of primary vortex with decreasing cell edge length (normalised with the edge length of the largest cell) and uniform mesh for the structured two-dimensional code.

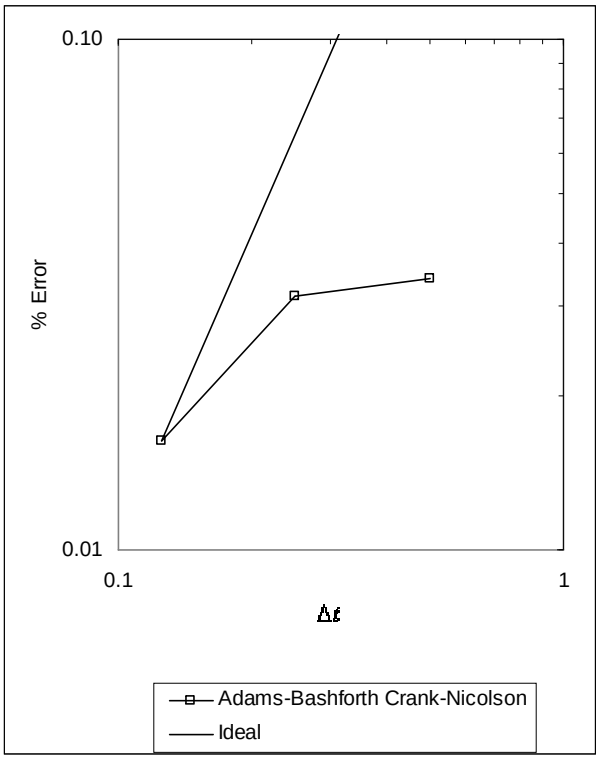

Figure 3.11 Strength of primary vortex with decreasing time step size (normalised with the largest time step size) and uniform mesh for the structured two-dimensional code.

The temporal order of accuracy was also investigated for this code. This is shown in Figure 3.11 for time step sizes of 0.004s, 0.001s and 0.0005s. The cell edge lengths were 0.025m, 0.0125m and 0.00625 respectively. The numerically obtained slope is moving towards the ideal slope, as in the case of reduced cell edge length stated above. The percentage error is going down at a significantly slower (with respect to time step size) rate, with about 40**%** difference, compared to the ideal slope hence further reduction of time step size (and also cell size) is required to achieve second order accuracy in time.

3.4.3 Unstructured, Three-Dimensional Flow Solver

This program extends the Adams-Bashforth Crank-Nicolson algorithm developed in the previous step to handle unstructured Cartesian grids by utilising the list building subroutines developed in the first step. The addition of the third coordinate direction is straightforward. The communication steps follow directly from the Poisson solver.

The west and east boundaries are assigned as symmetry boundaries, which means, the shear stress is zero on this boundary. The normal stress for a symmetry boundary is not zero but for the purpose of comparing results from this code to those obtained form the structured two-dimensional code above, convective and diffusive fluxes in the momentum equations as well as the pressure gradient in the east-west direction are set to zero.

This step is a continuation of the work done in developing the Poisson solver described earlier in this chapter. The momentum equations for the structured grid code developed previously were modified for the unstructured grid, taking into account the third coordinate direction for three dimensional flows. The set of lists built for the Poisson solver was extended to cater for the numerical solution of the splitted momentum equations via the Adams-Bashforth Crank-Nicolson algorithm.

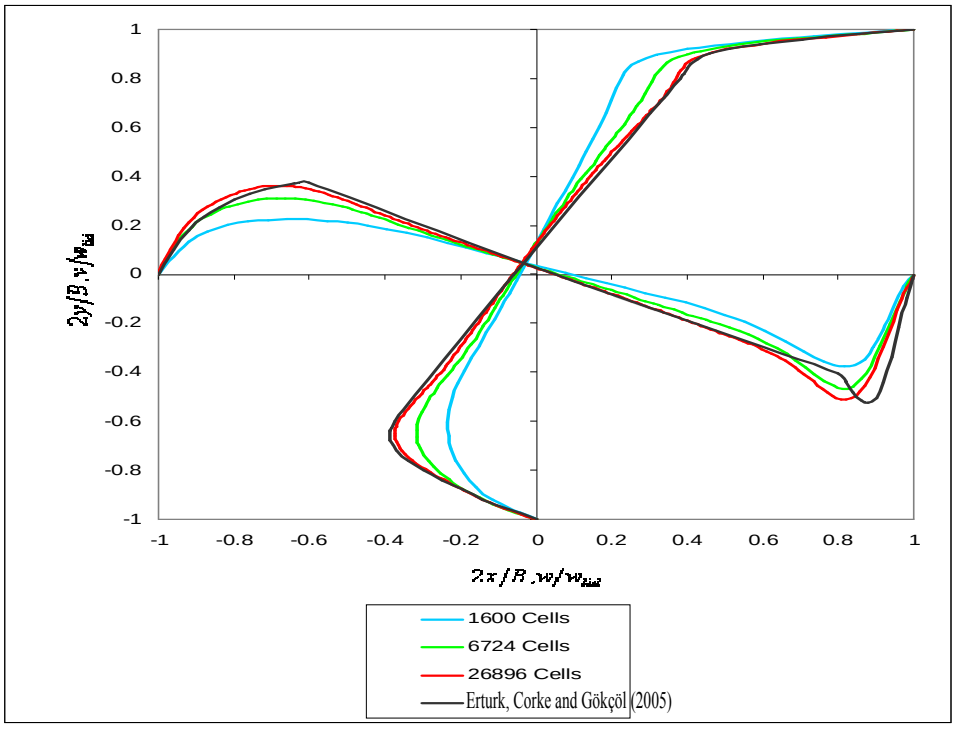

Figure 3.12 *u* and *v* velocity profiles along the vertical centreline.

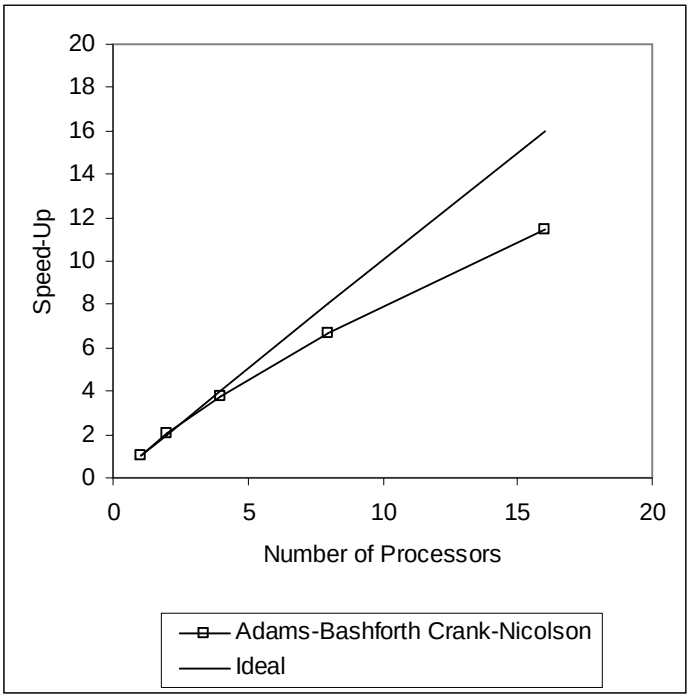

Figure 3.13 Speed-up of the three-dimensional unstructured Adams-Bashforth Crank-Nicolson code.

As illustrated in Figure 3.12, the spatial discretisation error reduces in a monotonous fashion as the grid size is doubled in both directions. Good agreement with the results of Erturk, Corke and Gökçöl (2005) for a laminar flow at a Reynolds number of one thousand based on the length of the lid and lid velocity magnitude is obtained by the finest grid. However, in regions of relatively strong convection, in comparison to diffusion, the differences are still significant.

The speed-up obtained when using up to sixteen processes from a test case with 80^3 cells shown in Figure 3.13 is quite satisfactory. With eight processes, the speed-up obtained was about seven. It is highly possible that the speed-up will improve by increasing the number of cells in the computation, thus decreasing the serial fraction of the code as given by Amdahl's law.

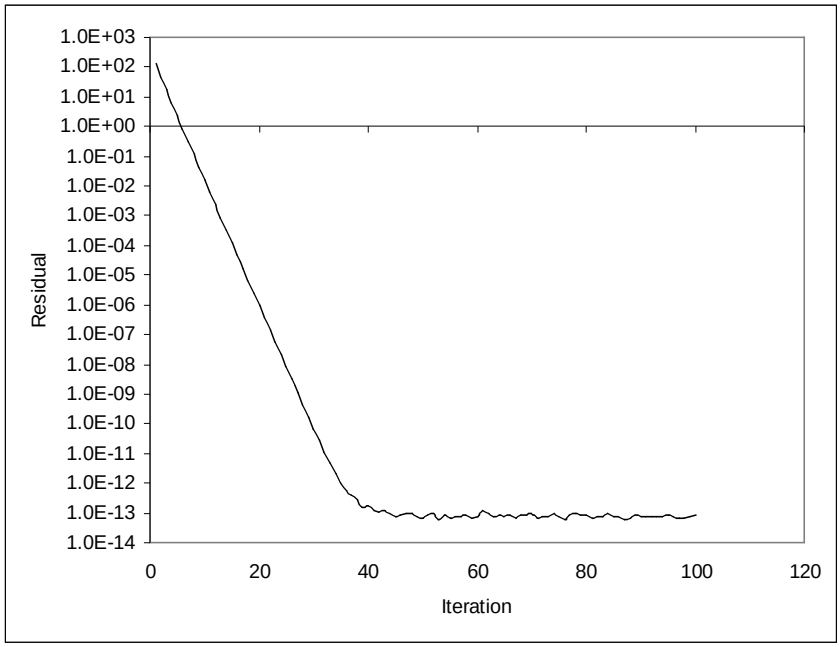

Figure 3.14 Reduction in the value of residual as iteration progresses.

The change in residual values as a function of iteration number of the linear algebraic equation solver for the first time step is shown in Figure 3.14. The field variables were initialised to zero in the domain and on the boundaries. The *y*-axis is on a logarithmic

scale whereas a linear scale is maintained on the *x*-axis. From the start of iteration until about thirty five time steps, the reduction of the residual values formed almost a straight line and beyond thirty five time steps, a steady average value of the residual at approximately 1.0E-13 was obtained. This plot helps in determining the maximum number of iterations for the RGMRES linear algebraic equations solver assuming that the successive time steps have a similar residual plot as the first one.

An attempt was carried out to perform overlapping computation and communication with the unstructured flow solver but results were not encouraging. The original form of the parallel program performed better in terms of wall clock time. Another strategy to improve this parameter is to group smaller messages into one big bundle and to reduce the total message volume. Ding and He (2001) realised this approach by employing a shrinking sub-domain method which do not require values of field variables at ghost cells to be updated for every single time step. Memory access time can also be reduced by resizing the coefficient matrix into smaller block matrices to fit cache size.

3.5 Closure

This chapter has described the specific form of the Navier-Stokes equations required to solve large eddies together with some physical insight into the process of filtering. Finite volume discretisation of the splitted momentum equations in the framework of the second-order accurate in time Adams-Bashforth Crank-Nicolson flow solver has also been carried out. Modifications required near a solid no-slip wall boundary on the turbulence model and differencing scheme has also been outlined.

Furthermore, the stages in the development of the Adams-Bashforth Crank Nicolson flow solver have been described in this chapter. This was followed by a presentation of results related to the validation of the source codes which indicates that the flow solver is behaving satisfactorily. Up to this point, only laminar flows have been considered. The next chapter will introduce the turbulence model into the code to solve a three-dimensional lid-driven cavity flow problem.

CHAPTER 4

Driven Cavity Flow

The goal of carrying out this simulation is to apply the flow solver developed in Chapter 3 to compute a true three-dimensional flow (with no symmetry boundaries as in Chapter 3). The goal is also to investigate the behaviour of the turbulence model by comparing simulation results to available data based on experiments and simulations. This case was chosen since steps to implement the no-slip wall boundary condition are well documented; consequently the geometry can also be easily meshed. In other words, this case presents a jump not too big from the development phase in Chapter 3 and other reference data widely available.

4.1 Test Case Description

In this sub-section, the geometry, boundary, fluid and initial conditions are described in detail, also discussed is the setting for the turbulence model constant.

Three different mesh sizes were used to investigate whether grid-independent solution is achievable. The number of cells used was 60^3, 80^3 and 100^3; hereafter denoted by Grid A, Grid B and Grid C respectively, with all cells having uniform edge lengths.

Comparison of profiles of mean velocity, root mean square velocity and the $\overline{w'v'}$ shear stress were carried out. Comparison was also made between results with and without law of the wall. The time-trace of instantaneous w velocity was also carried out. Using the same set of data, the power spectra of w velocity was plotted. These quantities are of

interest since they give indication on the flow structure inside the computational domain and they also clarify how well the turbulence model performs. If the value of the Smagorinsky constant C_s is too high, it causes excessive damping of the resolvable turbulence. On the other hand, if the value of this parameter is too low, excessive energy is accumulated at the higher wavenumbers in the one-dimensional energy spectra. The structure of the flow was provided by plots of velocity vector field at various cross-sections of the domain.

The Reynolds number of the flow was 10,000 based on the lid length of 0.15m and a steady-state lid velocity of 0.0667m/s. The dynamic viscosity of the fluid was set to 0.001Pas while the density was set to 1000kg/m^3.

At solid walls, the no slip condition was applied for velocities while the viscous normal stress was set to zero. The calculation of shear stresses at the walls has been described in detail in Section 3.1 and Section 3.3. If the mesh is fine enough, this can be considered as integrating to the wall which may tend towards DNS as the mesh is refined in the near wall region in which case all eddy sizes are considered resolved. Another way out is to refine the mesh to a level where the viscous sub-layer is resolved. The turbulence model must also be altered to account for the dominating effect of viscous stresses over turbulence stresses in this region. An example is given by Wang and Moin (2000). In their case, the wall shear stress was obtained from a simplified turbulent boundary layer equation and a mixing-length model with near wall damping. This resembles a two-layer low Reynolds number turbulence modelling approach frequently encountered in Reynolds averaged Navier-Stokes turbulence modelling. The sub-grid scale model was then applied to regions with $y^+>40$ which is outside the near wall region. The law of the wall was also utilised as an alternative method to the integration to the wall, even though the complicated flow structure of a driven cavity flow resulting in a non-regular development of the boundary layer poses here, a challenge, for the former.

The turbulence model used in this case was the Smagorinsky model as described by Equations (3.16) to (3.24). The difficulty at solid boundaries occurs due to the fact that

the energy-containing eddies is a function of the Reynolds number in this region where the size of energy-bearing eddies and smaller eddies overlap. Consequently, more responsibility is placed on the turbulence model to produce correct sub-grid scale stresses. Sub-grid scale stresses decrease sharply approaching the wall boundary; hence the need arises for C_s to be reduced. It is also desirable to have a value of zero for the eddy viscosity at the wall. The van Driest damping function described earlier in Section 3.1 can be used to satisfy these requirements.

Pressure at wall boundaries was extrapolated using a one-sided Taylor series expansion as described in Section 3.3. By using this expansion, the value of modified pressure at the walls was extrapolated from the neighbouring internal cell nodes. The pressure gradient was treated as a source term in the computation of velocity components at the new time level.

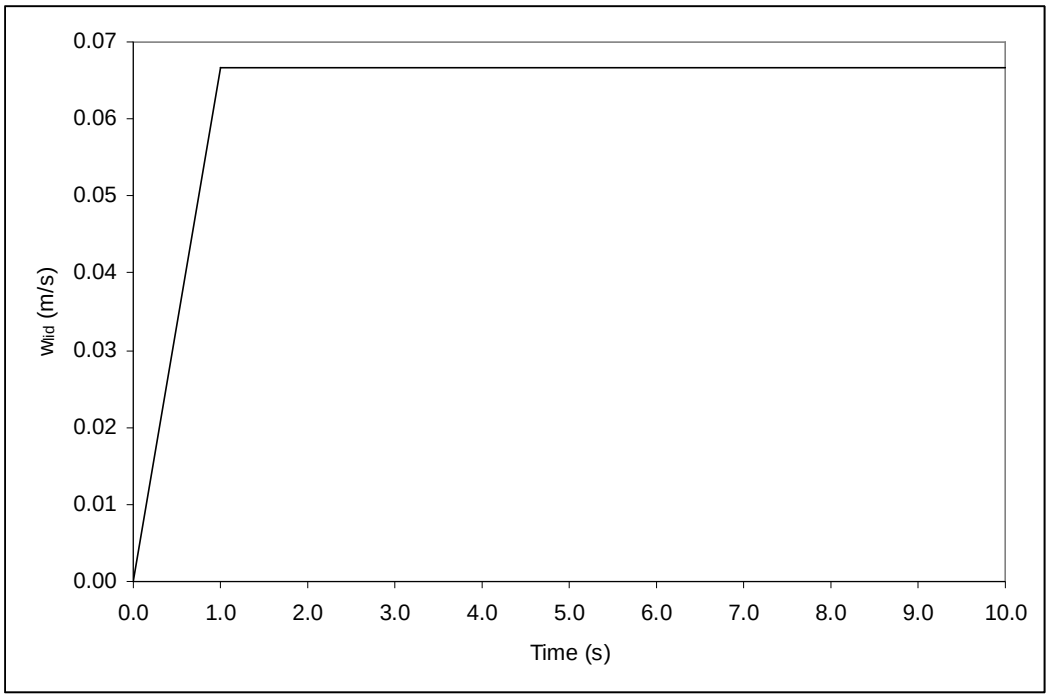

Figure 4.1 Lid velocity profile.

The initialisation of the flow field is as follows. All field variables inside the flow domain and at the boundaries are set to zero. The lid velocity magnitude is ramped up from zero

at time t=0s to a steady state value of 0.0667m/s as shown in Figure 4.1. This was carried out to ensure stability of the computation at start-up by avoiding sudden jumps as noted by Gavrilakis (1992). The maximum number of iteration was set to fifty for the linear algebraic solver at each time step.

The Restarted Generalised Minimum Residual (RGMRES) diagonal (or Jacobi) left-preconditioning subroutine of PIM by da Cunha and Hopkins (1994) was employed for the solution of the linear algebraic set of equations. The tolerance for stopping the RGMRES iteration was set to 1.E-10. These are described in more detail in Chapter 3. Results from the experimental work by Prasad and Kosef (1989) and Migeon, Texier and Pineau (2000) are be used to validate the code. It is noted that an LES of a compressible flow past a deep cavity has been performed by Larchevêque et al. (2003) whereby accurate description of the expansion rate of the shear layer and full recovery of the dynamics of the coherent structures were obtained.

4.2 Observations and Discussion

Grid partitioning in this chapter was carried out by METIS. The result for sixteen sub-domain partitioning has been illustrated in Figure 4.2.

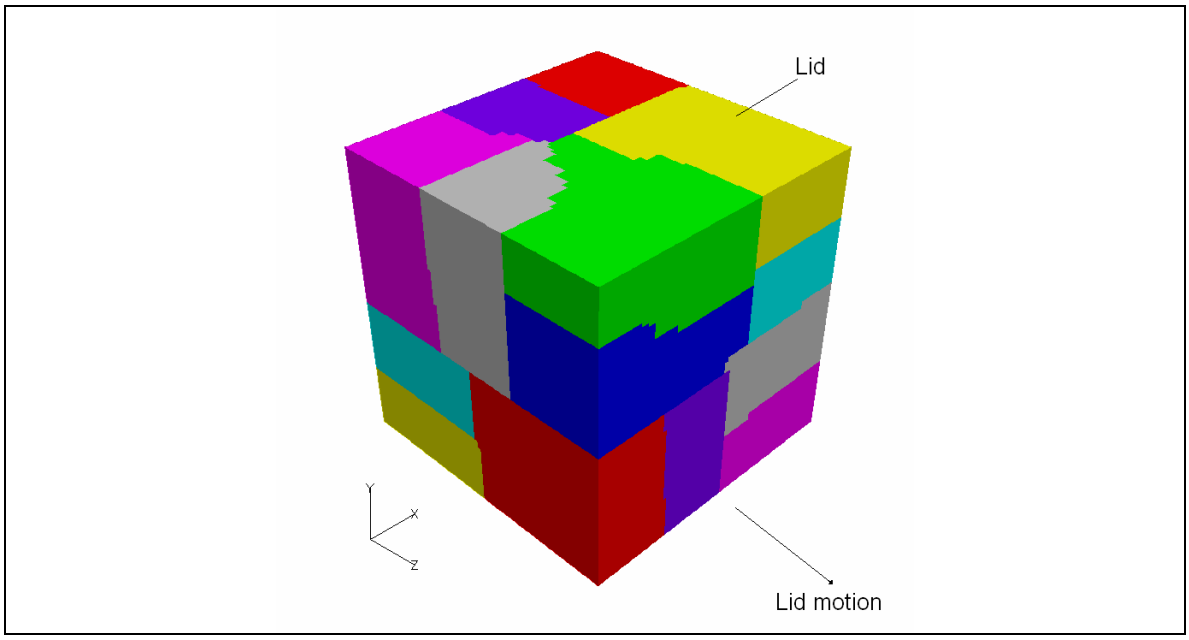

Figure 4.2 Subdomains from partitioning of the cavity mesh by METIS.

For this test case, the coordinate centre corresponds to the centre of the cavity with the coordinate directions shown in Figure 4.2. The mesh size employed in the visualisation of the flow field is the one prescribed for Grid B. The lid was set to move in the positive z-direction. The lid is the boundary perpendicular to the y coordinate direction with the face visible in Figure 4.2. The boundaries normal to the x-direction are the end walls. The downstream side wall is formed by the boundaries normal to the z-direction visible in Figure 4.2.

For Grid A and Grid B, from the starting of simulation until 13.3 lid cycle time (flow time t=30.0s), the time step size Δt was set to 0.001s. One lid cycle time corresponds to the time taken for the lid to travel the length of the cube edge. Beyond that, the time step size Δt was increased to 0.01s. This change was carried out in a stepwise manner. The Smagorinsky model was applied once the steady lid velocity is reached at time t=1.0s. The differencing scheme used for this test case for the internal cells was still the second-order central scheme as described in Chapter 3. For Grid C, a smaller time step size compared to the two coarser grids was implemented. The time step sizes used in the simulations are shown in Table 4.1.

	Grid A	Grid B	Grid C
0.0s<t≤10.0s	0.001s	0.001s	0.001s
10.0s<t≤30.0s	0.001s	0.001s	0.004s
30.0s<t≤100.0s	0.010s	0.010s	0.004s

Table 4.1 Time step sizes for three different mesh sizes and at various levels of time-integration during the simulation.

A number of runs were carried out to investigate the stability of the time marching method with different time step sizes Δt. To ensure stability of the numerical methods, the parameters defined below were considered useful:

$$\sigma = \max\left\{\Delta t\left(\frac{|u|}{\Delta}+\frac{|v|}{\Delta}+\frac{|w|}{\Delta}\right)\right\} \tag{4.1}$$

$$d = \nu\frac{\Delta t}{\Delta x^2} \tag{4.2}$$

Equation (4.1) is a parameter obtained from applying the finite volume discretisation to a hyperbolic partial differential equation on a uniform mesh. σ is the Courant number which can be obtained by cycling through all finite volume cells inside the flow domain. The rule is, for stability of the numerical solution to the partial differential equation, this number must be less than unity, for many explicit time stepping schemes. Equation (4.2) is a parameter obtained upon applying finite volume discretisation to a parabolic partial differential equation, also, on a uniform mesh. The parameter d is the ratio of time step Δt to the characteristic diffusion time $\Delta x^2/\nu$ where ν is the kinematic viscosity of the fluid. For stability of the numerical solution to the partial differential equation, this number must be less than ½, again, applicable for many explicit time stepping schemes. These constraints are specific to the type of partial differential equation, the method of time advancement and spatial differencing scheme as well as the boundary type in use.

	Grid A	Grid B	Grid C
0.0s<t≤10.0s	2.67E-2	3.56E-2	4.45E-2
10.0s<t≤30.0s	2.67E-2	3.56E-2	1.78E-1
30.0s<t≤100.0s	2.67E-1	3.56E-1	1.78E-1

Table 4.2 Courant numbers for three different mesh sizes and at various levels of time integration during the simulation.

The actual Courant numbers experienced by the grids (based on steady state lid velocity magnitude) at different simulation stages are given in Table 4.2. These figures show that the stability of the process of time integration process is not of concern since the values are a lot smaller than unity.

Three runs were made, each with an increasing time step Δt of 0.014s, 0.024s and 0.040s to investigate the limit for numerical stability. A stable run with small residuals of the same order as those using a smaller time step was obtained when using Δt=0.014s. The solution started to become unstable at Δt=0.024s with the number of time step equal to 67 before the residual exceeded the maximum limit of 1.0E+10. With Δt=0.040s, the number of time step to exceed the same limit was decreased to 16.

If the parameter defined in Equation (4.1) is used and the largest velocity magnitude inside the domain is set equal to that of the lid for the worst case scenario, this will give a Courant number σ of 0.9 and with v equal to $10^{-6}m^2/s$, the diffusion number d is equal to 0.0071. Since the maximum internal value of the eddy viscosity was not monitored, the Courant number based on this parameter was not available.

The maximum time step for stability is closer to that associated with a hyperbolic equation (σ, given by Equation (4.1)). Since the velocity magnitude involved in the CFL condition for a hyperbolic equation is related to the inertial forces while viscosity involved in the von Neumann stability criterion is related to viscous forces, it seems that the tilt of the stability criterion towards that of a hyperbolic equation is related to the relatively high bulk Reynolds number of the flow that implies the dominance of convection over diffusion. According to Peyret and Taylor (1983), the analytical criterion of stability for the Adams-Bashforth Crank-Nicolson scheme is unknown.

$$\sum_{\alpha} \sigma_{\alpha}^{2} / d_{\alpha} \leq 2/3 \qquad (2.2)$$

Using the approximate stability criterion proposed by Wesseling (1995), the summation in Criterion (2.2) stated again above, was approximately equal to a value of 1.3 based on the mean velocity magnitude of the cells closest to the centre of the plane on the lid at 26.7 lid cycle time (using Grid A), a value of sub-grid scale kinematic eddy viscosity (at the same monitoring location for the spectrum plot in Figure 4.32) equal to 3.E-6m^2/s and Δt set to 0.01s. The figure obtained here is about twice the limit set by Criterion (3.2) which may be attributed to the fourth order central differencing scheme for the

convection term used by Wessseling (1995) instead of the second order scheme used in this instance. The discrepancy may also be related to the fact that the criterion developed by Wesseling (1995) is an approximation towards a more accurate solution which can be found numerically. Piomelli, Scotti and Balaras (2001) noted that another time constraint is imposed by the time scale of the smallest resolved eddies but the order of magnitude of this parameter is similar to the one given by the Courant number which did not seem to cause any difficulties with stability during computations. This is because the maximum time step size for the simulation on this grid was of the same order associated with the Courant number.

The cell Reynolds number or Peclet number is proportional to the edge length of the finite volume cell taking part in the computation. In this case, the Peclet number of Grid C was 11.1 based on the lid velocity and kinematic eddy viscosity used previously with Equation (2.2). Even though this is considerably larger than the critical value of two, the time marching, using this grid, did not become unstable. A plausible explanation for this finding is that the values of strain rates in the region next to the lid are significantly higher than those at the monitoring point, resulting in a much higher value of kinematic eddy viscosity in the former region.

The resolved velocity vector field after 12.4 lid cycle time (t=28.0s) on an yz-plane at a non-dimensional distance of $2x/B$=0 (x=0m) where B is the lid length and x is the distance perpendicular to the wall measured from the cavity centre, was compared with the experimental result of Migeon, Texier and Pineau (2000), described in Figure 4.4. The obvious flow feature from this experimental result is the primary vortex. The centre of this vortex can be seen to be in good agreement with the computational velocity vector field in Figure 4.3. This implies that a reasonably accurate time step size Δt was used in the simulation up to the time specified. The slight variation in the location of the primary vortex centre can be attributed to the fact that, in the experiments, the lid achieved its final velocity instantaneously whereas in the simulation, the velocity of the lid was ramped up to the final value, which was the velocity after t=1.0s. The primary vortex centre may also fluctuate in space resulting in the difference of the vortex centre between

the computed instantaneous streamlines and the measured instantaneous streamlines. Averaging the resolved velocity components for an adequately long period of time in order to average out the effect of fluctuating eddies will most likely result in a smoother computed streamlines.

Fluid located next to the moving lid receives momentum from the lid due to viscosity. This energetic fluid is dragged to the upper right corner of the cavity where it is deflected downwards by the downstream side wall (vertical wall on the right side). Due to the adverse pressure gradient (with the lower right corner acting as a stagnation point) and friction with the downstream side wall, the wall-jet decelerates and consequently separation is induced. This is clearly evident from the plot shown in Figure 4.4.

Referring to Figure 4.3, the location of the primary vortex is in reasonable agreement with the reference data. It is situated slightly to the upper right of the plane centre. The secondary vortices at the lower left and right corners (downstream and upstream secondary vortices) and also at the top left corner (upper secondary vortex) are visible. It must be noted that the streamlines from the computation are 0.4 lid cycle time ahead of the reference data and this may have an influence on the difference between these two plots. To add to this, the reference case was subjected to a step jump during start-up of the experiment as opposed to the ramp input applied to the computation.

However, almost directly above the primary vortex centre at $2y/B \approx 0.4$, the streamlines are not that smooth compared to the reference data. This may be explained by the presence of turbulent eddies numerically produced by the unrealistic value of the eddy viscosity produced by the turbulence model in that region.

The surface separating the primary vortex from the secondary ones can be regarded as concave ‘walls’ and a consequence of this is the existence of centrifugal forces exerted by the fluid particles acting on these ‘walls’. It can also be seen that the size of secondary eddies relate directly to the pressure distribution.

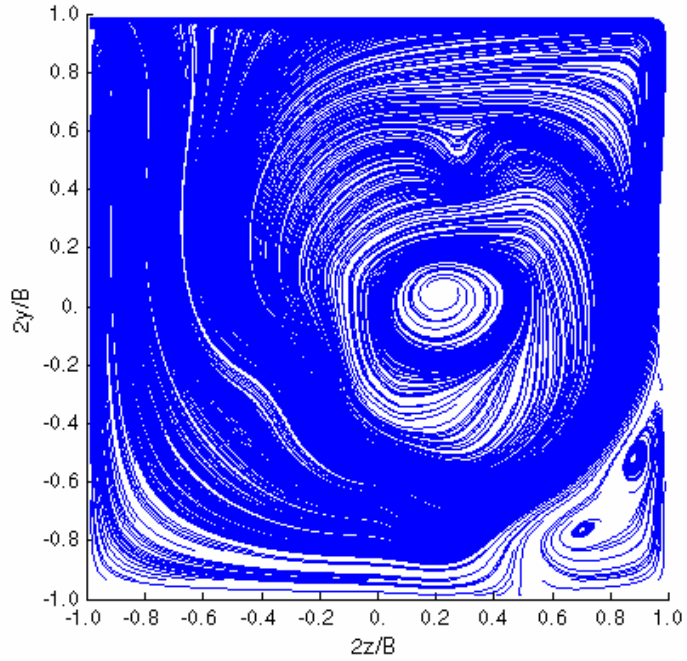

Figure 4.3 Instantaneous streamlines on the *yz*-plane, at *2x/B*=0 and 12.4 lid cycle time with the centre of primary vortex at *2z/B*=0.23 and *2y/B*=0.04.

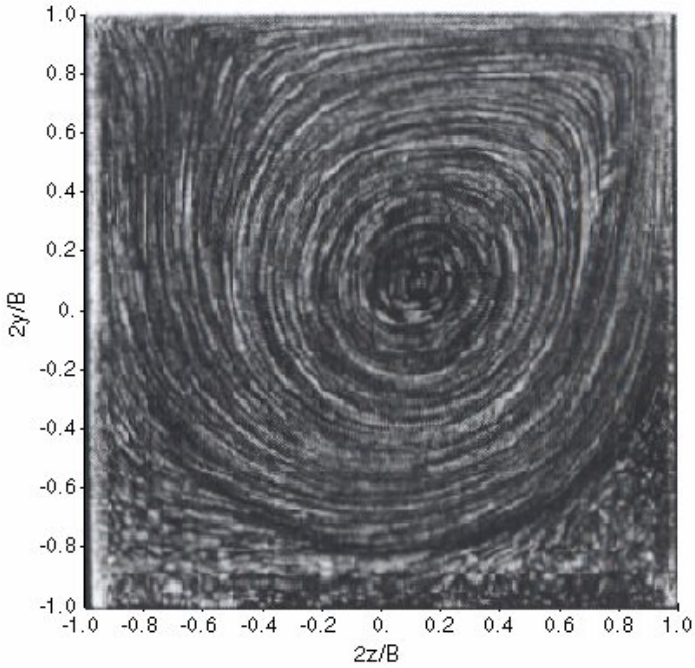

Figure 4.4 Instantaneous streamlines on the *yz*-plane, at *2x/B*=0 and 12 .0 lid cycle time with the centre of primary vortex at *2z/B*=0.14 and *2y/B*=0.09 from Migeon, Texier and Pineau (2000).

Figure 4.5 shows the presence of pressure lobes or regions of relatively low pressure extending radially outwards from the primary vortex region. The middle of the plane is occupied by the low-pressure centre of the primary vortex. Regions of relatively high pressure can be seen to be located along the lower boundary and upper right corner of the plane. The solid black lines in this figure (and in some following figures) are subdomain boundaries which indicate proper communication between neighbouring subdomains.

It can be seen that the primary vortex centres on planes closer to the end-walls are located about $2y/B \approx 0.093$ below the primary vortex centre on the midplane shown in Figure 4.3. The jet-like movement of fluid above the upstream secondary vortices on these two planes is weaker compared to the one on the mid-plane. This may be due to the damping effect of the end walls.

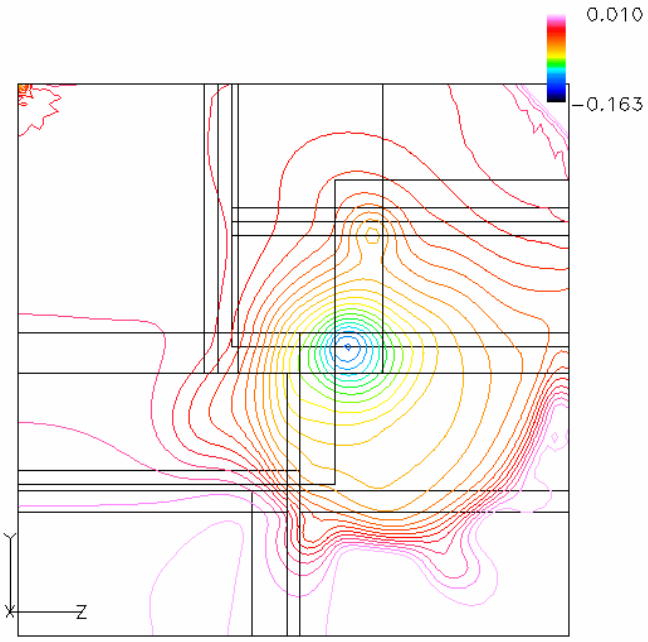

Figure 4.5 Contour of instantaneous modified pressure (Pa) on the *yz*-plane, at$2x/B$=0 and 12.4 lid cycle time.

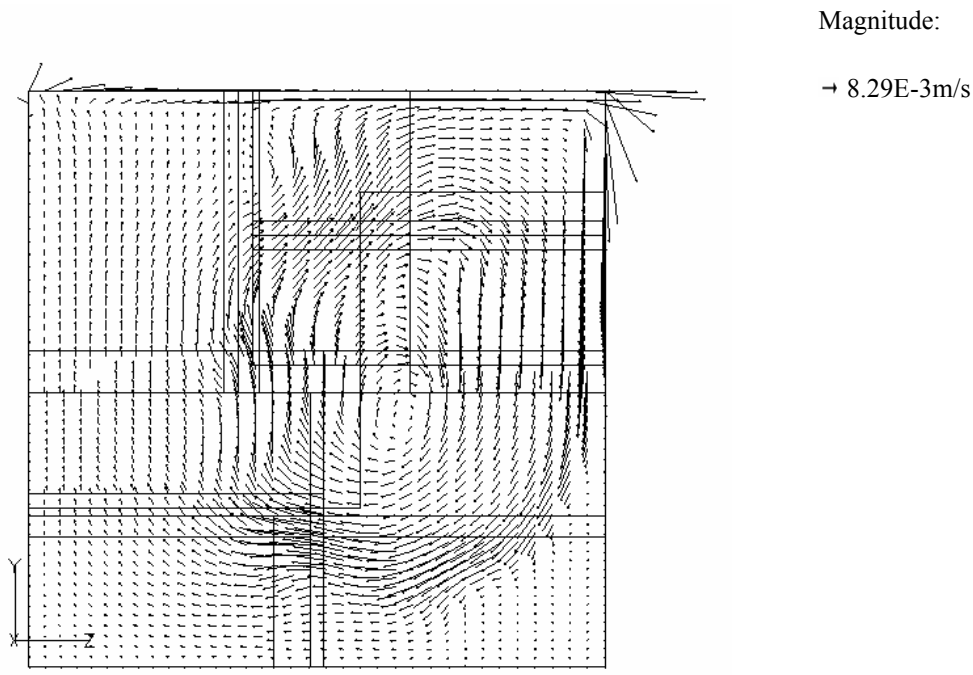

Figure 4.6 Instantaneous velocity vector field on the *yz*-plane, at *2x/B*=0.4 and 12.4 lid cycle time.

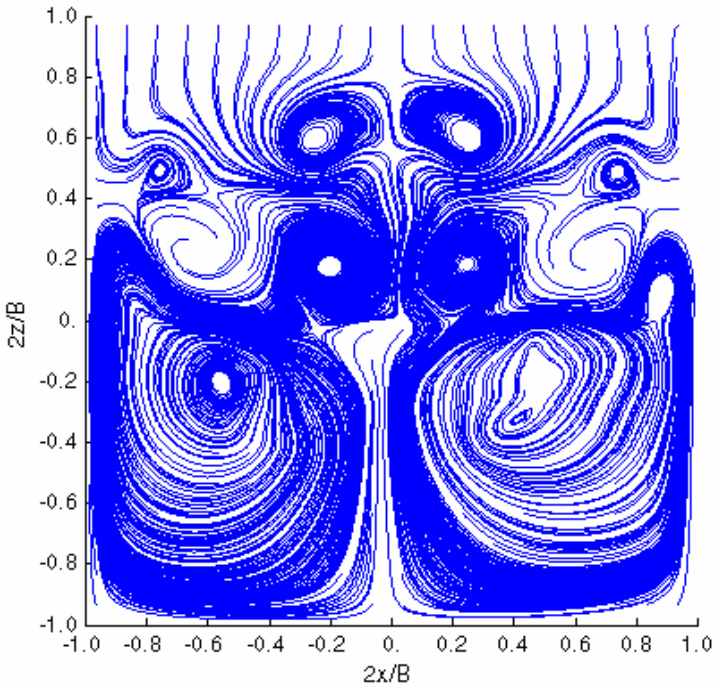

Figure 4.7 Instantaneous streamlines on the *xz* plane, at *2y/B*=0 and 12.4 lid cycle time.

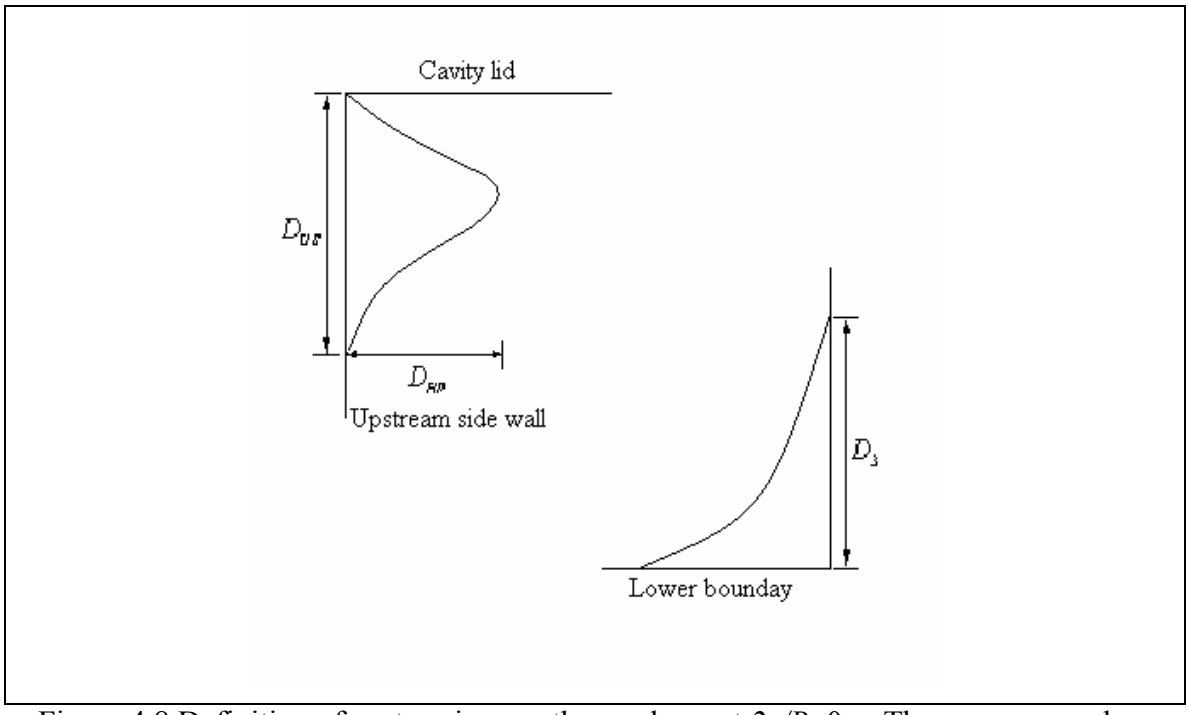

Figure 4.8 Definition of vortex sizes on the *yz* plane, at *2x/B*=0m. The upper secondary eddy is on the upper left corner and the downstream secondary eddy on the lower right corner. Solid curved lines are the dividing streamlines.

Referring to Figures 4.3 and 4.8 from manual measurement of the streamline plots, the length of the instantaneous downstream secondary eddy, D3, on the mid-plane, normalised by the cavity depth is approximately 0.396; while the lengths of the upper secondary eddy D_{US} and D_{HP}, normalised by the same length are 0.40 and 0.09 respectively. These lengths will definitely change as the simulation progresses. This is due to the reason that these measurements were taken while the flow was still in a transient stage and there is a net transfer of momentum from the lid to the fluid.

Prasad and Koseff (1989) noted that three-dimensional features of the flow inside the computational domain can be partly related to the presence of end walls. This increases damping of turbulence or dragging on the fluctuating velocity components.

Figures 4.7 and 4.9 show that the flow is highly three-dimensional in regions occupied by the downward jet-like stream near the downstream side wall. The instantaneous flow structure is almost symmetrical about the *x*-axis centre. The presence of three-

dimensional flow features can be attributed to the interaction of the end walls and corners with the flow near the downstream side wall through the effect of viscosity.

It has been reported by Koseff and Street (1984) and Prasad and Koseff (1989) on the existence of Taylor-Görtler like vortices in the region of the downstream secondary eddy. These vortices exist under the influence of centrifugal forces when fluid flows over concave walls. They argue that the function of these vortices is to transfer momentum between the core region and lower boundary layer. In Figures 4.10 and 4.11, there is no indication of the presence of these vortices suggesting that the flow has not reached a fully steady state (in a statistical sense) and is still in a transient stage.

After 26.7 lid cycle time (t=60.0s) as illustrated in Figure 4.12, the streamlines have undergone some changes compared to those at 12.4 lid cycle time (t=28.0s) shown in Figure 4.3. The downstream and upstream secondary eddies and also the upper secondary vortices are still present.

However, the primary vortex centre has now moved to a position at about 2y/B=0.1 to the bottom of the plane centre. In addition to the absence of Taylor-Görtler like vortices, the changing location of the primary vortex centre provides further evidence that the flow is still in transient stage.

As shown in Figures 4.12, 4.14 and 4.15 after 26.7 lid cycle time, the sizes of corner vortices have been reduced on all planes compared to the results on the same set of planes 14.3 lid cycle times, found earlier.

A likely explanation for this is the increase in momentum of the downwards moving jet, close to the downstream side wall which delays separation. At the mid-plane, the size of the downstream secondary vortex has been reduced to about 60% of that at 12.4 lid cycle time.

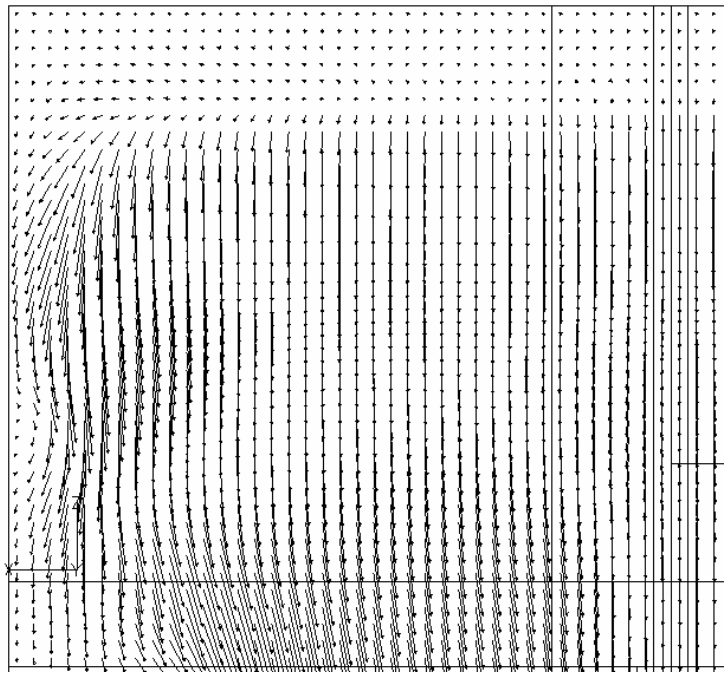

(a) Upper left quadrant

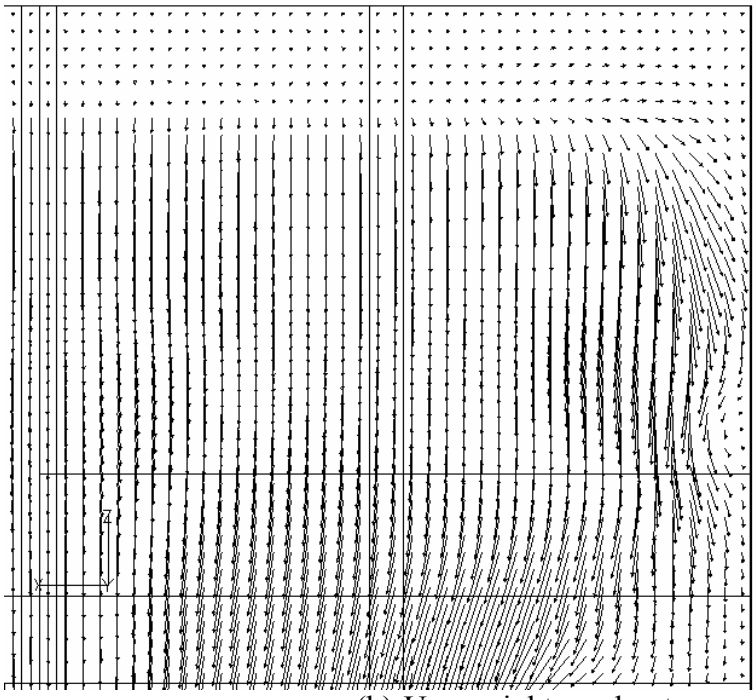

(b) Upper right quadrant

Figure 4.9 Instantaneous velocity vector field on the *xz*-plane, at *2y/B*=-0. 4 and 12.4 lid cycle time.

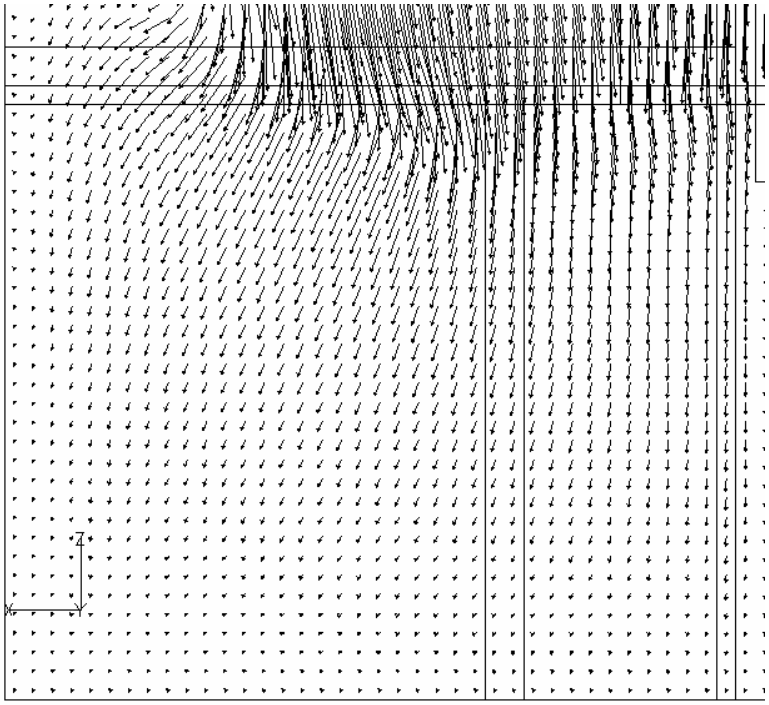

(c) Lower left quadrant

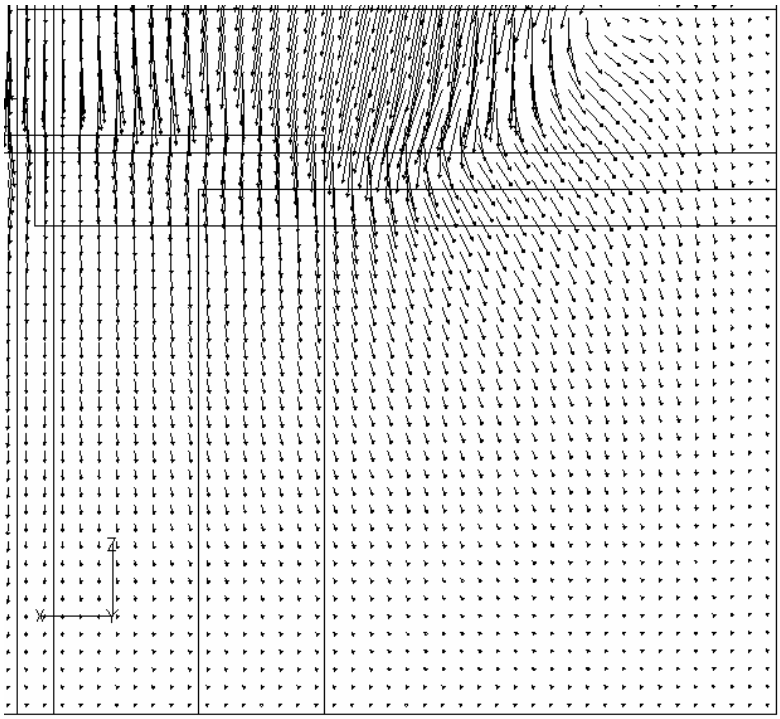

(d) Lower right quadrant

Figure 4.9 Instantaneous velocity vector field on the *xz*-plane, at *2y/B*=-0. 4 and 12.4 lid cycle time (continued).

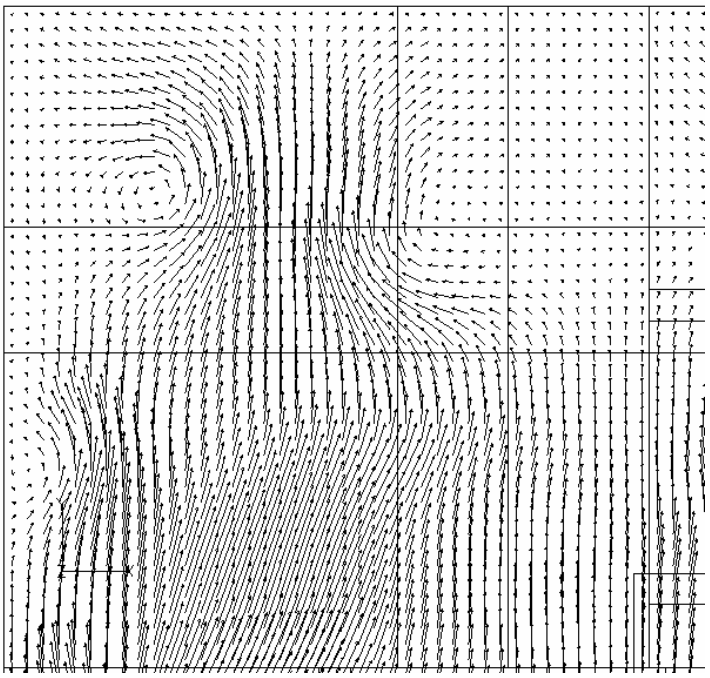

(a) Upper left quadrant

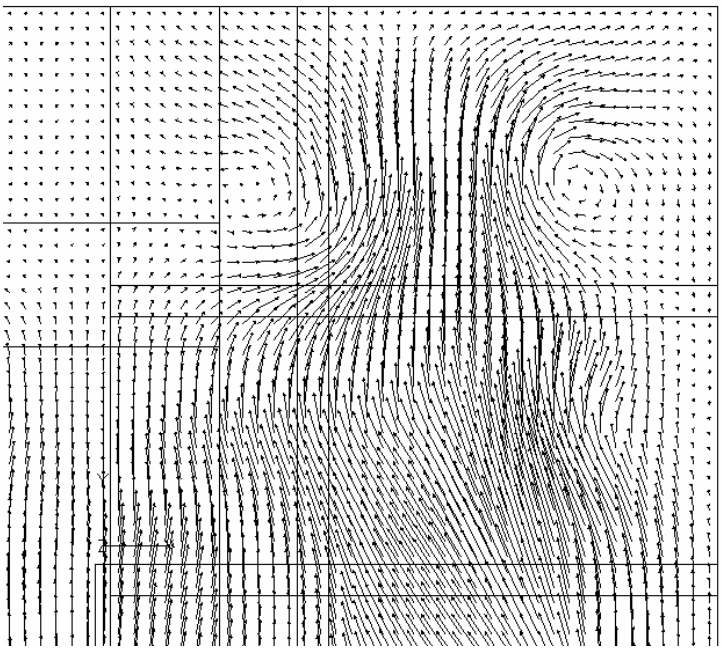

(b) Upper right quadrant

Figure 4.10 Instantaneous velocity vector field on the *xy*-plane, at *2z/B*=0 and 12.4 lid cycle time.

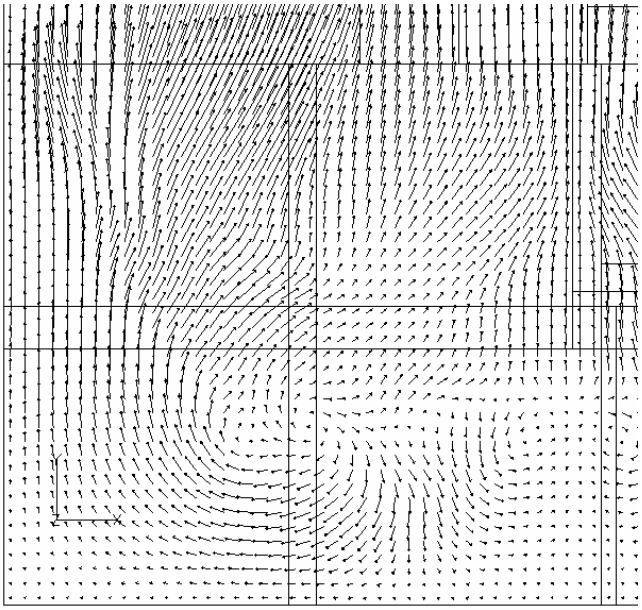

(c) Lower left quadrant

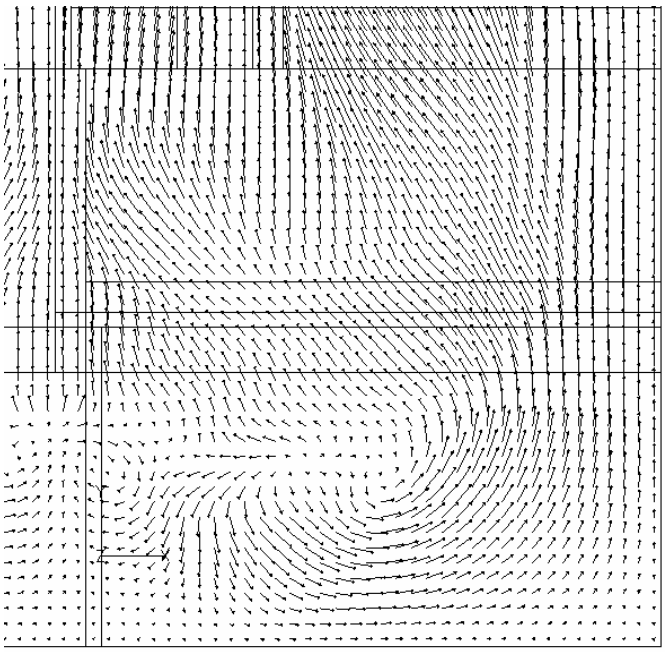

(d) Lower right quadrant

Figure 4.10 Instantaneous velocity vector field on the *xy*-plane, at *2z/B*=0 and 12.4 lid cycle time (continued).

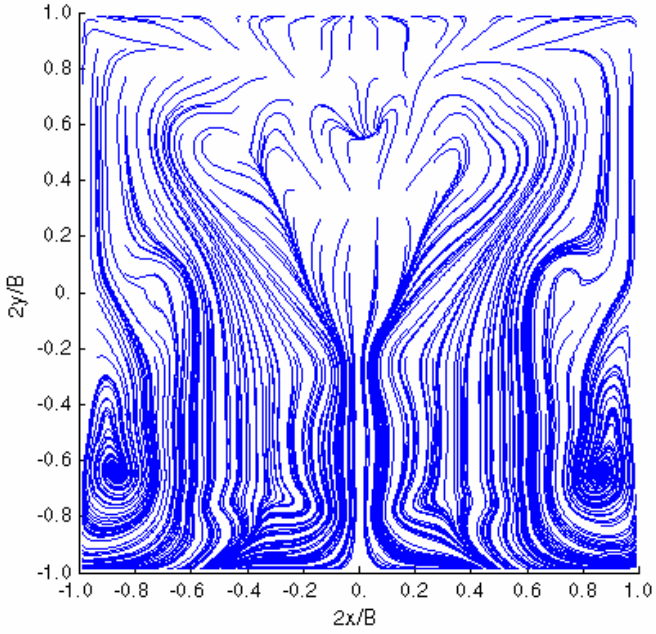

Figure 4.11 Instantaneous streamlines on the *xy*-plane, at *2z/B*=0. 4 and 12.4 lid cycle time.

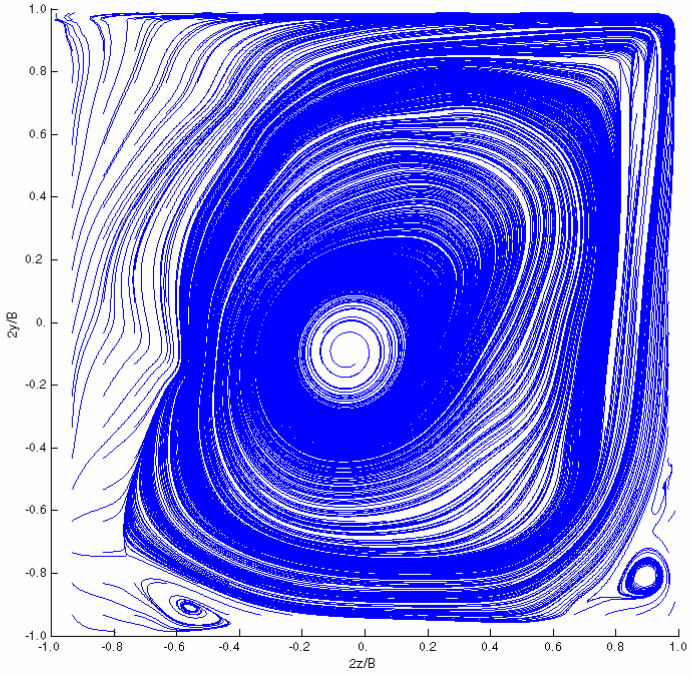

Figure 4.12 Instantaneous streamlines on the *yz*-plane, at *2x/B*=0 and 26.7 lid cycle time.

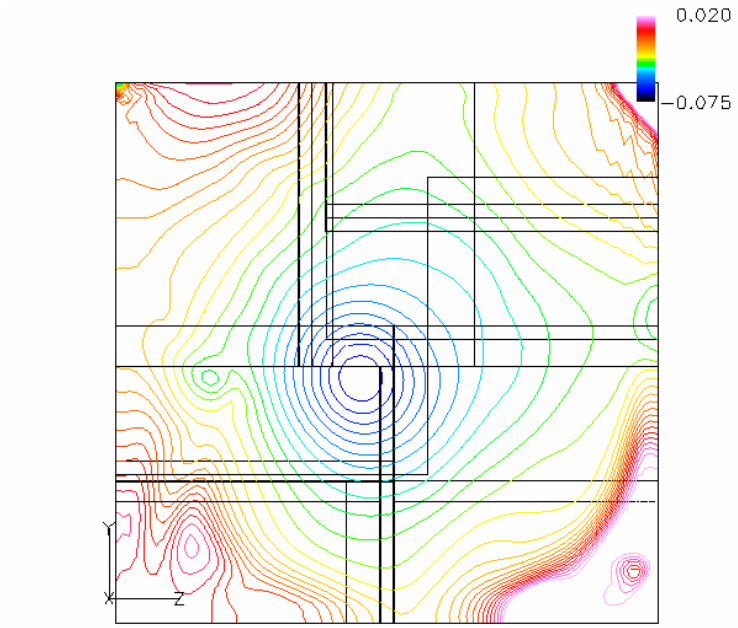

Figure 4.13 Contour of instantaneous modified pressure (Pa) on the *yz*-plane, at *2x/B*=0 and 26.7 lid cycle time.

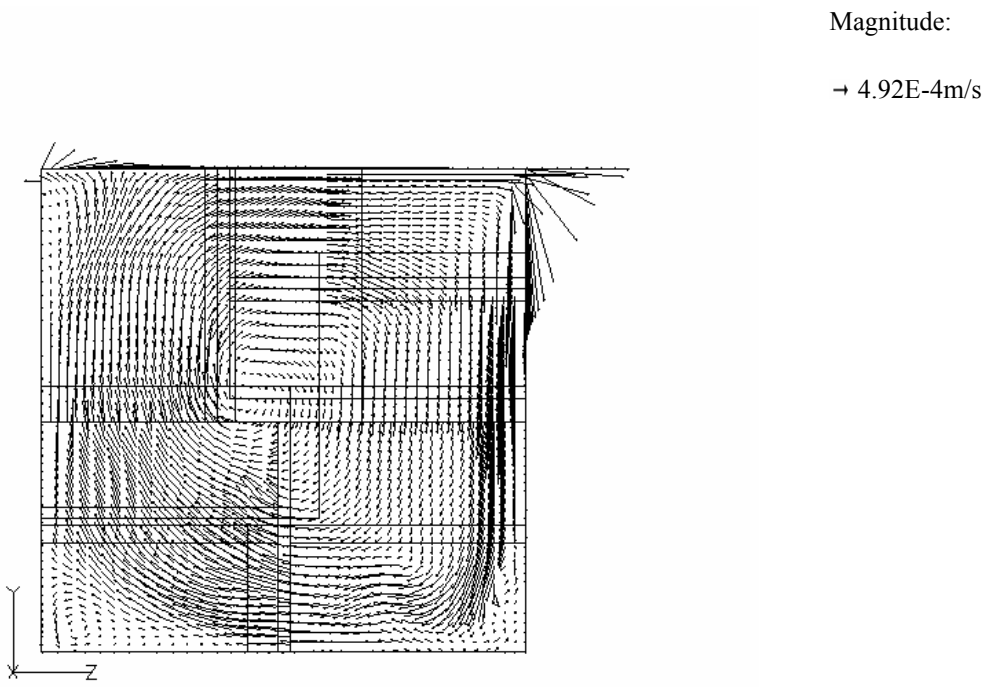

Figure 4.14 Instantaneous velocity vector field on the *yz*-plane, at *2x/B*=-0. 4m and 26.7 lid cycle time.

Figures 4.16 and 4.17 show a number of vortical structures close to the downstream and upstream side walls. The corner vortices close to where the end walls and upstream side wall meet are visible in Figure 4.17. A pair of vortices close to the mid-span of the upstream side wall can also be seen on this plane. The interaction between the inertia forces of the primary vortex and viscous forces near the walls could provide an explanation for this observation. Putting it in a different way, the vectors related to viscous stresses are in general not aligned with the driving pressure or inertia forces resulting in the three-dimensional flow structures.

The plot in Figure 4.17 shows that the flow structure is not symmetrical (instantaneously at least) which may be caused by turbulence and low-frequency "organised structure" fluctuations. Compared to the streamlines on the same plane at 12.4 lid cycle time (t=28.0s), the flow structure seems to exhibit a more random and chaotic nature after 26.7 lid cycle time (t=60.0s). The three dimensional feature of the flow inside the cavity is again shown clearly in Figures 4.14 to 4.17. The main difference between the flow structures in Figures 4.16 and 4.17 is that there are fewer vortices in the latter and these are concentrated within the bottom quadrants of the plane. The code performed the time integration process in a stable manner judging from the decrease in residual values with respect to the number of time steps at a monitoring cell node during the transient stage. In addition, the time step sizes were chosen so that they do not violate the stability limits.

As described earlier, an important feature of the lid driven cavity flow is the presence of secondary flow in the form of vortices occurring in pairs in regions close to the downstream secondary eddy. The mechanism of formation of these secondary flows is described briefly as follows. The centrifugal forces acting on the fluid moving along the concave 'wall' results in the formation of Taylor-Görtler like vortices as the primary instability. This induces early transition of the boundary layer and produces secondary instabilities characterised by relatively high-frequency fluctuations as the transition develops. This is described in more detail by Kohama (2000). In their study, Raverdy et al. (2003) used LES to simulate flow around a low-pressure turbine blade. It is found that the transition region and the Kelvin-Helmholtz mechanism of instability were well

captured in the computations conducted by them.

That Taylor-Görtler like vortices can be found in the boundary layer of surfaces moving curvilinearly relative to the surrounding fluid has been supported by Nikishova and Gorbatyuk (1991). These secondary vortices are also present in curved channels as demonstrated by Kobayashi and Maekawa (1995); this can be good for mixing of chemicals. These vortices can also be found on the pressure surface of turbine blades and on aircraft engines and wings, which in this case is detrimental since high skin friction drag leads to higher fuel consumption and greenhouse gas emissions. Wang et al. (1997) studied the secondary flow in a region close to the endwall of a plane turbine blade cascade with blade shapes similar to those used in high performance turbine stages. They provided evidence of the existence of a periodically fluctuating horseshoe vortex system with varying number of vortices near the leading edge of the cascade.

The instantaneous streamlines in Figure 4.18 shows two pairs of sharp, counter-rotating vortices at an almost equal distance from the *x*-axis bisector. This feature bears a lot of resemblance to the Taylor-Görtler like vortices shown in Koseff and Street (1984) for lid driven cavity flows with Reynolds number in the 1,000 to 10,000 range. However, this feature is not present on the same plane at 12.4 lid cycle time (t=28.0s) as shown in Figure 4.11 and on the downstream plane at 26.7 lid cycle time (t=60.0s), shown in Figure 4.19. This indicates that this feature occurs intermittently and exists in a localised region of the flow which may relate to the distorting effect of turbulence on these structures. According to Prasad and Koseff (1989), the structures of the Taylor-Görtler like vortices are distorted by the high-frequency fluctuations of turbulence when the Reynolds number of the flow reaches 10,000. This is in agreement with the results shown in Figures 4.11 and 4.19.

When these vortices have a regular periodicity both in time and space, they are called pseudo-turbulence which is different from real turbulence in that the latter can never sustain this periodicity in time and space.

The main function of the Taylor-Görtler like vortices in this case is to transfer mass, momentum and energy from the inner region of the domain to the lower boundary. As a consequence, a practically important side effect is the increase in skin friction coefficient and wall shear stresses as reported by Dris and Johnson (2005).

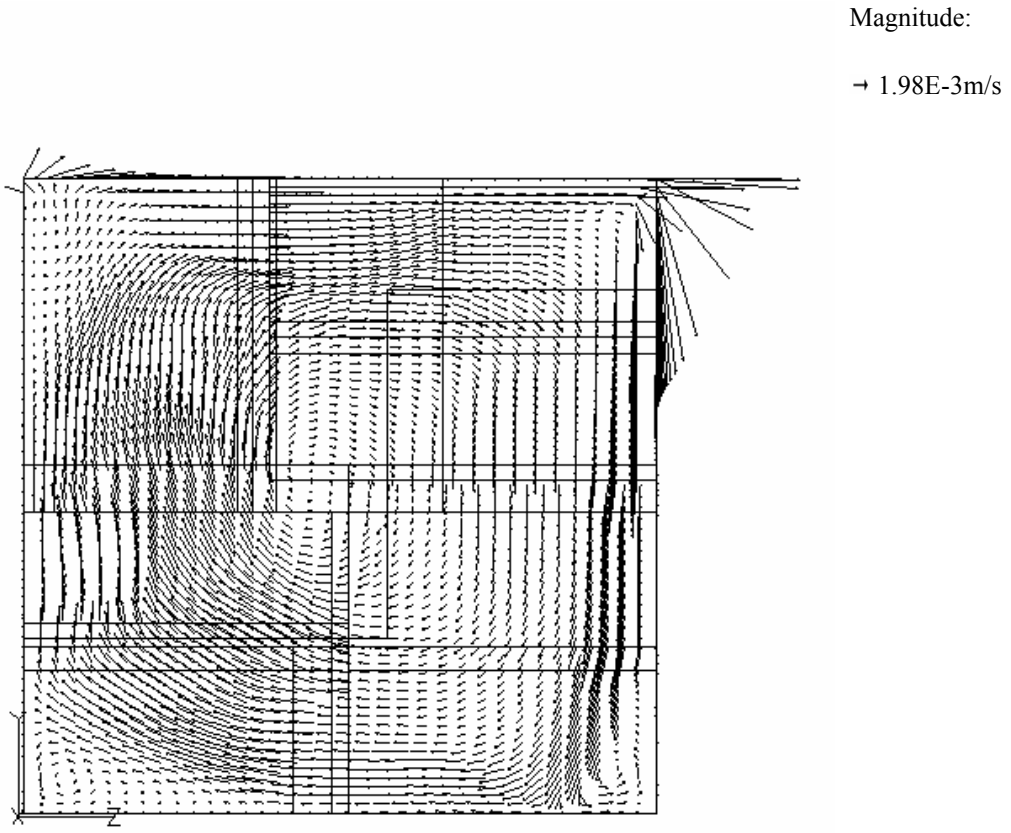

Figure 4.15 Instantaneous velocity vector field on the *yz*-plane, at *2x/B*=0.4 and 26.7 lid cycle time.

It is believed that the function of the Taylor-Görtler like vortices is to transfer momentum from the lower boundary layer into the core region of the primary vortex. According to the study of Prasad and Koseff (1989), the Taylor-Görtler like vortices exist in flows with bulk Reynolds number of 3,000 to 4,000 and is destroyed by the high amplitude fluctuation at Re=10,000. Hence, the Taylor-Görtler like vortices in Figure 4.19 may be

experiencing a transition period where the coherence of the vortices is under siege by the high amplitude fluctuations.

Referring to the definition shown in Figure 4.8, a comparison of instantaneous eddy sizes with published data was carried out and results are shown in Table 4.3. D_3^*, D_{US}^* and D_{HP}^* (corresponding to D_3, D_{UE} and D_{HP}) are normalised by the vertical depth of the cavity.

	Computation (26.7 lid cycle time)	Erturk, Corke and Gökçöl (2004)	Koseff and Street (1984)
D_3^*	0.30	0.44	0.32
D_{US}^*	0.3	0.3	0.3
D_{HP}^*	0.07	0.2	0.1

Table 4.3 Comparison of normalised eddy sizes.

The D_{HP}^* value is about 30% lower than the result obtained by Koseff and Street (1984). The difficulty in visualising the upper secondary eddy both in the simulation and experiment may contribute to this considerable disagreement. Erturk, Corke and Gökçöl (2005) performed a two-dimensional computation and they did not use any turbulence model when performing their computation resulting in a lower effective viscosity. This explains the presence of large difference in eddy sizes here, in contrast to other data related to the absence of end walls. It must also be noted that Koseff and Street (1984) performed their experiments on a cavity with a spanwise aspect ratio (ratio of the span in the *x* direction to the width in *z* direction in Figure 4.2) of 3:1. It is widely known that the spanwise aspect ratio plays a major role in the behaviour of the flow inside the flow domain and as such results must be treated with caution. The computational result itself is not free of discretisation error, and more importantly, this may have an effect on eddy sizes.

Going back to the results after 12.4 lid cycle time (t=28.0s), the size of D_3^* has reduced

from 0.40 to 0.30. The same trend is shown by D^*_{US} and D^*_{HP}. This can be explained by the fact that the flow was still in a transient stage and there is a net transfer of momentum from the lid to the fluid.

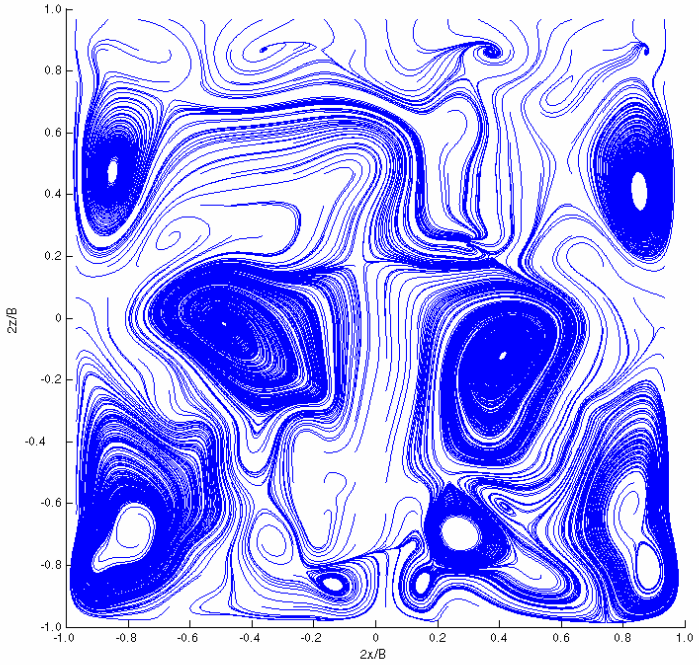

Figure 4.16 Instantaneous streamlines on the *xz*-plane at *2y/B*=0 and 26.7 lid cycle time.

In addition to the test cases ran at a bulk Reynolds number of 10,000, an excursion for a case at a bulk Reynolds number of 66,666 was also carried out using a relatively large time step size of Δt=0.01s.

The velocity vector field is shown in Figure 4.20 where the primary vortex can clearly be seen. The downstream and upstream secondary vortices as well as the upper secondary vortex are still present. However, unlike the case with bulk Reynolds number of 10,000, there seems to be more than one downstream secondary vortex as indicated by the velocity vector field. This could be a temporary or transient feature of the flow at higher Reynolds number such as the one used for this test case.

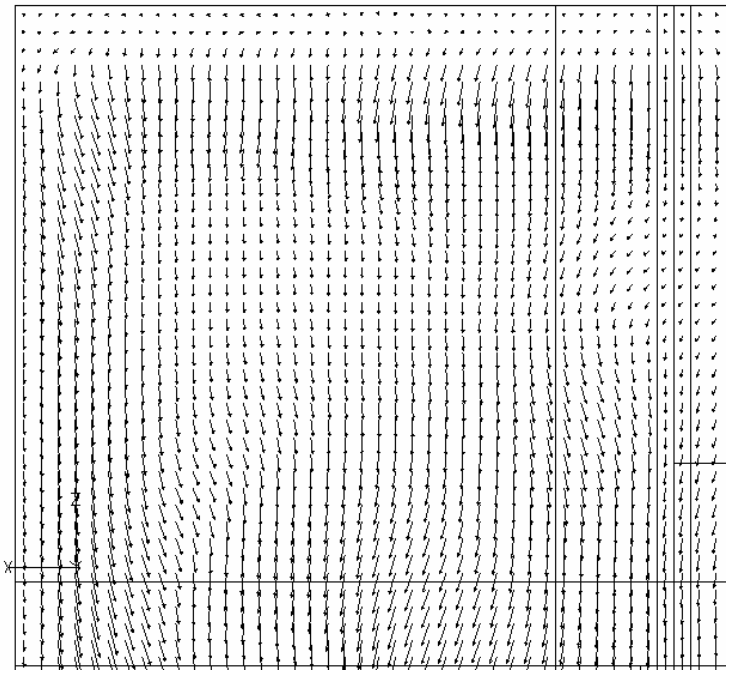

(a) Upper left quadrant

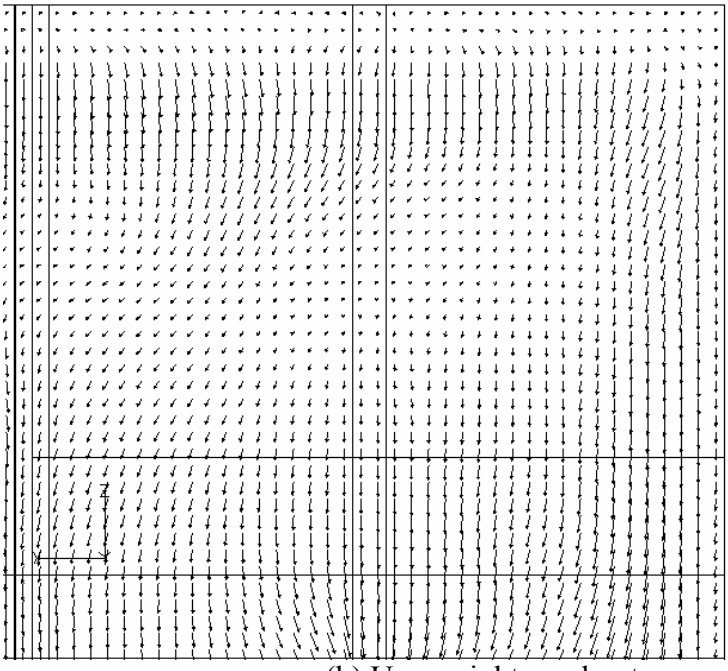

(b) Upper right quadrant

Figure 4.17 Instantaneous velocity vector field on the *xz*-plane at *2y/B*=-0.4 and 26.7 lid cycle time.

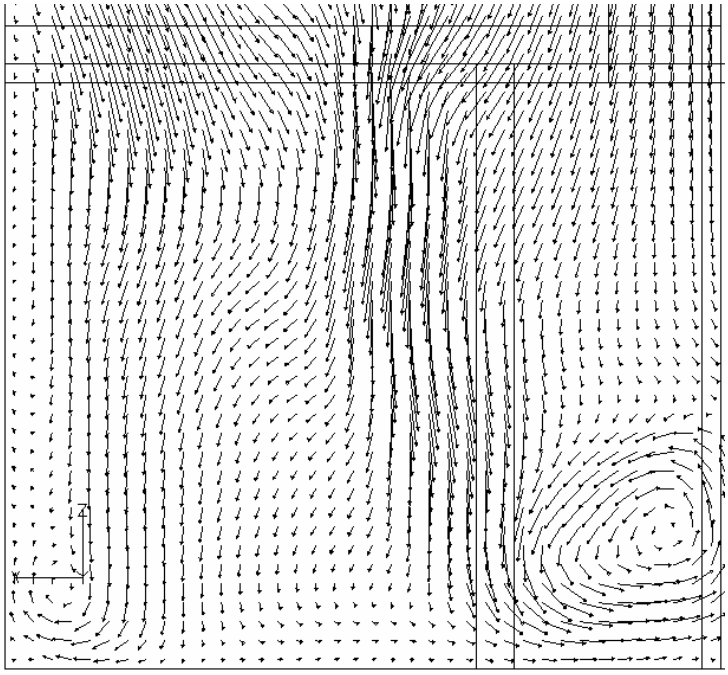

(c) Lower left quadrant

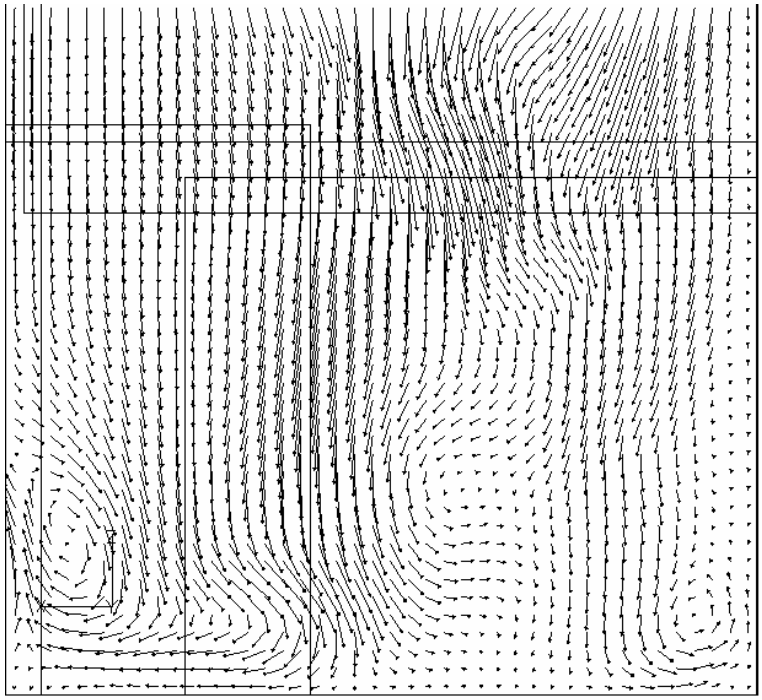

(d) Lower right quadrant

Figure 4.17 Instantaneous velocity vector field on the *xz*-plane at *2y/B*=-0.4 and 26.7 lid cycle time (continued).

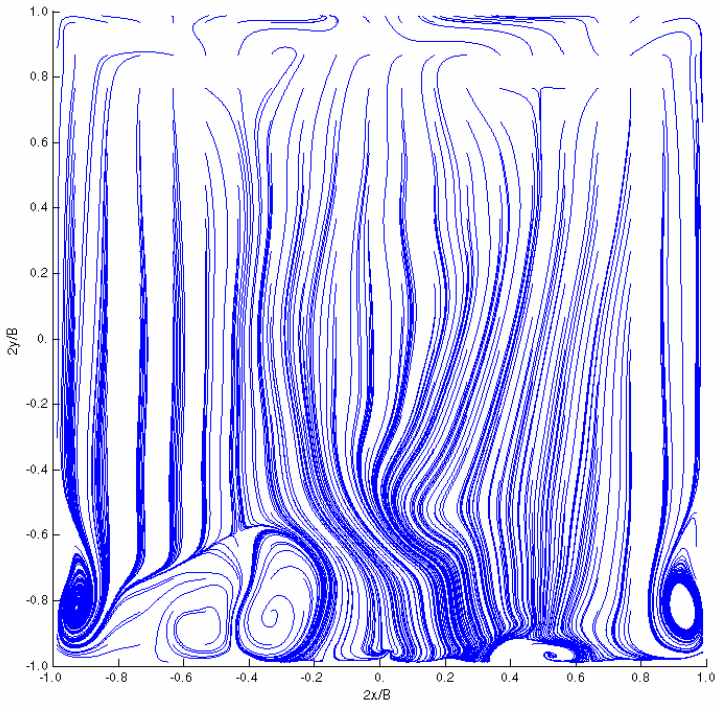

Figure 4.18 Instantaneous streamlines on the *xy*-plane, at *2z/B*=0.4 and 26.7 lid cycle time.

Figure 4.21 shows the time averaged velocity profiles on the *yz*-plane at a non-dimensional distance of *2x/B*=0 (which is equivalent to *x*=0m) on lines bisecting the cavity for Grid A where *B* is the lid length.

Unless otherwise stated in this chapter, time averaging was performed using 2,000 consecutive time steps up to the time specified in the plots. This figure was chosen to reduce the instantaneous effect of fluctuating eddies on the averaged quantities.

The vertical and horizontal centrelines divide the plane into four equal quadrants. The values of average velocity are normalised by the steady lid velocity.

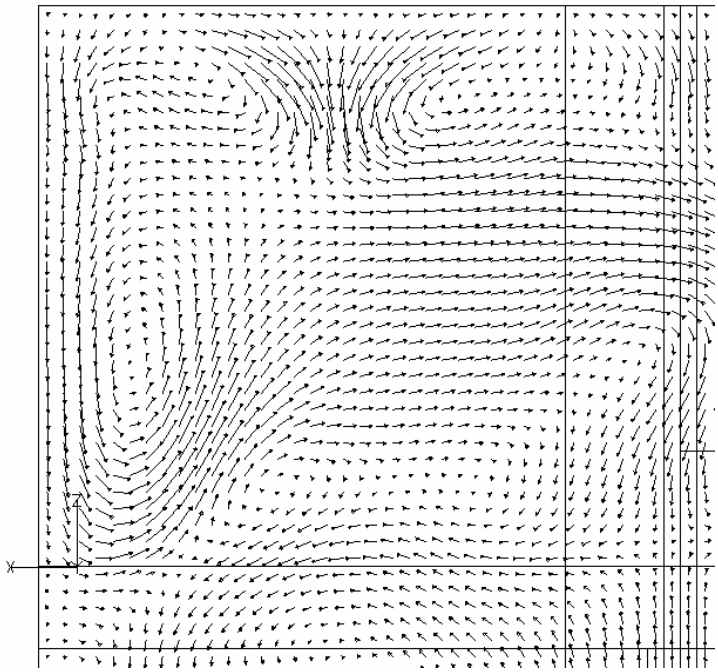

(a) Upper left quadrant

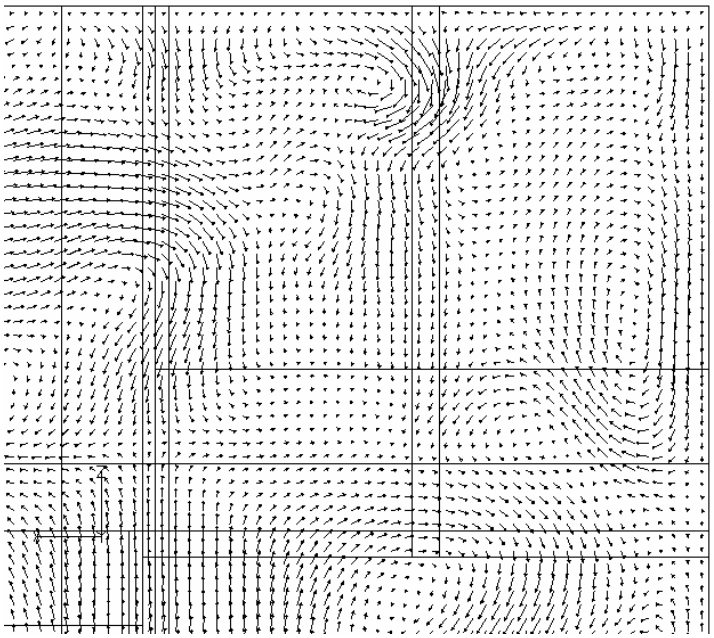

(b) Upper right quadrant

Figure 4.19 Instantaneous velocity vector field on the *xy*-plane, at *2y/B*=0 and 26.7 lid cycle time.

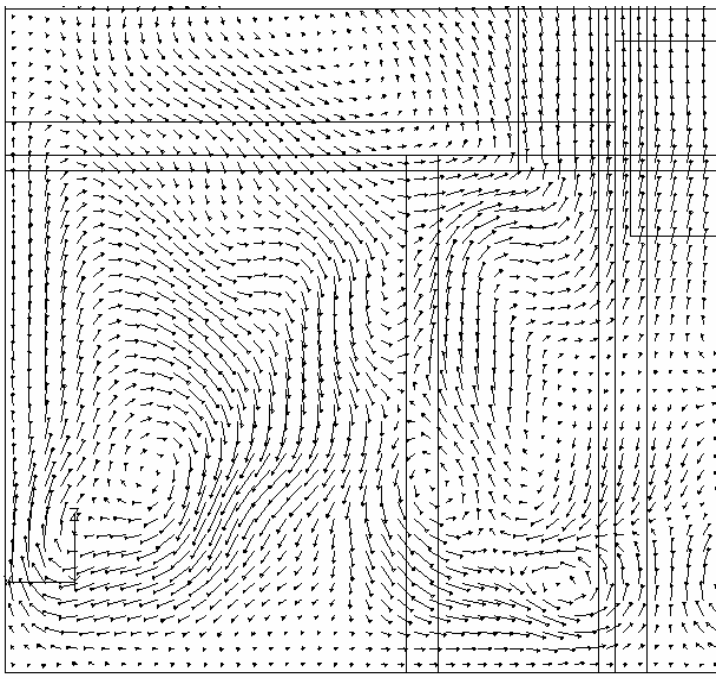

(c) Lower left quadrant

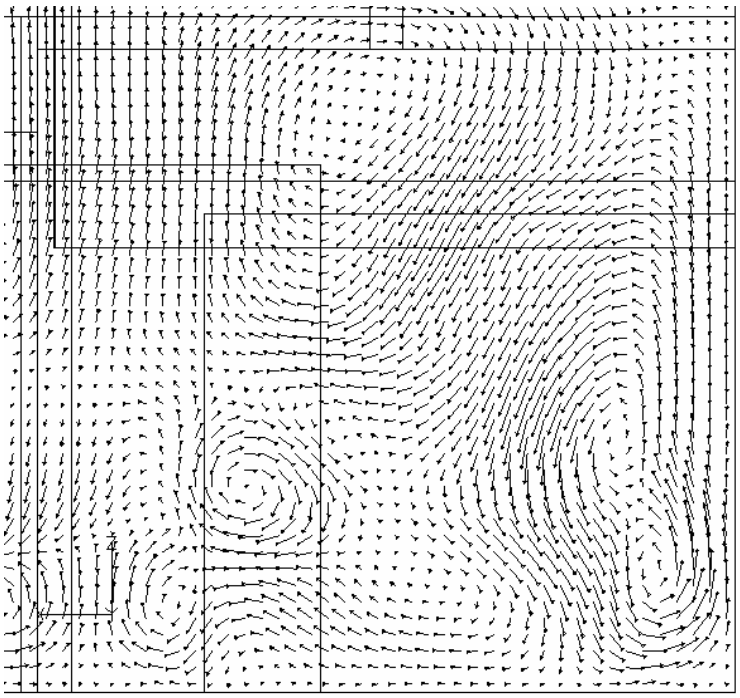

(d) Lower right quadrant

Figure 4.19 Instantaneous velocity vector field on the *xy*-plane, at *2y/B*=0 and 26.7 lid cycle time (continued).

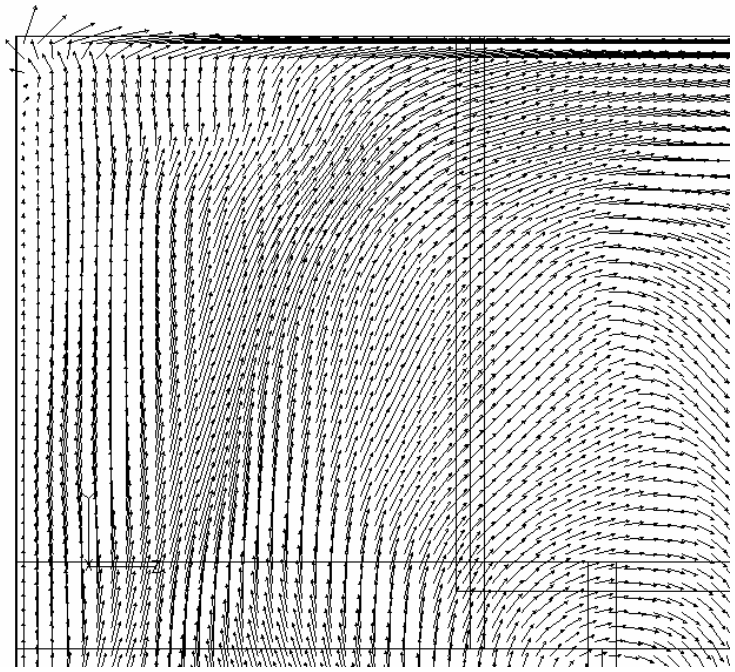

(a) Upper left quadrant

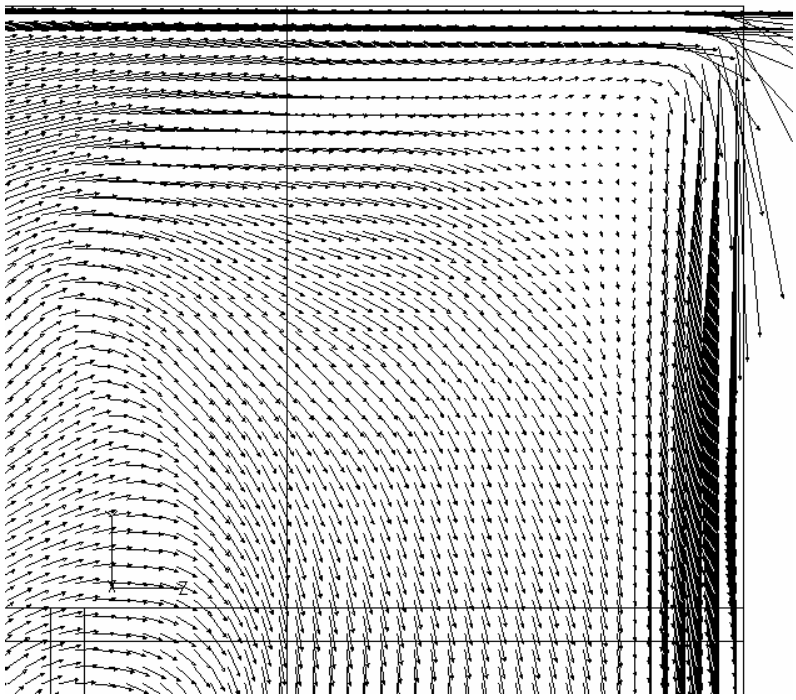

(b) Upper right quadrant

Figure 4.20 Instantaneous velocity vector field on the *yz*-plane, at *2x/B*=0 and 26.7 lid cycle time for the test case with bulk Reynolds number set to 66,666.

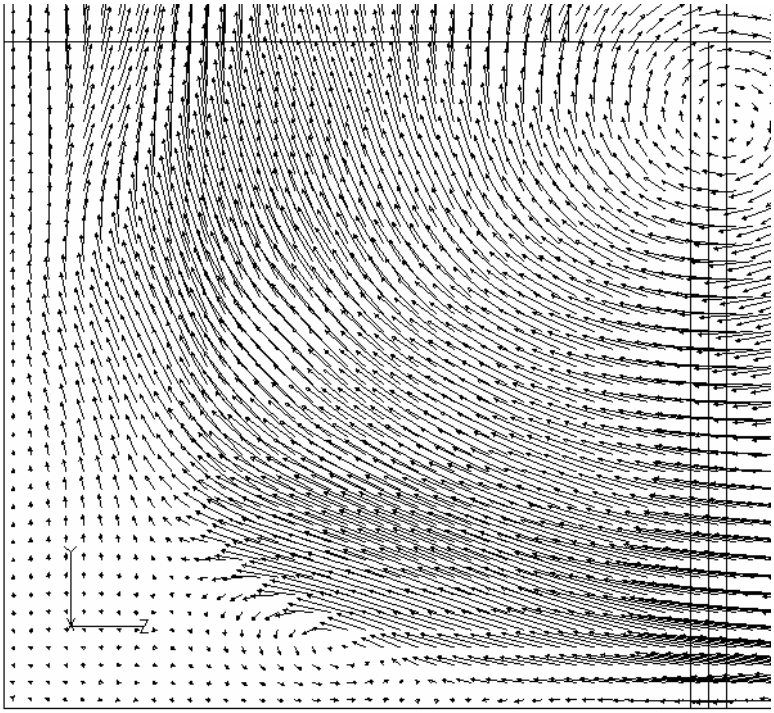

(c) Lower left quadrant

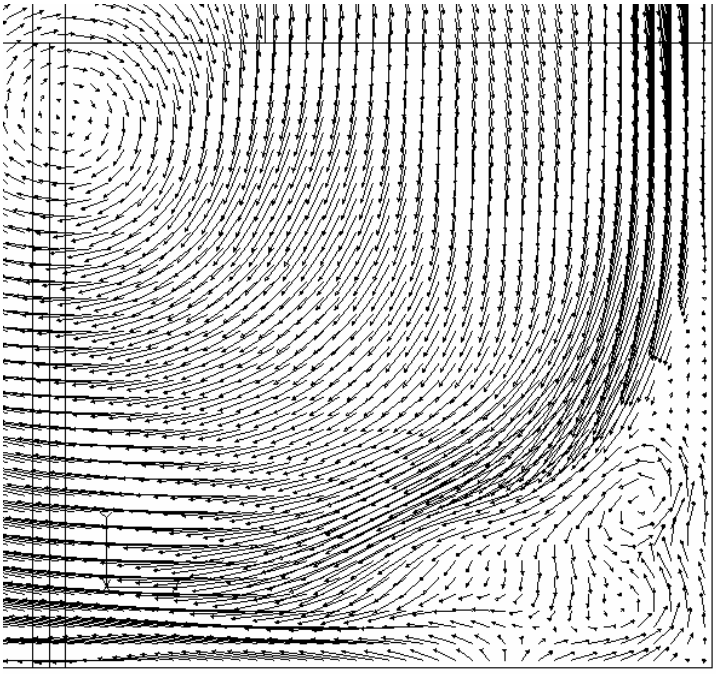

(d) Lower right quadrant

Figure 4.20 Instantaneous velocity vector field on the *yz*- plane, at *2x/B*=0 and 26.7 lid cycle time for the test case with bulk Reynolds number set to 66,666 (continued) .

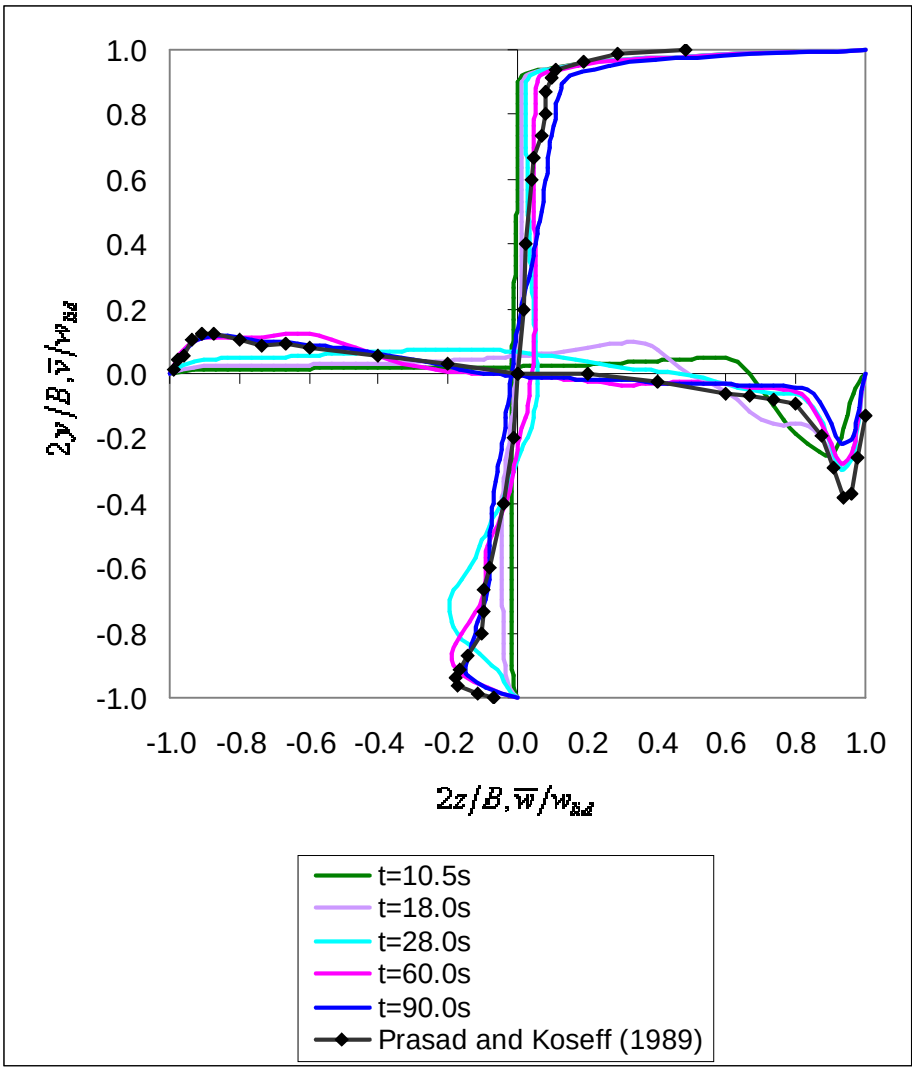

Figure 4.21 Mean velocity profiles for Grid A at various times on the plane normal to the *x*-direction along the lines bisecting the walls.

The time evolution of velocity profiles conforms to the observation which describes the primary vortex as moving from the upper right corner where the lid meets the downstream side wall to the centre of the plane and at the same time gaining momentum from the lid. Details of the profile such as the shifting of the peak velocity value closer to the reference data as flow time increases provide more support for this observation. The profile after 26.7 lid cycle time (t=60.0s) gave a reasonable approximation to the profile after 40 lid cycle time (t=90.0s) as well as the reference data and therefore it is quite safe to state that the flow has reached a steady-state condition (in a statistical sense) at t=60.0s.

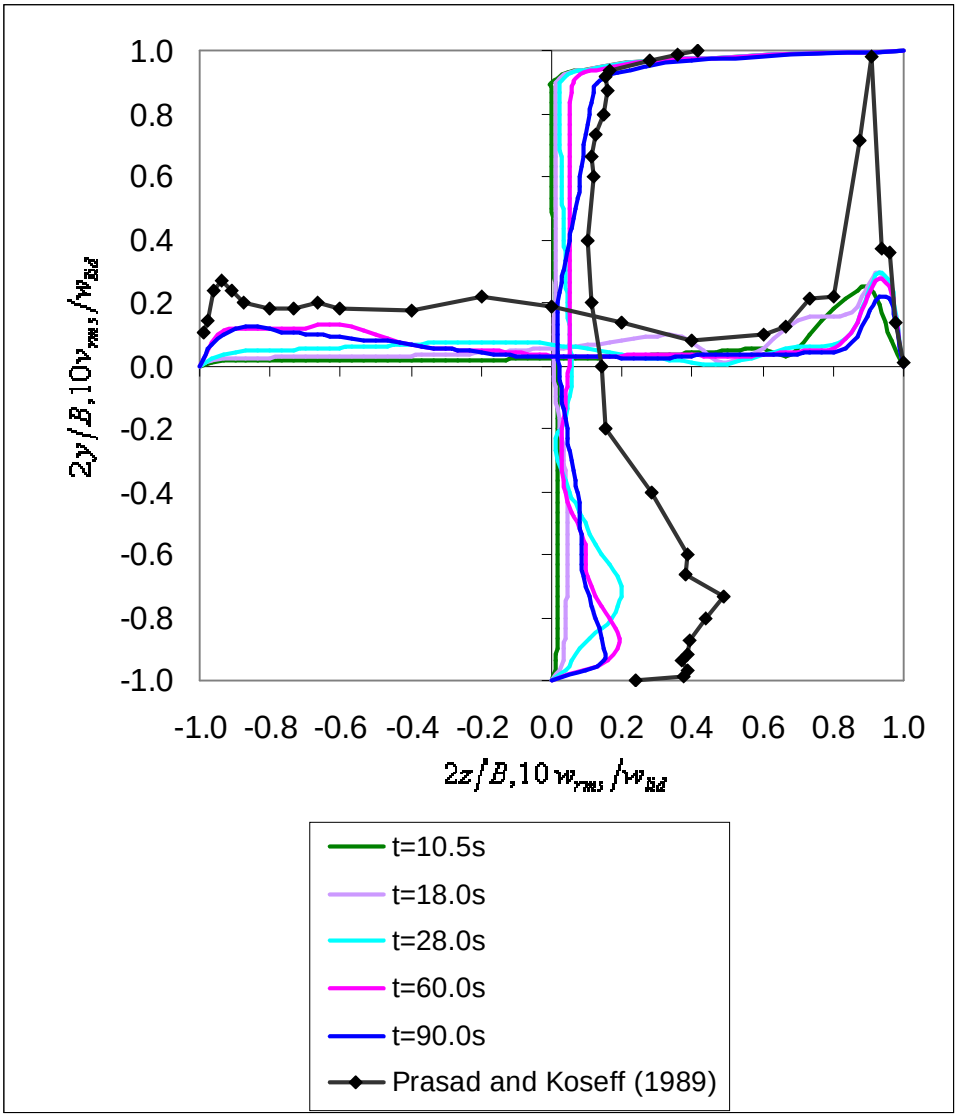

Figure 4.22 Root-mean-square velocity profiles for Grid A at various times on the plane normal to the *x*-direction along the lines bisecting the walls.

After 26.7 lid cycle time (t=90.0s), the $\overline{w}$ profile on the upper half of the monitoring vertical line ($2y/B$>0.24 or y>0.1874m) overestimated the experimental data. This was offset by the surplus (in the opposite direction) in the region $2y/B$<0.24 or y<0.1874m. An explanation for this could be provided by the deficiency of the turbulence model in getting the correct rate of dissipation of turbulence kinetic energy from the modelled small scales. The $\overline{v}$ profile agrees well with the reference data except for the peak region near the downstream side wall. This bears a strong resemblance to the profile shown in

Figure 4.11 wherein the peak average velocity was under estimated. The most convincing explanation for this is the insufficient grid resolution leading to large discretisation errors and for the same reason, it can be stated that the dissipation of turbulence kinetic energy was overpredicted. The non-smoothness of these profiles may result from the instantaneous effects of resolved eddies and to overcome this, a longer averaging period might be necessary.

The presence of Taylor-Görtler like vortices acts as a mechanism for the transfer of momentum from the fluid in the region next to the lower boundary to the primary vortex core. This results in a decrease of the $\overline{w}$ magnitude at the peak near the lower boundary and at the same time increasing the magnitude of $\overline{w}$ in the region of the primary vortex core. In this instance, the magnitude of $\overline{w}$ in the primary vortex core region was overpredicted implying that what was overpredicted was the strength of the Taylor-Görtler like vortices.

The root-mean-square velocity profiles are a statistical measure indicating the amplitude of, in this instance, fluctuating velocity components. Figure 4.22 for Grid A shows the root-mean-square velocity profiles on the *yz*-plane bisecting the cavity where *B* is the lid length. The vertical and horizontal monitoring lines are normal to the walls and are equidistantly spaced between the corners of the plane. At 8 lid cycle time (t=18.0s), the root-mean-square profiles are only slightly above zero. The fluid layer located immediately next to the lid receives momentum as soon as the lid moves. At 12.4 lid cycle time (t=28.0s), the v_{rms} values for $2y/B$<0.4, starts to move towards the reference profile. Closer to the lid, the profile is still dormant, implying that the fluid in this region has not received momentum from the lid, but as t increases, the computed profile in this region inches forward to the reference data. This is different from what is going on the lower half of the plane where it can be seen that, except in the peak region ($2y/B$≈0.7), the profiles are not changing that dramatically. The profile at 12.4 lid cycle time gives an agreeable location of this peak with a difference of approximately 48% compared to the experimental data but as time progresses, this difference increases and the peak moves closer to the lower wall. The vertical w_{rms} profiles between 26.7 and 40 lid cycle times

(t=60.0s and t=90.0s respectively) changed considerably indicating that there is a build-up of large scale fluctuations within this period of time.

Results from computation clearly underestimated the measured data even after 40 lid cycle time (t=90.0s). The largest difference corresponds to the peak next to the downstream side wall where the reference value is five times that of the computed value. This can be attributed to the discretisation error which resulted from using a large time step and to a lesser extent, the discretisation error from the finite volume cell size used in the computation. Another concern is, the value of the Smagorinsky parameter used in the computation may not be physically correct as to achieve correct dissipation of turbulence kinetic energy. This may also contribute to the discrepancy with the reference data as shown in Figure 4.22. To verify the value of the model parameter, a more capable dynamic procedure such as the one proposed by Germano et al. (1991) can be utilised. In this method, typically a test filter is used in addition to the cut-off filter to produce an effective subgrid scale field. A subgrid scale Reynolds stress tensor obtained from this field can be used to compute the value of the model parameter and can be compared to the constant value as it is used in this instance.

It is important to note that root-mean-square contributions are not only from high-frequency turbulent fluctuations but also from low-frequency organised structure fluctuations such as those exhibited by the Taylor-Görtler like vortices described earlier. To separate genuine turbulence from fluctuations of the Taylor- Görtler like vortices, a digital filter must be applied to the time series data but this was not carried out due to the shortage of time.

The $\overline{w'v'}$ correlation plotted in Figure 4.23 indicates how the velocity fluctuations in two perpendicular coordinate directions are related to each other. This may provide some clues to how the secondary flows interact with the primary structure. w' and v' in this context are the fluctuating parts of the velocity about an average value of w and v from standard averaging (as applied in Reynolds averaged Navier-Stokes computation).

For the vertical profile, at 4.67 and 12.4 lid cycle times (t=10.4s and *t*=18.0s respectively) $\overline{w'v'}$ correlations are small which indicating that the flow inside the domain is predominantly laminar. At 12.4 lid cycle time (*t*=28.0s), positive correlations with peak at *2y/B*≈ -0.7 and negative correlations with peak at *2y/B*≈ -0.4 and *2y/B*≈ -0.9 were obtained from the computation. This is considerably different when compared to the trend shown by the reference data, with a negative peak at *2y/B*≈ -0.8 and a positive peak next to the lower boundary. This can be explained by the fact that the jet-like flow of the primary vortex is still in transition and located relatively far from the lower boundary as shown in Figure 4.3 which implies that turbulence is non-stationary. The increasing strength of the primary vortex resulted in positive values for w' and v', leading to a positive correlation.

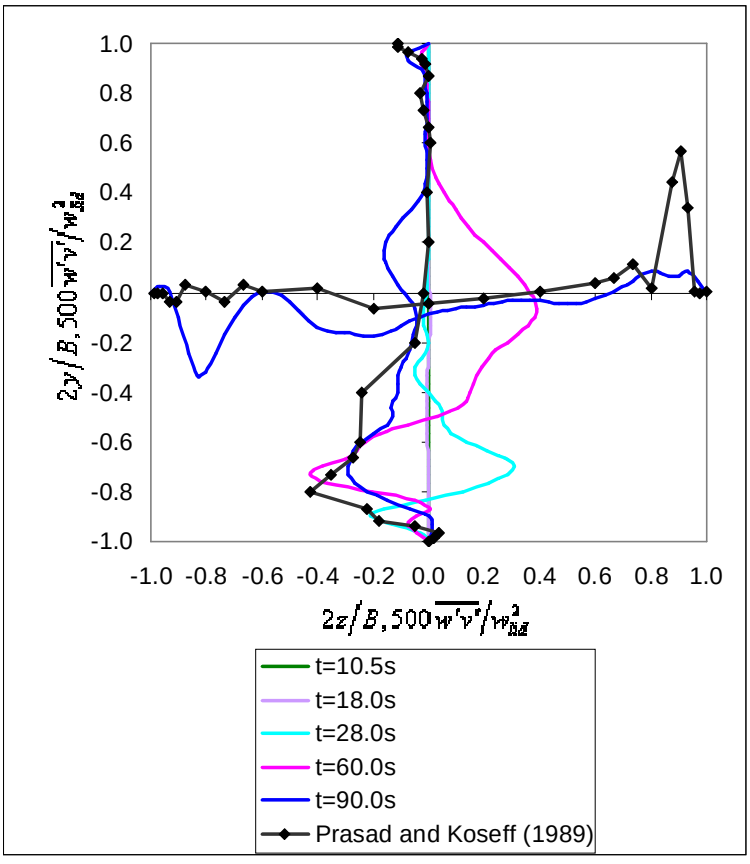

Figure 4.23 $\overline{w'v'}$ stress profiles for Grid A at various times on the plane normal to the *x*-direction with along the lines bisecting the walls.

After about 26.7 lid cycle time (t=60.0s) for the vertical profile, there is a large positive correlation in the core region of the primary vortex as shown in Figure 4.23. This may be related to the increase and overprediction of the w_{rms} profile as shown in Figure 4.22. The positive correlation exhibited by the reference data in the region adjoining the lower boundary was not captured in the computed results. Instead, the computed correlation in this region is opposite hinting that as the primary vortex evolved, the magnitude of the v velocity component in this region underwent reduction. The peak with the larger magnitude close to the lower boundary agrees well with the value from the experiment but it is located at a position approximately 29% higher from the lower boundary, which is in contrast to the reference data. Due to an omission in the subroutine for post-processing, the only horizontal profile available was at t=90.0s.

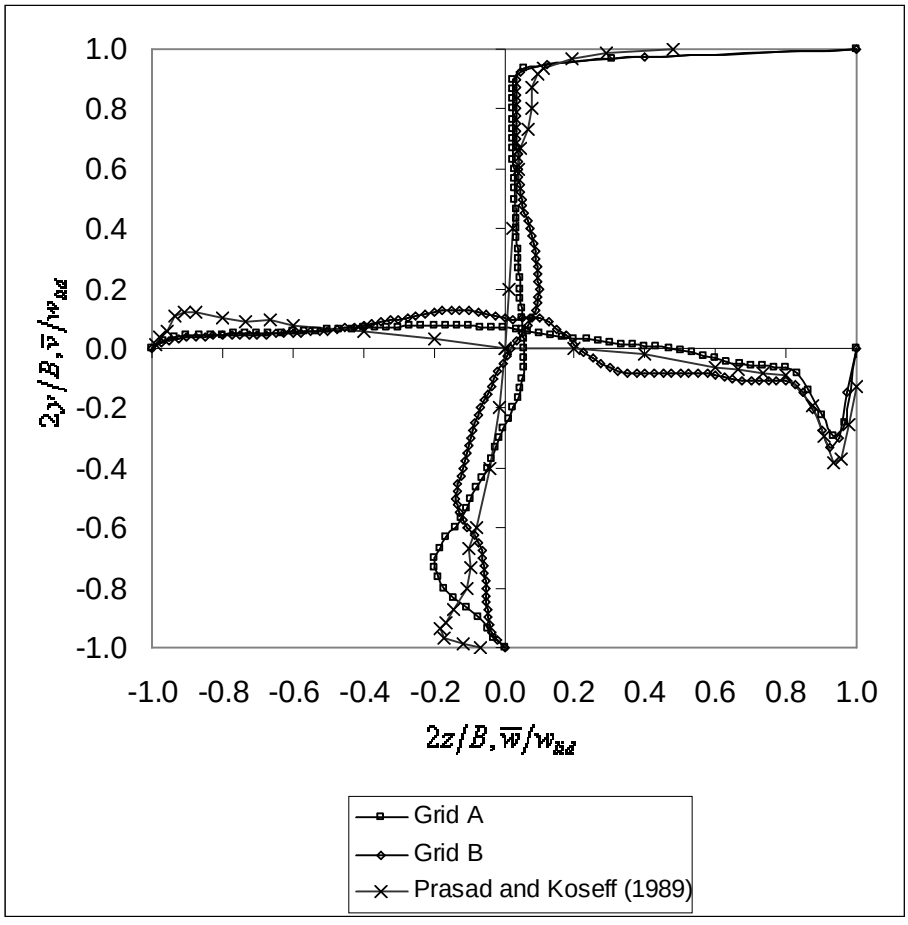

Figure 4.24 Comparison of mean velocity profiles between Grid A and Grid B at 12.4 lid cycle time on the plane normal to the x-direction along the lines bisecting the walls.

Moving forward in time and inspecting the vertical profile after 40 lid cycle time (t=90.0s), it can be stated that the computed $\overline{w'v'}$ profile follows the reference data more closely compared to the profile at 26.7 lid cycle time (t=60.0s). This is because the flow structure is now a lot closer to the statistically steady condition as shown in Figure 4.23. However, the computed $\overline{w'v'}$ profile underestimates the reference profile in most regions along the monitoring line except in the primary vortex core. The positive correlation adjacent to the lower boundary implies that there is transfer of turbulence kinetic energy from the mean flow to the large scale eddies associated with this trend of correlation. This can also mean that the presence of the Taylor-Görtler like vortex pair shown in Figure 4.19 (which transfers momentum from the lower boundary layer into the primary vortex core region) resulted in a positive w' due to the decreasing magnitude of w and v' due to the increasing value of v in the positive y direction.

The horizontal $\overline{w'v'}$ profile in the region $2z/B$<-0.6 in Figure 4.23 has a similar pattern to the vertical profile near the lower boundary suggesting a similar physical process taking place in that region. The horizontal $\overline{w'v'}$ profile shows an underestimation of the spike near the downstream side wall. This observation may be coupled with the lower mean velocity gradient, and lower peak value of the mean velocity profile, in Figure 4.21. Possible explanations for this deficiency are the large discretisation error associated with the large time step used inside the flow solver and the highly anisotropic turbulence found in this region, making the uniform value of Smagorinsky constant used in the computation, unrealistic. The discrepancy may also be related to the imperfect analogy between molecular transport of momentum and turbulence upon which this turbulence model is based on.

Differences in the mean profiles in Figure 4.24 are larger than those in Figure 4.25. At 40 lid cycle time or t=90.0s (statistically steady flow), differences in the mean profiles between the two grids are marginal, except in the region next to the downstream side wall, where fluid is moving downwards in a jet-like motion. Since the variation in time step size during the simulation for both grids is identical, the discrepancy between the

results of the two grids shown in Figure 4.25 occurs largely, due to the spatial discretisation error. The mean value from Grid B is approximately 30% less than that of the reference data at the peak next to the downstream side wall which is mostly attributed to the combination of spatial and temporal discretisation error.

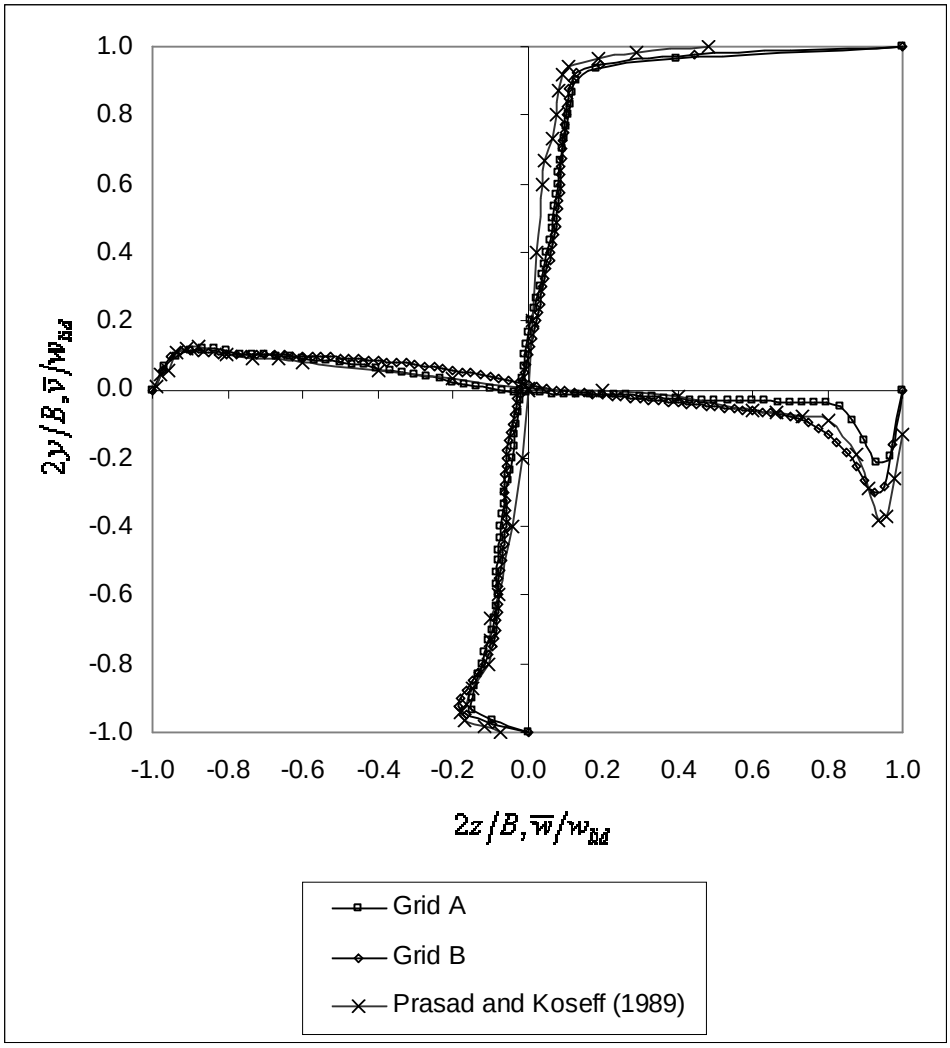

Figure 4.25 Comparison of mean velocity profiles between Grid A and Grid B at 40 lid cycle time on the plane normal to the *x*-direction along the lines bisecting the walls.

The root-mean-square plot in Figure 4.26 shows that the profiles are severely under-predicted especially in regions next to the downstream side wall and lower boundary as well as in the primary vortex core region. The difference in root-mean-square values between the two grids are marginal, except in the region next to the downstream side wall, where fluid is moving downwards in a jet-like motion. This can be explained by the

fact that the amplitude of fluctuations, be it from turbulence or secondary flow structures, are small; and also, the relatively short time period taken for averaging related to the formation of the large scale structures, is still infrequent. It is also possible that the rate of large eddy formation produced by the computer model is lower than that from the experiment. The mean velocity is close to the reference profile and hence it is unlikely that discrepancies in the mean profile are affecting the root-mean-square data.

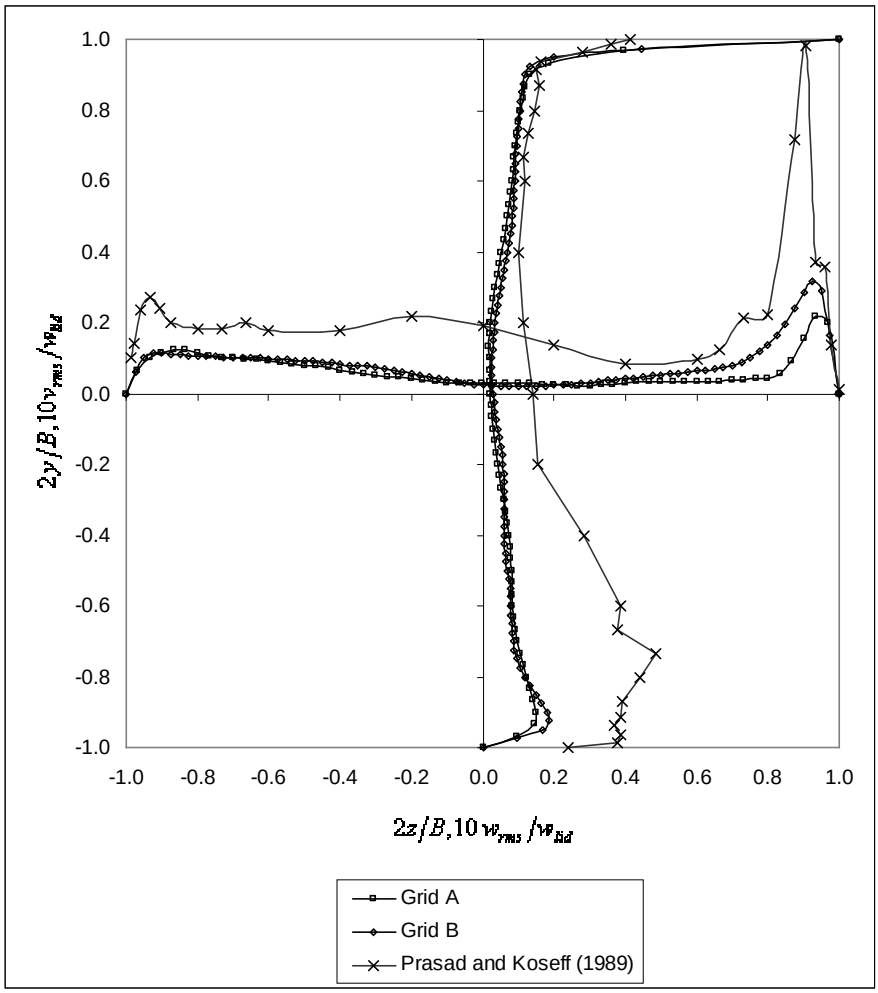

Figures 4.26 Comparison of root-mean-square velocity profiles between Grid A and Grid B at 40 lid cycle time on the plane normal to the *x*-direction along the lines bisecting the walls.

The $\overline{w'v'}$ correlation shows a considerable difference when using two different mesh sizes as shown in Figure 4.27. These results are sensitive to the local resolved velocity gradient and filter width which is in this case the cell edge length. The uniform value of

the Smagorinsky constant is also suspect and may not be appropriate at least in this case, which occurs due to the anisotropy of turbulence. The treatment of solid wall boundary does not seem to have a major influence because profiles near the walls (except the lower boundary) are in good agreement with computation results. The region in the primary vortex core shows a high root-mean-square value and a strong magnitude of $\overline{w'v'}$ correlation, probably, as a result of taking the averaging from the start of simulation and the relatively short time period taken for averaging.

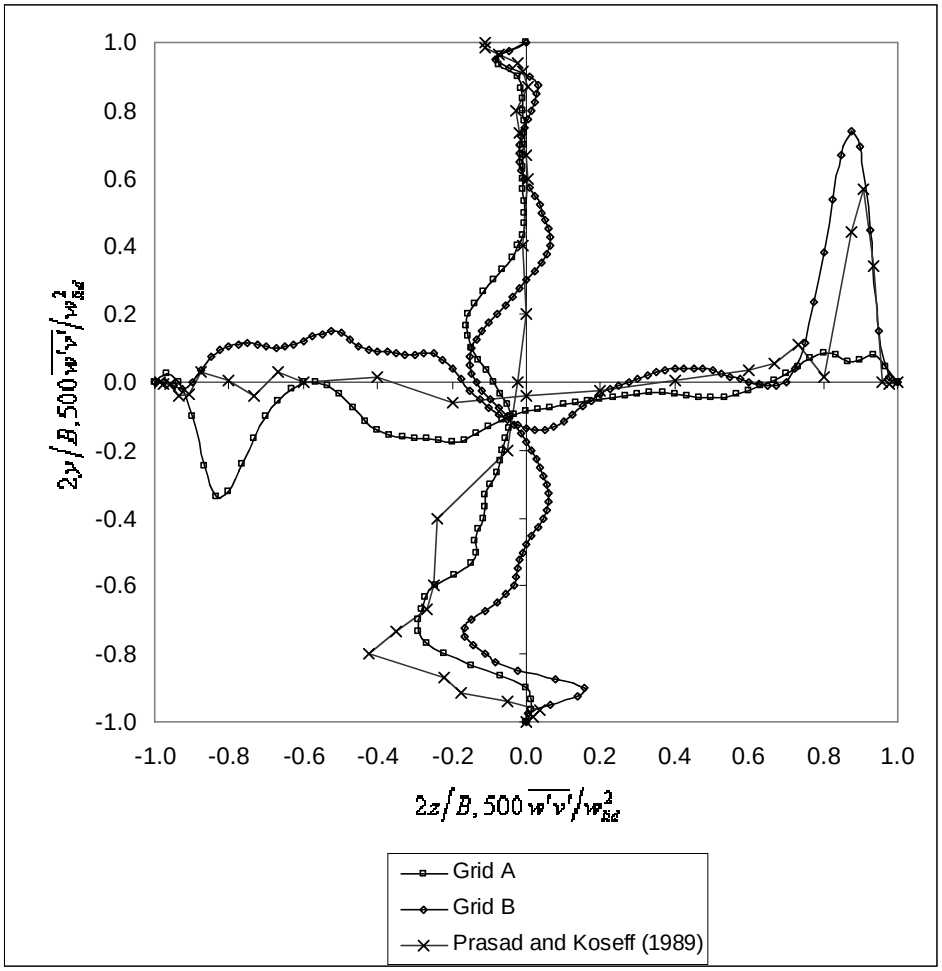

Figures 4.27 Comparison of $\overline{w'v'}$ stress profiles between Grid A and Grid B at 40 lid cycle time on the plane normal to the x direction along the lines bisecting the walls.

In Figure 4.28, the peak value of $\overline{w}$ next to the downstream side wall at 8 lid cycle time (t=18.0s) is closer to the reference value compared to similar data from coarser grids

plotted in Figures 4.21 and 4.24. This gives an idea on the amount of spatial discretisation error associated with the coarser grids.

In general, the transient profiles tend towards the steady state values as the simulation progresses. In order to investigate how the period of averaging influences the statistical profiles, this parameter was increased to eight seconds for the profile at 22.2 lid cycle time (t=40.0s). Good agreement with the experimental data was obtained at the same moment. In this instance, the largest error in the mean profiles is the velocity in the z-direction at $2y/B \approx 0$. The velocity magnitudes near all walls (except the upstream side wall) are underpredicted but these are better in terms of approximating the experimental data compared to those of Grid A and Grid B.

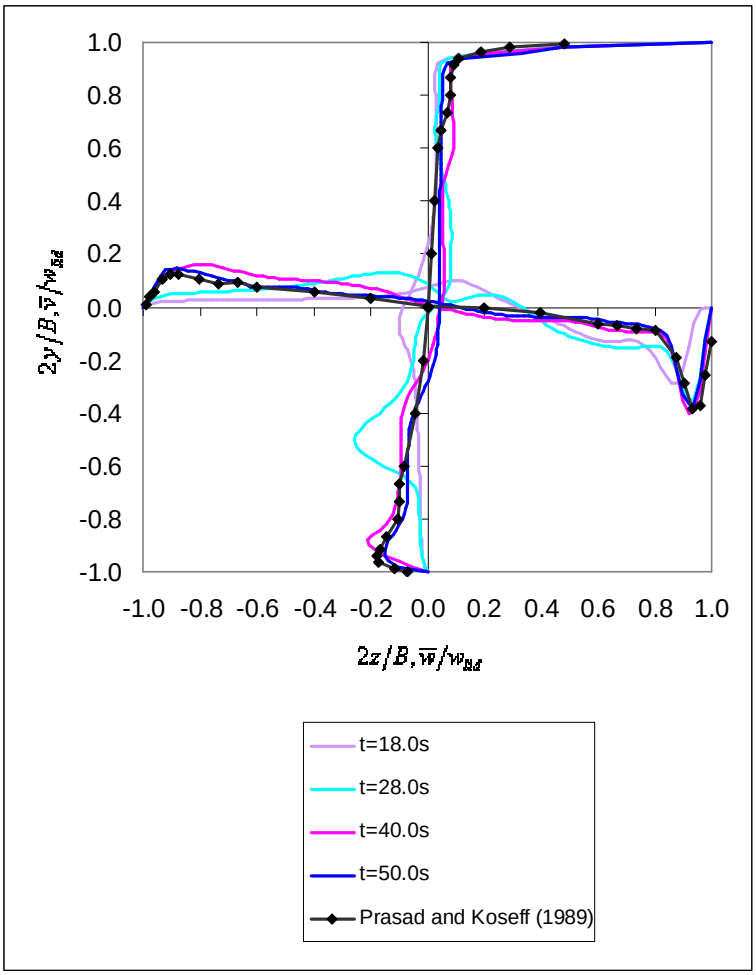

Figure 4.28 Mean profiles for Grid C at various times on the plane normal to the x-direction along the lines bisecting the walls.

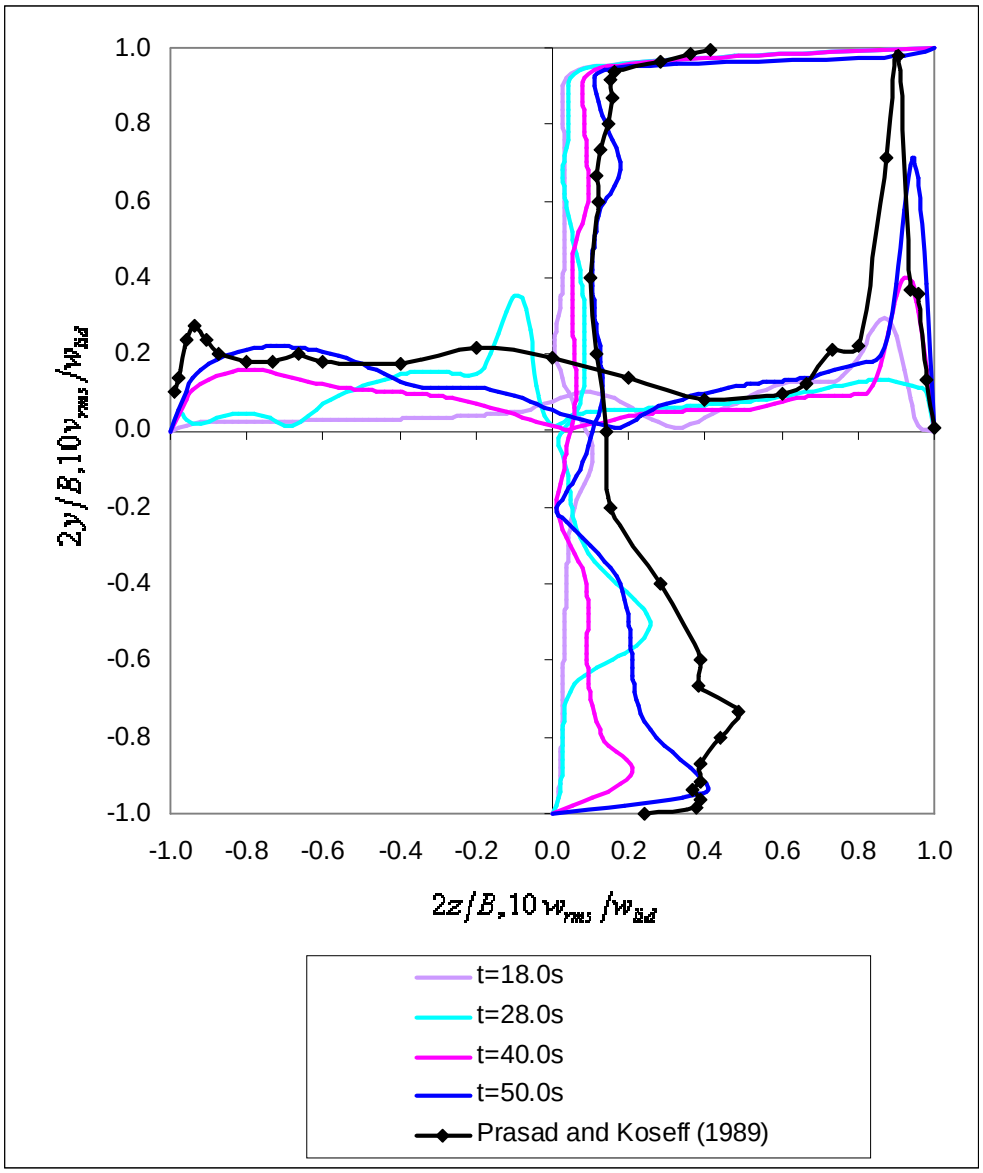

Figure 4.29 Root-mean-square velocity profiles for Grid C at various times on the plane normal to the *x*-direction with along the lines bisecting the walls.

The root-mean-square profiles plotted in Figure 4.29 show an irregular behaviour from time *t*=18.0s to *t*=28.0s (8 and 12.4 lid cycle times respectively). For instance, the peak near the downstream side wall decreases in magnitude and in the region near the centre of the plane, the values fluctuate strongly moving in the *y* and *z*-directions. This can be explained by the transient nature of the flow structure at the early stages of the simulation. The profiles start to move towards the reference values at 17.8 lid cycle time

(t=40.0s). At 22.2 lid cycle time (t=40.0s), as the flow is within the statistically steady zone, it can be stated that the root-mean-square profiles give reasonable agreement with the reference data, considering the simplicity of the turbulence model used. The peak value near the downstream side wall is about 30% lower than the reference value. The horizontal profile underestimated the reference data in the primary vortex core region. This is also the case for the vertical profile defined by the region $-0.8<2y/B<0$ though these are a lot better than results at 17.8 lid cycle time.

From the results at 22.2 lid cycle time (t=40.0s) it can be said that both discretisation error and (probably to a lesser extent) period of averaging exerts a significant influence on the accuracy of the results obtained in comparison with results shown in Figures 4.26. The period of averaging must match the time scale of the resolved eddies. The turbulence model or modelling error takes less responsibility to produce the correct value of SGS stresses as the mesh is refined which also contributes to the improvement in results shown in Figure 4.29. Even so, the turbulence model is still responsible for the discrepancy in results. Specifically, this is related to the constant value of the Smagorinsky parameter used and the inability of small (unresolved) eddies to exert their influence such as the transfer of energy to the large (simulated) eddies.

The $\overline{w'v'}$ correlation profile at 8 lid cycle time (t=18.0s) in Figure 4.30 gave a good approximation to the reference profile in the region of the peak next to the downstream side wall with the peak value, about 6% less than, the reference data. However the core region of the primary vortex shows a high magnitude of correlation compared to the experimental data. This can be expected since the flow structure is still in a transient stage.

At 12.4 and 17.8 lid cycle times (t=28.0s and t=40.0s respectively), the peak next to the downstream side wall was severely underpredicted. The same phenomenon was observed at the lower boundary. The region close to the upstream side wall saw a negative value of $\overline{w'v'}$ moving in the positive z-direction at 17.8 lid cycle time. This differs from the

experimental profile whereby the $\overline{w'v'}$ correlation fluctuates in sign while moving in the positive z-direction. This could be a feature of the transient flow moving towards the fully developed state.

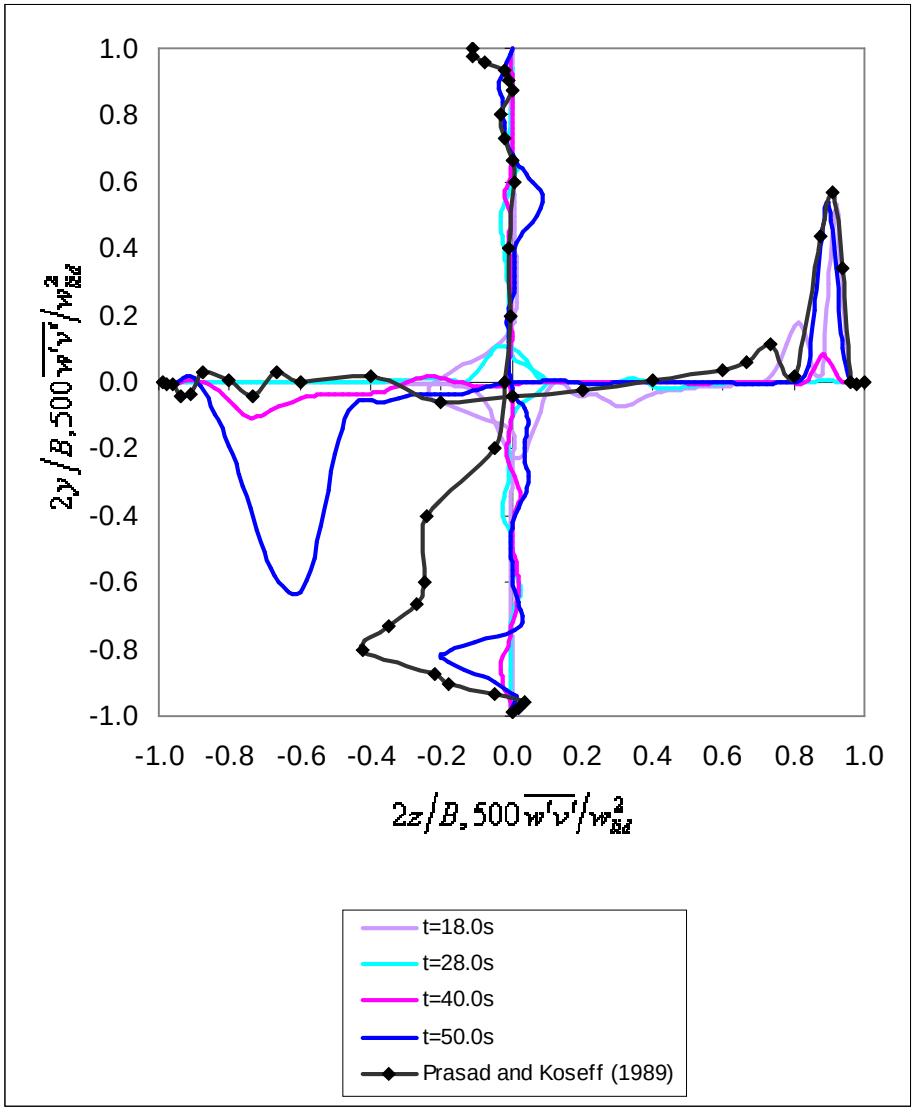

Figure 4.30 $\overline{w'v'}$ stress profiles for Grid C at various times on the plane normal to the x-direction along the lines bisecting the walls.

At 22.2 lid cycle time (t=40.0s), the trough at $2z/B \approx 0.8$ was not indicated by the profile. Nevertheless, the value of the peak close to the downstream side wall was in good agreement with the experimental data. At the lower boundary, the negative peak was underpredicted with a difference of approximately 40% from the experimental value.

This may be accounted for by the smaller amplitude of fluctuations of the nascent Taylor-Görtler like vortices. The positive $\overline{w'v'}$ part next to the lower boundary was successfully captured by the simulation at t=40.0s. A distinctive feature of the horizontal profile shown in Figure 4.30 is the over-prediction of $\overline{w'v'}$ at $2z/B \approx$ -0.6 which is probably related to the presence of slowly varying regular fluid motion such as the Taylor-Görtler like vortices. These vortices are also formed in this region due to the existence of a concave 'surface' upstream along the wall. Also to note, the limitation of the turbulence model itself (for example, using a uniform value of filter width) may have a strong influence on the accuracy of the stress tensor.

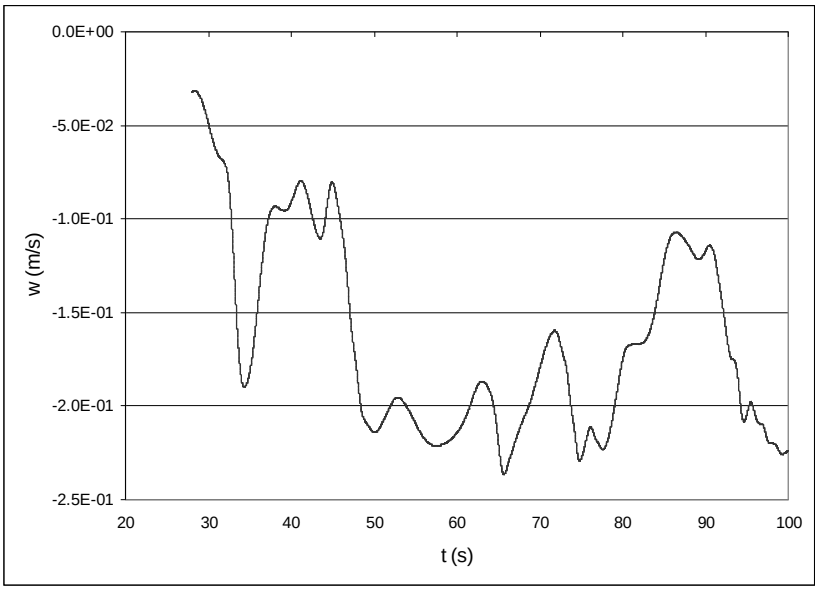

Figure 4.31 Time-trace of the *w* velocity component monitored at a location 4mm above the lower boundary, on the vertical centreline of the *yz*-plane bisecting the cavity.

The time-trace plot in Figure 4.31 shows the existence of apparently random fluctuations indicating the presence of genuine turbulence. The monitoring location coincides with the peak of the average velocity profile to a level above the lower boundary layer. As stated earlier in this chapter, a steady flow (on average with time) was achieved afterwards at about 22.2 lid cycle time (t=40s). This data can be filtered further to attenuate high frequency oscillations due to genuine turbulence leaving out low frequency oscillations from secondary flow motion such as the Taylor-Görtler like vortices. The frequency of

this secondary flow can then be estimated.

Using data from Figure 4.31, the power spectrum for the resolved *w* velocity component was obtained. It was obtained by applying discrete Fourier transform (in the form of Fast Fourier Transform) to the time series data and then squaring the magnitude of the imaginary numbers obtained from the Fast Fourier Transform. To avoid aliasing error, the Nyquist frequency restriction was applied by reducing the frequency to half of the original maximum value. No windowing was applied to the time series data implying that leakage might be found at the low frequency end of the spectrum.

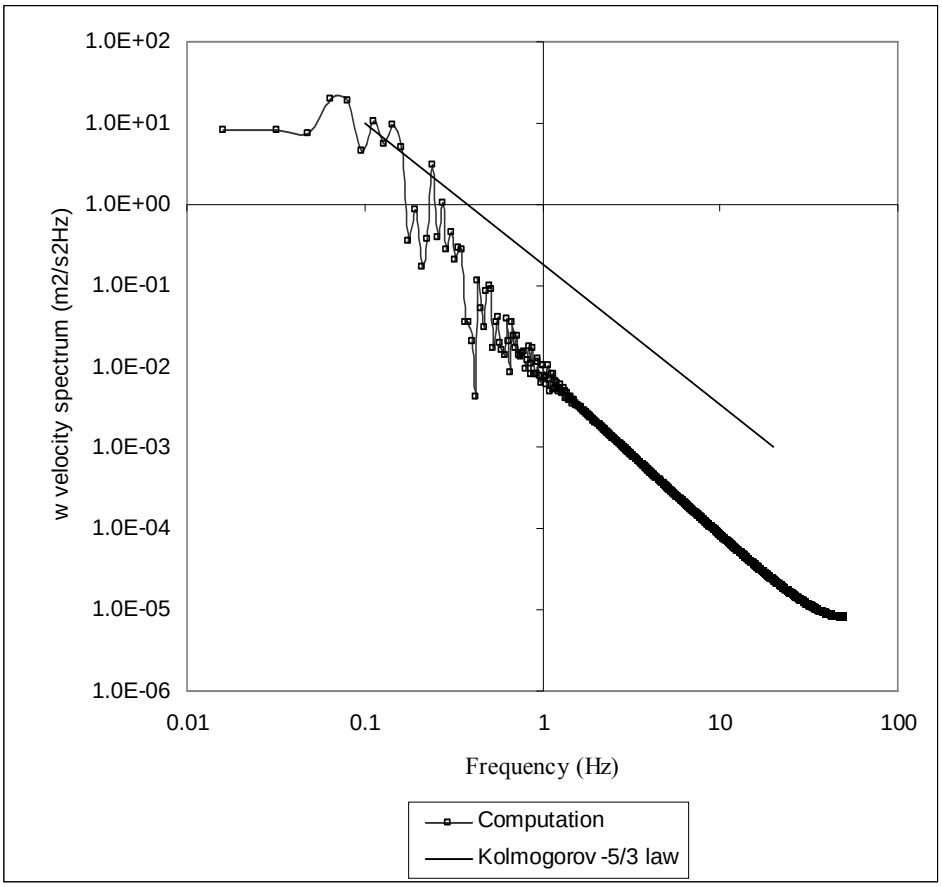

Figure 4.32 *w* velocity spectrum monitored at a location 4mm above the lower boundary, on the vertical centreline of the plane bisecting the cavity.

Figure 4.32 indicates the presence of the inertial sub-range as hypothesised by Kolmogorov (1991). The *w* velocity spectrum of another point approximately 0.0324m

above the first observation point was carried out, but in this instance, the time step size was an order of magnitude less than that was used to obtain the previous spectrum. This point is relatively far away from the boundary layer region compared to the first case; the existence of the inertial sub-range zone is evident from Figure 4.33. The main difference between these two spectrums is in the level of energy contained in fluctuations of a given frequency. In the latter case the energy spectrum level is about two orders of magnitude lower than the former.

The *w* velocity component spectrum gave an agreeable result, probably because the production of turbulence kinetic energy did not take place in the boundary layer region (with very simple treatment or computation of wall shear stress and relatively coarse mesh) but in regions well inside the computational domain which is not subjected to the difficulty with varying integral length scale size with Reynolds number from the wall as seen in Figure 4.34. Referring to Figures 4.26 and 4.29, it is clear why the profiles are underpredicted near the lower boundary. Figure 4.34 shows that this region has a negligible amount of turbulence kinetic energy *k* resulting in the low root-mean-square values predicted by the simulation.

A slightly milder gradient in the frequency range of 1Hz to 10Hz was shown in Figure 4.32 which may be connected to the locally anisotropic (inhomogeneity and differences of velocities at separate points are not invariant under rotations and reflections in the space of the vectors connecting the points) turbulence in the flow domain. This violates the conditions upon which Kolmogorov (1991) theory was based upon. The occurrence of intermittency (described in Chapter 2) may also play a role in deviating the computed slope from the one given by the -5/3 law.

Figures 4.34 to 4.39 show the distribution of turbulence kinetic energy and $\overline{w'v'}$ shear stress on various planes in the domain. The $\overline{w'v'}$ term in Figure 4.35 overlaps the high turbulence kinetic energy region in Figure 4.34 but are also significant (compared to other regions on the plane) in the downstream secondary eddy region. This suggests that the distortion of this structure is due to the interaction with the Taylor-Görtler like

vortices sweeping in the direction normal to the plane.

On the *xz*-plane of Figures 4.38 and 4.39, the high turbulence kinetic energy and $\overline{w'v'}$ stress term region is close to the downstream side wall. The values are comparable in magnitude to those on the *yx*-plane. This coincides with the region of high turbulence kinetic energy and $\overline{w'v'}$ stress term shown in Figures 4.34 and 4.35 respectively.

Figures 4.34 and 4.35 show that regions of high turbulence kinetic energy and $\overline{w'v'}$ stress are coupled to the location of the Taylor-Görtler like vortices. This result supports the statement that the Taylor-Görtler like vortices is responsible for the production of turbulence kinetic energy in the computational domain.

With increasing mesh size and decreasing time step size, increasingly smaller scales will be simulated. The spectrum will represent smaller and smaller scales until a point where fluctuations are caused by numerical (discretisation, iteration and round-off) errors. When this stage is reached, the spectrum will flat out at a relatively small value associated with the field variable.

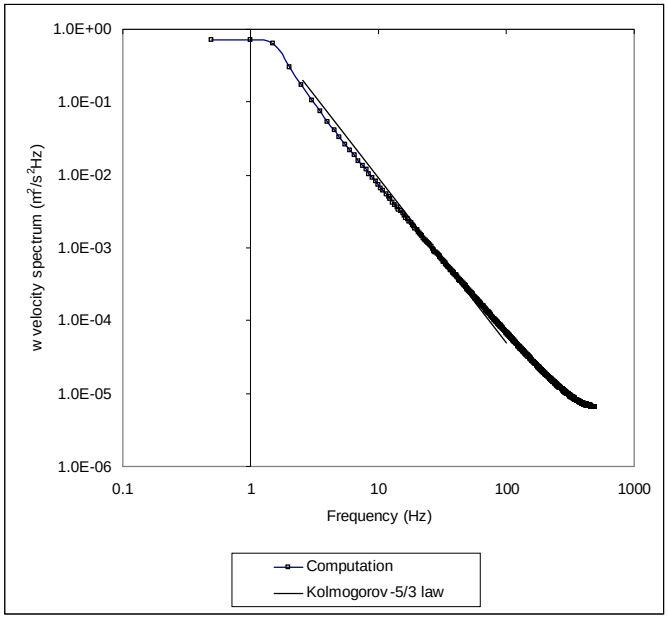

Figure 4.33 *w* velocity spectrum monitored at a location 4mm above the lower boundary, on the vertical centreline of the plane bisecting the cavity.

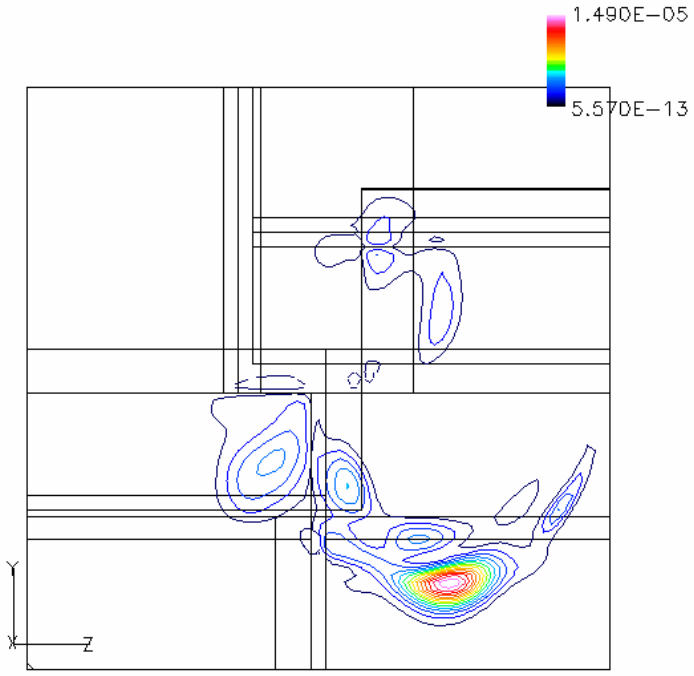

Figure 4.34 Turbulence kinetic energy per unit mass (m^2/s^2) on the *yz*-plane, at *2x/B*=0 and 26.7 lid cycle time.

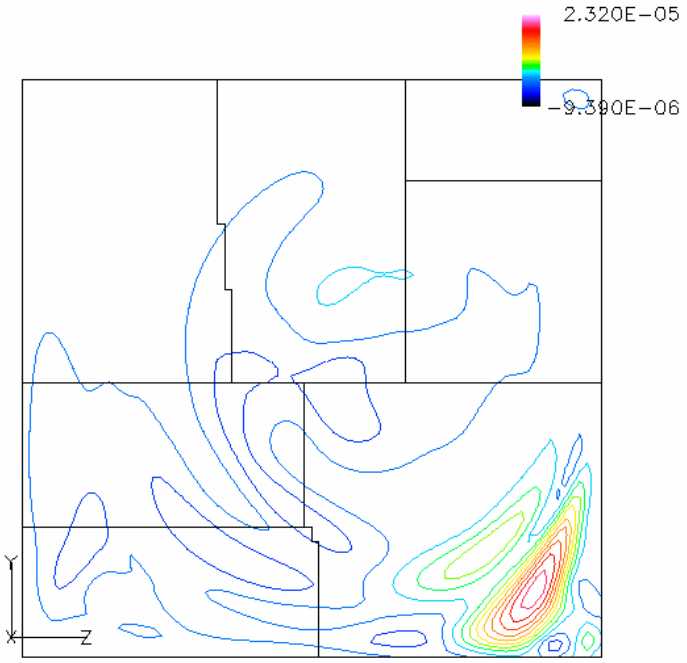

Figure 4.35 $\overline{w'v'}$ (m^2/s^2) on the *yz*-plane, at *2x/B*=0 and 26.7 lid cycle time.

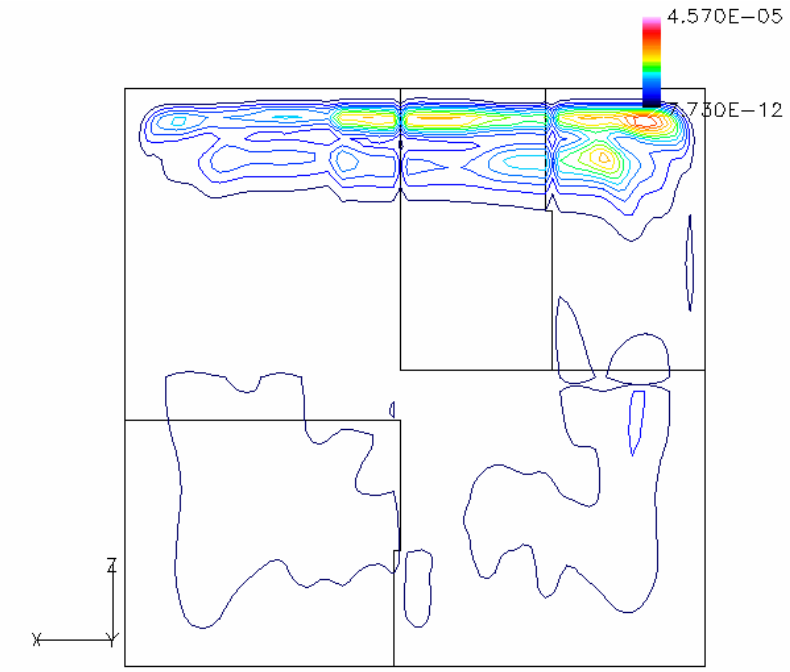

Figure 4.36 Turbulence kinetic energy per unit mass (m^2/s^2) on the *xz*-plane, at *2y/B*=0 and 26.7 lid cycle time.

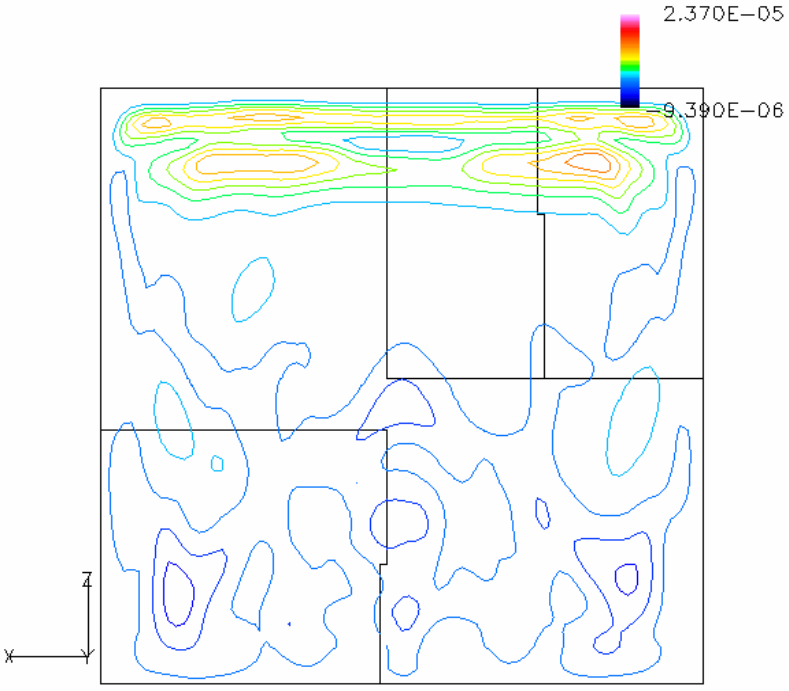

Figure 4.37 $\overline{w'v'}$ (m^2/s^2) on the *xz*-plane, at *2x/B*=0 and 26.7 lid cycle time.

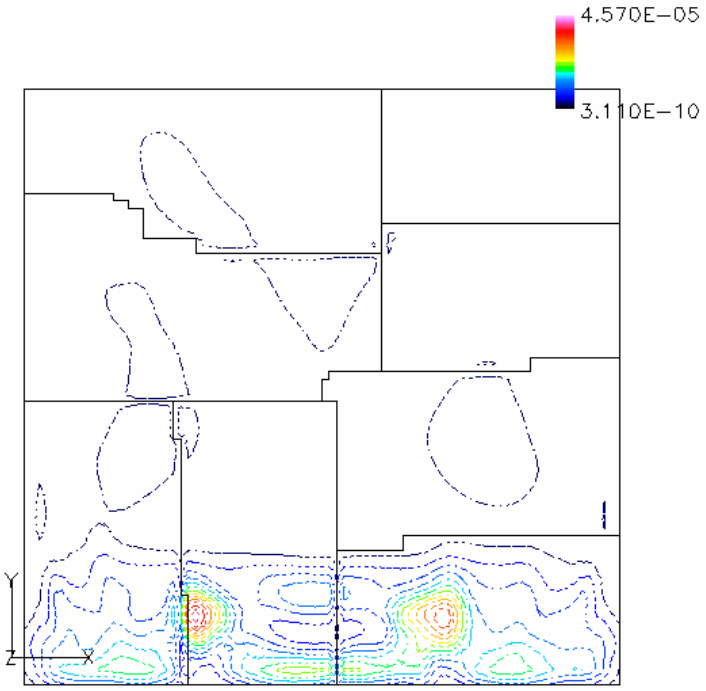

Figure 4.38 Turbulence kinetic energy per unit mass (m^2/s^2) on the *xy*-plane, at *2z/B*=0 and 26.7 lid cycle time.

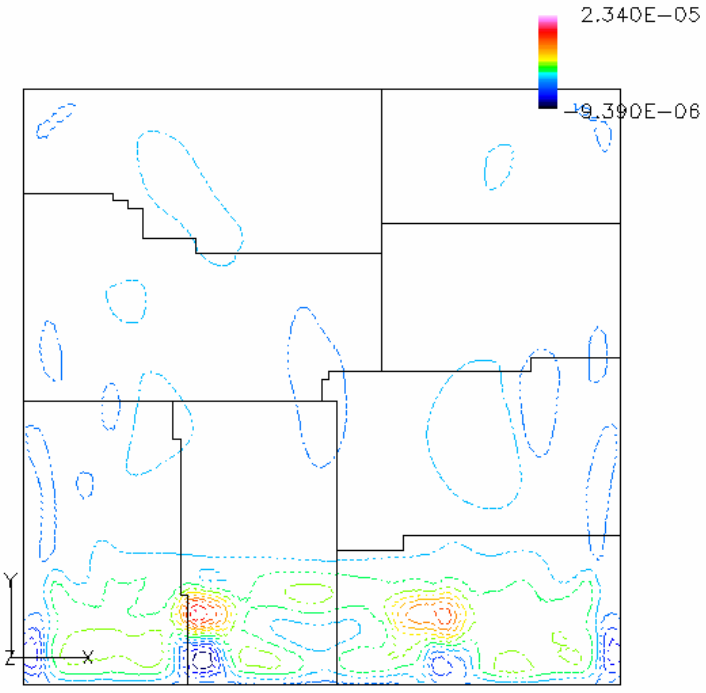

Figure 4.39 $\overline{w'v'}$ (m^2/s^2) on the *xy*-plane, at *2z/B*=0 and 26.7 lid cycle time.

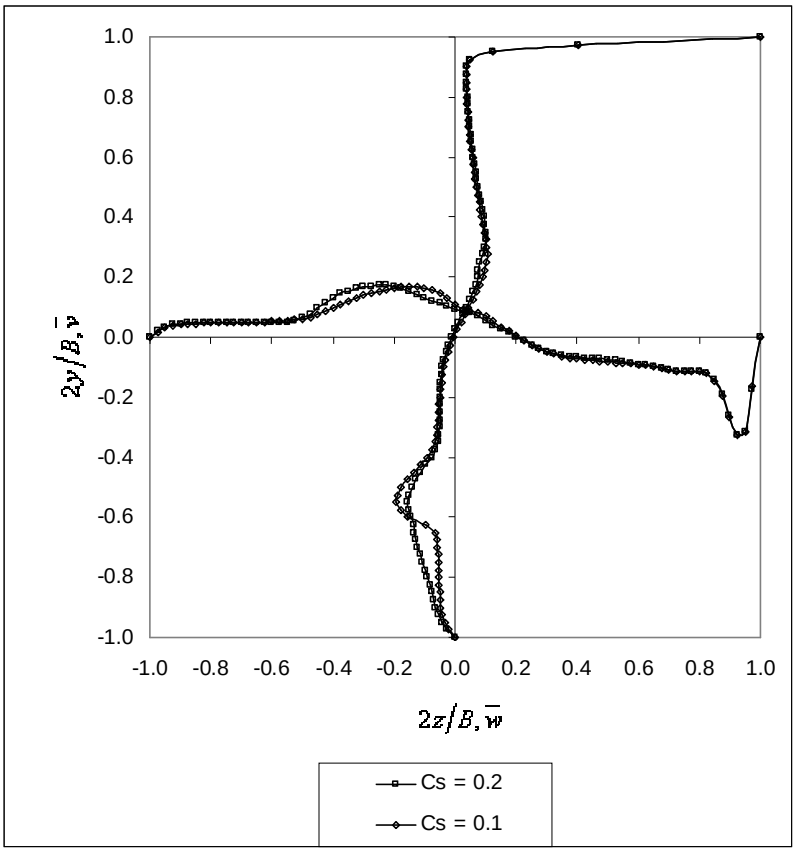

Figure 4.40 Profiles of mean velocity components with two values of C_s.

The effect of using different values of Smagorinsky constant C_s was also investigated for this test case using Grid B. The average velocity profiles with C_s=0.2 shown in Figure 4.40 indicate that peaks within the domain far from walls are located slightly behind those with C_s=0.1. The magnitude of these peaks is reduced as the value of the constant is doubled. Gradients in the vicinity of these peaks are milder when using the larger value of C_s. These results are to be expected and the explanation is provided as follow. The larger C_s value means a larger magnitude of the sub-grid scale eddy-viscosity inside the computational domain. This leads to an excessive damping of resolvable turbulence and an increase in the rate of dissipation of turbulence kinetic energy. The reasons why the peak region next to the downstream side wall is in good agreement for both values of C_s may be related to the use of wall damping and also the high velocity gradients in this region, making the sub-grid scale eddy viscosity less sensitive to the value of C_s.

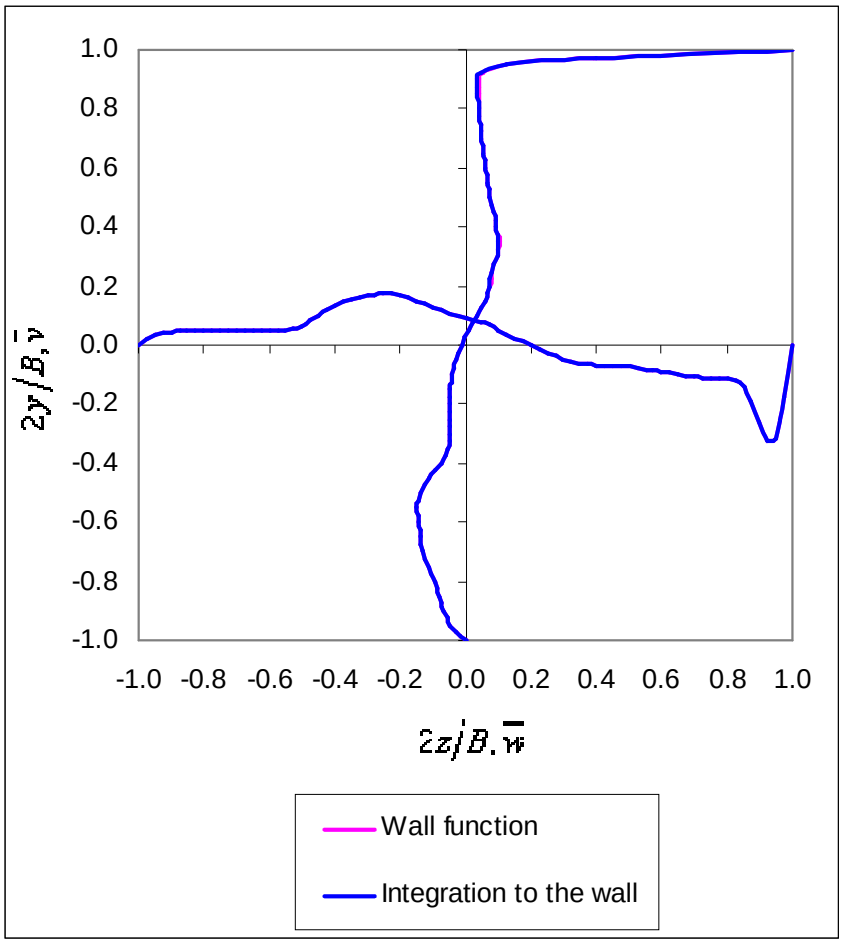

Figure 4.41 Profiles of mean velocity components with wall function and integration to the wall.

An alternative to the integration to the wall treatment of solid boundaries is the wall function frequently used for example in high Reynolds number Reynolds averaged Navier-Stokes computation with the standard k-ε turbulence model. This was tried by restarting the simulation at 13.3 lid cycle time (t=30.0s). It was found that the time marching became unstable when using a time interval Δt equal to 0.001s and as a consequence, the simulation was performed with a smaller time step of Δt=0.0001s for 2000 time steps. The physical assumptions and equations involved when using the wall function has been explained in Section 3.1.

The deteriorating time-marching stability limit may be related to the increase in the value of the shear stress at the wall since the value of y^+ calculated using Equation (2.23) is less than the limit for a logarithmic region. In other words, the cell layers next to the walls

were located within the viscous sub-layer region but the profile was assumed to be logarithmic in the calculation of shear stress on the wall. To maintain stability, this must be compensated by lowering time step size and/or increasing the cell size. In this case the former was chosen.

The y^+ values on the downstream side wall were found to be mostly within the viscous sub-layer region, not in the logarithmic region as required by Equation (2.26) which gives the shear stress at the wall. This suggests a non-negligible modelling error at the boundaries when using the wall function. It is therefore expected that the integration to the wall would give a more realistic solution of the profile. However results in Figure 4.41 show that there is negligible difference between the two methods of treating the boundary layer region. This can be explained by the fact that the averaging period was too short to make any noticeable difference to the profile.

The fact that the energy spectrum plot in Figure 4.32 agrees well with Kolmogorov's -5/3 law may also be related to the matching condition of using integration to the wall with the values of y^+ for the cells next to wall boundaries.

The values of the components of resolved strain rates at a monitoring location, 4mm above the lower boundary, were investigated by using Grid B and results at 13.3 lid cycle time (t=30.0s) is shown in Figure 4.42. Unlike $\partial\overline{u}/\partial z$ and $\partial\overline{v}/\partial x$, the magnitude of $\partial\overline{w}/\partial y$ is relatively large and is comparable to that of $\partial\overline{u}/\partial x$ as shown in Figure 4.42. This matches the mean profile shown in Figure 4.28 where at this point, the magnitude of the gradient is relatively large. It was found that the magnitude of $\partial\overline{w}/\partial y$ is comparable to that of $\partial\overline{w}/\partial z$ which means that the second term in the strain rate equation can be relatively large and may have a non-negligible contribution to the modelling error. This may also be one of the reasons why there is a significant deviation in the correlation data stated in Figure 4.30. However the modelling error depends to some extent on the coordinates of the monitoring location, since, the flow structure of the driven cavity is not regular, at least, in space. It is also interesting to note that the $\partial\overline{w}/\partial y$ strain rate term

increases in magnitude, as the simulation progresses, but the other two terms stay almost constant in value, with respect to time.

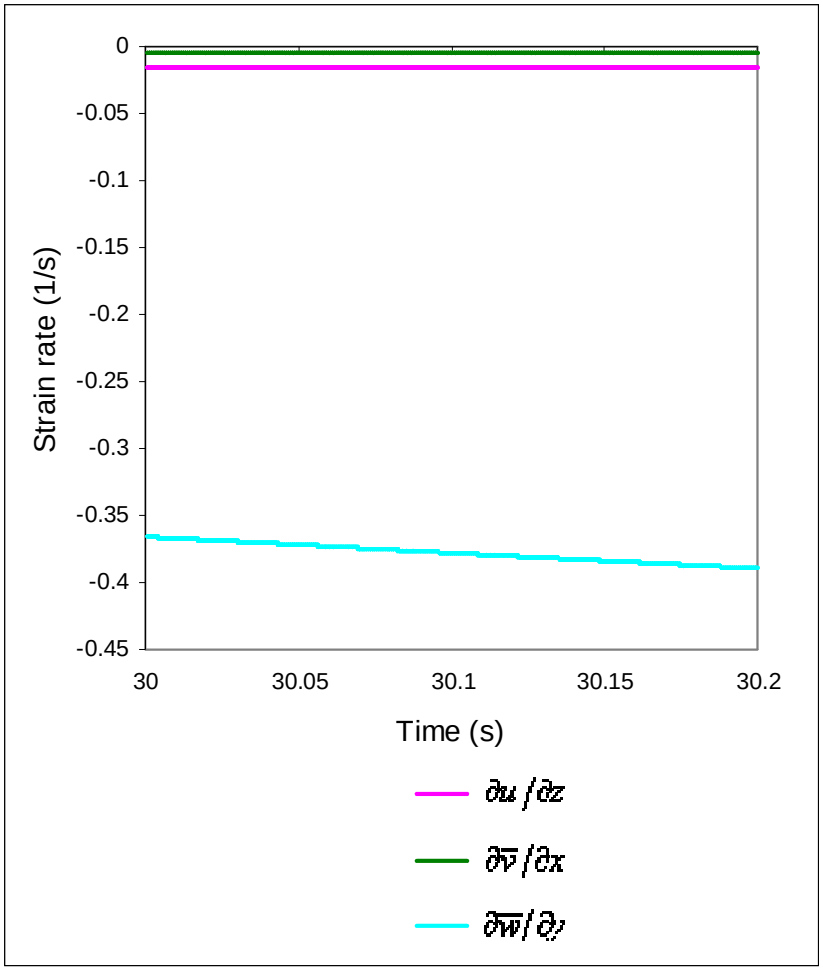

Figure 4.42 Variation of strain rate with time.

4.3 Closure

This chapter has demonstrated the application of the flow solver for a turbulent three-dimensional driven cavity flow by using three uniform grids with varying densities. In many instances, computational results agree reasonably well with the reference data. A number of important conclusions can be drawn from this case:

- Important flow features such as the primary vortex, downstream and upstream secondary vortices, the upper secondary vortex and the Taylor-Görtler like vortices were successfully reproduced by the flow solver.

- With the current aspect ratio of the domain, the flow is highly three-dimensional, even on planes bisecting the domain.

- After about twenty lid cycle time, the mean velocity profiles gave a good approximation to the reference data except in the region next to the downstream side wall.

- The root-mean-square values of the velocity components in the y and z directions were underpredicted, but in general, the profiles from computation follow the trend exhibited by the reference data.

- The $\overline{w'v'}$ stress profiles approach that of the reference data after about forty lid cycle time, but at earlier monitoring times, the behaviour was spatially erratic with some zones severely overpredicted, while at other locations, the opposite took place.

- The turbulence kinetic energy spectrum plots show the presence of inertial subrange eddies though the level of energy may vary with respect to the location of the monitoring points.

- The turbulence kinetic energy plots show that this parameter is produced in the region where the Taylor-Görtler like vortices reside.

- The use of the wall function produced very small values of y^+ due to the chaotic nature of the flow impeding the development of well behaved boundary layers. This, however, has a minor impact on the turbulence statistics computed, since the production of turbulence kinetic energy occurs predominantly in the region where

the Taylor-Görtler like vortices exist.

- The value of Smagorinsky constant C_s was found to have a non-negligible influence on the average profiles of the velocity components.

CHAPTER 5

Synthetic Turbulence

In order for LES to tackle flow problems in more general geometries, the use of inlet and outlet boundaries is inevitable. With the inlet boundary, to reduce the cost of computation and cut turbulent flow development time, realistic turbulence fluctuations need to be introduced at the inlet. Moreover, the synthetic generation of turbulence at the inlet should promote the development of turbulence as the flow moves downstream. The inflow boundary may exert a strong influence on what goes on inside the computational domain such as the development of a boundary layer. This means that the turbulence generation method must be able to promote the correct physics with the numerical methods employed and at the same time keep computational costs down.

5.1 Test Case Description

The type of flow of interest here is a developing turbulent internal flow. The geometry of the test case is that of a square duct as shown in Figure 5.1. The aspect ratio of the duct was set to 10 based on the streamwise and inlet edge lengths. Another test case was also carried out with an extended aspect ratio of twenty. The fluid has a constant density of 1,000kg/m^3 and a constant dynamic viscosity of 0.001Ns/m^2. The Reynolds number based on the mean inlet velocity and hydraulic diameter (equivalent to the domain edge length at the inlet) was approximately 10,000.

The fluid occupies a domain bounded by four planes forming two pairs of wall

boundaries. The walls making up the pairs are parallel to each other and walls from a pair are perpendicular to the walls from the other pair. The inlet and outlet are planes normal to the positive z-direction in Figure 5.1. This direction is also referred to as the streamwise direction in the following results as well as in the discussion sections of this chapter. The origin of this domain is corner A in Figure 5.1; while the x, y and z-directions correspond to the u, v and w velocity components. Fluid moves from the inlet boundary (uniform w velocity) to the outlet boundary. Zero initial velocity and pressure fields are applied to the internal cells to avoid numerical difficulties during start-up.

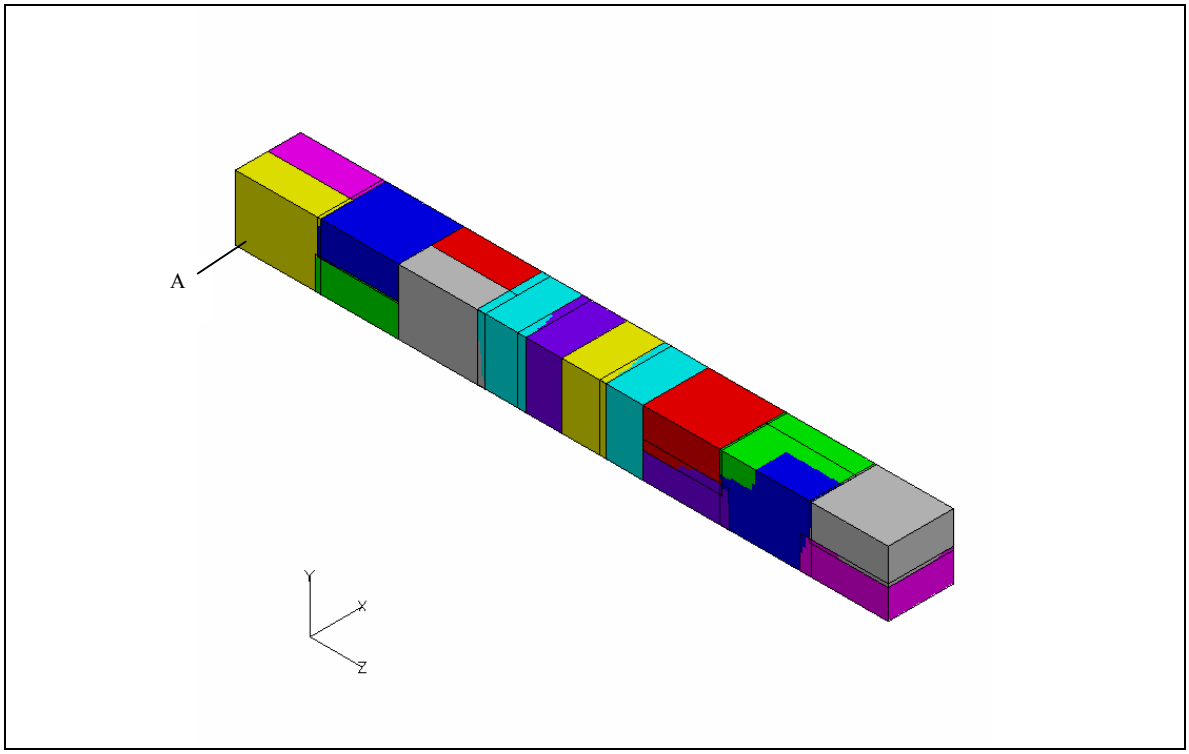

Figure 5.1 Test case geometry, partitioning and orientation.

A uniform mesh with cell edge lengths equal in all three coordinate directions was used. The total number of cells employed for this case was 640,000 for the duct with the aspect ratio set to 10. The same mesh density was used for the extended aspect ratio duct. A relatively coarse mesh was used since it is expected that to achieve statistically steady flow, a large number of time steps or a large number of eddy turnover times must be simulated to keep computing cost low. In addition, the main purpose of this test was to measure the influence of different turbulence generation schemes on the streamwise rate

of flow development downstream of the inflow boundary; while, absolute accuracy of the statistical properties of turbulence was a secondary goal. Furthermore, three different types of turbulence generation at the inlet were considered, requiring a lot of computing resources.

Eddies with length scales smaller than the cell edge length were modelled. The sub-grid scale eddy viscosity controlling dissipation was obtained using the Smagorinsky model. The value of Smagorinsky constant C_s was set to 0.1 and no attempt was made to find an optimum due to time constraints.

Boundaries parallel to the direction of the flow were set to no slip walls. No wall functions were used to approximate the velocity profile near the walls though the code is capable of performing this type of computation. Unlike the shear stresses (in general), normal stresses at the walls were set to zero. van Driest damping was applied to damp the value of characteristic length near the wall.

At the inflow, the velocity component normal to the boundary plane was set to a steady uniform value of 0.217m/s (to three decimal points), invariant with the time step level. This value is taken as the bulk velocity u_b. Both normal and shear stresses were assumed to be non-zero at the inlet. Upon setting the time step size to 0.0001s the Courant number was, 0.0174.

Three different turbulence generation methods were implemented at the inflow and they were superimposed on the uniform velocity component. These methods have been described in detail in Chapter 2, the methods are, namely:

1. Random perturbation method.
2. Lagrangian vortex method.
3. Artificial turbulence generation method.

The fluctuations were applied to the velocity components in all three directions. At the

outflow boundary, a zero gradient condition for the velocity components was implemented followed by the application of the convective condition:

$$\frac{\partial \phi}{\partial t} + U_{conv} \frac{\partial \phi}{\partial n} = 0 \tag{5.1}$$

where ϕ is a dependent field variable, U_{conv} is a convection velocity, in this case U_{conv} was set to the total mass flow rate out of the domain divided by the product of density and area of the outflow plane and n is a coordinate direction normal to the outflow plane. This step is necessary to avoid reflections of waves back into the domain at the outflow plane. The execution of the convective condition routine was followed by the widely used correction of mass flow rate through the outflow boundary. The value of the velocity component normal to every outflow boundary face was multiplied by the ratio of the total mass flow rate in to the total mass flow rate out in order to get the correct balance of mass flow rates in and out of the domain.

The Courant and diffusion numbers based on the cell edge length, time step size and bulk inlet velocity are 1.74E-2 and 6.40E-5 respectively. It is clear from these figures that convection dominates diffusion though the value of Courant number here is much smaller than unity, avoiding diverging solution as the time integration progresses. The limit of the time step size was not determined since the focus of this chapter is on the methods of synthetic turbulence generation.

The large value of the Peclet number which in this case is 271.25, requires the use of a spatial differencing scheme that fulfils the requirement of transportiveness, following this, the first order upwind scheme was used. The Courant, diffusion and Peclet numbers for these cases are given again in Table 5.1. All synthetic turbulence generator methods studied here were subjected to the same spatial differencing scheme meaning that turbulence statistics among these methods are fit to be compared, even though this scheme is diffusive. Unlike the previous case, filtering is carried out implicitly by the

grid. It is also interesting to note that velocity fluctuations from the artificial turbulence method and the enhanced vortex particle method have already been filtered at the inlet.

	Aspect ratio 10	Aspect ratio 20
Courant number	1.74E-2	1.74E-2
Diffusion number	6.40E-5	6.40E-5
Peclet number	2.71E+2	2.71E+2

Table 5.1 Courant, diffusion and Peclet numbers for two duct lengths.

The sequence of operations for the outflow boundary must be executed in the order described above. If, for example, the convective condition step is swapped with the mass flow rate correction step, the mass flow rate going out of the domain was found to decay as time marching progresses. Shear stresses at the outflow boundary were set to zero while normal stresses were computed.

In the Poisson equation for modified pressure (Equation (3.30)), a zero normal gradient was specified for modified pressure at the outflow boundary. The gradients of modified pressure normal to the walls are in general, non zero. The value of modified pressure at the walls was extrapolated from the neighbouring internal cell nodes using Taylor series expansion. A similar treatment of modified pressure was implemented at the inflow boundary.

At the inlet, the streamwise velocity component was set to the uniform value, constant in time. Velocity components normal to the streamwise direction were set to zero, as is the case with modified pressure.

The average velocity profiles were measured along the wall normal bisectors parallel, to the x-direction, and are normalised by the bulk velocity value w_{inlet}. These give an indication whether or not the flow has reached a fully developed stage, and that the average field variables have a constant value with time and space. The turbulence can also be said to be stationary or have a constant average value spatially and temporally.

The lines are located at a distance of z/L=0.25 and z/L=0.75 from the inflow plane. Hereafter, these lines will be referred to as Line A and Line B respectively. Sample data were obtained every 0.0001s for 2,000 time steps.

5.2 Results and Discussion

The time history of the outcome from three turbulence generation methods in the x-direction are shown in Figure 5.2 which shows that the synthetic or artificial turbulence generation method contains low frequency fluctuations with relatively high amplitudes as opposed to the random perturbation method. It must be noted that the data plotted in Figure 5.2 are true values of the synthetic turbulence fluctuations and these are not normalised by any parameter.

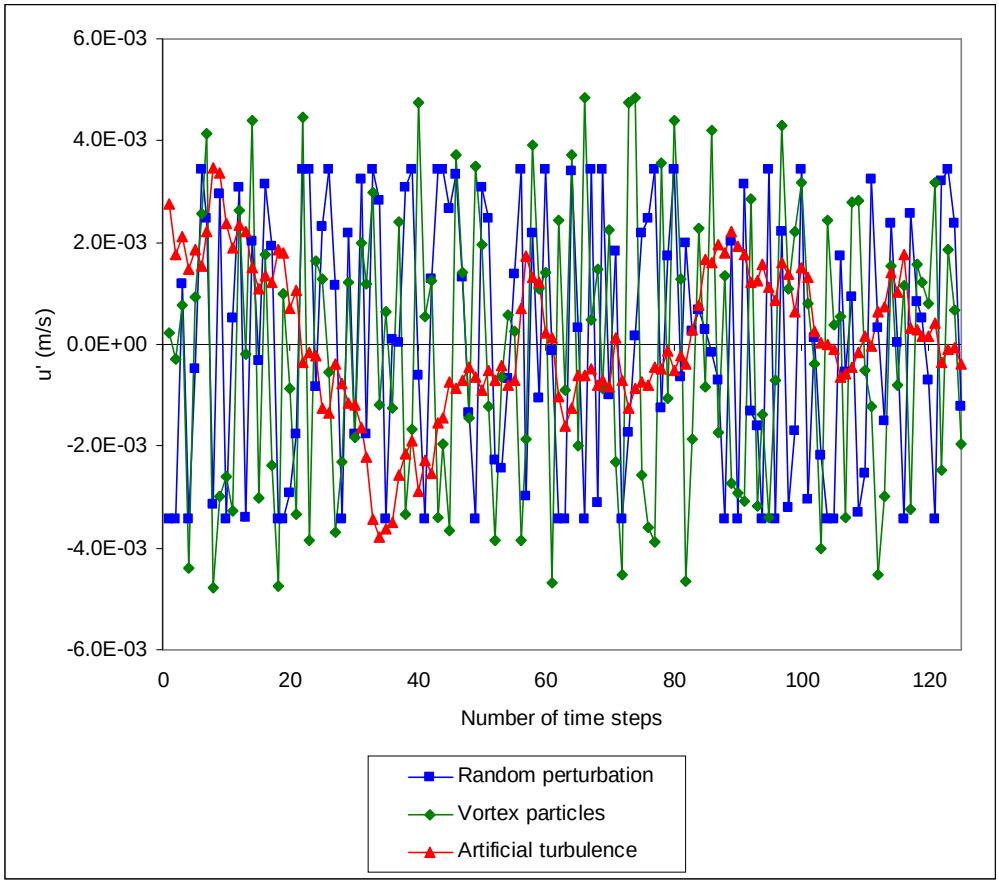

Figure 5.2 Time history of fluctuation data from three turbulence generation methods at the inlet of the square duct monitored at a point on the vertical wall bisector 0.00125m above the floor of the duct.

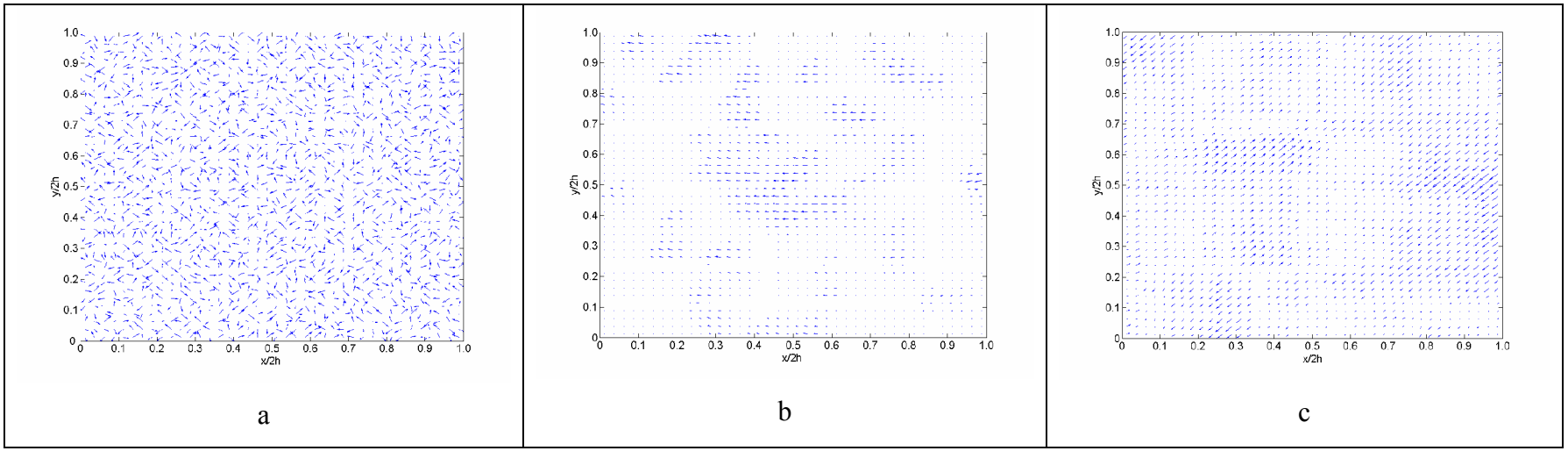

Figure 5.3 Velocity vector fields at the start of simulation from the a) Random perturbation method b) Enhanced vortex particle method c) Artificial turbulence generation method, to be superimposed on the inlet plane, with a common scale for comparison.

Figure 5.3 illustrates the instantaneous velocity vector field from different synthetic turbulence generators at the start of simulation. From this figure, the method of random perturbation clearly shows the spatially uncorrelated velocity vectors as opposed to the method of artificial turbulence method. The enhanced method of vortex particle requires an increase in the number of vortex particles evenly spread on the inlet plane to obtain a similar level of average turbulence kinetic energy as in the other two methods.

Instantaneous velocity vector fields from the simulation with random inlet perturbation are shown in Figures 5.4 to 5.7. The result of randomly disturbing the inlet velocity after 1.1 residence time (at time t=2.5s) from the start of simulation is shown in Figure 5.4. Residence time is defined as the time lapse from the moment a particle entering the domain at the inlet, until it goes out through the outlet of the duct (with aspect ratio set to 10), based on, the value of the mean inlet velocity. The velocity vector plots were not fixed to a single scale but a scale is given for each plot. Near the walls, the magnitude of the velocity components transverse to the streamwise direction was large. This is explained as follows. The uniform velocity component in the streamwise direction on the inlet plane is physically unreal especially at the boundaries, as the sudden introduction of walls at the inlet and viscosity of the fluid means the existence of wall shear stresses acting on the fluid.

The spatial development of the instantaneous secondary velocity vector fields at 1.1 residence time (t=2.5s) are shown in Figures 5.4 to 5.7 for the random generation case. In general a rapid change in the secondary flow pattern was observed moving downstream from the inlet. At z/L=0.25, where L is the length of the duct (aspect ratio set to 10) in the streamwise direction, secondary flows are in the direction towards the walls away from the interior of the domain. It must be noted that the velocity vector plots are not fixed to a scale since the magnitude of velocities from one plot to the other may have a large difference and as such, in order to highlight important flow features, different scales were used. At z/L=0.75, close to the wall bisectors, secondary flow is in the direction approximately parallel to the walls. Near the corners, the direction of the flow is parallel to the corner bisectors. On the outflow plane, a pair of counter-rotating vortices was

observed at each corner of the domain. This feature was also observed by Gavrilakis (1992), Huser and Biringen (1993) and also by Pettersson Reif and Andersson (2002), however this does not mean that a fully developed flow has been achieved at the outlet since the strength of these vortices may be lower than that obtained from a fully developed flow.

It is suspected that the high numerical diffusion resulting from the use of a low-order upwind scheme causes an excessive distribution of momentum resulting in symmetrical velocity vector fields as evident in Figures 5.4 to 5.7. The velocity vector field on the outlet plane of the duct with twice the length in the streamwise direction show a similar secondary flow structure and directions.

For the enhanced vortex particle and artificial turbulence cases shown in Figures 5.8 to 5.15, the velocity vector field at the inlet can be described as being smoother and orderly, compared to the random generation case. For the no inflow turbulence case, fluctuation levels are negligible on the inflow plane as shown in Figure 5.15.

On the *xy*-plane at z/L=0.25 and 1.1 residence time (t=2.5s), the flow structure from all other methods are similar to that of the random case. It can be seen for example in Figure 5.9 that the fluid is moving away from the core region towards the wall. Moving downstream to the *xy*-plane at z/L=0.75, Figure 5.10 shows a layer of fluid next to the wall moving away from the corners marking the start of the formation of vortices of the secondary flow. The same structure was produced by all other methods. On the outflow plane, all methods produce a pair of counter rotating secondary flow vortices similar to the random generation case. This can be seen clearly in Figures 5.7, 5.11, 5.15 and 5.19. However the dimensions of this secondary flow appear to differ depending on the turbulence generation method used. The vortices of the artificial turbulence case seem to be more developed than the enhanced vortex particle case.

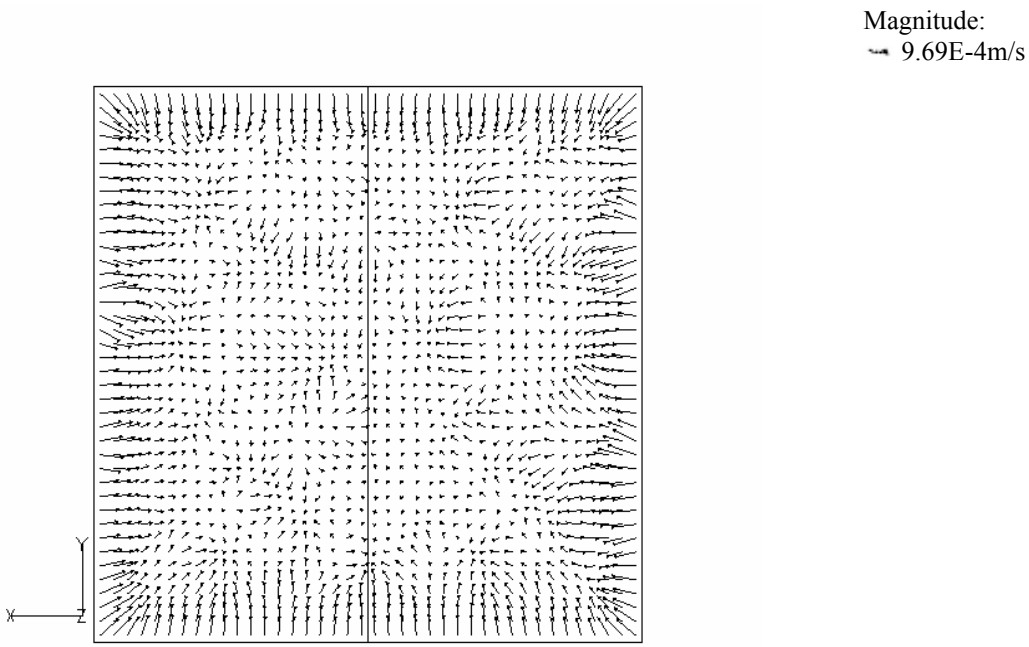

Figure 5.4 Instantaneous velocity vector field on the *xy*-plane, at *z/L*=0 and 1.1 residence time, random inlet perturbation.

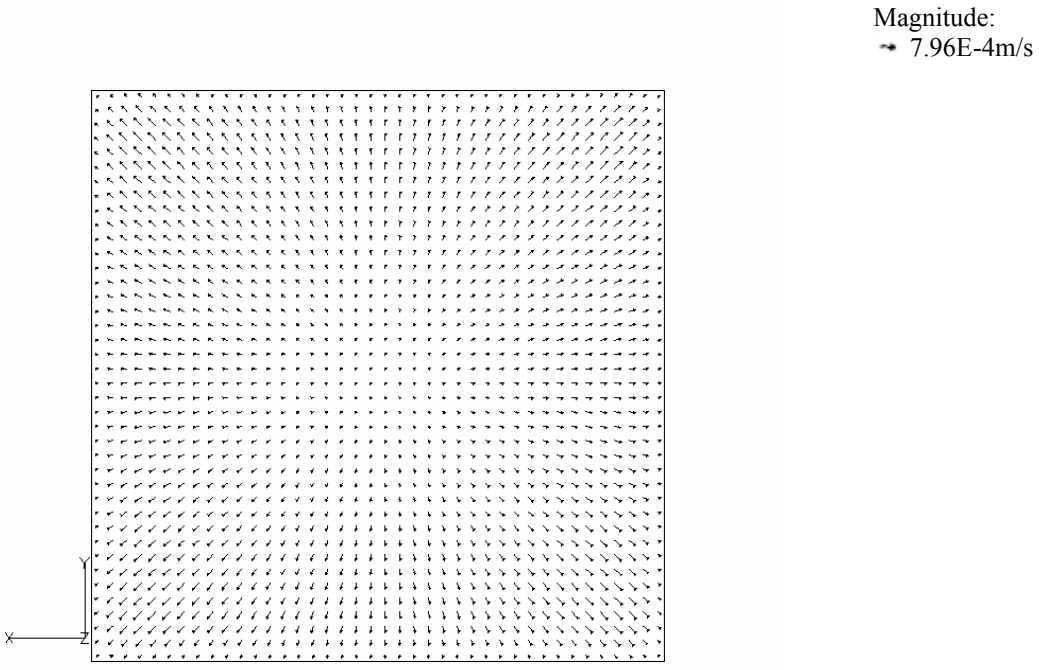

Figure 5.5 Instantaneous velocity vector field on the *xy*-plane, at *z/L*=0.25 and 1.1 residence time, random inlet perturbation.

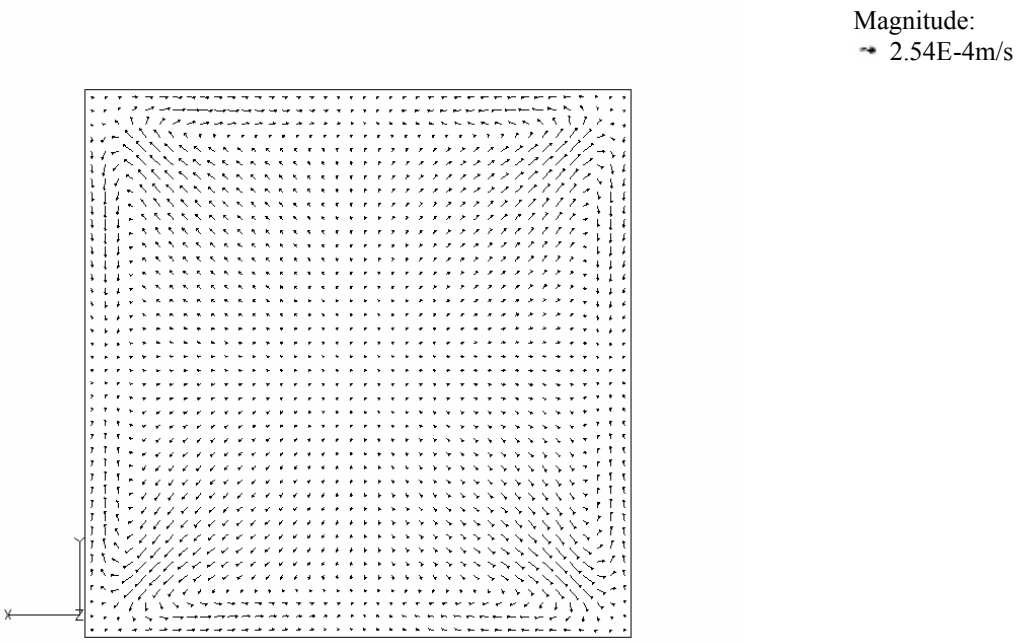

Figure 5.6 Instantaneous velocity vector field on the *xy*-plane, at *z/L*=0.75 and 1.1 residence time, random inlet perturbation.

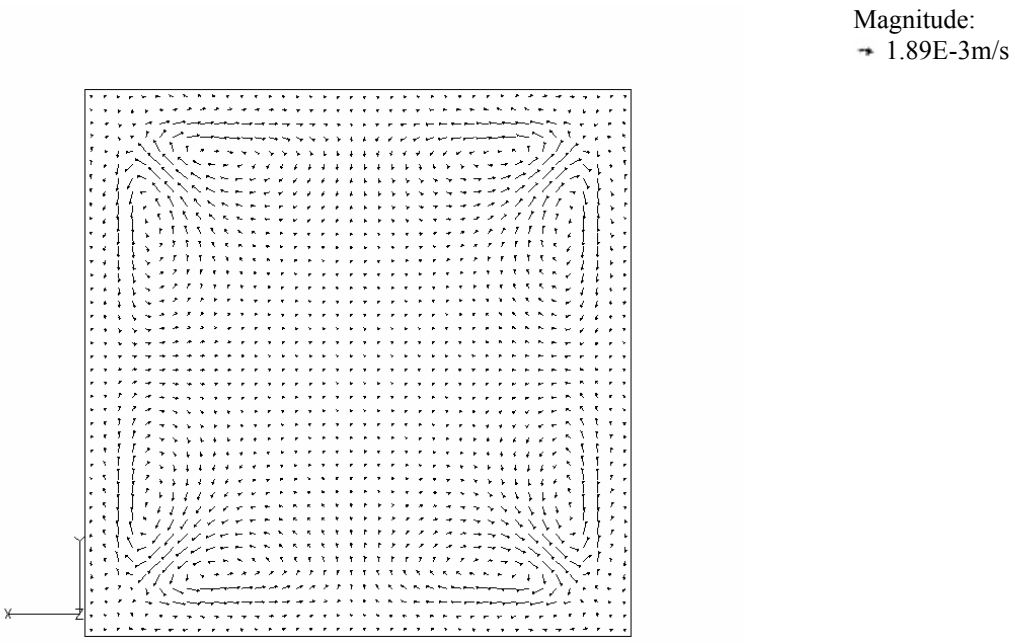

Figure 5.7 Instantaneous velocity vector field on the *xy*-plane, at *z/L*=1.0 and 1.1 residence time, random inlet perturbation.

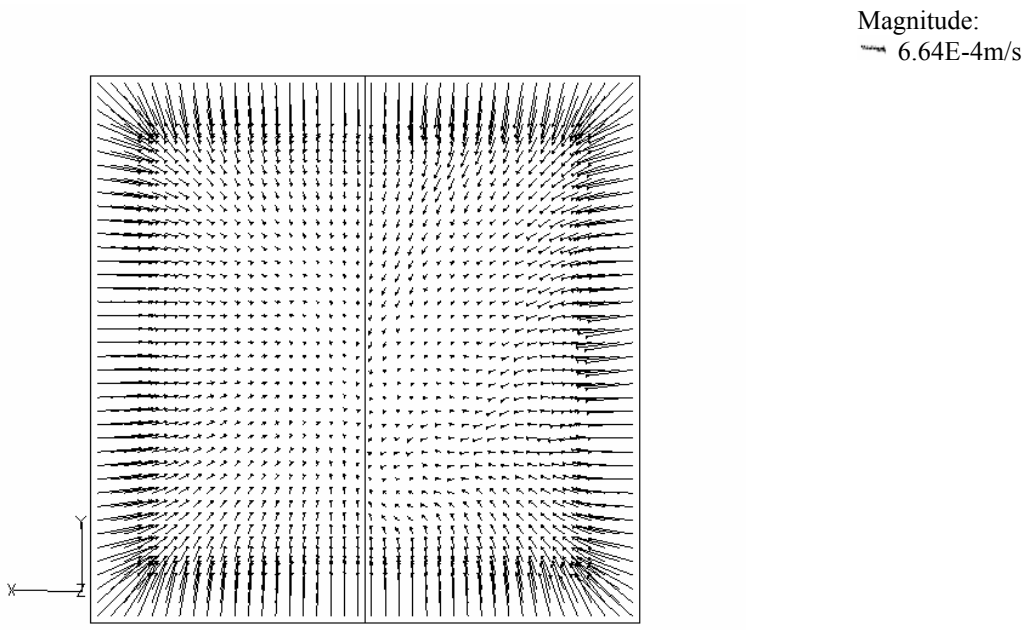

Figure 5.8 Instantaneous velocity vector field on the *xy*-plane, at *z/L*=0 and 1.1 residence time, enhanced vortex particle method.

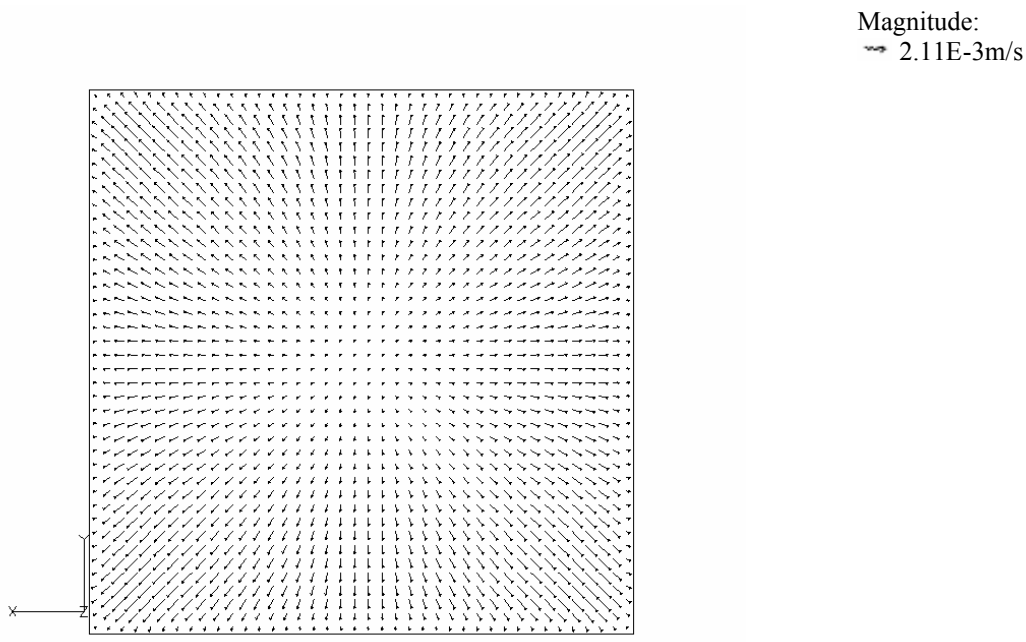

Figure 5.9 Instantaneous velocity vector field on the *xy*-plane, at *z/L*=0.25 and 1.1 residence time, enhanced vortex particle method.

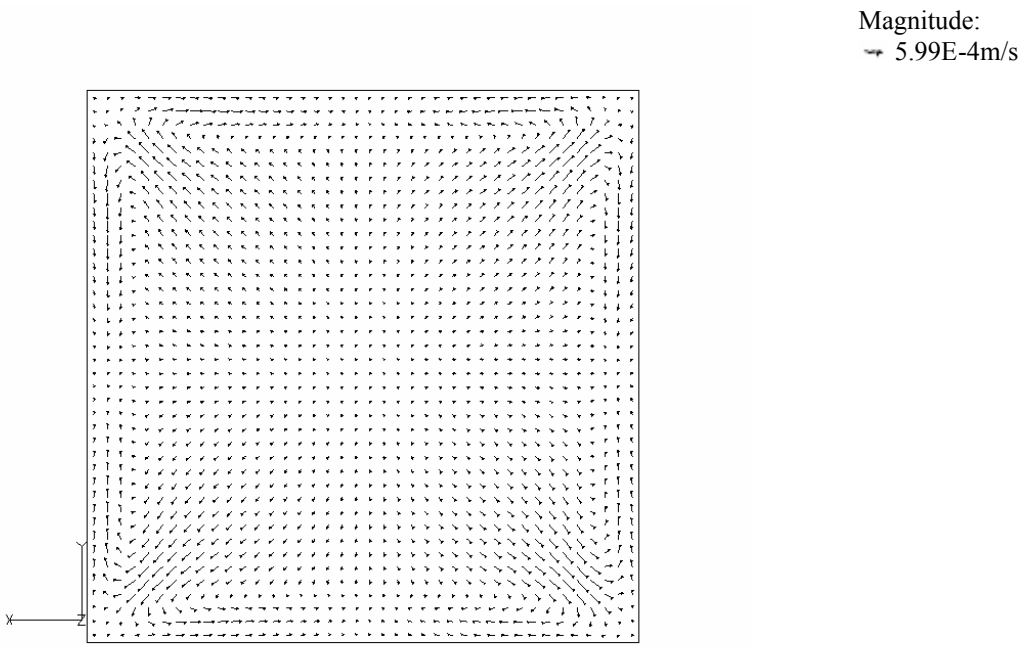

Figure 5.10 Instantaneous velocity vector field on the *xy*-plane, at *z/L*=0.75 and 1.1 residence time, enhanced vortex particle method.

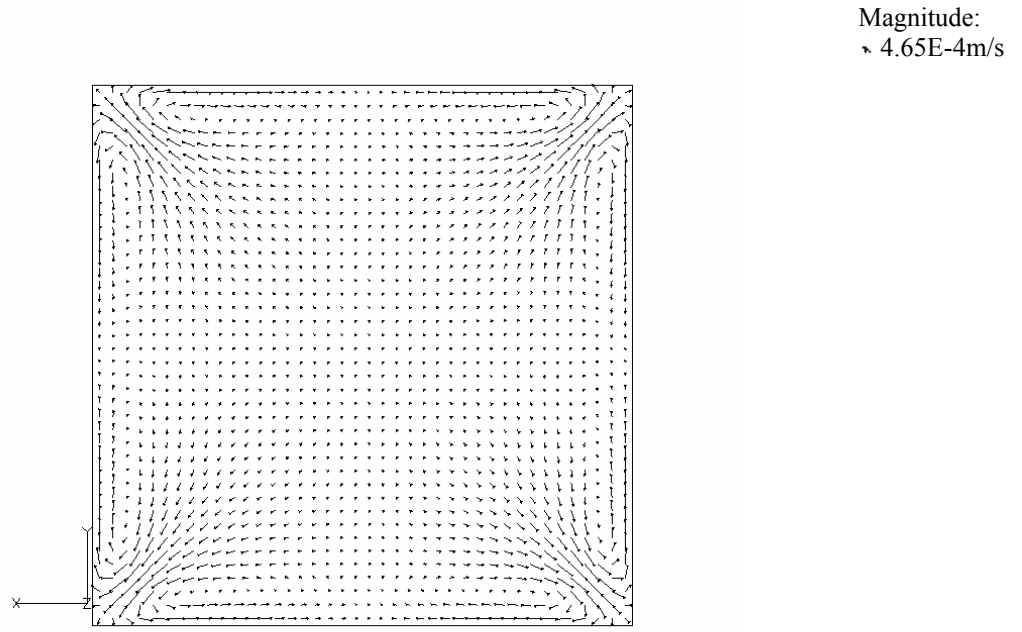

Figure 5.11 Instantaneous velocity vector field on the *xy*-plane, at *z/L*=1.0 and 1.1 residence time, enhanced vortex particle method.

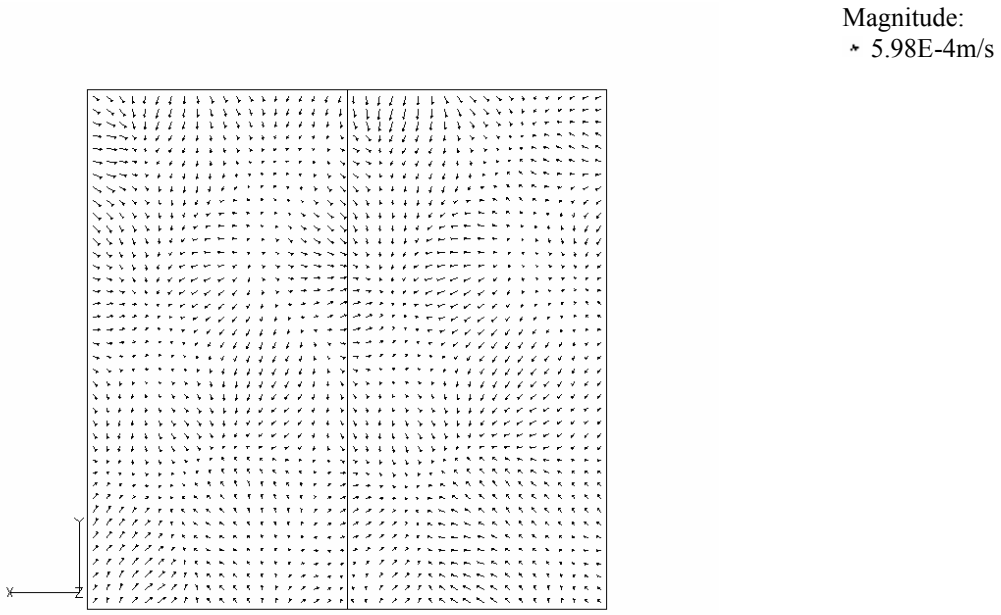

Figure 5.12 Instantaneous velocity vector field on the *xy*-plane, at *z/L*=0 and 1.1 residence time, artificial turbulence generation method.

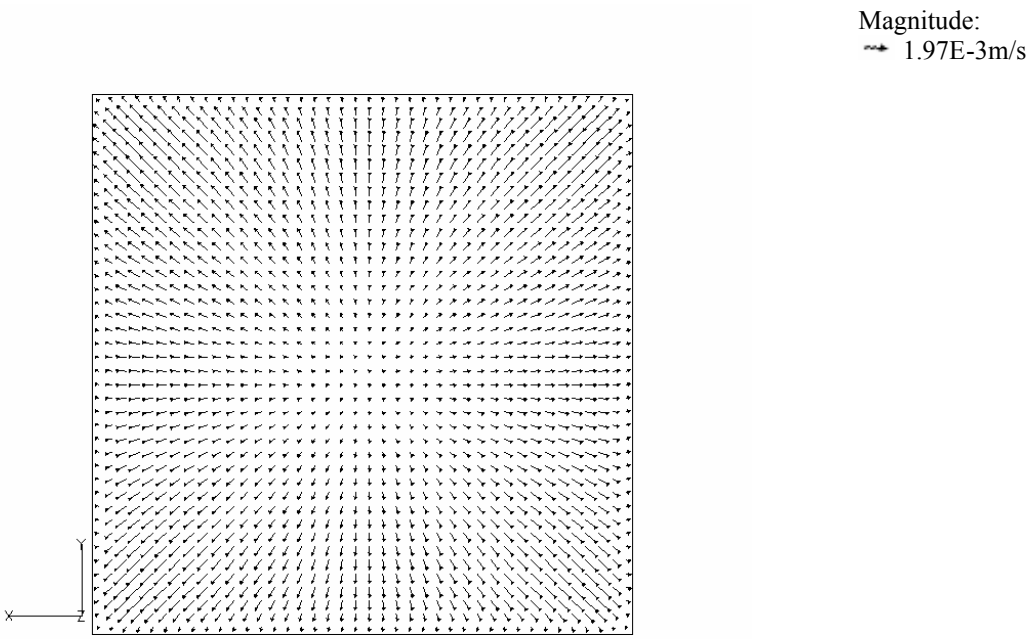

Figure 5.13 Instantaneous velocity vector field on the *xy*-plane, at *z/L*=0.25 and 1.1 residence time, artificial turbulence generation method.

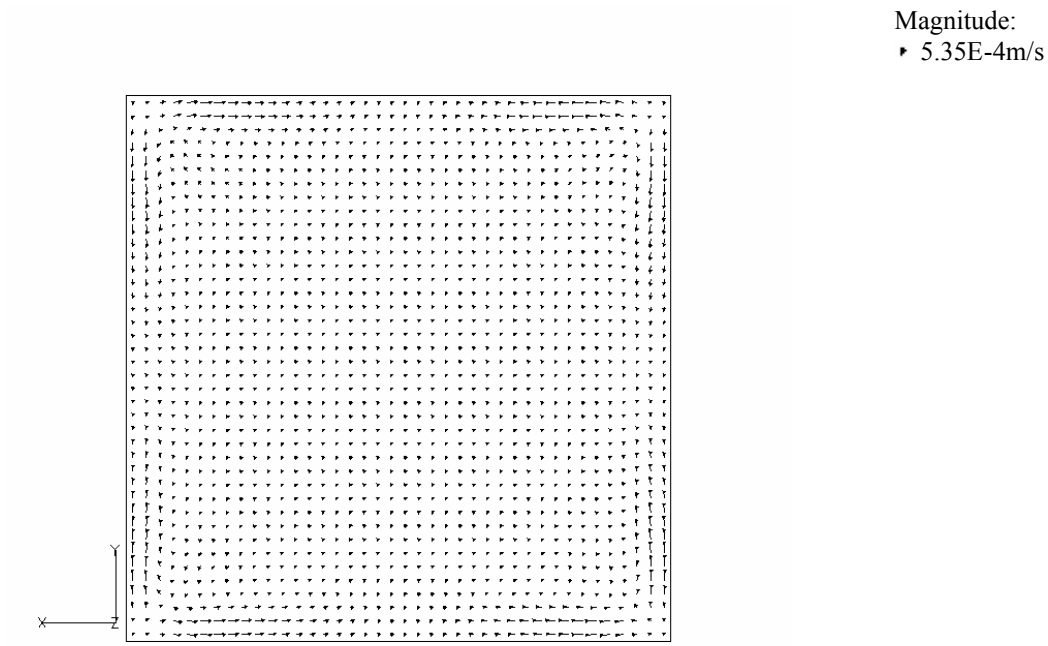

Figure 5.14 Instantaneous velocity vector field on the *xy*-plane, at *z/L*=0.75 and 1.1 residence time, artificial turbulence generation method.

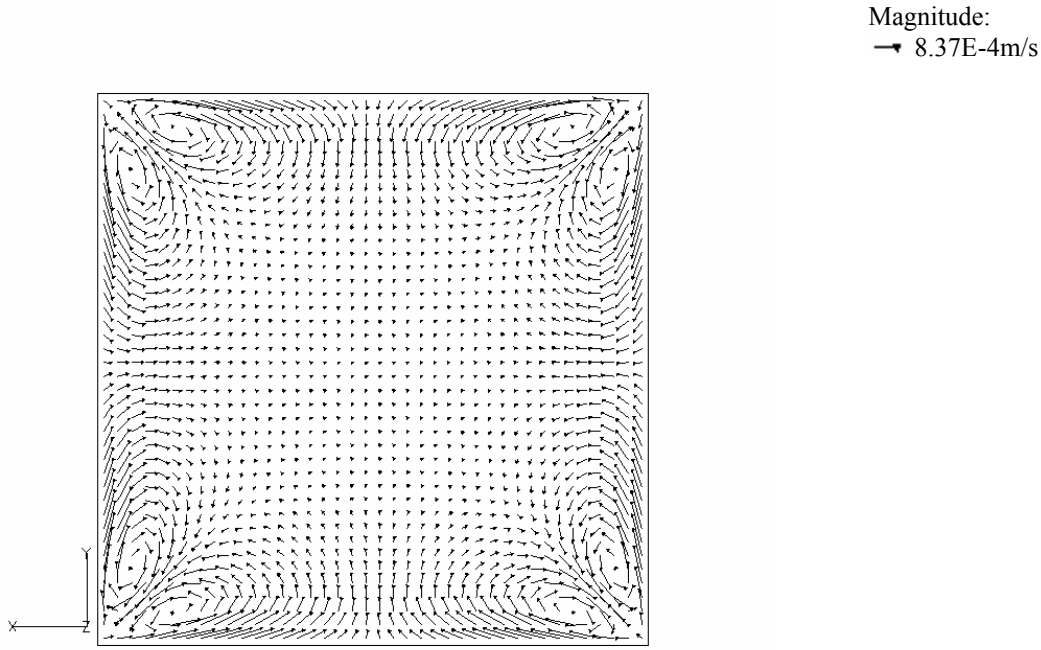

Figure 5.15 Instantaneous velocity vector field on the *xy*-plane, at *z/L*=1.0 and 1.1 residence time, artificial turbulence generation method.

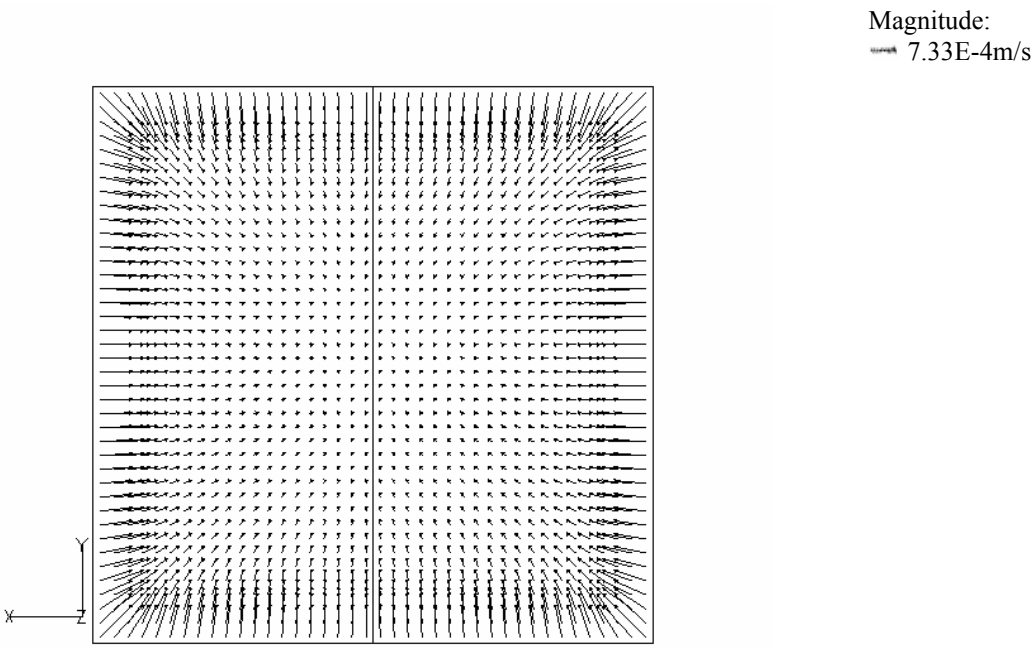

Figure 5.16 Instantaneous velocity vector field on the *xy*-plane, at *z/L*=0 and 1.1 residence time, no inflow turbulence case.

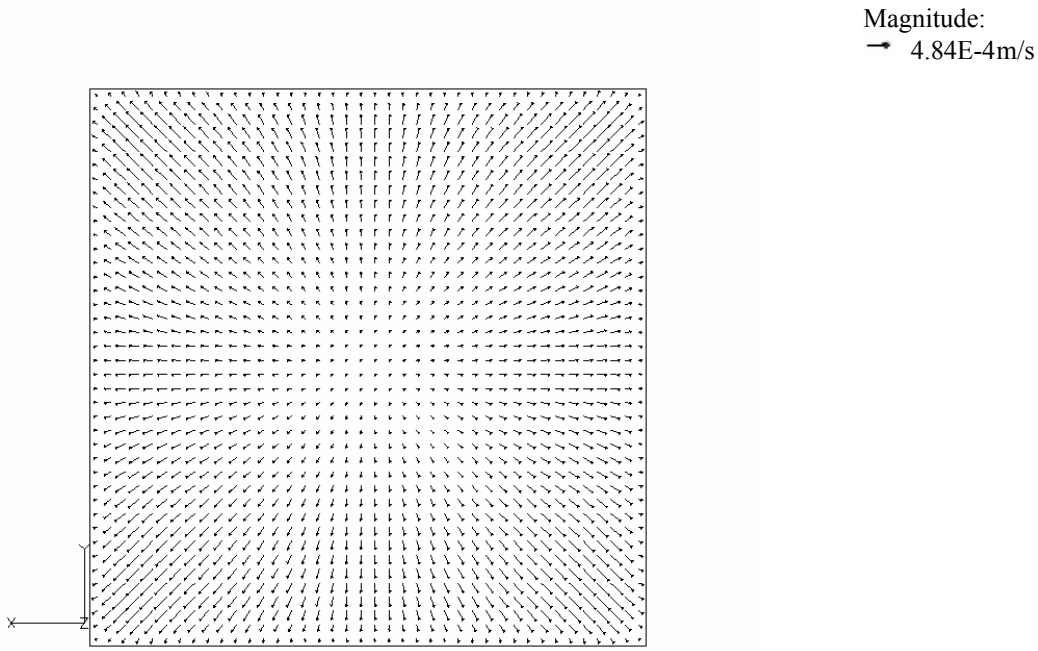

Figure 5.17 Instantaneous velocity vector field on the *xy*-plane, at *z/L*=0.25 and 1.1 residence time, no inflow turbulence case.

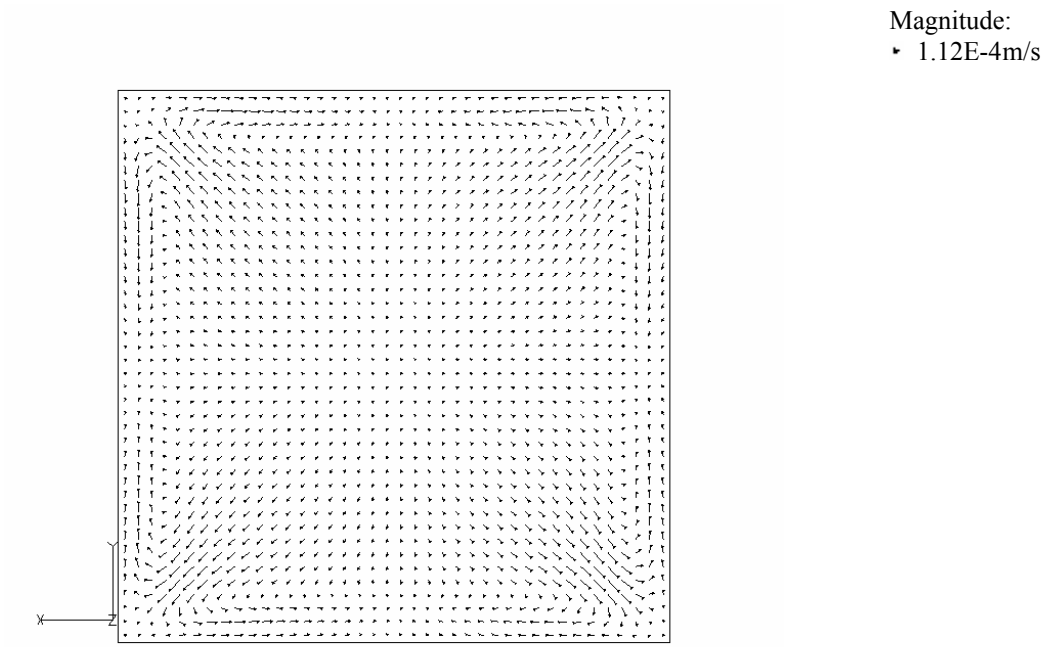

Figure 5.18 Instantaneous velocity vector field on the *xy*-plane, at *z/L*=0.75 and 1.1 residence time, no inflow turbulence case.

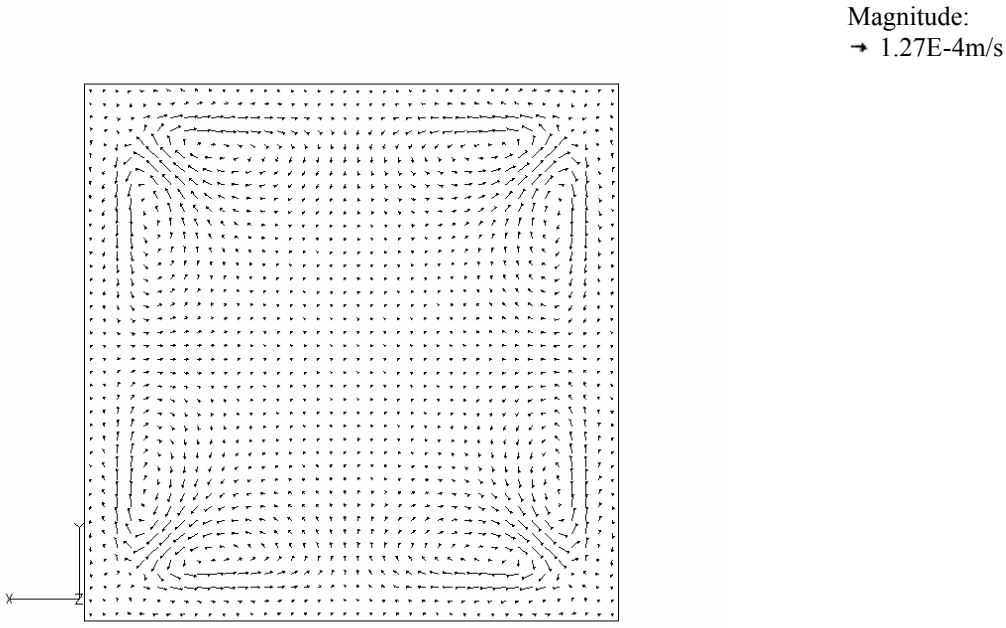

Figure 5.19 Instantaneous velocity vector field on the *xy*-plane, at *z/L*=1.0 and 1.1 residence time, no inflow turbulence case.

The instantaneous velocity vector field plots show a clear development of the flow structure taking place throughout the entire length of the duct. The use of a uniform mean inlet velocity profile is not an issue in this case since the goal of this chapter is to look at developing flows and using the streamwise rate of development to judge the effectiveness of the methods of specifying the inlet turbulence. The inlet plane corresponds to the value of z=0m. If mean velocity vector field plots are available, these can be used to judge how developed the flows are but the post-processing subroutine was not set-up to carry out this task during the simulation.

After about four residence time (at t=7.5s), the instantaneous fluctuations from the random generation method in Figure 5.20 yielded an instantaneous secondary velocity vector field defined by a pair of vortices located at each corner of the plane as shown in Figure 5.21. Compared to the flow on the same plane after about 1.1 residence time (at t=2.5s) in Figure 5.7, there has been a substantial change in the flow pattern though the main features are still maintained. The pronounced inward component of velocity next to the walls at the inlet for the random perturbation and enhanced vortex particle methods as well as the no inflow turbulence case is due to the rapid dampening of velocity fluctuations in the streamwise direction and the sudden introduction of a wall at the inlet.

The fluctuating velocity components perpendicular to the streamwise direction on the inlet plane of the enhanced vortex particle method can clearly be seen in Figure 5.22. The secondary flow structure is very similar to that of the random perturbation method (probably due to the extra diffusion originating from the use of a low-order upwind scheme); while, the core region of the flow has very small magnitudes of velocity component parallel to the plane as shown in Figure 5.23.

Figure 5.24 shows a spatially correlated instantaneous velocity vectors from the artificial generation method of Klein, Sadiki and Janicka (2003). The outcome on the outflow plane is shown in Figure 5.25. It has similar features to that of the random perturbation case. The same can be stated on the outlet plane of the case with no inflow turbulence with the velocity vector field shown in Figure 5.27. This suggests that the main features

of the flow are not heavily influenced by the fluctuating signal on the inflow plane as the flow progresses towards the steady-state values.

As expected, no fluctuations are visible on the inflow plane of the no turbulence case, which can be seen from Figure 5.26. The velocity vector field on the outlet plane of the lengthened duct (aspect ratio set to 20 and cell size equal to the duct with aspect ratio set to 10) after about one residence time in Figure 5.28 shows a fairly well developed corner vortices, implying that the development of the secondary flow is dependent on time, and also downstream distance.

Contour plots of the statistical quantities relating to turbulence and mean flow were captured on the exit plane of the artificial turbulence method after about four residence time (at t=7.5s). The number of time steps for averaging was set to 2,000.

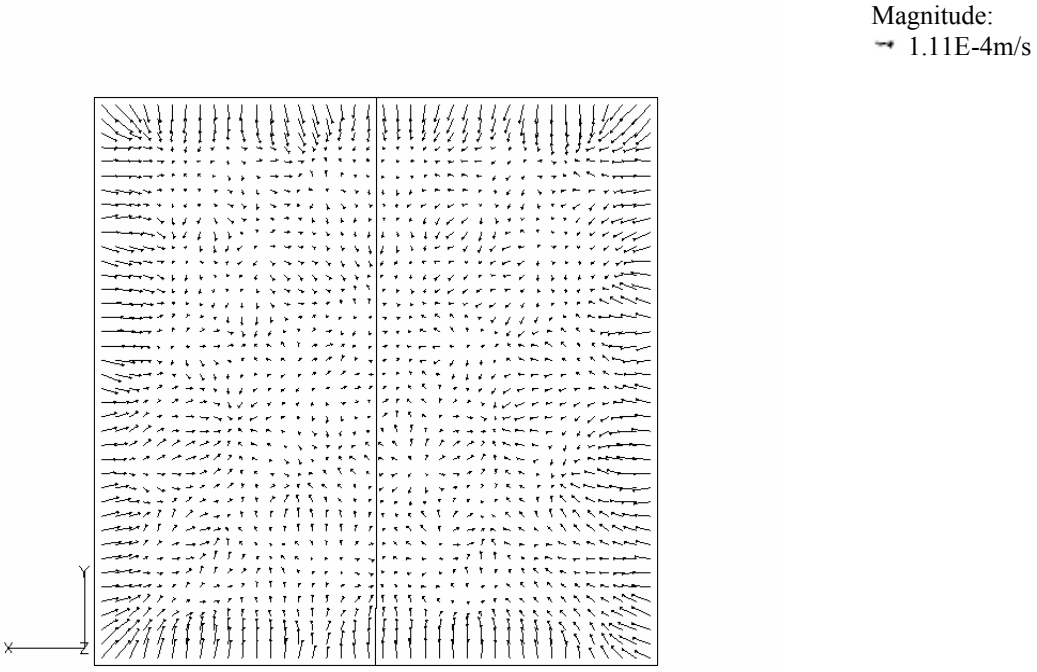

Figure 5.20 Instantaneous velocity vector field on the *xy*-plane, at *z/L*=0 and four residence time, random perturbation method.

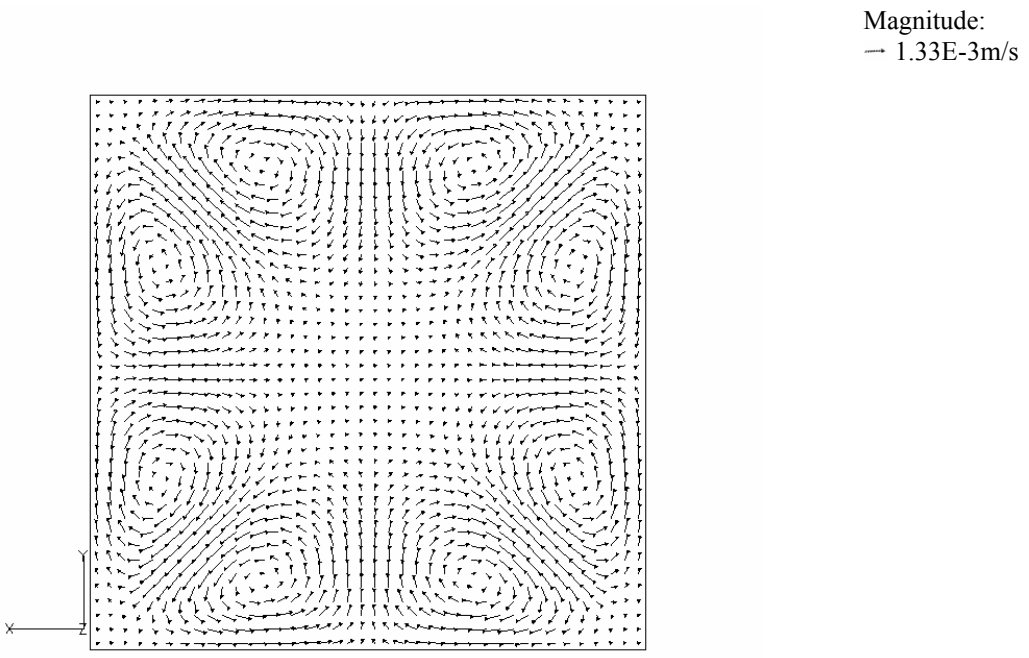

Figure 5.21 Instantaneous velocity vector field on the *xy*-plane, at *z/L*=1.0 and four residence time, random perturbation method.

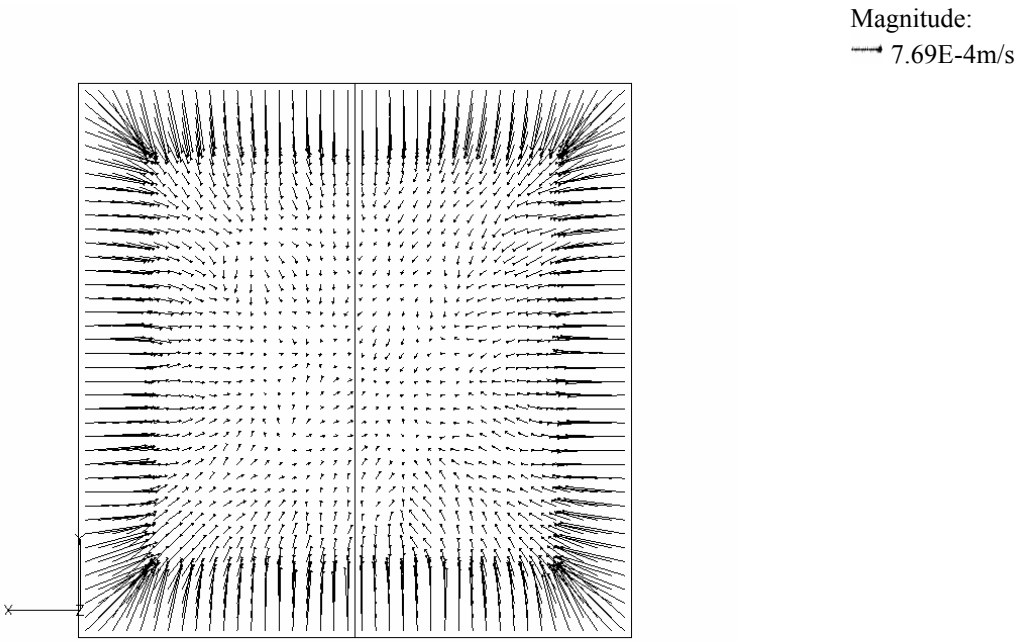

Figure 5.22 Instantaneous velocity vector field on the *xy*-plane, at *z/L*=0 and four residence time, enhanced vortex particle method.

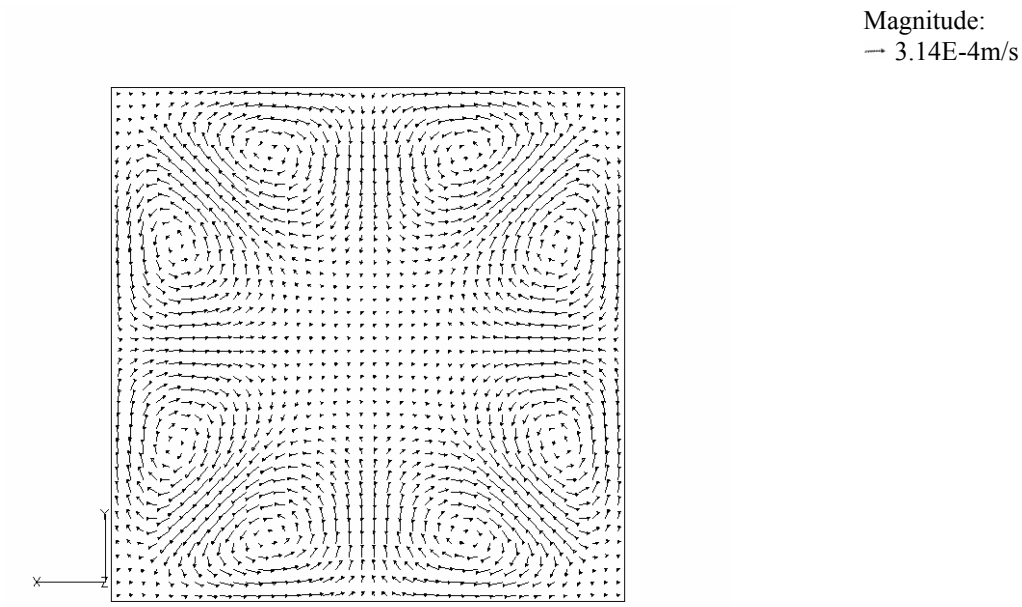

Figure 5.23 Instantaneous velocity vector field on the *xy*-plane, at *z/L*=1.0 and four residence time, enhanced vortex particle method.

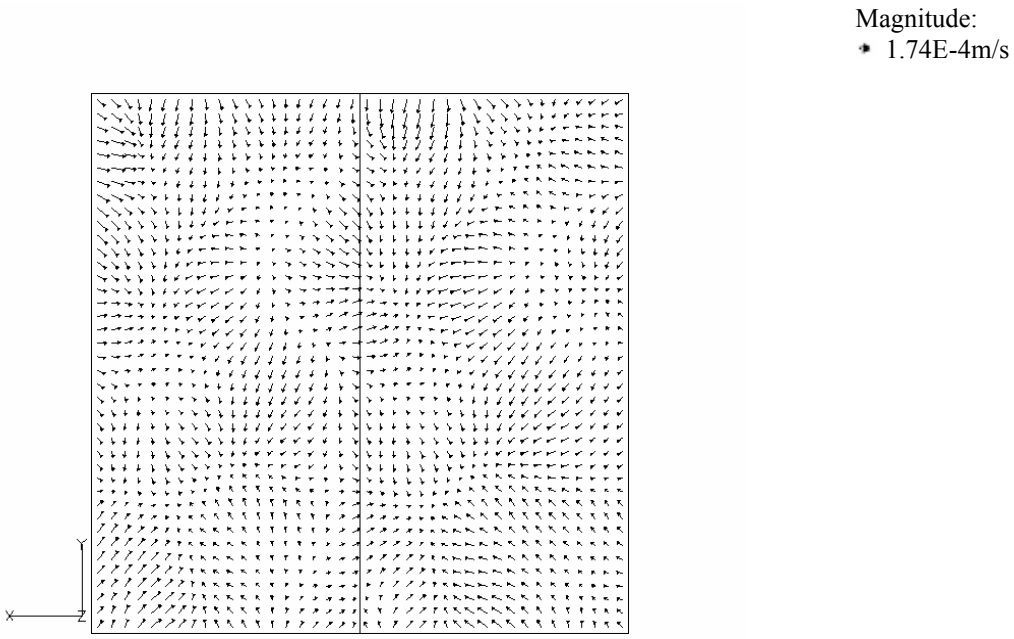

Figure 5.24 Instantaneous velocity vector field on the *xy*-plane, at *z/L*=0 and four residence time, artificial turbulence method.

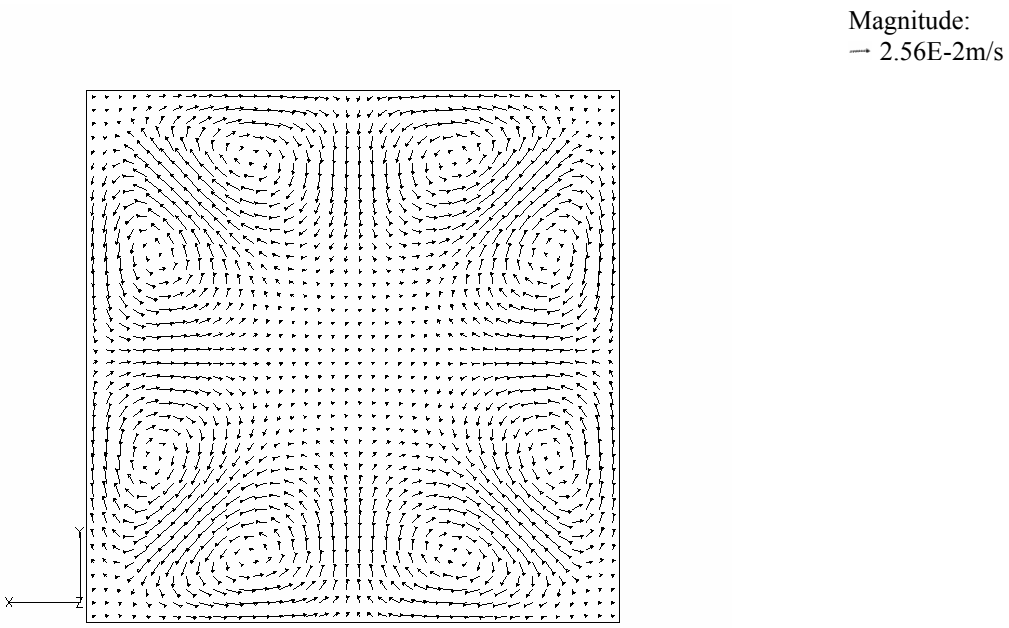

Figure 5.25 Instantaneous velocity vector field on the *xy*-plane, at *z/L*=1.0 and four residence time, artificial turbulence method.

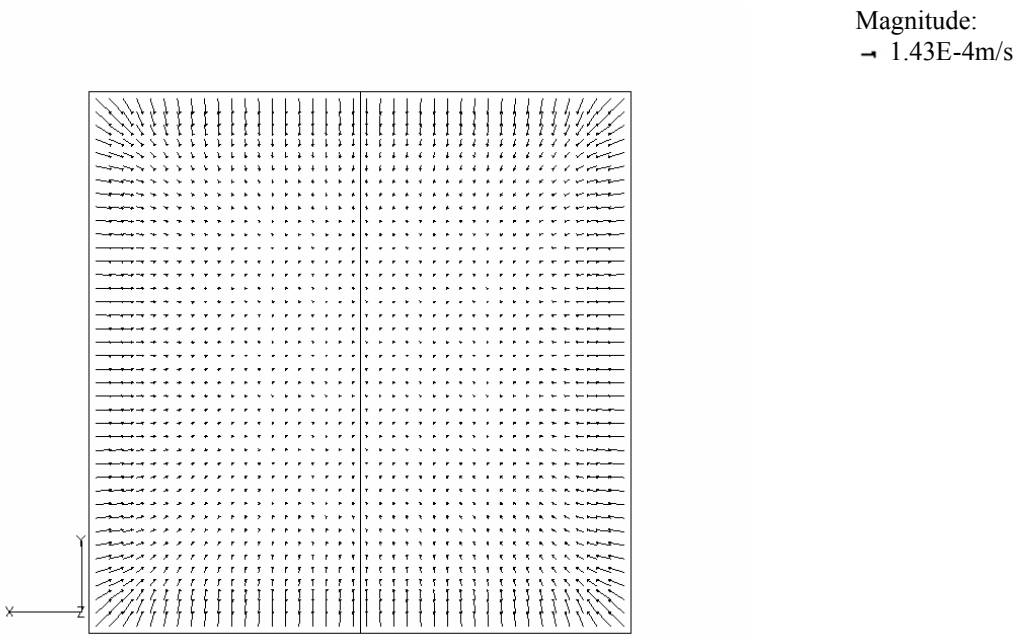

Figure 5.26 Instantaneous velocity vector field on the *xy*-plane, at *z/L*=0 and four residence time, no inflow turbulence.

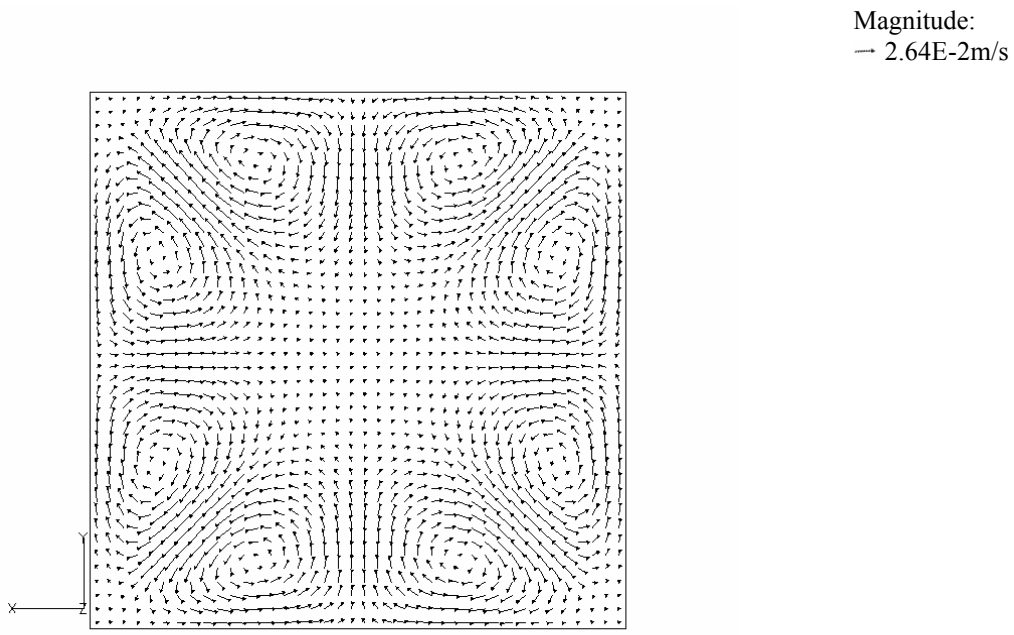

Figure 5.27 Instantaneous velocity vector field on the *xy*-plane, at *z/L*=1.0 and four residence time, no inflow turbulence.

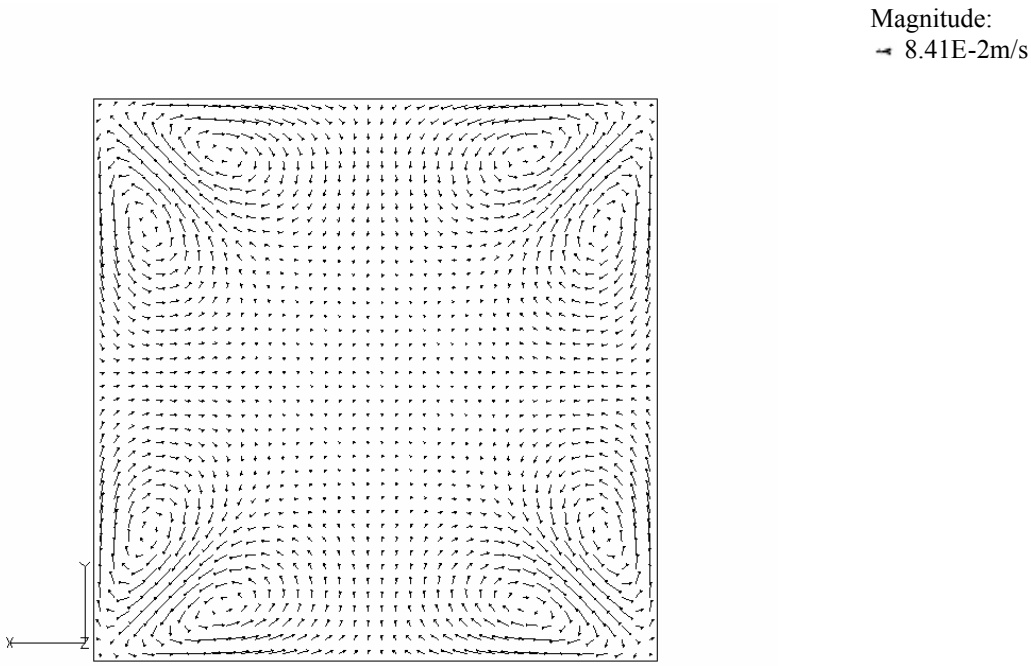

Figure 5.28 Instantaneous velocity vector field on the *xy*-plane, at *z/L*=2.0 and one residence time, no inflow turbulence.

The *w*-isovels shown in Figure 5.29 (which are lines of constant mean *w* velocity magnitudes) exhibit a slight bend towards each corner. This parameter has been normalised by the magnitude of the inlet velocity w_{inlet}. This distortion is considerably less than those obtained from Gavrilakis (1992) and Huser and Beringen (1993) but when the aspect ratio of the duct is increased to twenty, the bulge towards each corner on the outlet plane became more obvious, implying an increase in the strength of the secondary flow, as shown in Figure 5.30. It is thus clear that this difference is caused by the flow in the duct with aspect ratio of ten not reaching a fully developed stage. In the contour plots, the parameter *2h* is set equal to the edge length of the inlet. Gavrilakis (1992) argued that the function of this is to transfer streamwise momentum to the corners of the duct. It must be noted that the turnover time of Gavrilakis (1992) was around 16 on the finest grid; while, Huser and Biringen (1993) obtained a steady-state flow field after a fluid particle travelled a distance of 1300 times the duct width. Both reference cases have a bulk Reynolds number similar to the computations in this chapter.

The root-mean-square scalar plot of the fluctuating velocity component in the streamwise direction normalised by the magnitude of the uniform inlet velocity w_{inlet}, in Figure 5.31, shows that the distribution is unsymmetrical about the corner bisectors, though the distribution is mirrored in a more balanced manner about the normal bisectors of the wall. It is suspected that the reason for this is due to the flow not reaching a fully developed stage as it is also the case with $\overline{w}$ mentioned above. The root-mean-square plot confirms the contemplation that the turbulent fluctuations occur close to the solid walls. When the length of the duct in the streamwise direction was doubled it can be seen from Figure 5.32 that the fluctuations on the outlet plane after one residence time is concentrated close to the corners and is more symmetrical compared to the plot in Figure 5.31. This gives some evidence to the argument that the unbalanced distribution of the scalar plot in Figure 5.31 is due to the developing nature of the flow. The relatively low intensity is probably due to the diffusive numerical scheme employed in the computation but as the aspect ratio extends beyond ten, fluctuations due to turbulence start to build up, overcoming the numerical diffusion.

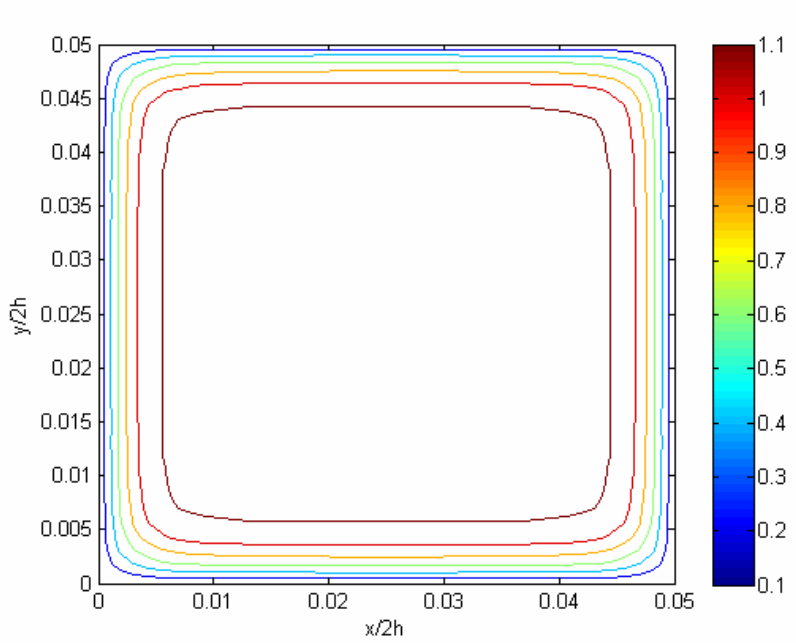

Figure 5.29 Scalar plot of the mean velocity in the streamwise direction $\overline{w}/w_{inlet}$ at the outlet after four residence time, on the outlet plane of the duct with aspect ratio set to 10, artificial turbulence method.

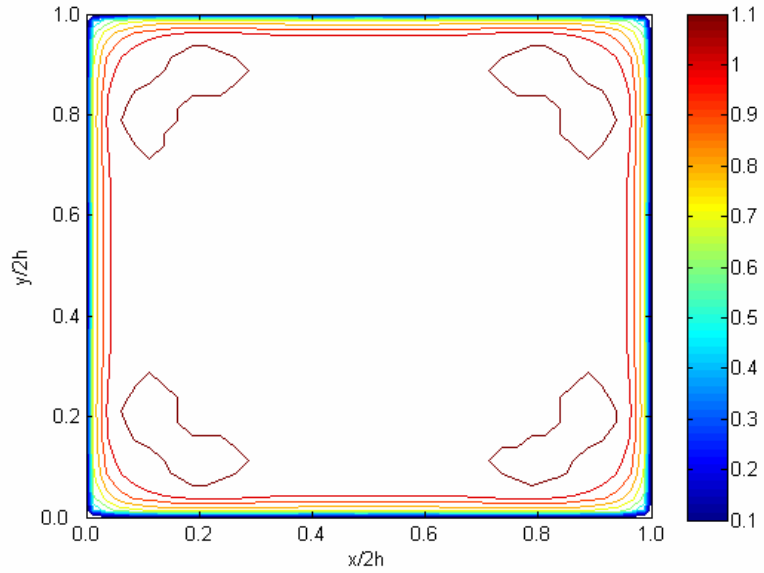

Figure 5.30 Scalar plot of the mean velocity in the streamwise direction $\overline{w}/w_{inlet}$ at the outlet after one residence time, on the outlet plane of the duct with aspect ratio set to 20, artificial turbulence method.

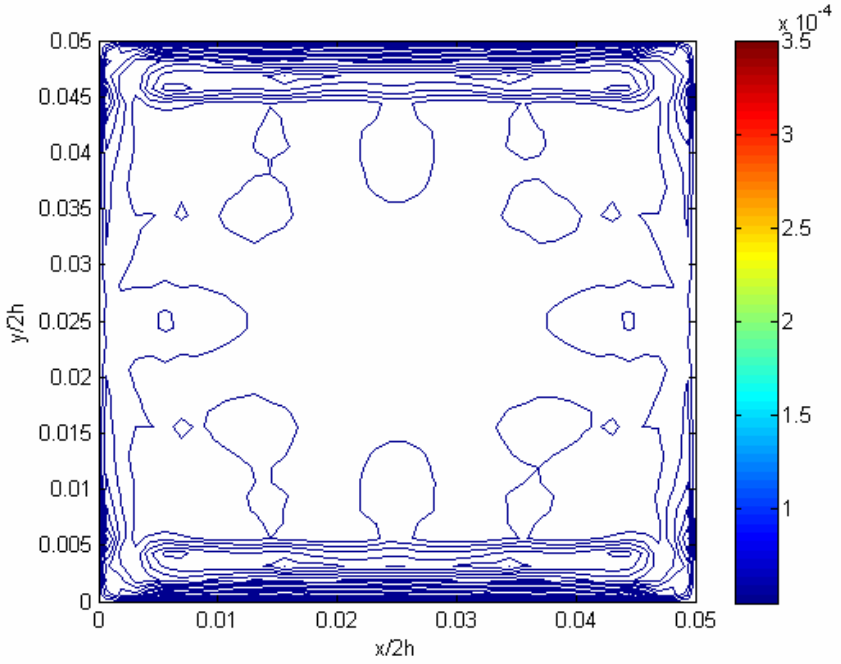

Figure 5.31 Root-mean-square scalar plot of the fluctuating velocity in the streamwise direction, w_{rms}/w_{inlet} after four residence time, on the outlet plane of the duct with aspect ratio set to 10, artificial turbulence method.

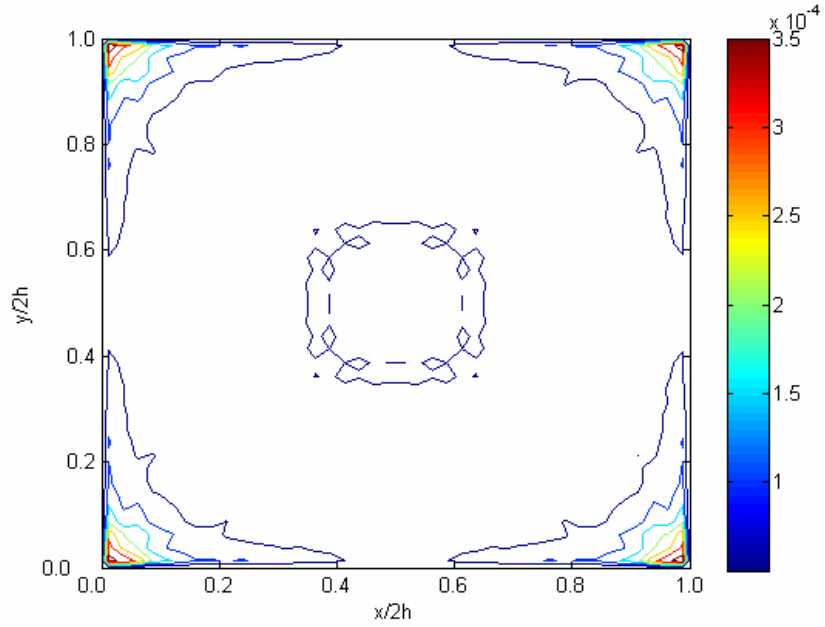

Figure 5.32 Root-mean-square scalar plot of the fluctuating velocity in the streamwise direction, w_{rms}/w_{inlet} after one residence time, on the outlet plane of the duct with aspect ratio set to 20, artificial turbulence method.

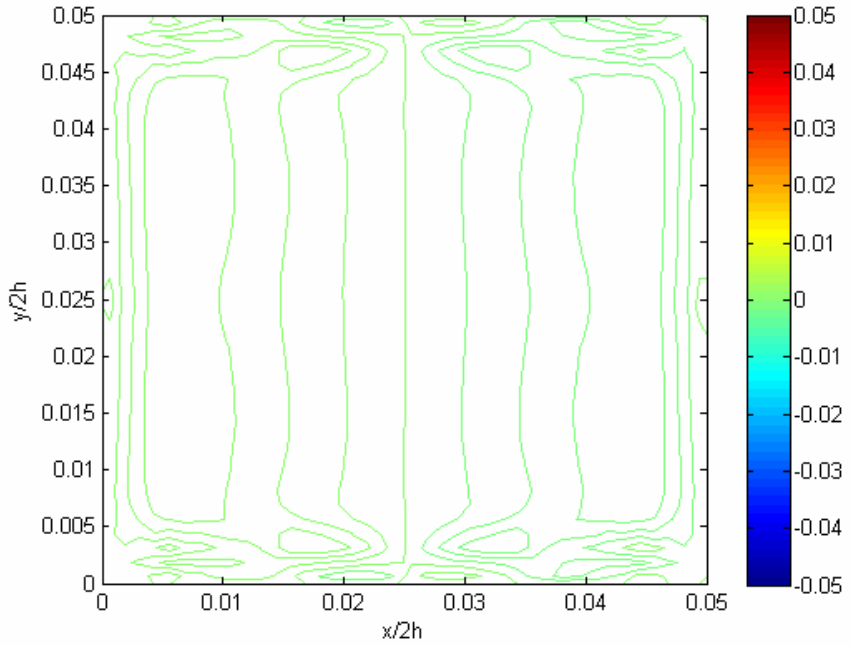

Figure 5.33 Scalar plot of the $100\,w'u'/w_{inlet}^2$ shear stress after four residence time, on the outlet plane of the duct with aspect ratio set to 10, artificial turbulence method.

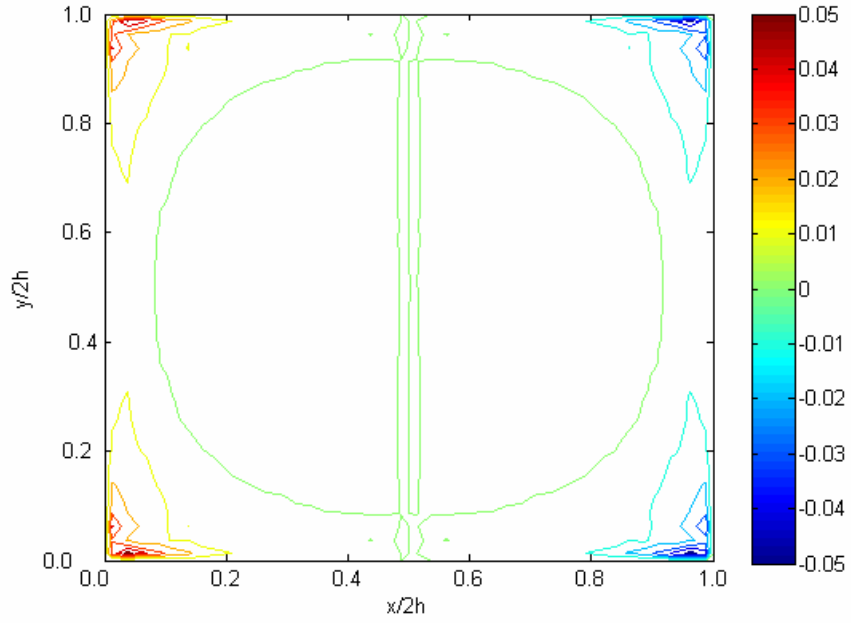

Figure 5.34 Scalar plot of the $100\,w'u'/w_{inlet}^2$ shear stress after four residence time, on the outlet plane of the duct with aspect ratio set to 20, artificial turbulence method.

The right half of the $\overline{w'u'}$ plot in Figure 5.33 normalised by the square of the inlet velocity magnitude w_{inlet}^2 which is multiplied by a factor of 100, gave a predominantly negative value of the stress component as opposed to the left half of the plane. This could be due to the vortices of the secondary flow moving towards the core region of the domain, as a result of the flow still in transient stage. The polarisation in the $\overline{w'u'}$ stress term between the right and left half of the outlet plane can also be seen in Figure 5.34 for the lengthened duct.

As a precaution, comparison of results between the two ducts with different streamwise lengths must be made with care as results from the lengthened duct is at about one residence time earlier than those from the standard duct (aspect ratio set to 10).

A comparison of the mean streamwise velocity profile on Line A between the standard mesh and a fine mesh with 56x56x140 cells (aspect ratio set to 4) after 0.5 residence time is shown in Figure 5.35. It can be seen from this figure that at *x/2h*=0.5, the case with the standard mesh has a value of $\overline{w}$ which is approximately 15% lower than the case with the fine mesh. In the latter case, the peak near the walls is more explicit and clear compared to the former case. This gives some idea on the level of discretisation error involved when using the standard mesh carried out to investigate the performance of synthetic turbulence generation methods.

It is expected that as the fluid moves in the downstream direction, the profiles of mean velocities obtained from computation will develop and approach those of a fully developed flow. Results for the random perturbation case in Figures 5.36 and 5.37 show improvement in the streamwise profile within the core region of the flow and this difference is about 13% at *x/2h*=0.50 measured on Line B after two residence time compared to the reference data indicating that the flow is still in a development stage. However, the region near the walls was under predicted. Pettersson Reif and Andersson (2002) using results of a fully developed flow in a square duct with periodic boundaries in the streamwise direction argued that the reason for this deviation is the inability of the turbulence model to predict the cross-stream intensity of the secondary mean flow field

correctly. The relatively coarse mesh used in the computation leading to significant discretisation error almost definitely has a non-negligible influence on this discrepancy by dampening the fluctuations of velocity as the flow moves downstream from the inlet resulting in low turbulence intensities near the outlet and producing symmetrical velocity vector fields on the outlet plane.

For the vortex particle method after two residence times, Line A shows a better approximation for the region near the wall compared to the random turbulence generation method. The core region gives a similar profile to the random turbulence generation method. Moving downstream to Line B in Figure 5.37, it is clear that the vortex method gave a better profile in the core region compared to the random perturbation method with a difference of 9% at $x/2h$=0.5, compared to the reference data. A reason for this is the relatively large time scales of large eddy structures moving downstream from the inflow plane where the low wave-number component is correlated in time and space to some extent as explained earlier in this chapter.

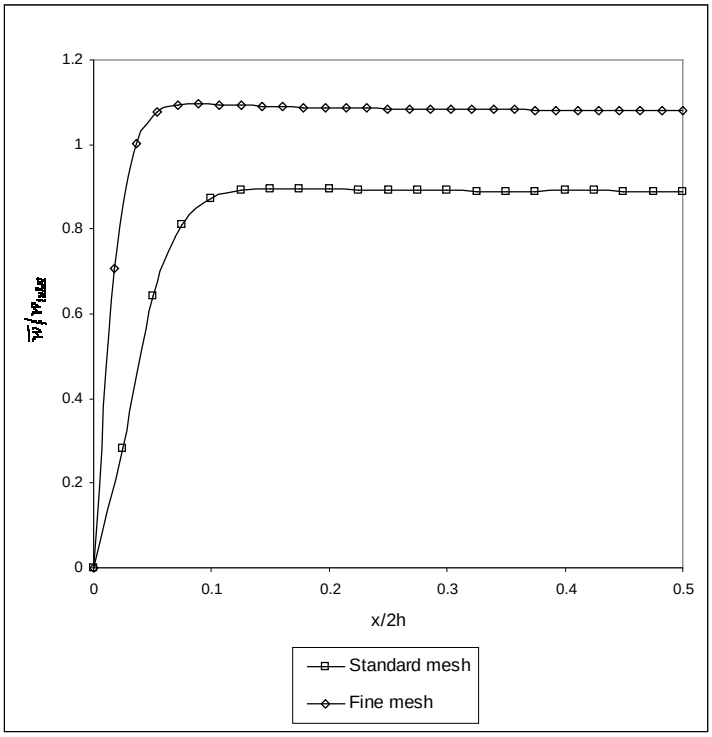

Figure 5.35 Mean profiles of the resolved velocity component in the streamwise direction on Line A after 0.5 residence time.

With the artificial turbulence generation method and no turbulence at the inlet after 1.1 residence time (t=2.5s), the mean profiles are very similar to those of the vortex particle method as shown in Figures 5.36 and 5.37. The similarity of the profiles of the no inflow turbulence case to those of the vortex particle method may be related to the low values of subgrid scale Reynolds stresses which underpredicts the strength of vorticity associated with the secondary mean flow as argued by Pettersson Reif and Andersson (2002). An analysis of a component of shear stress $\overline{w'u'}$ is carried out below. The presence of large eddies might also help in achieving a comparable mean profile to those of the random perturbation method.

After 1.1 residence time, the root-mean-square values of the velocity component in the streamwise direction were found to be very close to the mean profiles (Figures 5.38 and 5.39). There is no indication of the presence of a peak near the wall region where production of turbulence kinetic energy takes place. This indicates a possibility that the averaging period is much shorter than the time scale associated with large eddies and the flow not being in a fully developed stage resulting in the amplitude of fluctuations being considerably smaller than the reference data. This could also be explained by the fact that the relatively coarse mesh used in this case results in a diffusive numerical scheme and excessive lost or dissipation of turbulence kinetic energy. This is especially true in the region next to the wall where the production of turbulent kinetic energy is prevalent. A common approach to tackle this problem economically is to increase the mesh density near the wall until correct y^+ values are obtained allowing integration to the wall for the computation of shear stresses to be carried out properly. However, due to time constraints, local mesh refinement was not built into the code for this study. The profiles in these two figures must not be confused with the plot in Figure 5.31, since in the latter the contour plot of the fluctuating velocity (not the resolved velocity) is plotted.

Line A shows that there is a negligible difference in the root-mean-square values when using different methods of turbulence generation at the inlet as shown in Figure 5.37. The random method seems to produce the profile with the largest root-mean-square values

compared to the other methods in the core region along Line B as plotted in Figure 5.39. The root-mean-square values in these figures are normalised by the value of the bulk velocity. The root-mean-square results are not compared to some reference data since those published, use periodic boundaries, and the available results are also from fully developed flows, unlike the case here.

The root-mean-square profile of the duct with the aspect ratio set to 20 on a line lying on the outlet plane parallel to and downstream of Line B was monitored after one residence time. Profiles shown in Figure 5.40 indicate that the lengthened duct has peaks on the profile closer to the wall compared to those of the shorter duct. The peak region of the lengthened duct occupies a more compact space compared to the other cases. These results indicate that fluctuation levels in the boundary layer region are strongly dependent on the downstream distance from the inlet and there is scope for improvement in the capability of the inlet turbulence generation method to promote or match turbulence fluctuations with the physics of the flow by varying the characteristics of fluctuations depending on the region of the inlet plane. The simplest way to cater for the increased level of turbulence intensities near the walls is to vary the distribution of turbulence kinetic energy k with the x and y-coordinates using data from auxiliary simulations at the expense of extra computation cost

An important parameter which needed to be computed was the value of the resolved shear stresses at the walls. This parameter affects the strength of vorticity near the corners of the duct. Turbulence anisotropy is in turn influenced by the strength of vorticity in this region.

Analysis of the $\overline{w'u'}$ term after 1.1 residence time indicates that the random perturbation method produces significantly lower levels of this stress term compared to other methods of generation of turbulence. The case with no inflow turbulence produces the highest level of $\overline{w'u'}$ shear stresses. The shear stress values shown in Figures 5.41 and 5.42 are normalised by the square of the inlet bulk velocity value and magnified by a factor of 100. The artificial turbulence generation and enhanced vortex particle methods sit in

between these two extreme cases. An interesting feature of this method is the increase in the magnitude of $\overline{w'u'}$ stress moving downstream, from Line A to Line B. The lower $\overline{w'u'}$ values produced by all the methods considered compared to those of Pettersson Reif and Andersson (2002), are most probably due to the excessive damping caused by the numerical scheme on a coarse mesh.

The change in sign from Line A to Line B may be related to the fact that in the development and transient stage, the *u* velocity component changes direction, that is, from negative on Line A to positive on Line B referring to the coordinate system shown in Figure 5.1. The positive correlation is due to the increasing strength of the vertical velocity component moving in the positive (upwards) direction on Line A, and the reverse is true, moving downstream on Line B. The $\overline{w'u'}$ values shown in Figure 5.43 for the random perturbation case shows that the fluctuations are damped as the simulation progresses in time.

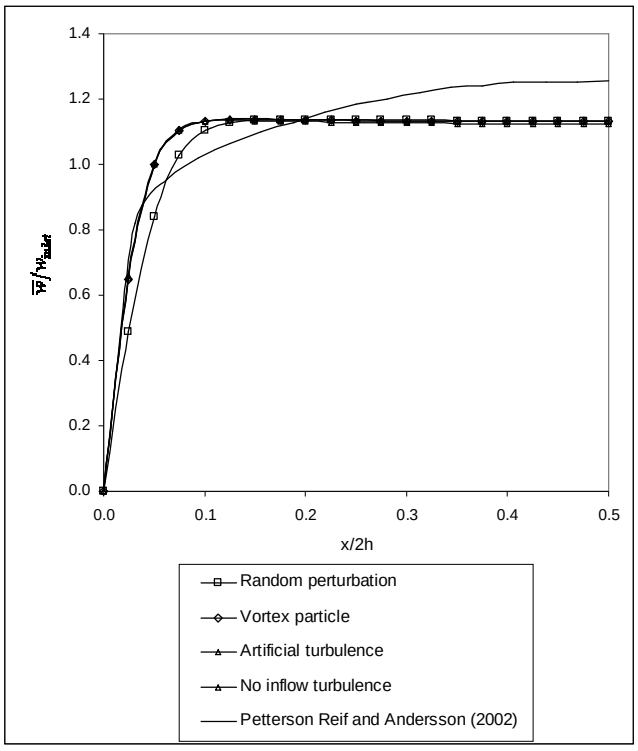

Figure 5.36 Mean profiles of the resolved velocity component in the streamwise direction on Line A after 1.1 residence time.

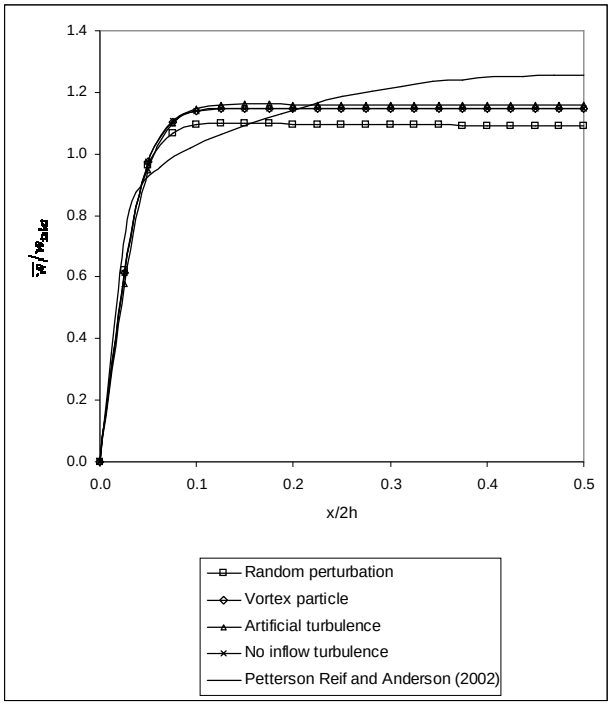

Figure 5.37 Mean profiles of the resolved velocity component in the streamwise direction on Line B after 1.1 residence time.

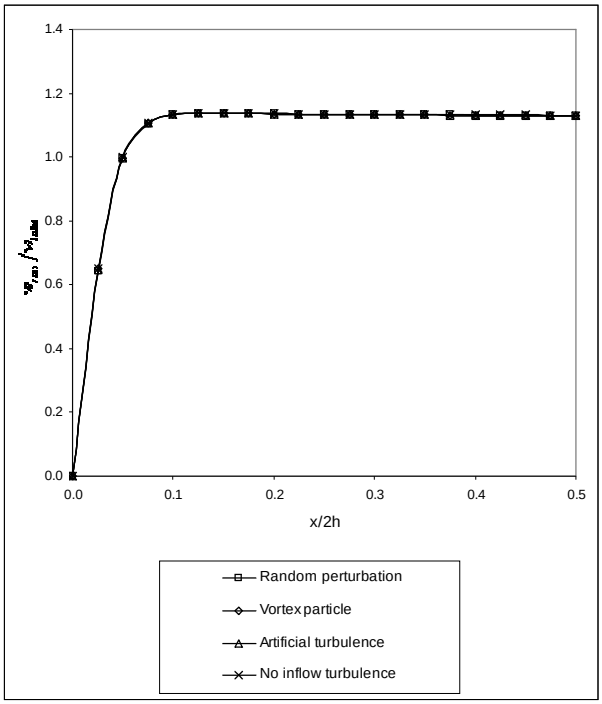

Figure 5.38 Root-mean-square profiles of the resolved velocity component in the streamwise direction on Line A after 1.1 residence time.

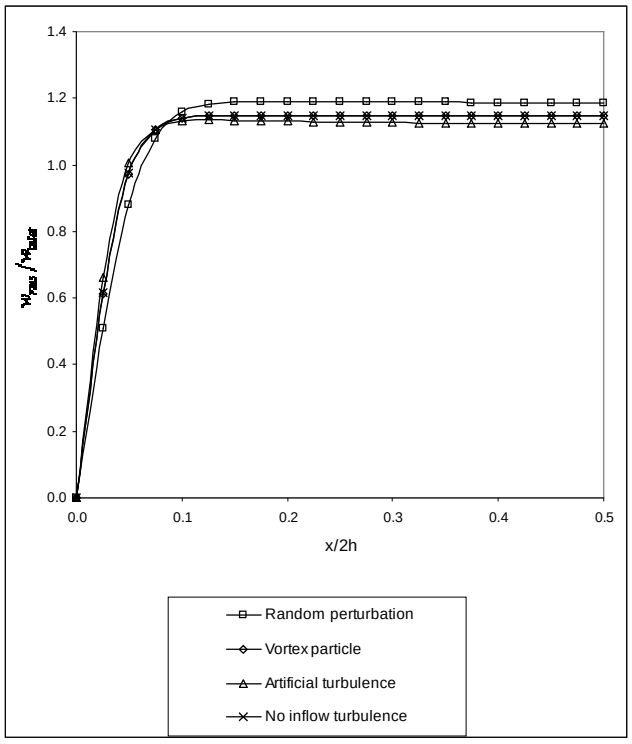

Figure 5.39 Root-mean-square profiles of the resolved velocity component in the streamwise direction on Line B after 1.1 residence time.

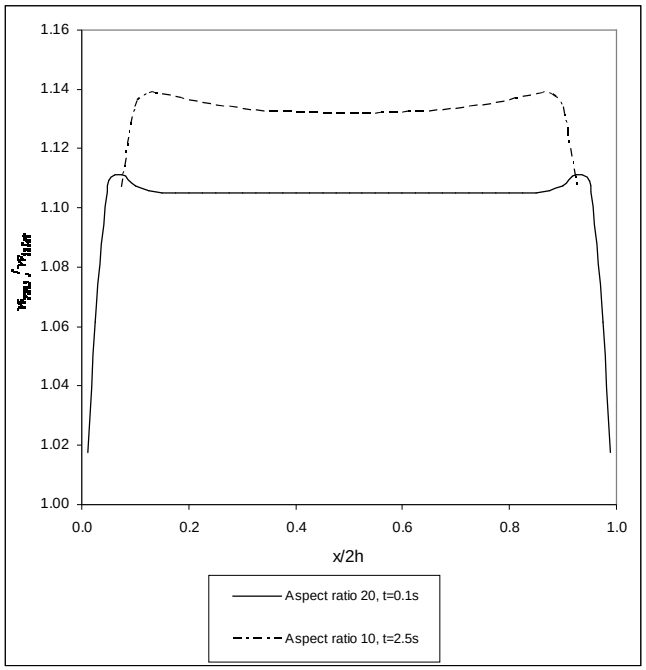

Figure 5.40 Root-mean-square profiles of the resolved velocity component in the streamwise direction with two different duct lengths in the streamwise direction showing the peak regions near the walls.

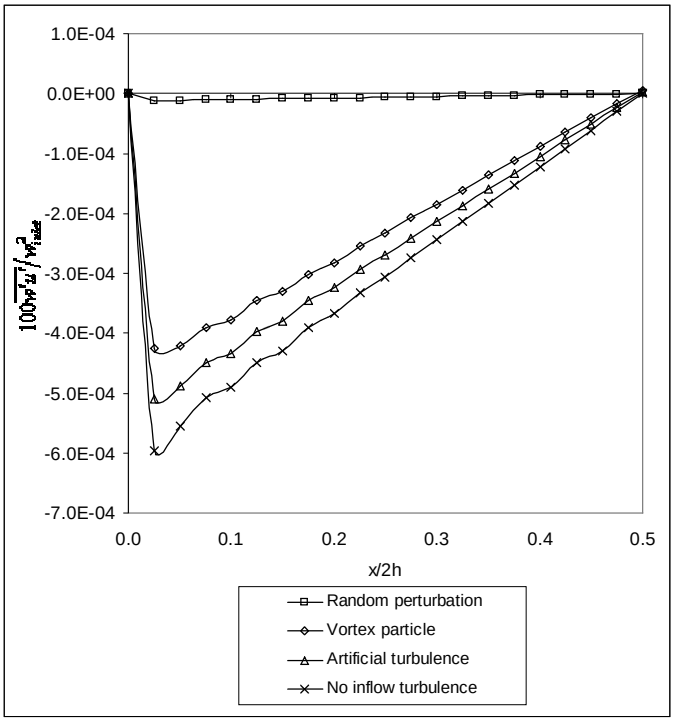

Figure 5.41 $\overline{w'u'}$ stress profiles Line A after 1.1 residence time.

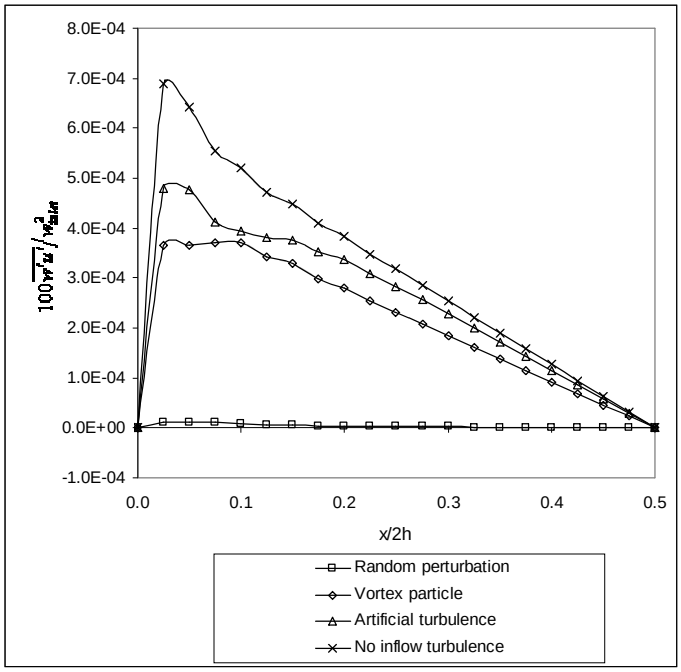

Figure 5.42 $\overline{w'u'}$ stress profiles Line B after 1.1 residence time.

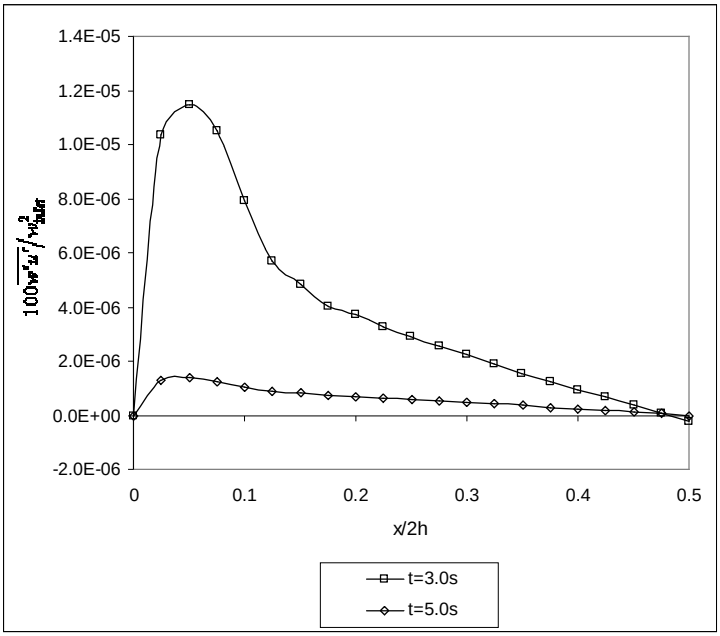

Figure 5.43 $\overline{w'u'}$ stress profiles Line B, random perturbation case at 1.3 and 2.2 residence times.

After about four residence time (at *t*=7.5s) on Line A, the value of the mean velocity in the streamwise direction, $\overline{w}$ (normalised by the value of bulk inlet velocity) has increased by approximately 1.3% from the one at 1.1 residence time (*t*=2.5s); while on Line B the increase is 6.1%, taking an average value of the different turbulence generation methods, under study as shown in Figures 5.44 and 5.45. This clearly shows the transient nature of the flow, occurring, as the simulation progresses. The difference in the values of $\overline{w}$ amongst different methods used here is very small, which is in the order of 0.01% of the reference peak value at *x/2h*=0.5 on Line B. This meagre difference is a result of the random number generators all having a mean value of zero and an averaging period, long enough to eliminate small time-scale differences amongst the methods of turbulence generation.

In addition to Line A and Line B, another monitoring line, Line C, located at *y/2h*=0.25 in the negative *y*-direction, adjacent and parallel to Line B, were added to monitor the mean values of the resolved velocity component in the *y* direction, $\overline{v}$. The profiles of $\overline{v}$ (normalised by the value of bulk inlet velocity) on these lines, shown in Figure 5.46 are also very similar with respect to the different turbulence generation methods used as is

the case with $\overline{w}$ above. This profile was not compared to any reference data since the secondary flow is still in transient mode and not in a fully developed stage. Next to the wall, the LES model produced a zone bounded by $0<x/2h<0.3$ with a positive value of $\overline{v}$. This corresponds to the region next the lower left corner of the plane in Figure 5.26 with Line C cutting through the vortex below the corner bisector.

The root-mean-square profiles shown in Figures 5.47 and 5.48 are essentially similar for all the methods of turbulence generation considered here, and once again, the peak region close to the wall at the start of the core region is absent, or only slightly produced. The main culprit here is the excessively dissipative spatial discretisation scheme used.

The $\overline{w'u'}$ stress profiles in Figures 5.49 and 5.50 exhibit a significant difference in the magnitudes of $\overline{w'u'}$ with regards to the different turbulence generation techniques used. It is clear that the method of artificial turbulence gave the highest levels of $\overline{w'u'}$ at all *x/2h* values compared to the method of random perturbation and the no turbulence case. This indicates that the correlated large-scale structures generated at the inlet by the method of artificial turbulence is able, to some extent, to resist the onslaught of damping imposed by the spatial discretisation scheme better than the uncorrelated fluctuations of the random method. Data from the no inflow turbulence case show that the flow is still not fully developed to produce energy-containing eddies since the energy levels are much lower than those from other methods.

The level of energy from the vortex particle method is approximately half of that obtained from the method of artificial turbulence. The $\overline{w'u'}$ profile of this method is considerably lower than those of the artificial turbulence case because the fluctuations in the *z*-direction were not designed to correlate with the fluctuations in the perpendicular directions to it. Even if there are non-zero correlations, these occur on a non-regular basis and are relatively weak compared to the *z*-direction $\overline{w'w'}$, the normal stresses.

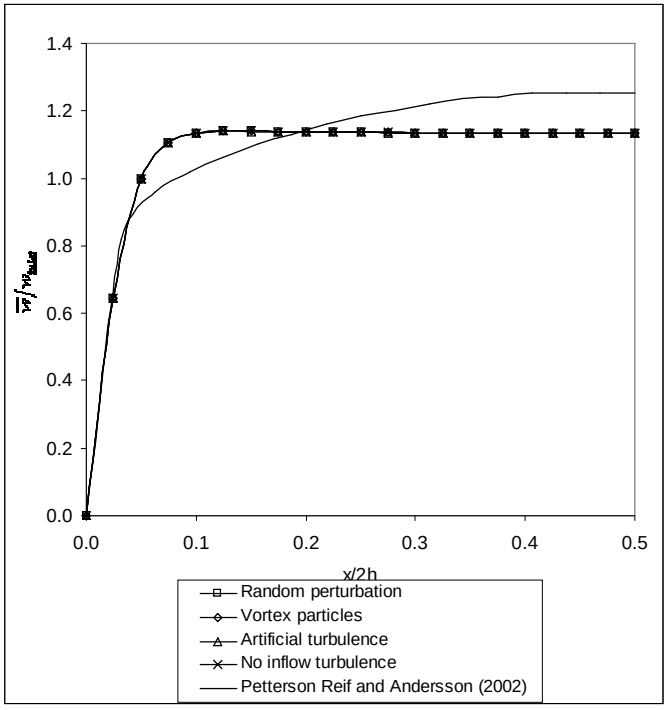

Figure 5.44 Mean profiles of the resolved velocity component in the streamwise direction on Line A after four residence time.

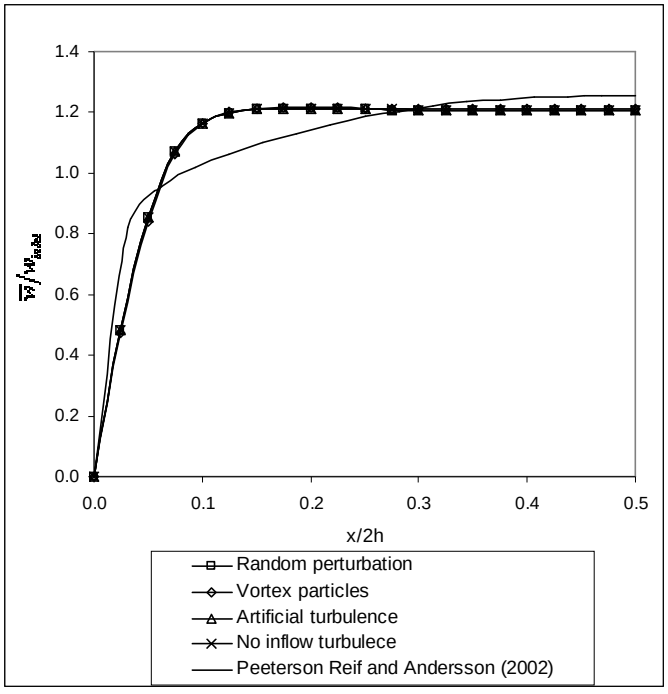

Figure 5.45 Mean profiles of the resolved velocity component in the streamwise direction on Line B after four residence time.

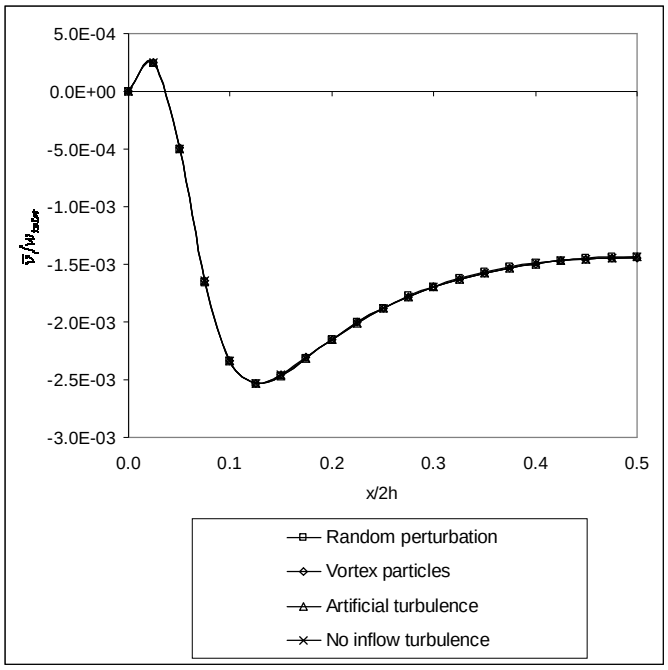

Figure 5.46 Mean profiles of the resolved velocity component in the *y*-direction on Line C after four residence time.

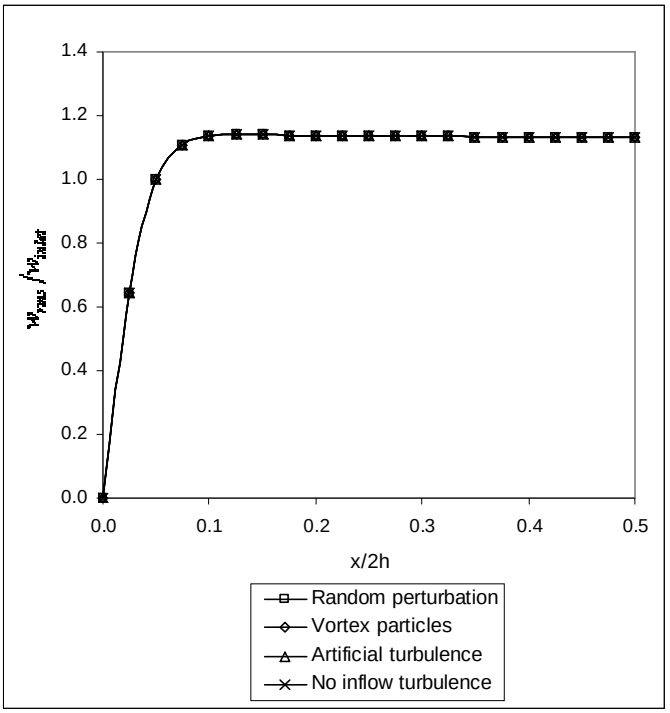

Figure 5.47 Root-mean-square profiles of the resolved velocity component in the streamwise direction on Line A after four residence time.

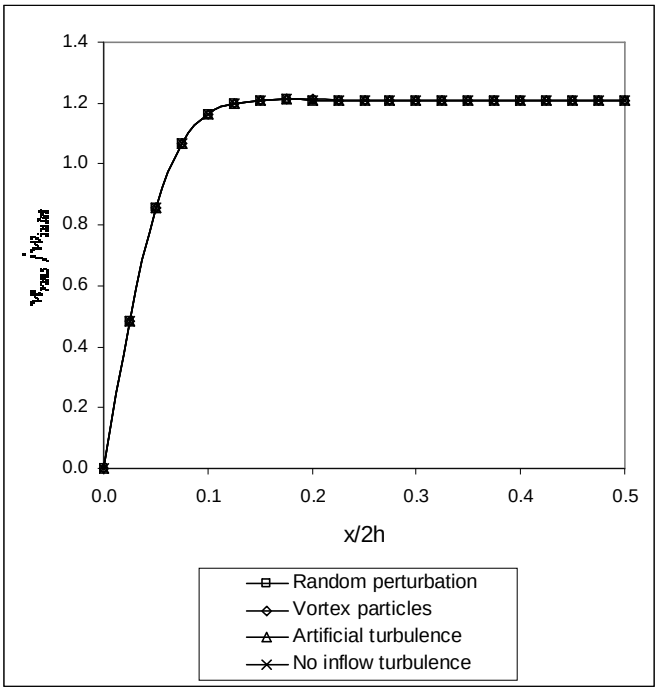

Figure 5.48 Root-mean-square profiles of the resolved velocity component in the streamwise direction on Line B after four residence time.

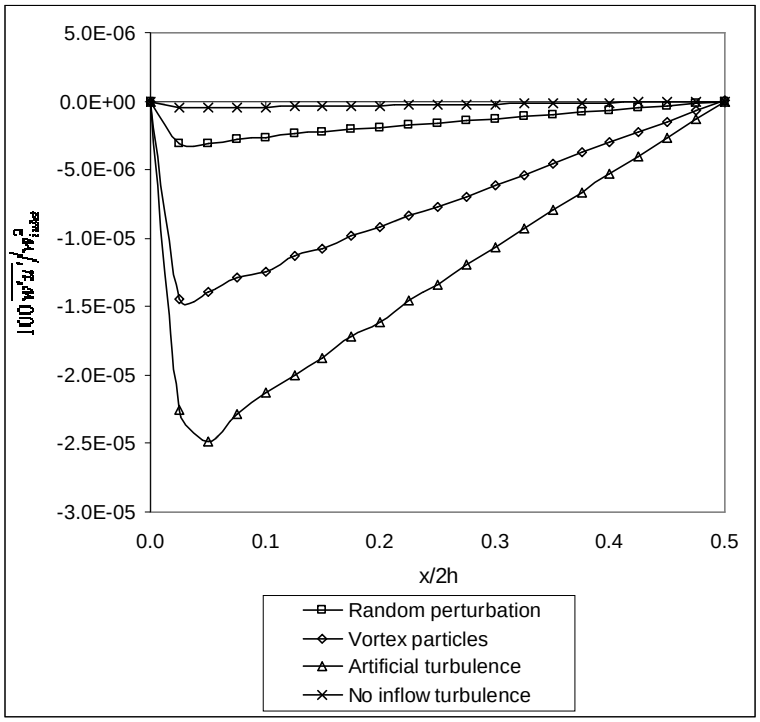

Figure 5.49 $\overline{w'u'}$ stress profiles on Line A after four residence time.

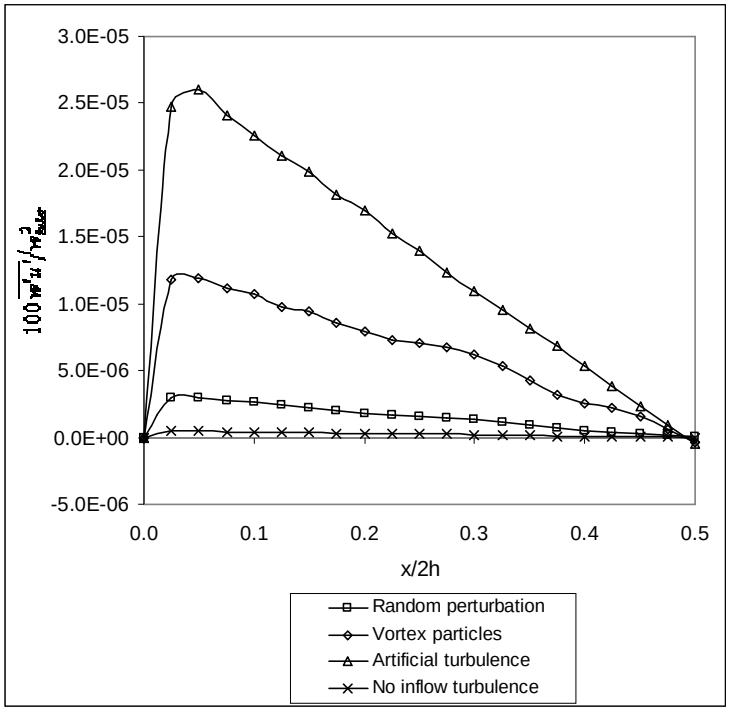

Figure 5.50 $\overline{w'u'}$ stress profiles on Line B after four residence time.

The streamwise two-point correlation plot is useful in determining the length scale of the largest turbulence structure and helps in judging the required dimensions of the flow domain. In addition to these, Wilcox (2002) showed how the micro-time and micro-length scales (Taylor microscale) are related to the two-point time and space correlations respectively with the help of the Taylor series of the correlation function. An observation of this parameter was carried out with a reference point located in the middle of the computational domain. The averaging was performed at every time step of the simulation.

Results for the random inlet perturbation case are shown in Figure 5.51. The characteristic shape of a sinc function was approximated by the correlation data as evident in this figure. Based on these data, the correlation coefficients are close to zero for the random perturbation case starting at z=0.14m measured from the reference point. Non-dimensionalising this figure with the duct length gives a value of 0.28 which is approximately 43% lower than that of Huser and Biringen (1993). This figure gives some evidence that the domain length in the z-direction is adequate to resolve large scale

eddying motions. However it must be recalled from the velocity vector field plots that the flow has not reached a fully developed stage within the computational domain. This may have an influence on the length associated with the large scale eddying motions. The same argument can also be related to the asymmetric nature of the correlation data about the axis perpendicular to the streamwise direction passing through the centre point of the domain.

The two-point correlation data after 2.2 residence time (at time t=5.0s) show that there is very little or no correlation present at this time for the random generation case because from Figure 5.52, there are a number of peaks with magnitudes larger than or comparable to that at z/L=0.5. This is still the case after four residence time as shown in Figure 5.53. This also means that the transient stage of the flow has some influence on the turbulence structure of the flow since after 1.1 residence time there is a greater degree of correlation compared to the data after 2.2 residence time.

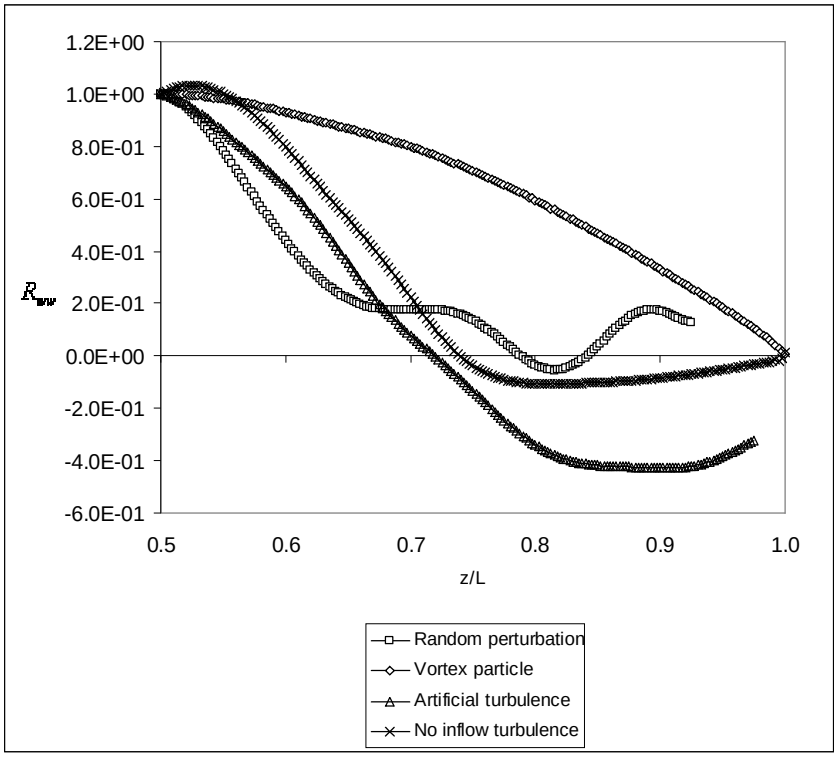

Figure 5.51 Two-point velocity correlation coefficient R_{ww} at a location corresponding to the centre of the domain after 1.1 residence time.

After four residence time, there is a relatively high degree of correlation exhibited by the artificial turbulence generation method as evident in Figure 5.53 with a gradual decrease in the R_{ww} value moving downstream from the centre of the domain. The first intersection with the z-axis occurs at $z/L \approx 0.96$. A similar trend is shown by the no turbulence case with the intersection occurring earlier at $z/L \approx 0.88$ signifying a lower degree of correlation compared to the method of artificial turbulence. The enhanced vortex particle method gave a profile close to that of the artificial turbulence case but the intersection with the x-axis occurred earlier at about z/L=0.92.

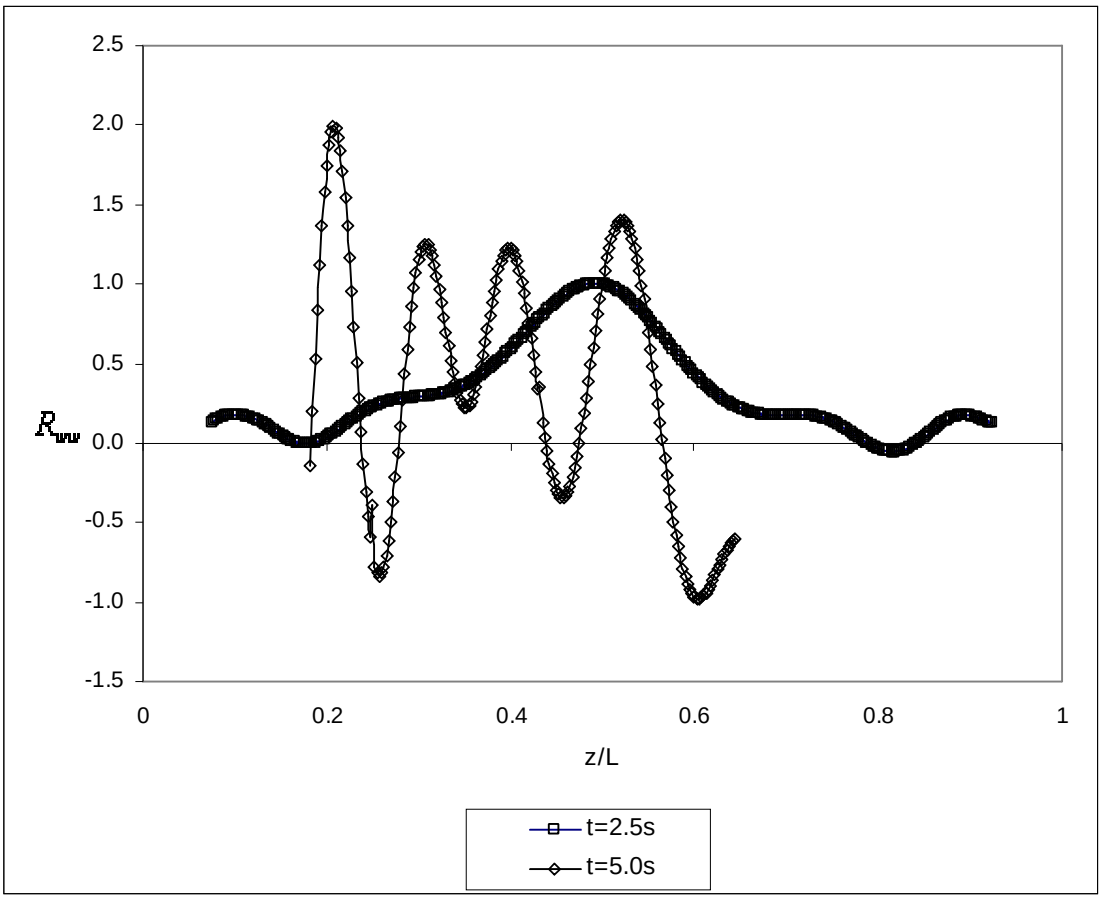

Figure 5.52 Two-point velocity correlation coefficient R_{ww} at two different times for the random turbulence generation case.

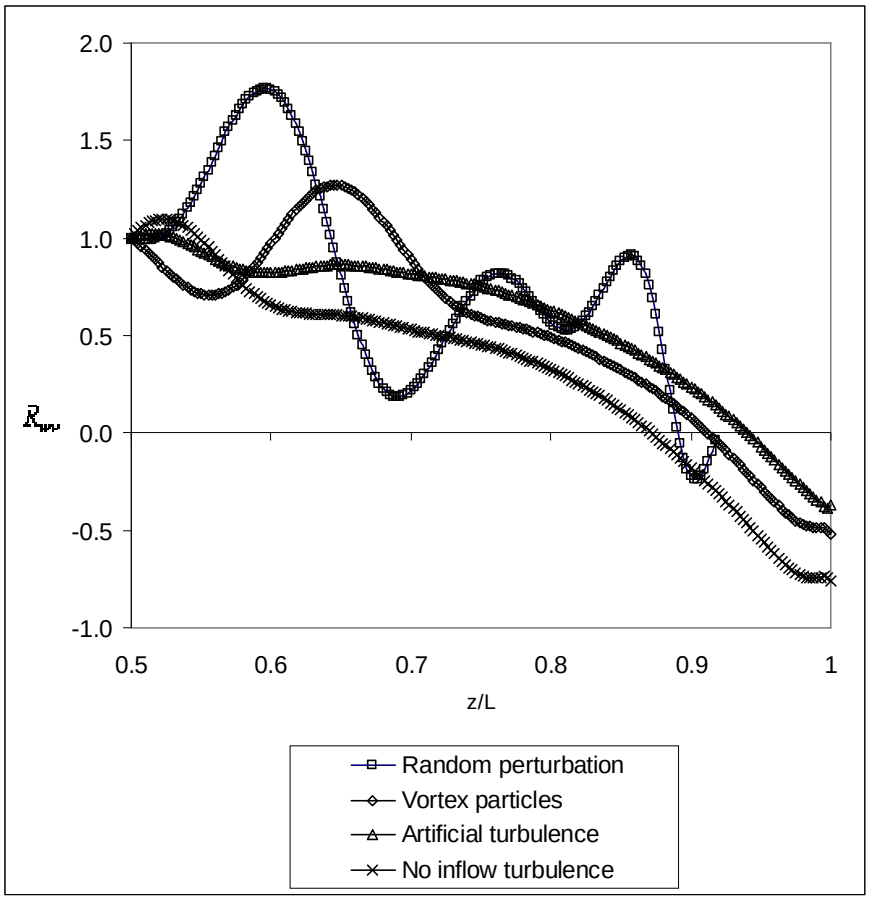

Figure 5.53 Two-point velocity correlation coefficient R_{ww} at a location corresponding to the centre of the domain after four residence time.

A useful parameter to evaluate the performance of different methods of turbulence generation at the inlet as described earlier in this chapter and check for the correct implementation of these methods is the turbulence kinetic energy spectrum which was observed at two points on a vertical line normal to a wall. This line passes through the centre of the domain. The first point is located at $x/2h$=0.5, $y/2h$=0.125 and z/L=0.5 while the second point has a coordinate of $x/2h$=0.5, $y/2h$=0.5 and z/L=0.5, which is the centre of the domain. These points will be labelled as Point A and Point B hereafter. Of particular interest is the level of turbulence kinetic energy available at these monitoring points and the range of frequencies over which this takes place. Comparing this parameter with available reference data will shed some light on how the different methods perform. Data were sampled at every time step during the simulation with the time step size Δt=0.0001s for 4,000 time steps. The highest frequency of fluctuation

obtainable was approximately 5,000Hz upon imposing the Nyquist condition with the lower bound at 2.5Hz.

Results in Figures 5.54 to 5.57 clearly show the existence of eddies or fluctuations associated with the inertial subrange (taking place in the frequency range of about 50Hz<f<120Hz where f is the frequency of fluctuation) for the artificial turbulence generation case at both monitoring points, in contrast, for other methods, the range of frequencies associated with the inertial subrange is not clear. Except for the artificial turbulence generation case, the turbulence kinetic energy spectrum levels at Point B is higher than that at the other point (closer to the boundary layer) by about two orders of magnitude probably due to the dissipation or damping of turbulent fluctuations with wavelengths larger than the thickness of the boundary layer next to the wall close to Point A.

Comparing the energy spectrum produced by different methods of turbulence generation, the important difference is the level of energy observed here at the monitoring points within the sampling period. After 1.1 residence time (t=2.5s), the energy levels of turbulence are similar in magnitude at Point B for all the methods of turbulence generation but at Point A, the method of artificial turbulence has a higher energy spectrum level compared to other methods which is especially true in regions with frequencies higher than 100Hz.

A quantitative comparison between the results from Huser and Biringen (1993) and the present study shows that the energy spectrum levels of low wavenumber eddies in the former study are about three orders of magnitude larger than results obtained from the latter, however, the range of frequencies for the inertial subrange eddies are in both cases similar. Results from Le, Moin and Kim (1994) shed some light on this observation. Their data show that the development of random fluctuations was impaired by the relatively coarse grid used. Lee, Lele and Moin (1992) discovered that it is possible to produce rapidly developing isotropic turbulence (in the downstream direction) from the random fluctuations at the inlet for their direct numerical simulation of compressible

turbulent flow. This statement gives some credence to the low level of energy spectrum obtained using the random method as shown in Figure 5.54 owing to the presence of only isotropic or small scale eddies in the domain. It is also possible that large anisotropic eddies have died out upstream of the monitoring point resulting in the low level of energy spectrum in Figure 5.54. This statement is supported by the fact that if the random fluctuations are maintained moving downstream from the inflow, the spectrum would be more uniform since turbulence kinetic energy is contained in a wider range of wavenumbers.

After about four residence time (t=7.5s), the turbulence kinetic energy spectrum was once again monitored. This time, instead of using Point B, another point located at 0.125m downstream of Point A was selected. This point is labelled as Point C hereafter. Observing the energy spectrums in Figures 5.58 and 5.59 after about four residence time from the start of simulation, it is not hard to observe that the random method together with the no turbulence case gave a significantly lower value of spectra at all frequencies calculated compared to the ones calculated using the method of artificial turbulence. This difference is about four orders of magnitude at a frequency of about 100Hz.

As with the case after 1.1 residence time, the decay in k moving downstream from Point A to Point C is again observed here implying that this feature persists even when the flow approaches the steady-state form.

For the methods of artificial turbulence and enhanced vortex particle, the inertial sub-range exists between frequencies of approximately 90Hz and 120Hz. For no inflow turbulence, on the other hand, this occurs between frequencies of 60Hz and 100Hz. The random perturbation case does not show a clear frequency range over which the inertial subrange took place. The value of the first point in the plot should not be taken too seriously because the time series data was not windowed to suppress leakage.

As the simulation progresses, moving from a residence time of 1.1 to 4, there is a decay in the amount of turbulence kinetic energy k (which is also the area under the energy

spectrum plots) produced by all methods though the degree of reduction differs from method to method. The artificial turbulence generation method was least influenced by this transient feature of the flow. From Figures 5.56 and 5.58, it can be stated that at Point A this decay does not exceed an order of magnitude which is a lot smaller than those of other methods. This seems to suggest that the increasing strength of the streamwise and secondary flows with time have a damping effect on both the production from the mean flow to large scale eddies.

Integrating the energy spectrum function in Figure 5.59 gives the turbulence kinetic energy per unit mass k, at Point C. Comparing this with k at a point on the inlet plane with similar x and y-coordinates as Point C (denoted as Point I) for the different inlet conditions (Table 5.2), it can be seen that the random perturbation method exhibits the largest drop in k by approximately seven orders of magnitude. The enhanced vortex particle method underwent the smallest reduction in k by about two orders of magnitude. The relatively lower value of k at the inlet for the vortex particle method may be due to the absence of particles at the point of monitoring.

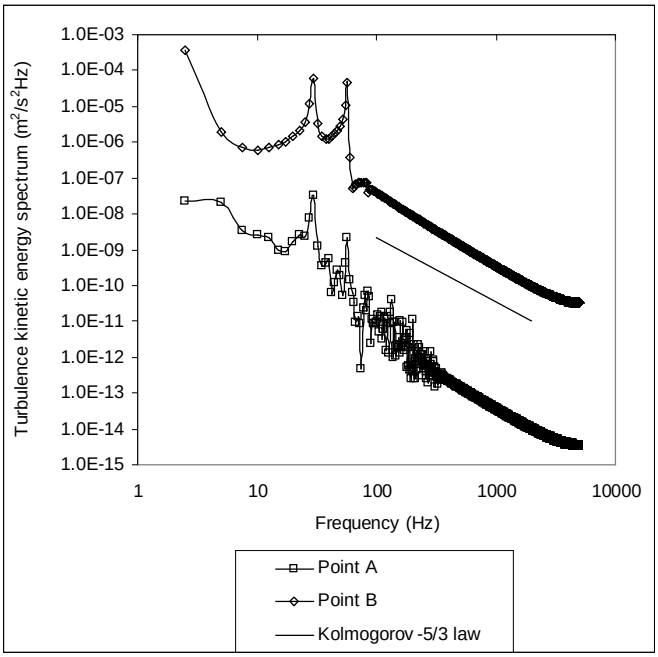

Figure 5.54 Turbulence kinetic energy spectrum after 1.1 residence time, random perturbation method.

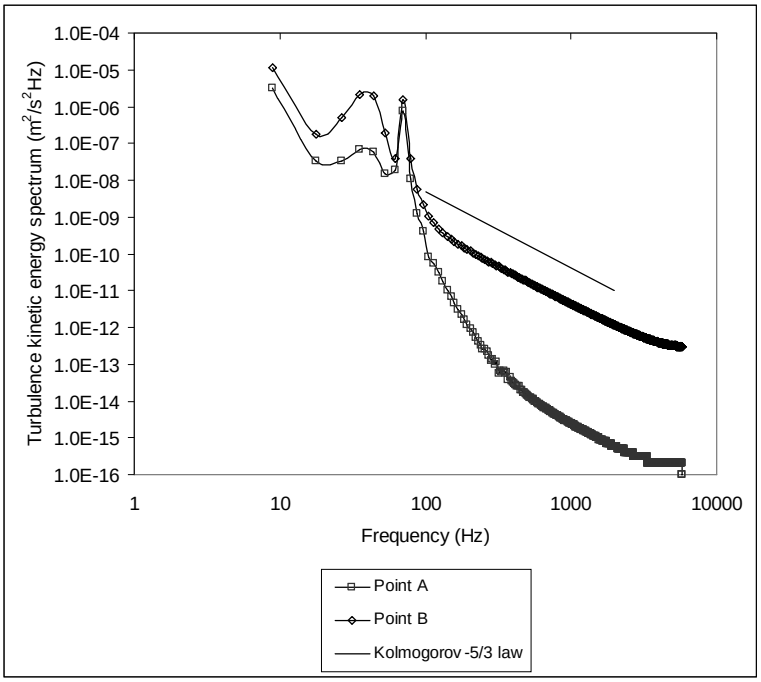

Figure 5.55 Turbulence kinetic energy spectrum after 1.1 residence time, enhanced vortex particle method.

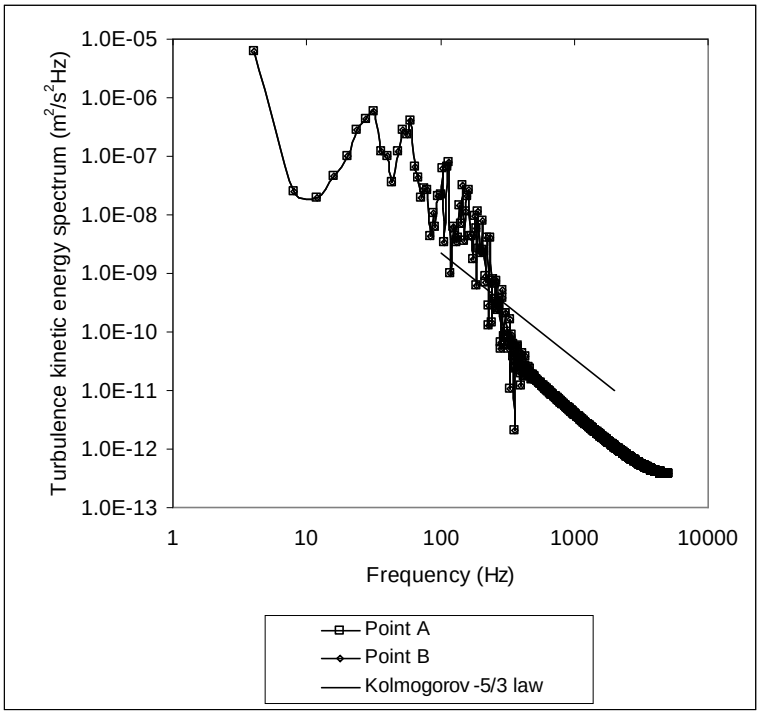

Figure 5.56 Turbulence kinetic energy spectrum after 1.1 residence time, artificial turbulence method.

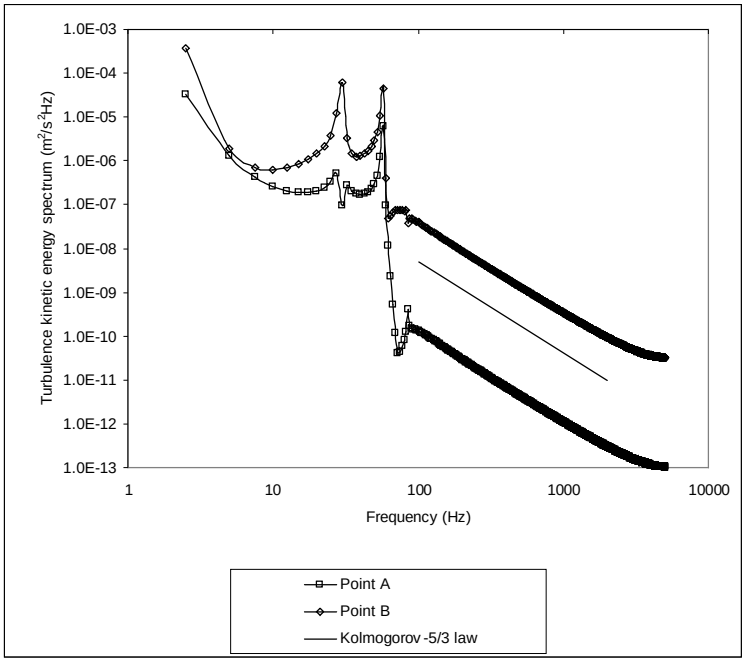

Figure 5.57 Turbulence kinetic energy spectrum after 1.1 residence time, no inflow turbulence.

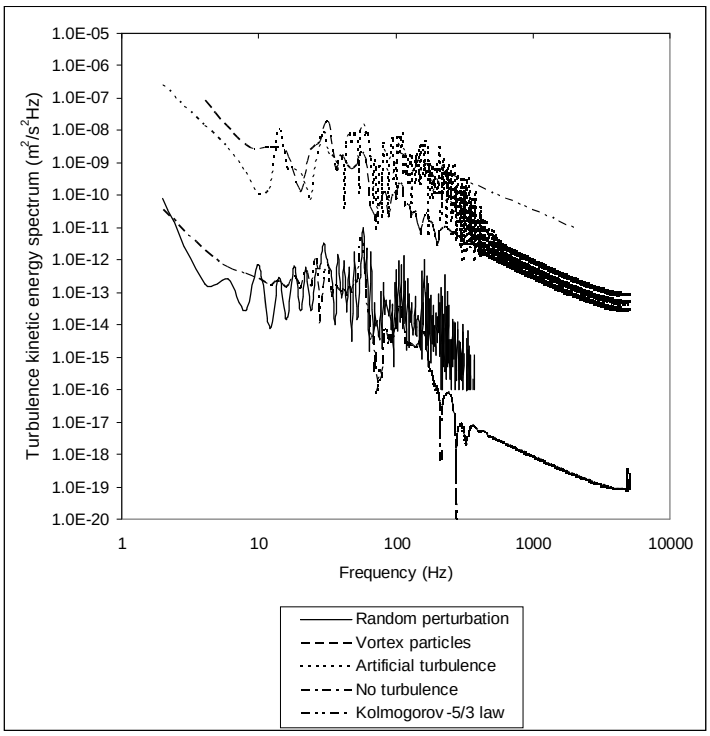

Figure 5.58 Turbulence kinetic energy spectrum at Point A, all methods after four residence time.

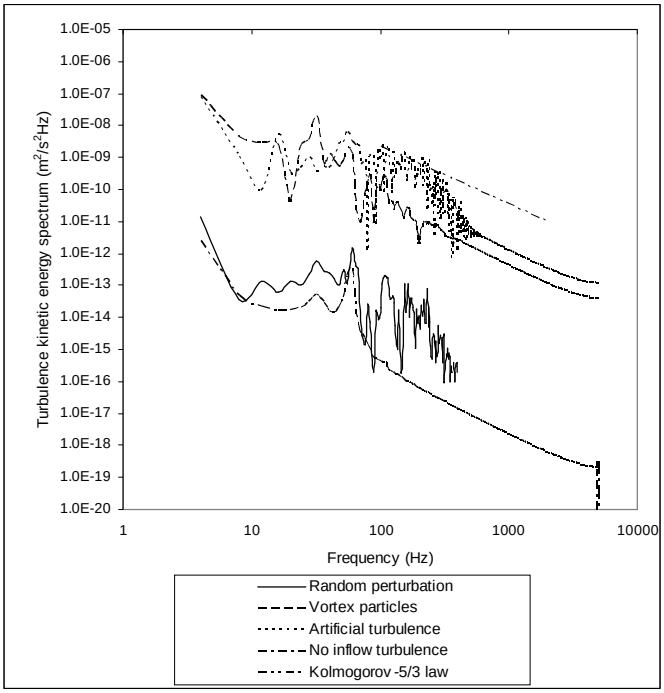

Figure 5.59 Turbulence kinetic energy spectrum at Point C, all methods after four residence time.

	Point I	Point C
Random perturbation	5.71E-4	5.24E-11
Vortex particle	4.98E-5	3.51E-7
Artificial turbulence	1.17E-3	4.19E-7

Table 5.2 Turbulence kinetic energy (m^2/s^2) at Point I (inlet) and Point C using different synthetic turbulence generators.

Treatment of wall boundaries was based on the value of the non-dimensional distance from the wall, y^+. The y^+ values of the boundary faces on a wall after 1.1 residence time t=2.5s) for the random inlet perturbation case is shown in Figure 5.61. It is assumed that this wall is typical of other walls with respect to the values of y^+. Since the y^+ values obtained indicate that the first layer of cells next to solid boundaries are close to the viscous sub-layer region of the boundary layer, the wall function was not used to compute the shear stresses even though the code is capable of doing so. Instead the integration to the wall treatment of solid boundaries was utilised in the computations for

all cases in this chapter.

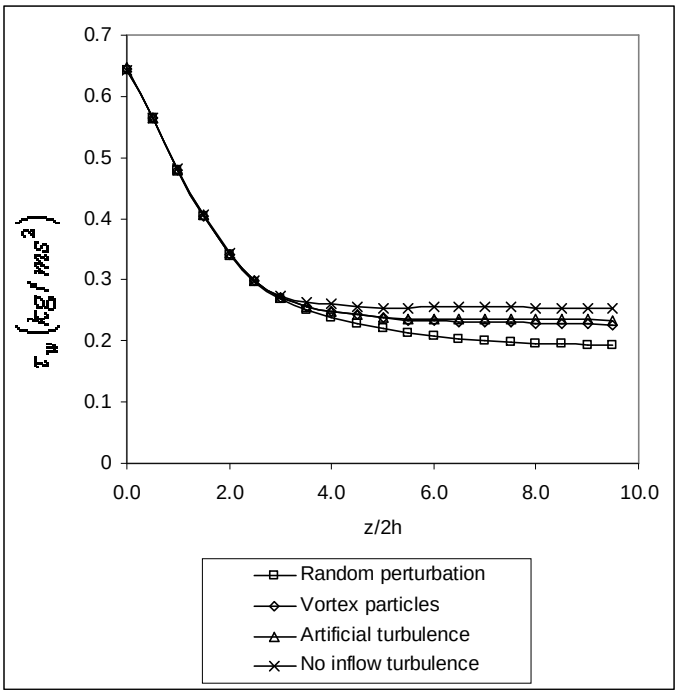

Figure 5.60 Wall shear stress along a wall centreline in the streamwise direction after 1.1 residence time.

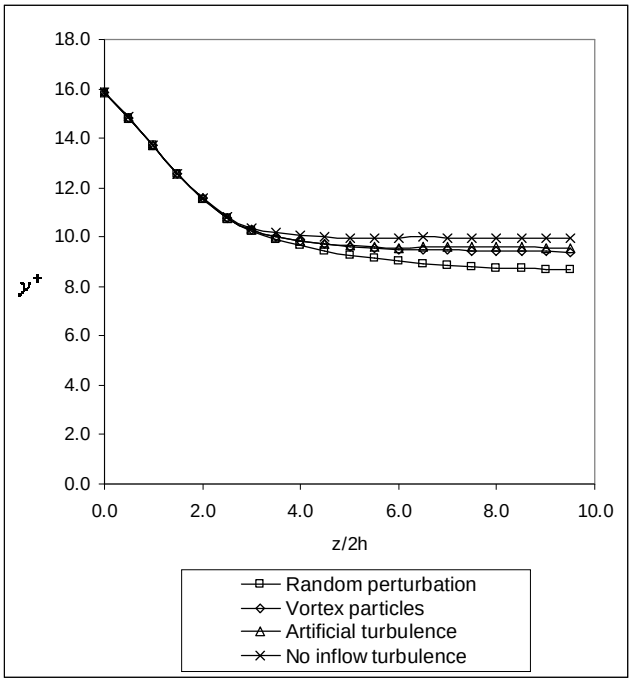

Figure 5.61 Non-dimensional distance from a wall centreline in the streamwise direction after 1.1 residence time.

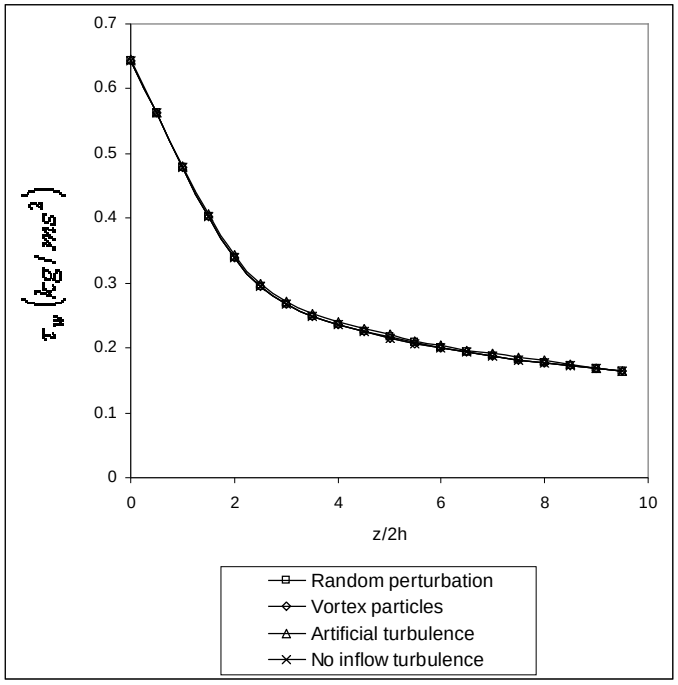

Figure 5.62 Wall shear stress along a wall centreline in the streamwise direction after 4 residence time.

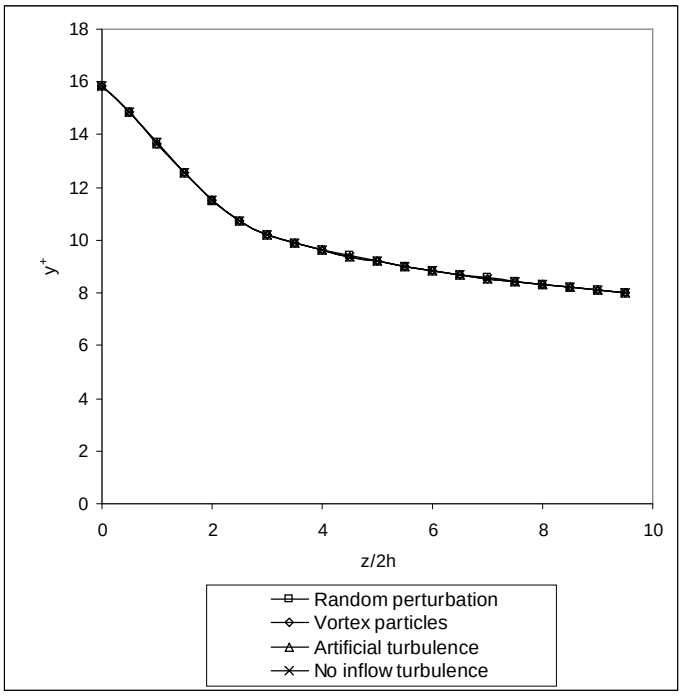

Figure 5.63 Non-dimensional distance from a wall centreline in the streamwise direction after 4 residence time.

The average value of the friction velocity over a wall after four residence time is denoted by u_* obtained by spatially averaging the value of resultant wall shear stresses from boundaries of a wall. Assuming that this average value is typical of those computed from other walls and normalising this parameter by the bulk velocity u_b, a comparison is made with reference data from Pettersson Reif and Andersson (2002) for each inlet turbulence generation method. The values of u_*/u_b are equal to 0.0151 for the no turbulence and random perturbation cases, 0.0153 from the artificial turbulence generation method and 0.150 from the enhanced vortex particle case. The value computed by Pettersson Reif and Andersson (2002) is about a factor of four larger than those computed. The difficulty in predicting the friction velocity is to be expected and this is related to the fact that the flow is still in development stage as stated by Lund, Wu and Squires (1998). The marginal difference in the values of u_*/u_b when using different methods of turbulence generation implies that, this parameter is insensitive to the fluctuations on the inlet plane. This parameter is likely to have a stronger connection to changes in the mean inlet velocity profile since the wall shear stress depends on the mean strain rates in a linear manner if the effective viscosity is kept constant with time and space.

The values of y^+ along a line bisecting a wall running from the inlet to the outlet are shown in Figures 5.61 and 5.63. From these figures it is clear that y^+ is decreasing moving in the z direction at both times. This can be explained by noting that the boundary layer thickness increases moving downstream from the inlet. The first cell centre node next to the wall boundary moves relatively closer to the start of the logarithmic layer within the boundary layer. At t=2.5s, the values of y^+ from different methods of turbulence generation are similar at all locations on the line satisfying $z/2h$<2.2 where h is the edge length of the inlet. Beyond this value of $z/2h$, the random method gives values of y^+ about 17% lower than that of the no turbulence case. The y^+ values from the enhanced vortex particle and artificial generation methods sit in between these two cases. The same trend is shown by the values of the shear stress in the z-direction shown in Figures 5.60 and 5.62. Even though the shear stress curves flat out moving downstream from the inlet (for example at $z/2h$=4 for the no turbulence case), suggesting a fully developed stage has been reached, it must be recalled that the flow is still in transient stage meaning that the

values of the shear stress at any *z/2h* position are still undergoing changes as the residence time increases.

From Figures 5.61 and 5.63, it can be stated that up to four residence time, the flow was in a transient stage since the values of y^+ decreases at the observation points especially in the region *z/2h*>3.0. Another observation from this data leads to the statement that with an aspect ratio of ten, the flow has not reached a fully developed stage.

After about four residence time (*t*=7.5s), there is negligible difference in the values of the shear stress and y^+ with respect to the different methods used. This implies that the random perturbation case gives a more rapid settling down time for y^+ and τ_w. There is a tendency to speculate, from this observation, that the imposed fluctuations at the inlet have some degree of influence on the build up rate of the turbulent boundary layer towards the steady state values or profiles. It is also possible that the adjusting flow immediately behind the inlet plane is unstable due to the sudden introduction of walls.

An assumption made in the calculation of τ_w and u_* is that the value of $\partial w/\partial y$ is at least an order of magnitude larger than $\partial u/\partial y$ on all wall boundaries and hence was not taken into account in the calculation of τ_w. This is a reasonable assumption since the magnitude of the flow in the streamwise direction is a lot stronger than those in the transverse directions and from Figure 5.46, this is in fact very much explicit.

Another aspect of this study which needs to be looked at is the number of floating point operations incurred to generate turbulence at the inlet by the different methods considered. The vortex particle method has an approximate flop count of $130N^2$ per time step where *N* is the number of vortex particles. The artificial turbulence method requires approximately $0.006N^5$ flops per time step where *N* equals that of the vortex particle method if the number of inlet faces are set equal to the number of vortex particles. In this example, the length scale for the presumed correlation function of the artificial turbulence generation case was set to 10% of the inlet edge length. These approximations get better with increasing value of *N*.

Regarding the stability of this case, applying Equation (2.2) gave a limit of 1.5E-5s on Δt but the value of this parameter used in the simulation is about six times larger than this limit with no numerical difficulties encountered. An explanation for this is the increase in effective viscosity due to the contribution from eddy viscosity.

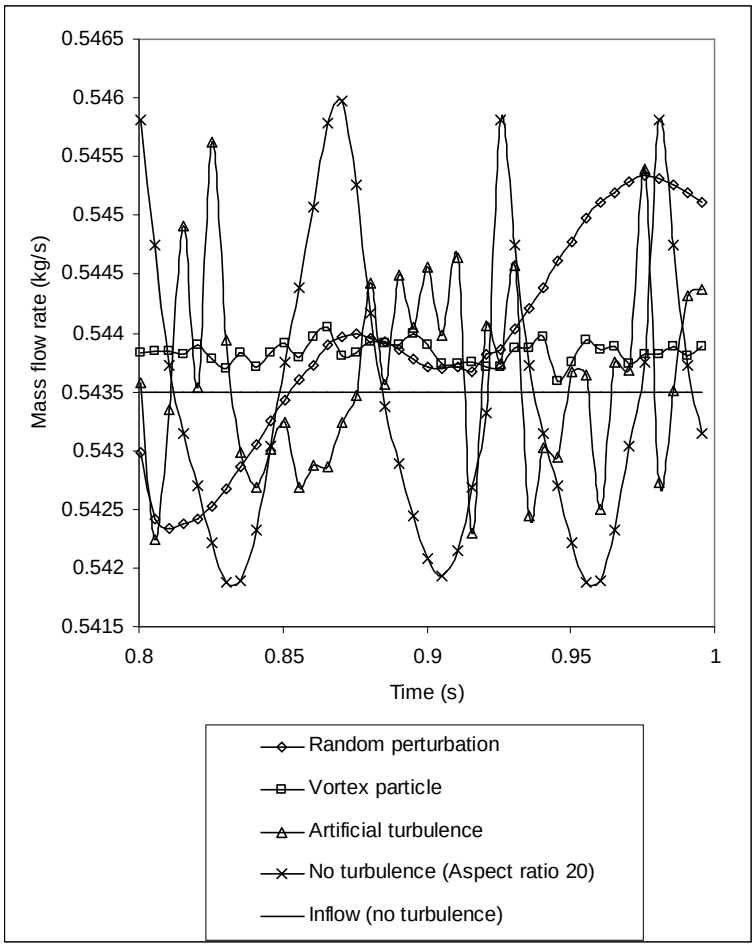

Figure 5.64 Time series of mass flow rate at the outlet.

The time series plot in Figure 5.64 indicates a fluctuating mass flow rate through the outlet for all methods of turbulence generation. The case with no inlet turbulence simulated with the duct with aspect ratio of 20 exhibits fluctuations of comparable frequency to but with a higher amplitude than it is in the method of artificial turbulence. The enhanced method of vortex particle fluctuated at the highest frequency but with the smallest amplitude when compared to other methods while the method of random

perturbation shows a smooth variation of mass flow rate through the outlet with respect to time. The difference in percentage between the mass flow rate in and that going out is 0.061% for the method of random perturbation, 0.075% for the enhanced method of vortex particle, 0.021% for the method of artificial turbulence and 0.000028% for the no inflow turbulence case. In short, the total mass inside the domain is well conserved by the flow solver.

5.3 Closure

This chapter has explored the properties of synthetic turbulence generators at the inlet of a square duct. The main conclusions from the runs are summarised as follows:

- The main features of the flow such as the corner vortices of the secondary flow are reproduced by the simulations.

- The contour plots of the mean velocity $\overline{w}$, root-mean-square velocity w_{rms} and $\overline{w'u'}$ from the duct with aspect ratio set to 20 produced features similar to those obtained from the statistically steady flow reference cases using periodic boundaries.

- The peak region close to the wall is captured by the root-mean-square velocity profile, w_{rms}, and the profile improves with increasing duct aspect ratio and mesh density.

- Differences in the mean and root-mean-square velocity profiles are marginal with respect to the turbulence generation method used after four residence times of a particle inside the domain.

- The artificial turbulence generation method produced the highest levels of $\overline{w'u'}$ resolved shear stress component after four residence time compared to the other methods.

- The two-point correlation data show that the random perturbation method produces very weakly correlated fluctuations while the artificial turbulence method produces fluctuations with the highest degree of correlation.

- The artificial turbulence generation and the hybrid methods generate the highest turbulence kinetic energy levels at the selected monitoring points and this parameter did not deteriorate moving downstream in the flow direction compared to the random perturbation method and the case with no inlet turbulence.

The advantages of the enhanced method of vortex particle and the method of artificial turbulence over the method of random perturbation and the no inflow turbulence case are clear. The next step is to apply one of the better performing methods to a flow of practical interest.

CHAPTER 6

Flow over Obstacles

This chapter describes the application of the method of artificial turbulence that produces turbulent fluctuations at the inlet of a channel with obstacles in the shape of cubes. The practical importance of this geometric configuration is described in the first sub-chapter; the description is followed by the setting-up of the test case aimed for computations. Results such as instantaneous velocity vector fields, turbulence statistics and turbulence kinetic energy spectrum plots are compared to published data. The main conclusions from this simulation are also explained here.

6.1 Introduction

The final application of the LES code was carried out on a geometric configuration consisting of multiple blocks in a channel as shown in Figure 6.1. Hence, the goal of this section is to measure the suitability of using inflow and outflow boundaries that can predict turbulent incompressible flow for this type of geometry. This configuration has a considerable practical importance and it is related to flows such as electronic cooling, atmospheric boundary layer and turbine blade cooling.

An important difference between the flow in a duct studied in the previous chapter and the flow with bluff bodies encountered here is the boundary layer normal pressure (form) drag dominating over the skin friction drag. The presence of bluff bodies result in the transfer of turbulence kinetic energy from the mean flow to the energy-bearing eddies with sizes comparable to that of the bluff bodies. From a numerical point of view, this is

a desirable effect as far as the computation cost is concerned, since the cell size required to resolve these eddies are not as demanding as the duct flow case. In other words, this is a suitable case to be simulated using the technique of large eddy simulation for the reason that the production of turbulence kinetic energy is predominantly caused by bluff bodies obstructing the flow.

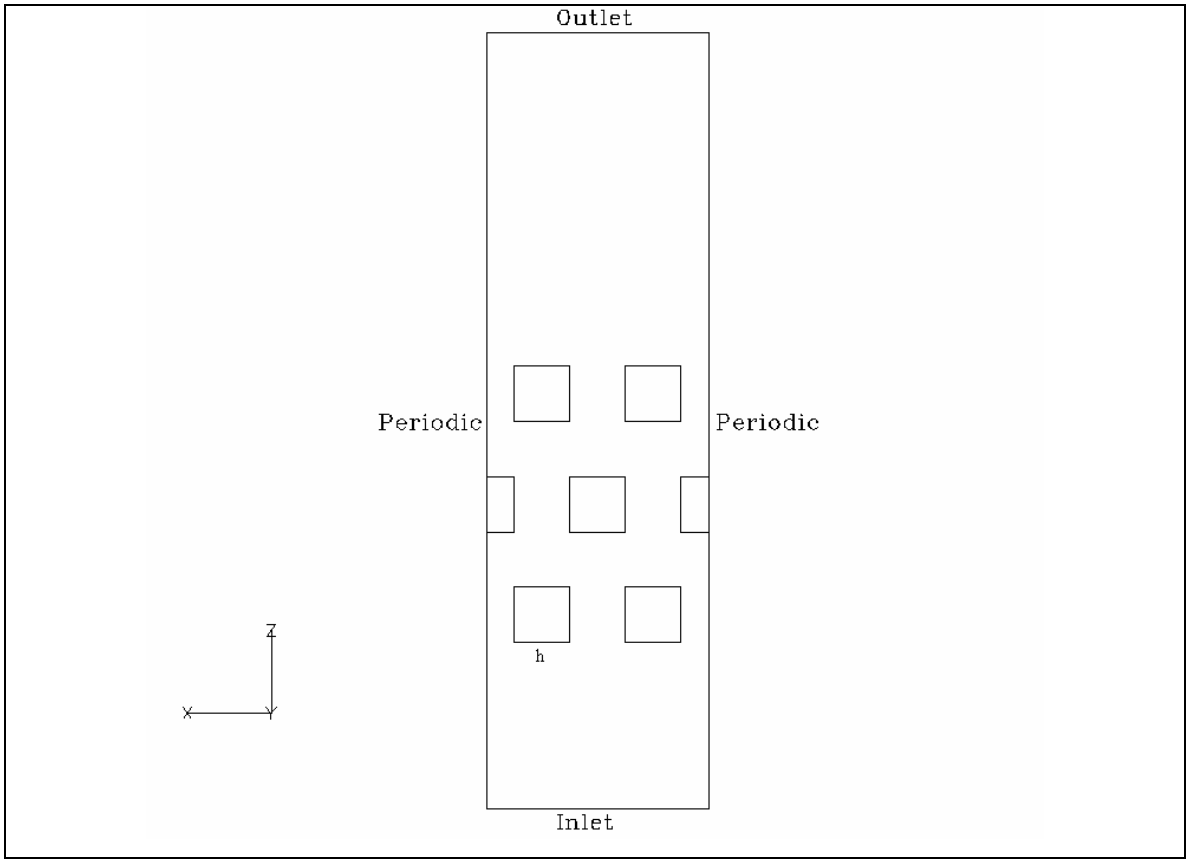

Figure 6.1 Plan view of the channel with obstructions.

6.2 Case setup

Inside this channel with an aspect ratio of ten, five full blocks and two half blocks were positioned in the region $z>3h$ and $z<9h$ where h is the edge length of a block. The computational domain is 0.08m in width and height. This corresponds to the x and y-directions shown in Figure 6.1 where the channel is viewed in the negative y-direction. The streamwise length is set to 0.28m. The fluid has a constant dynamic viscosity of 0.001Ns/m^2 and a constant density of $1{,}000\text{kg/m}^3$. The Reynolds number based on the

obstacle height and average inlet velocity is 4,200. The inlet edge length is $4h$ and the length of the channel in the streamwise direction is $14h$. In this figure, the inlet, outlet and periodic boundaries are marked clearly; other boundaries are designated as no-slip walls.

The first mesh used contained about 900,000 cells. A finer grid with about 1.9 million cells was used as the second mesh to estimate the discretisation error in the first mesh. Meshing was carried out with a purpose built program to handle this specific geometry. For the test case, partitioning of the mesh was carried out based on an in-house program without METIS, unlike previous cases. The reason for this is the lengthy period taken by METIS to execute the partitioning (more than 30 minutes of wall clock time on the front end servers). The time step size was set to a value of 0.0001s. The reason for using this figure as the time step size of all the simulations in this chapter was to counter or at least minimise the false diffusion due to discretisation error from using large time steps. Results from partitioning of the first grid are shown in Figures 6.2 to 6.4.

Similar to the previous test case, residence time is defined as the period of time a particle resides in the computational domain based on the value of the mean inlet velocity. With the time step size chosen for this flow, one residence time is equal to 1.29s.

The governing equations for the resolved velocity components, modified pressure and eddy viscosity are given in Chapter 3. The second order in time Adams-Bashforth Crank-Nicolson flow solver was summoned again to perform the time integration steps. The Restarted Generalised Minimum Residual routine of PIM by da Cunha and Hopkins (1994) was used with the maximum number of iteration steps set to fifty and the cut-off 2-norm of the residual value was set to 1.E-10.

An important difference from previous simulations with regards to the numerical scheme was the use of hybrid differencing scheme as opposed to a central scheme. The reason for this is the relatively coarse mesh used coupled with the oscillatory behaviour of the

central differencing scheme which violates the constraint imposed by the Peclet number associated with the filtered Navier-Stokes equations.

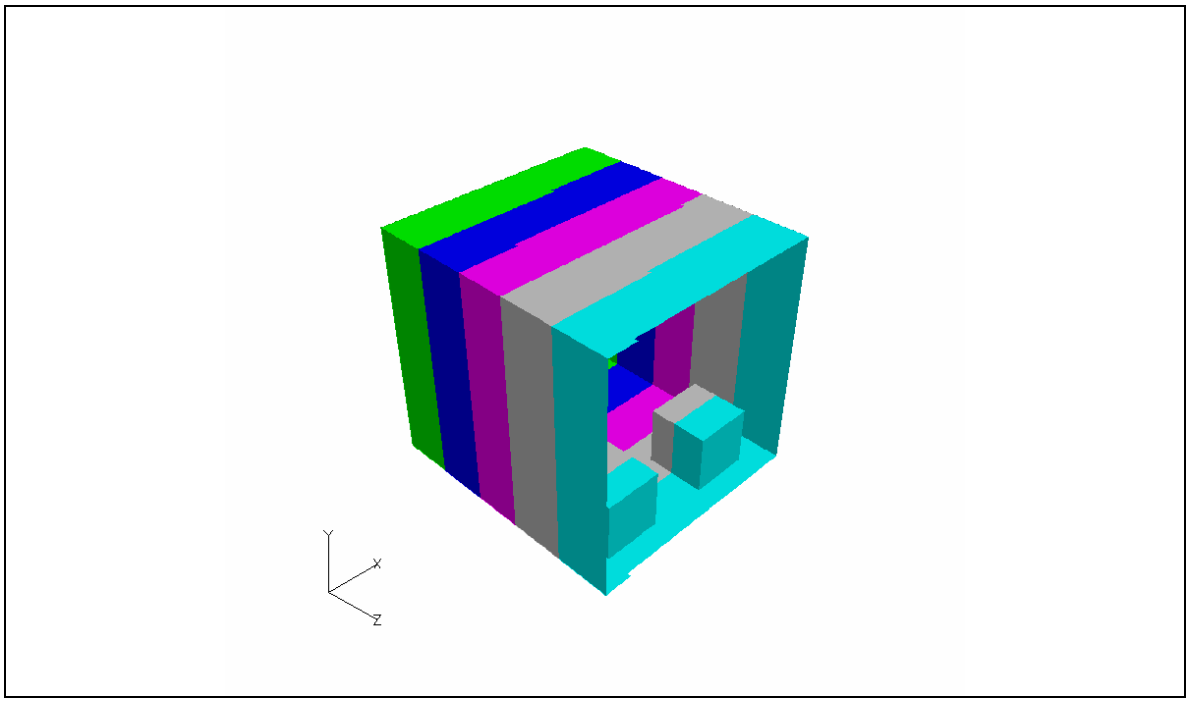

Figure 6.2 First five subdomains from partitioning of the mesh for the channel geometry.

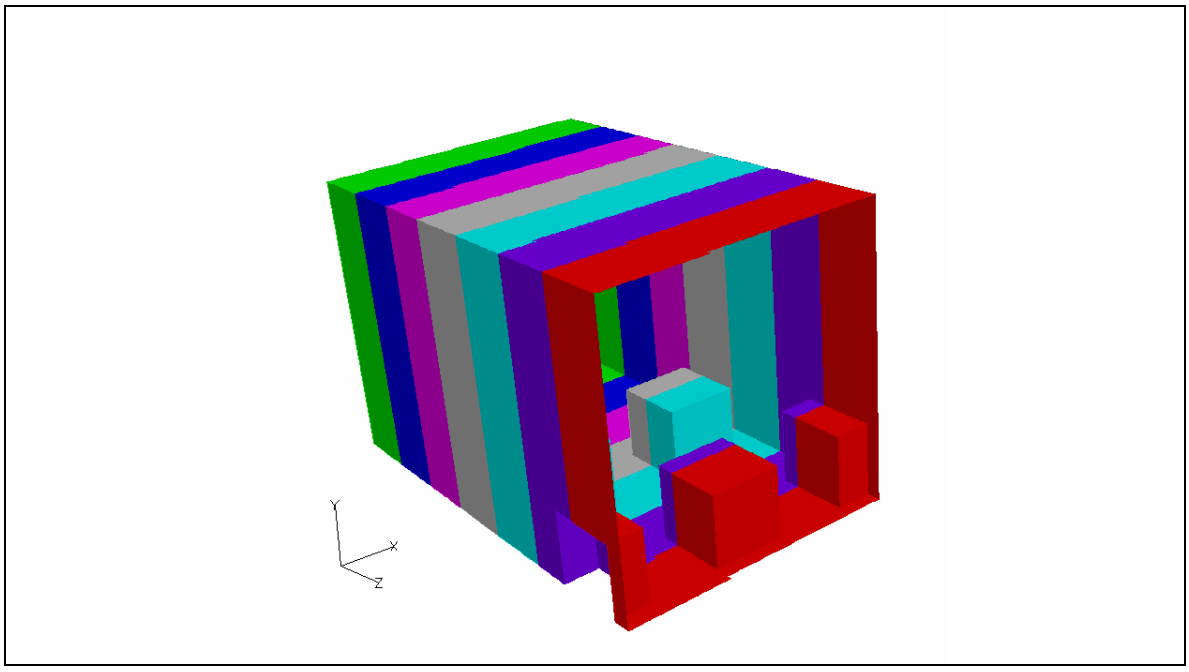

Figure 6.3 First seven subdomains from partitioning of the mesh for the channel geometry.

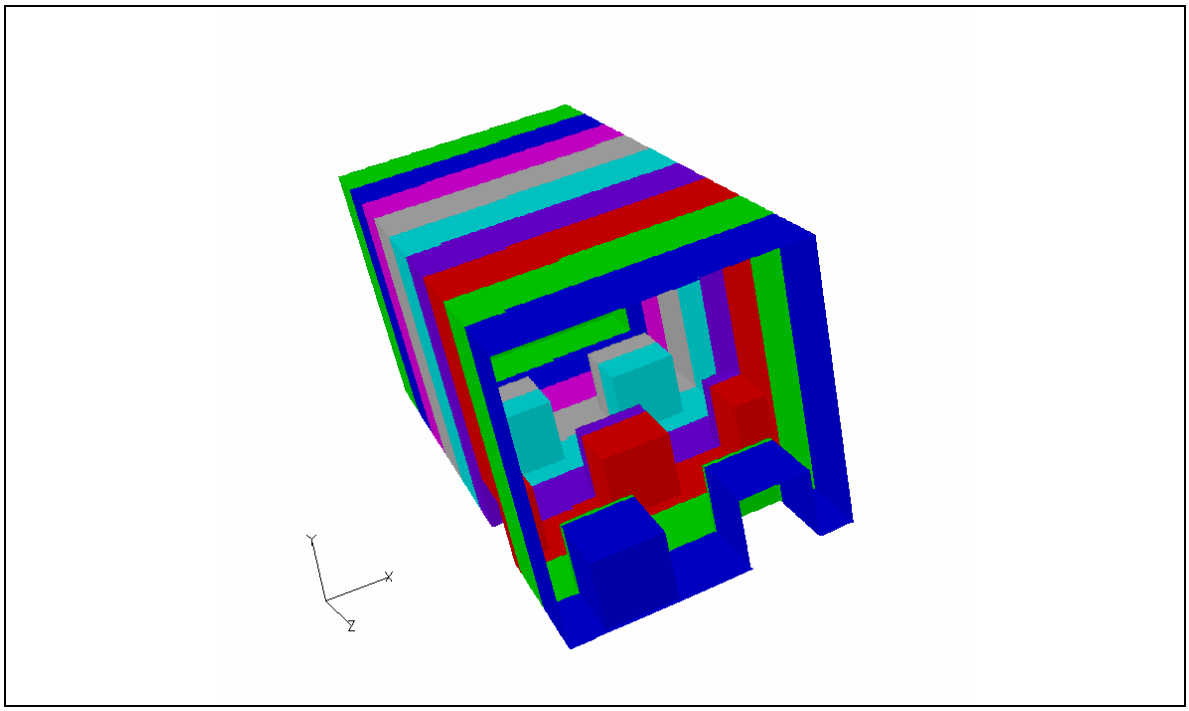

Figure 6.4 First nine subdomains from partitioning of the mesh for the channel geometry.

As mentioned in Chapter 5, in order to utilise LES in complex geometries and developing flows, it is imperative that the inlet and outlet boundaries be used. Current studies such as those by Xie and Castro (2006) utilised periodic boundaries. The numerical implementation of the outlet and no-slip wall boundaries is exactly the same as in the previous chapter. The reason for not using the wall function to compute the stresses at the wall is that the boundary layer will most likely not adhere to that of a smooth wall due to the presence of recirculating regions behind the cubes. At the inlet, the profile of the mean streamwise velocity component along the outlet centreline of the square duct case parallel to the *y*-direction was imposed on this boundary, and based on the results from the chapter, the method of artificial turbulence was again applied in this instance. The outlet is located at a larger distance from the nearest wall of the obstacles than the inlet in order to avoid the recirculating region of the flow behind the obstacle to intersect with the outlet boundaries, causing numerical difficulties. A desirable feature of the code with regards to the flow resulting from this type of geometry is the ability to handle local mesh refinement so that the regions surrounding the obstacles and adjacent to the walls can have a higher mesh density to capture the complicated flow physics.

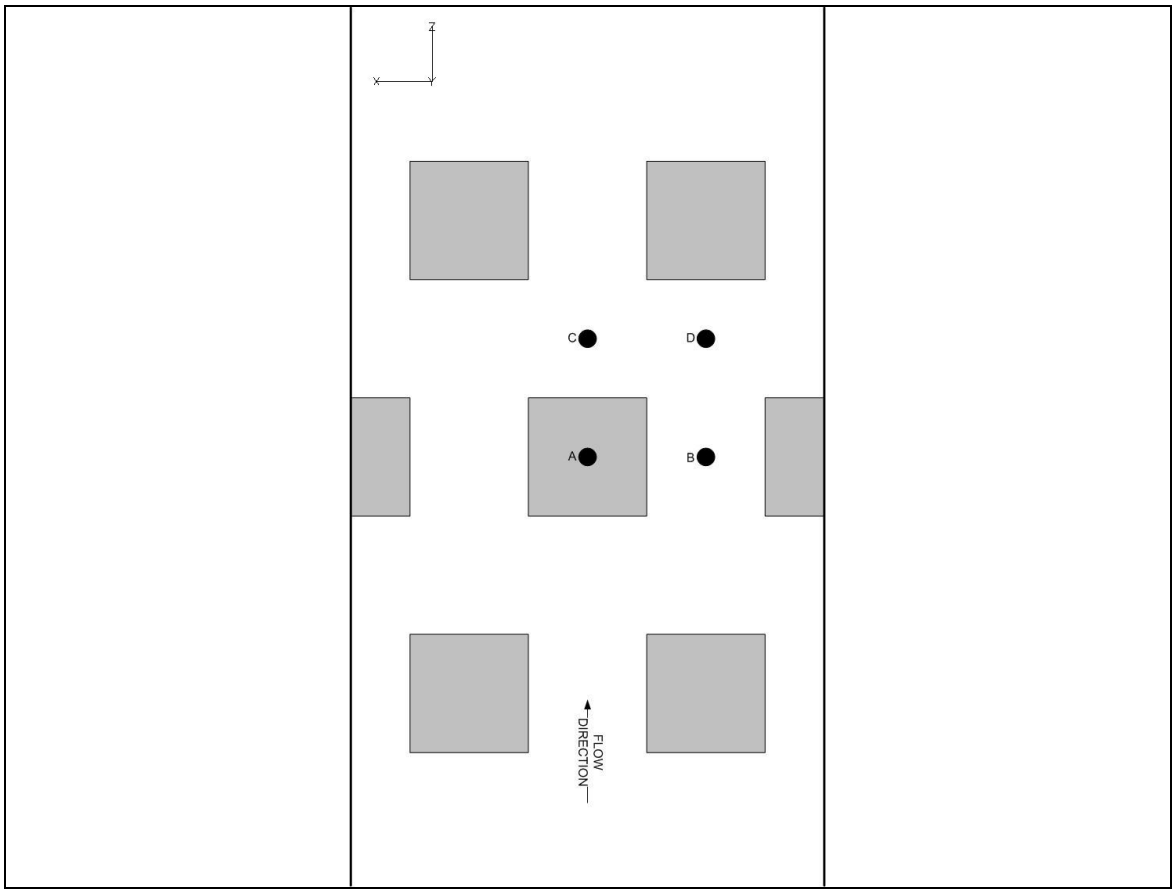

Figure 6.5 Monitoring locations for the post-processing of data.

The outer faces normal to the positive and negative *x*-directions are designated as periodic boundaries following Xie and Castro (2006). The values of velocity components on these boundaries take the corresponding values at the cell centres from the opposite side of the domain. Here, both the normal and shear stresses are computed while the value of modified pressure is extrapolated from the nearest two cell centre values as described in Chapter 3. If the periodic boundaries are perpendicular to the streamwise direction, a driving pressure gradient term should be included in the conservation momentum equations but since this is not the case here, no such term was introduced.

The Courant, diffusion and Peclet numbers based on a time step size of 0.0001s and an average bulk inlet velocity of 0.217m/s for both the coarse and fine grids are shown in Table 6.1. The number of time steps per flow through time based on these figures is 13,333.

	Coarse mesh	Fine mesh
Cell edge length (m)	6.25E-4	5.00E-4
Courant number *c*	3.47E-2	4.34E-2
Diffusion number *d*	2.56E-4	4.00E-4
Peclet number	136	108

Table 6.1 Stability related parameters for the case of flow with obstructions.

Details of the LES simulations performed by Xie and Castro (2006) are as follows. The bulk Reynolds number based on obstacle height and maximum mean velocity was 5,000. Perpendicular to the *x*-direction (Figure 6.1), boundaries were set to periodic. Periodic boundaries were also used in the streamwise direction together with a constant positive pressure gradient of -1.59 Pa/m as the driving force was imposed on every cell. The ceiling of the domain was set to symmetry boundaries while the floor was a no slip wall. The turbulence model used was the Smagorinsky model with the value of Smagorinsky constant set to 0.1. The mesh consisted of 0.75 million uniform orthogonal hexahedral cells with three layers of refinement. The log-law of the wall was used when $y^+>11.2$, otherwise integration to the wall was performed. The kinematic viscosity and fluid density were set to 1.5E-5m^2/s and 1.205kg/m^3 respectively. A second-order accurate central scheme in space was used while the temporal scheme was of the second-order backward implicit type. Data from Xie and Castro (2006) are used to validate results from this simulation. Related to this work, Afgan et al. (2007) studied the flow around a wall mounted cantilever cylinder mounted on a flat plate and they showed that at the root of the cylinder, irregular and intermittent vortex shedding occurs.

Initially, all the field variables inside the domain were set to zero to avoid numerical difficulties. Programs for this case were submitted as batch jobs to the Sun Fire 15K server running on sixteen processors. Post processing was carried out by plotting the instantaneous velocity vector fields, turbulence kinetic energy distributions and the $\overline{w'v'}$ stress distributions. Four monitoring lines were used to compare these parameters with

data from the large eddy simulation of Xie and Castro (2006). These lines are normal to the *xz*-plane and are marked A, B, C and D in Figure 7.5. Line A is located at x=0.04m and z=0.11m and Line B is 0.02m to the right of and parallel to Line A, facing the negative y-direction. Line C and Line D are 0.02m downstream of Line A and Line B respectively. The turbulence kinetic energy spectrum was also observed and the monitoring point is located on Line C 0.01m above the no-slip floor.

6.3 Results and Discussion

The instantaneous velocity vector fields for the case with periodic boundaries using the mesh with 900,000 cells after one thousand time steps are shown in Figures 6.6 to 6.11. The separation zone next to the top wall of the central cube can clearly be seen in Figure 6.6 as well as the reattachment region close to the leeward edge of the top wall. These features were also produced by the large eddy simulation of Xie and Castro (2006). Adjacent to the upper region of the leeward facing wall, a recirculation zone is present. Similar flow structures were shown by the plot in Figure 6.7 but moving closer to the periodic boundaries, these structures vanish.

The simulation with periodic boundaries did not proceed as smoothly as it was expected. After about 1000 time steps the magnitude of the residual started to grow and the time integration became unstable. To overcome this problem the periodic boundaries were switched to symmetrical ones with the intention to switch back to periodic boundaries once the flow was close to a statistically steady condition.

Figures 6.12 and 6.13 show the velocity vector fields on two planes perpendicular to the *x*-direction, after seven thousand time steps. Each velocity vector field is starting to show the existence of recirculating region behind the central cube. The separation and reattachment regions on the top wall of the central cube are also visible. The highly irregular flow structure next to the side wall of the central cube can also be seen. The wake region behind the central cube is not visible. But downstream of the two side walls in Figure 6.13, the recirculating regions of fluid flow can clearly be observed, and bear some similarity to the case with periodic boundaries.

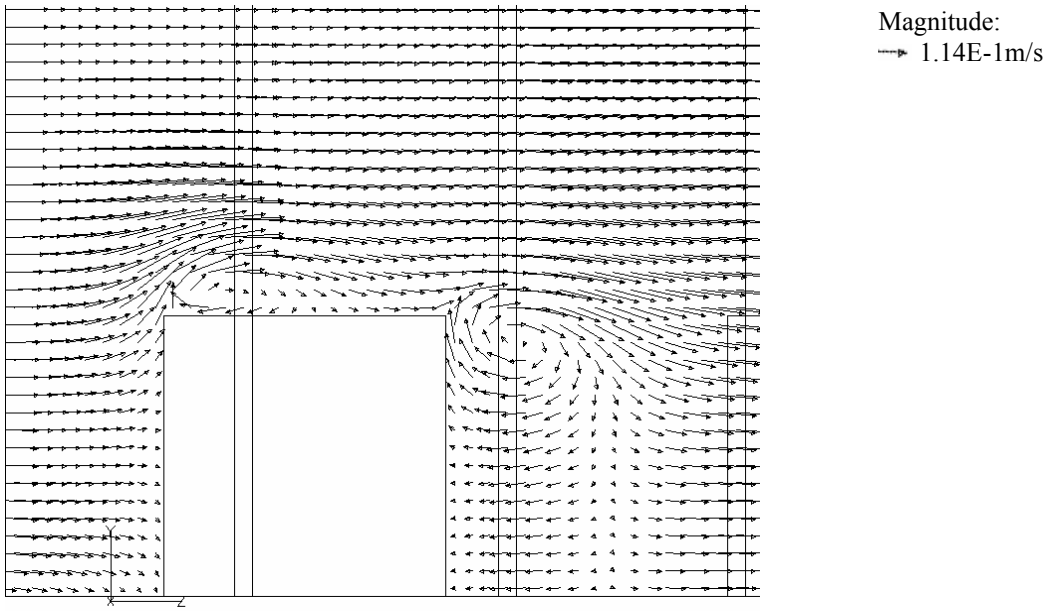

Figure 6.6 Instantaneous velocity vector field on the *yz*-plane at *x/h*=2 in the central cube region after 0.0775 residence time or 1000 time steps with periodic boundaries.

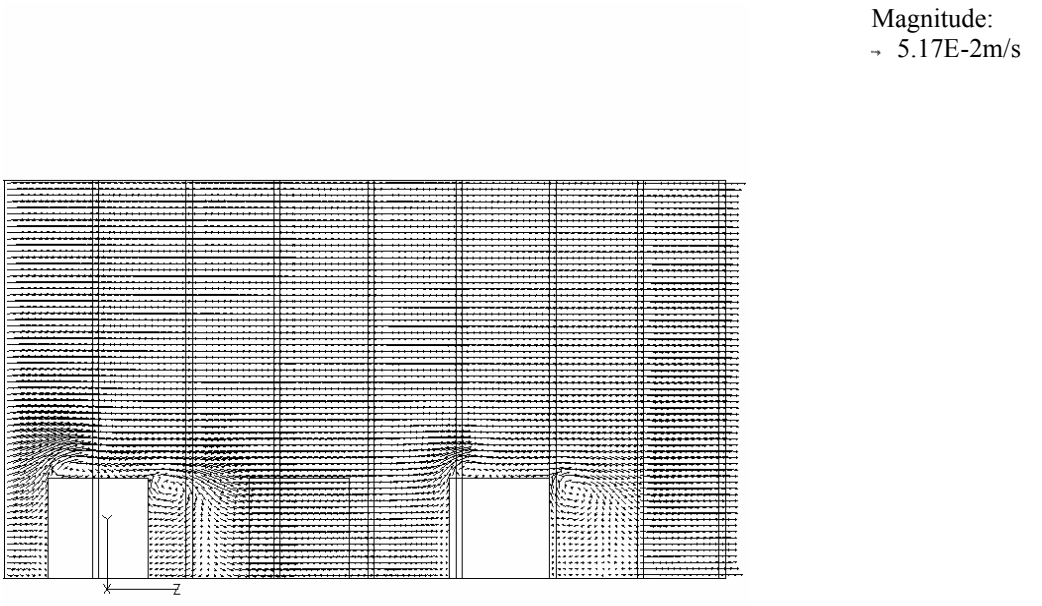

Figure 6.7 Instantaneous velocity vector field on the *yz*-plane at *x/h*=1 after 0.0775 residence time with periodic boundaries.

For the case with periodic boundaries, the *xz*-plane at *y*/*h*=0.5 above the floor shown in Figure 6.8 for all blocks and Figure 6.9 for the central block indicates the presence of a pair of counter-rotating swirling flow facing the downstream wall which forms the foundation of an arch vortex. While on the side walls, a separated region took place near the upstream edge of the face followed by a reattachment region downstream. The stagnation point and the reverse flow region next to the upstream wall were not captured in this computation possibly due to the flow not reaching a condition of steady-state yet. The stagnation point is expected to be located at approximately one obstacle edge length upstream of the windward face of the obstacle next to the lower wall based on the data from Xie and Castro (2006).

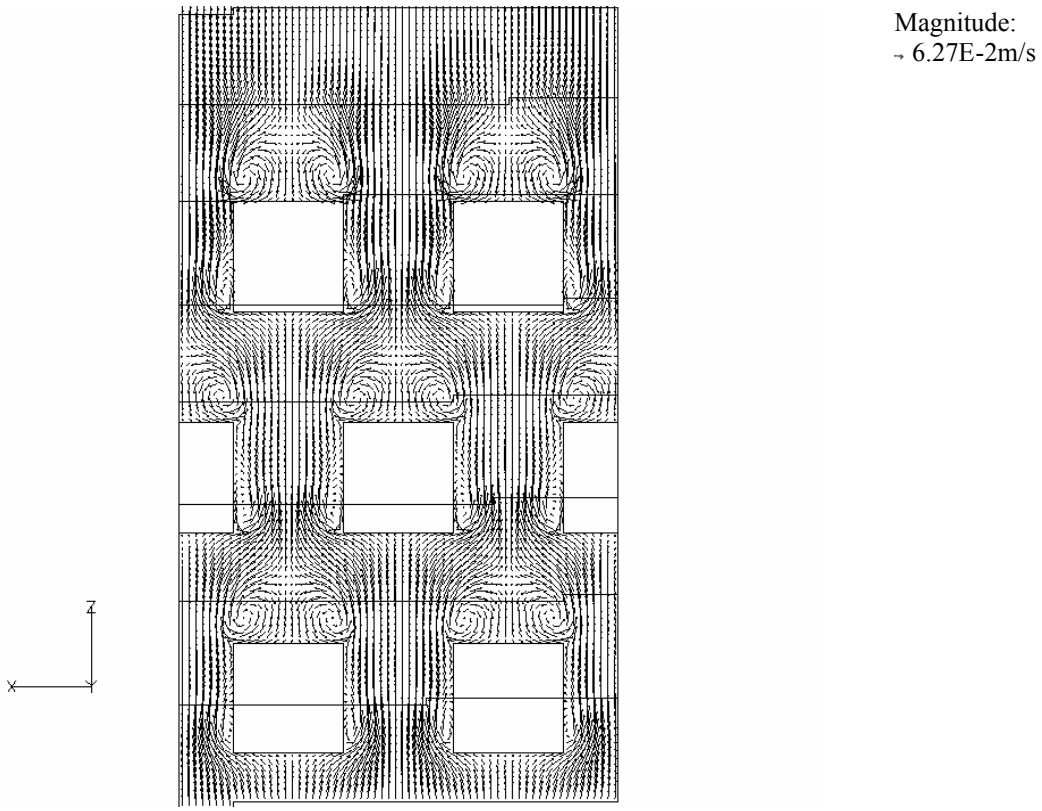

Figure 6.8 Instantaneous velocity vector field on the *xz*-plane at *y*/*h*=0.5 after 0.0775 residence time with periodic boundaries.

The flow pattern generated by the case with symmetry boundaries contains the same features described for the periodic boundary case but flows can be seen to be deflected

away from the walls next to the windward face and also the downstream half of the side walls as shown in Figures 6.14 and 6.15. The absence of the horseshoe vortex structure, near the edge where the block meets the floor, in Figures 6.10 and 6.11, for the periodic case, after one thousand time steps, implies that the flow is still in a development stage with respect to time. The corresponding velocity vector field plots for the symmetry case in Figure 6.16 shows a pair of vortices next to the side walls. These vortices which are still in a transient stage, might be connected to the horseshoe vortex formed when the flow has reached a statistically steady stage. The simulations could be repeated if local mesh refinement is possible so that the boundary layer could be properly resolved, based on y^+ data of current simulations (which was not monitored due to limited resources).

The contour plot of turbulence kinetic energy k displayed in Figure 6.17 shows that there is a region of relatively high turbulence kinetic energy next to the upper streamwise edges of the central cube, which coincides with regions of high velocity gradients in Figure 6.16.

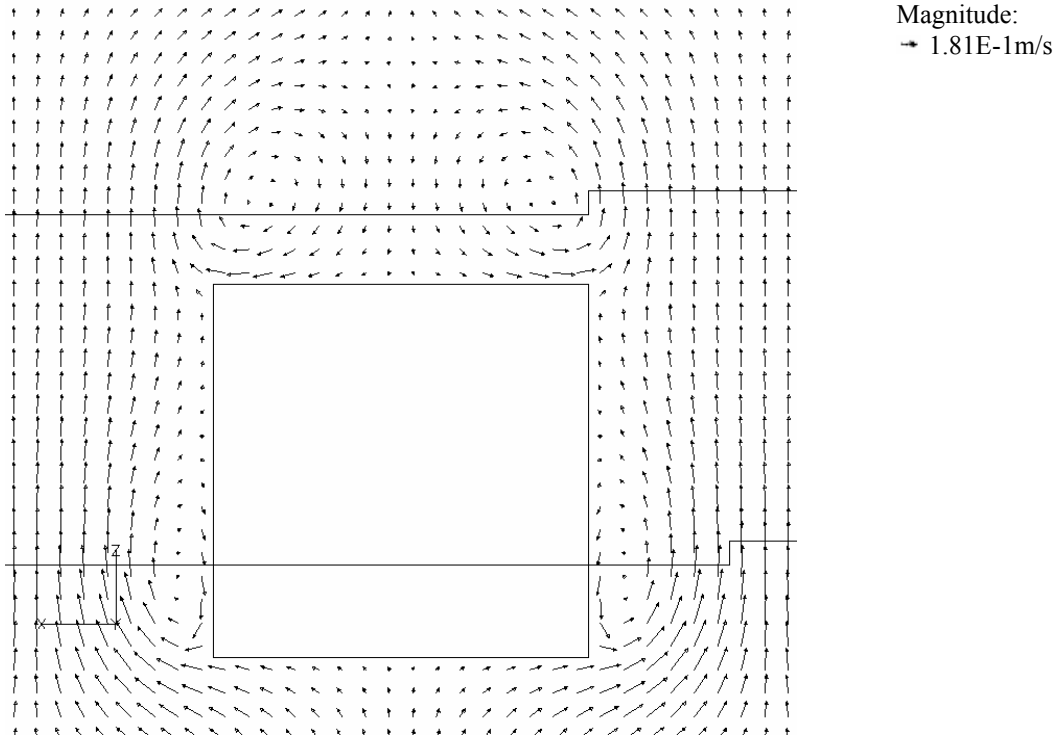

Figure 6.9 Instantaneous velocity vector field on the *xz*-plane at *y/h*=0.5 in the central cube region after 0.0775 residence time (1000 time steps) with periodic boundaries.

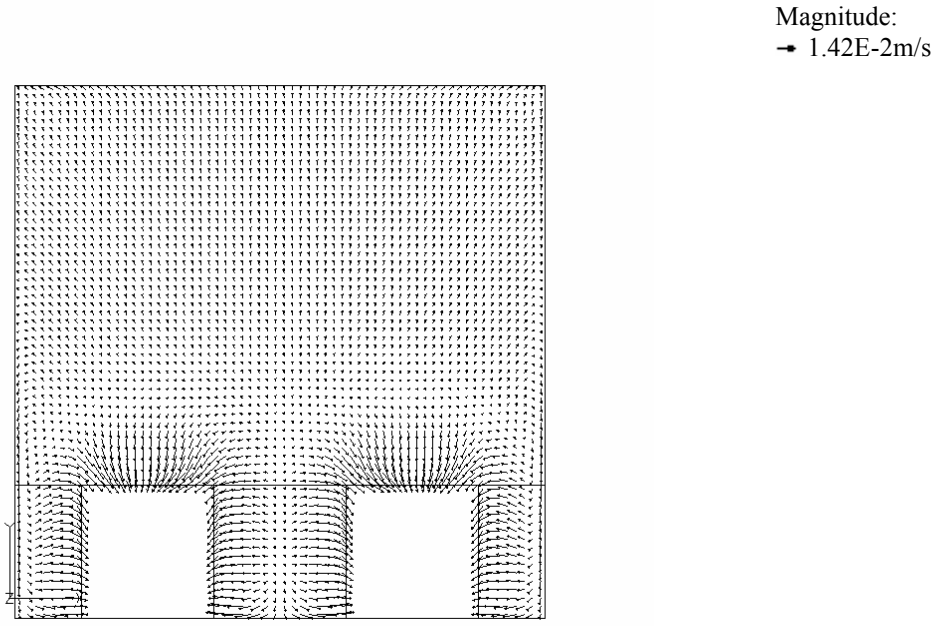

Figure 6.10 Instantaneous velocity vector field on the *xy*-plane at *z*/*h*=8 after 0.0775 residence time with periodic boundaries.

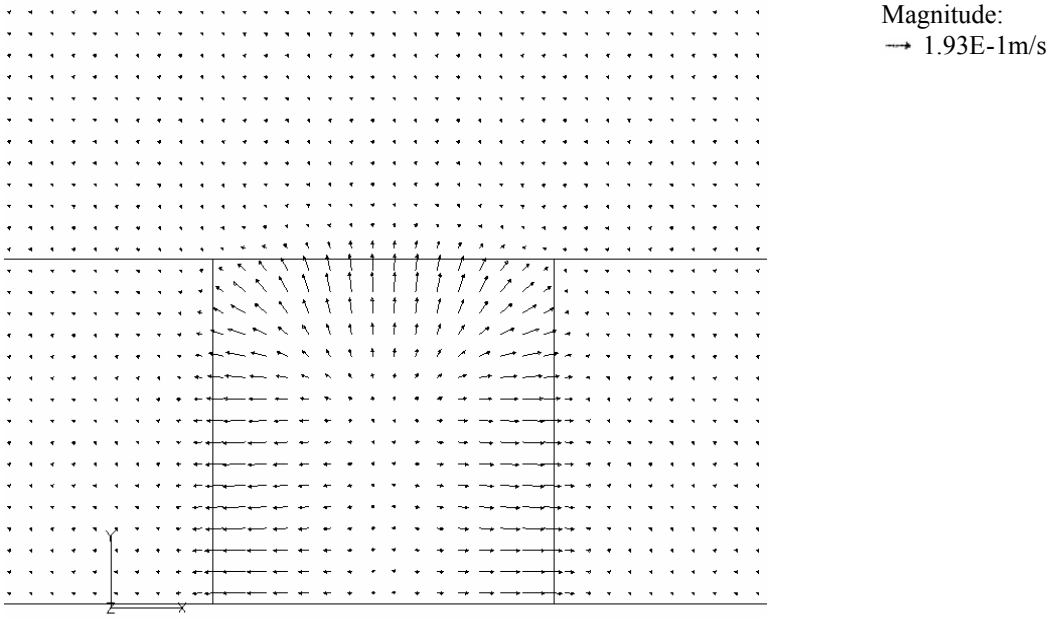

Figure 6.11 Instantaneous velocity vector field on the *xy*-plane at *z*/*h*=6 immediately behind the central cube region after 0.0775 residence time with periodic boundaries.

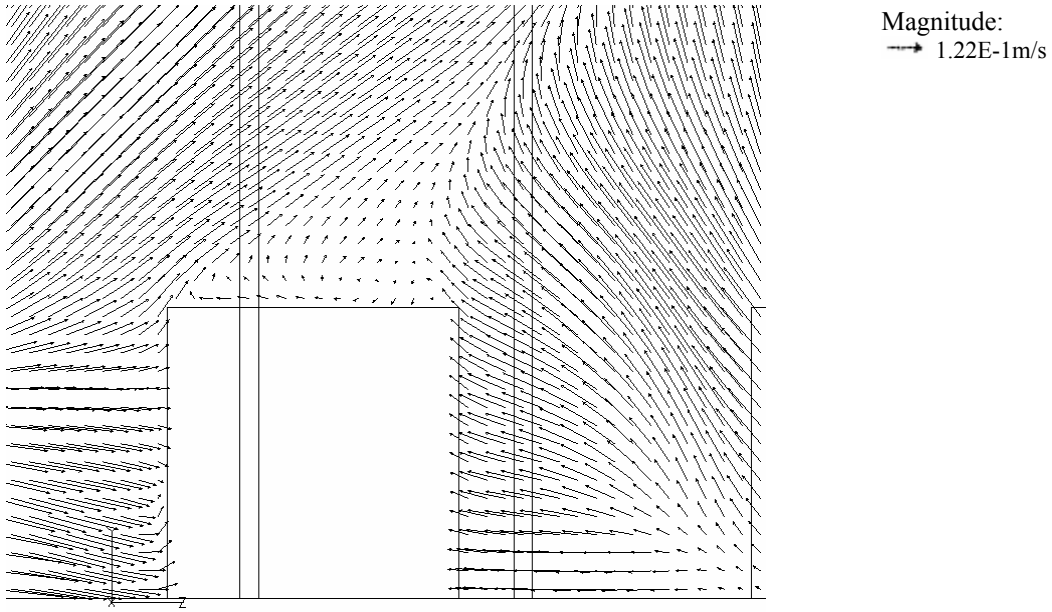

Figure 6.12 Instantaneous velocity vector field on the *yz*-plane at *x/h*=2 in the central cube region after 0.543 residence time or 7000 time steps with symmetric boundaries.

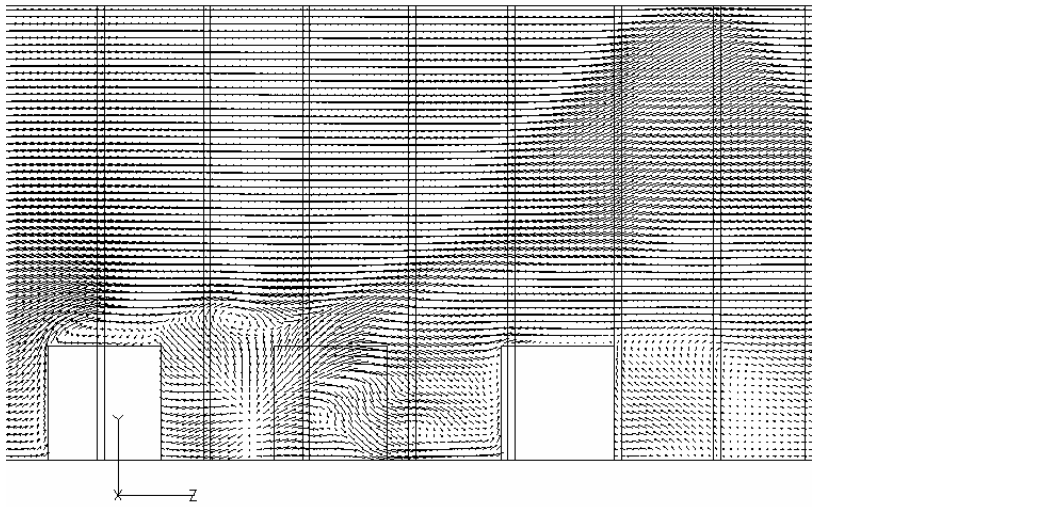

Figure 6.13 Instantaneous velocity vector field on the *yz*-plane at *x/h*=1 after 0.543 residence time with symmetric boundaries.

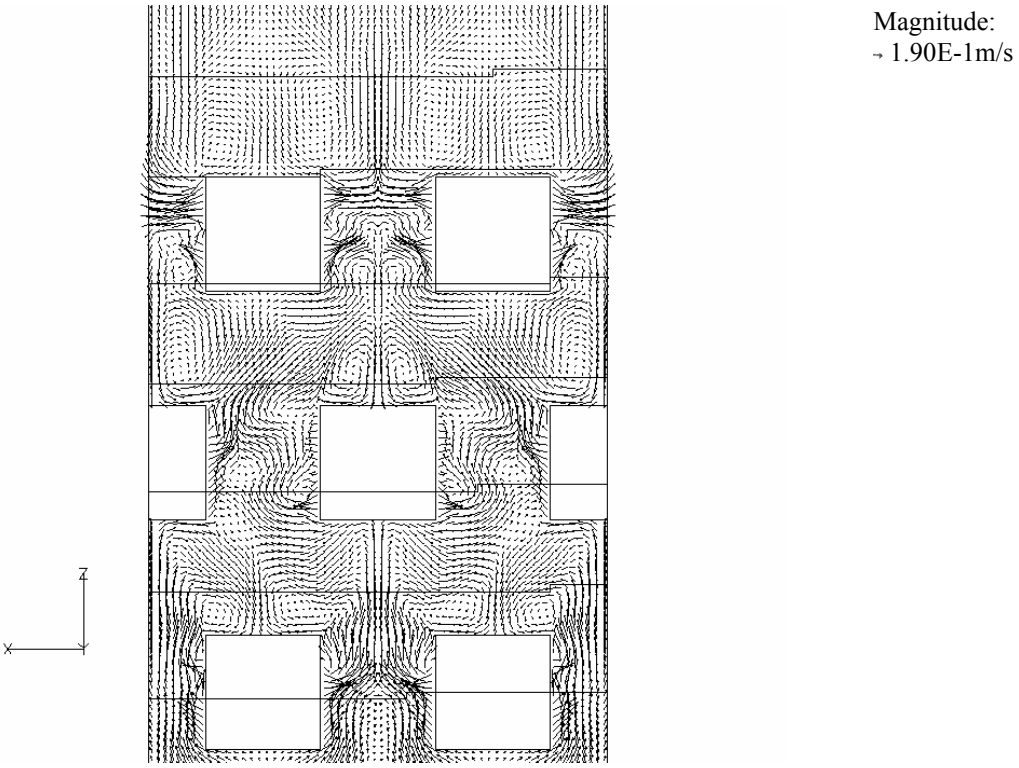

Figure 6.14 Instantaneous velocity vector field on the *xz*-plane at *y/h*=0.5 after 0.543 residence time with symmetric boundaries.

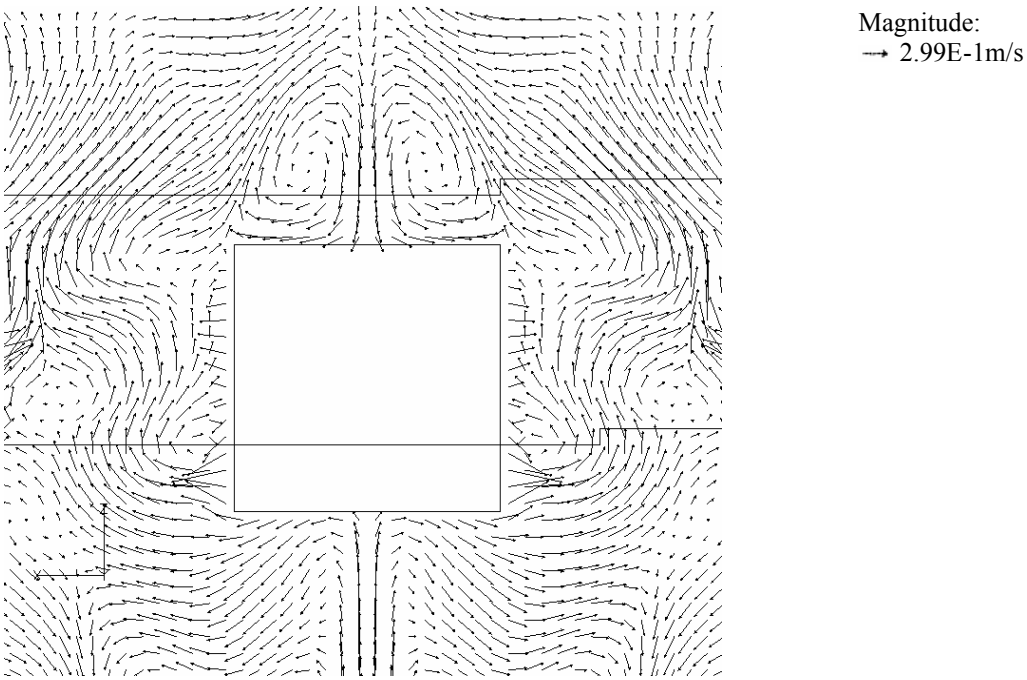

Figure 6.15 Instantaneous velocity vector field on the *xz*-plane at *y/h*=0.5 in the central cube region after 0.543 residence time with symmetric boundaries.

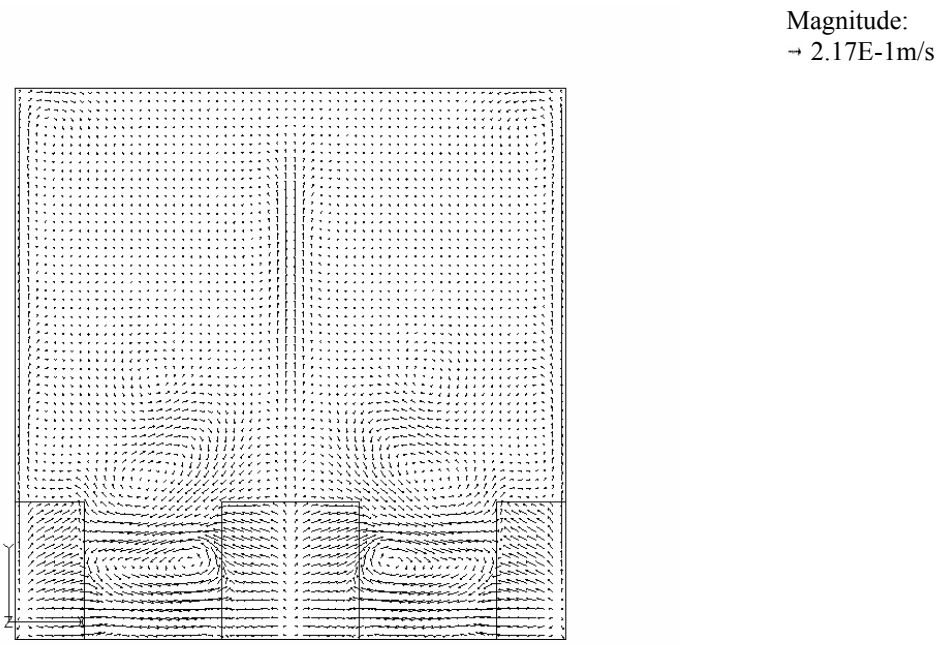

Figure 6.16 Instantaneous velocity vector field on the *xy*-plane at *z*/*h*=6 immediately behind the central cube after 0.543 residence time with symmetric boundaries.

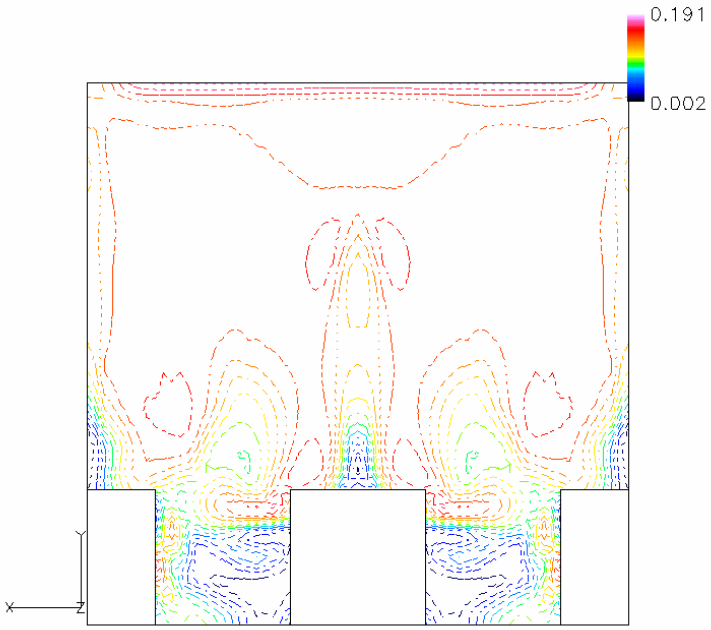

Figure 6.17 Contour plot of turbulence kinetic energy per unit mass (m^2/s^2) on the *yx*-plane at *z*/*h*=5.5 after 0.543 residence time with symmetric boundaries.

The mean velocity profiles and the root-mean-square velocity profiles in the *z*-direction along the monitoring lines shown in Figure 6.5 are normalised by the global friction velocity w_* which was set to $0.89u_\tau$ following Xie and Castro (2006), to take into account the effect of a driving pressure gradient acting on a rough-wall boundary layer. To obtain the global friction velocity from the computations, the friction velocity of a regular boundary layer, u_τ, was obtained form a laminar stress-strain relationship, averaging the wall shear stress values next to the lower wall (in the streamwise direction) on Line A to Line D in Figure 6.5. The $\overline{w'v'}$ stress profiles were normalised by the square of w_*. The profiles in Figures 6.18 to 6.29 are from computations that use a similar time step size which was set equal to 0.0001s.

Data from computations are compared to those obtained by Xie and Castro (2006) from their LES simulation but in their case, a symmetry boundary was imposed on the ceiling of the domain whereas in the computation, the no-slip wall boundary condition was applied. The presence of shear stress on the upper wall may have an influence on the flow in the canopy region but this demands a separate study to quantify the degree of influence.

Comparison of the mean velocity profiles for the case with symmetry boundaries in Figures 6.18 to 6.21 show that results from computations do not follow that of Xie and Castro (2006). This is because the profiles of the velocity component into the domain as well as the value of the bulk inlet velocity are considerably different from the reference case of Xie and Castro (2006) due to the use of periodic boundaries in the streamwise direction in the given reference as opposed to an inlet boundary in the computations. The flow can also be categorised as in an early transient stage due to the presence of very sharp changes in the profile close to the walls. Figure 6.20 gives a comparable value of the mean velocity $\overline{w}$ between the symmetric case and the reference data. The profile of the former is shifted roughly by about seven units in the negative direction of the *x*-axis. The periodic case also indicates the presence of the wake region behind the central cube by the slight depression in the profile. Profiles of $\overline{w}$ on Lines A, B and D hardly show

any reduction towards zero moving in the lower wall direction.

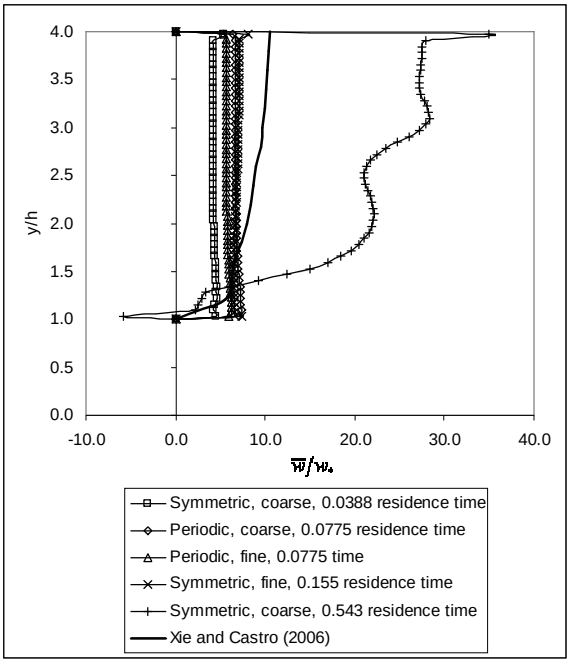

Figure 6.18 Mean profiles of the resolved velocity component in the streamwise direction on Line A.

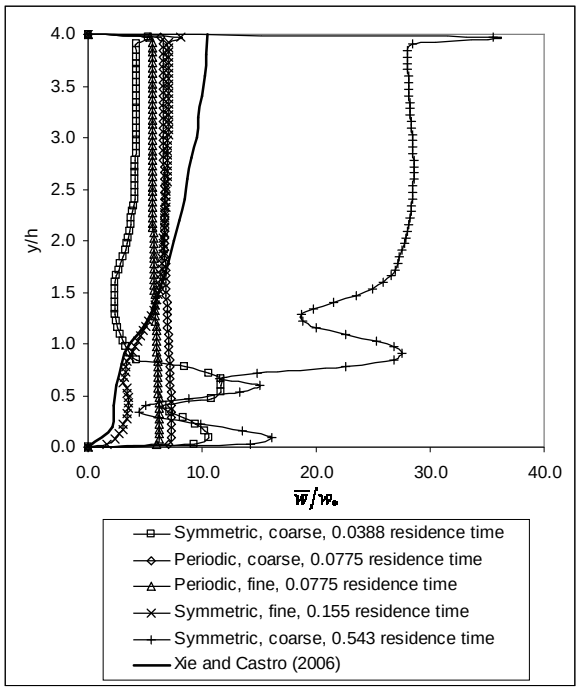

Figure 6.19 Mean profiles of the resolved velocity component in the streamwise direction on Line B.

The root-mean-square profile on Line B (Figure 6.23) for the symmetric case shows a very sharp peak occurring at $y/h \approx 0.5$ which corresponds to the recirculating region of the flow behind the cube.

The peak at $y/h \approx 1.25$ on Line B (Figure 6.24) is in close agreement with the reference data while the profile on Line D gave the best or closest approximation to the reference data compared to the corresponding profiles on Line B and Line C. No reference data was available for Line A. The root-mean-square values from the periodic case in Figures 6.24 and 6.25 show very uniform values of w_{rms} except for the depression which seems to follow the wake region behind the cube.

The computed $\overline{w'v'}$ stress profiles in Figure 6.26 gave a good approximation to the reference data though the peak value is underestimated by about 55% for the symmetric case. The case with periodic boundaries in Figures 6.27 and 6.28 have the peaks coincide with that of the reference data though these are underestimated by approximately 40% on Line C. The reasons for this discrepancy are the nascent stage of the transient flow combined with discretisation error from the differencing scheme. Behind the cube, the magnitudes of the $\overline{w'v'}$ profiles from the case with symmetry boundaries are at least an order of magnitude higher than the values of the reference data suggesting that large fluctuations in the resolved velocity occur in the early stage of the simulation with the symmetry boundary.

The mean velocity profile for the case with periodic boundaries and fine mesh after 1,000 time steps are very similar to the profile of the case with symmetry boundaries at 500 time steps as can be seen in Figure 6.22. The plot in Figure 6.24 shows that the periodic case with the fine mesh gave a better approximation to the mean and root-mean-square profiles compared to the coarse mesh case most probably due to the more accurate values of friction velocity predicted by the former. In Figure 6.25, the fine mesh periodic case has the same mean profile as the coarse one after 1000 time steps, but with values larger by approximately 30% on Line D. Figure 6.23 shows that the fine mesh with the periodic

boundary on Line B gave a better approximation to the root-mean-square profile compared to the coarse mesh case but features such as peaks and trough on the profile are absent.

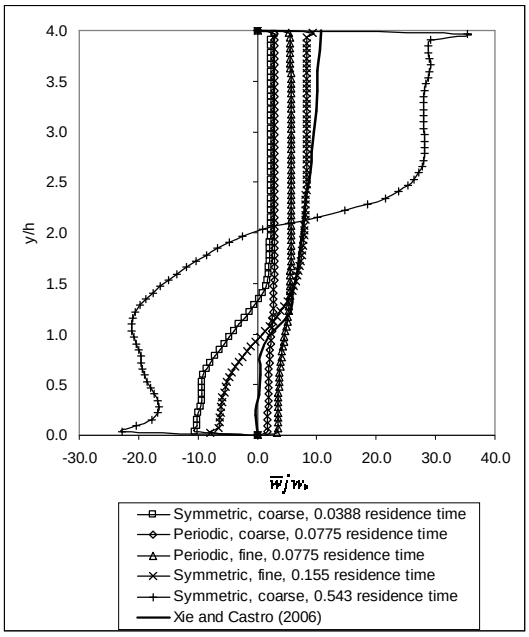

Figure 6.20 Mean profiles of the resolved velocity component in the streamwise direction on Line C.

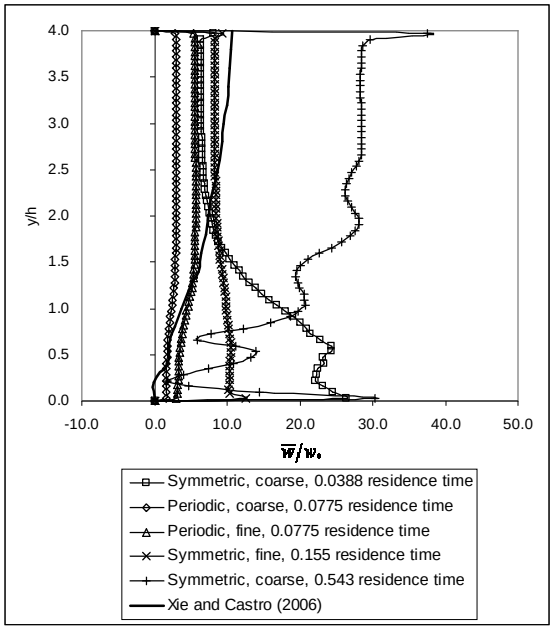

Figure 6.21 Mean profiles of the resolved velocity component in the streamwise direction on Line D.

After 7000 time steps, the mean profiles of the symmetric case followed the trends given by the reference data. However, the values are overpredicted by a factor of approximately three. An instance is given by Figure 6.21 where the values can be seen to decrease in a similar manner to the reference profile. At the same moment in time, the computed root-mean-square profiles produced values that are lower than those by Xie and Castro (2006) but the peaks corresponding to the cube height and close to the floor of the channel are present. As an example, in Figure 6.23, these peaks are located at about y/h=1.4 and y/h=0.4. It may be possible to get a better result for the root-mean-square profiles by tuning the value of the Smagorinsky constant C_s and running the simulation further, so that the flow is closer to the steady-state condition. The $\overline{w'v'}$ profiles show a highly erratic behaviour moving along the monitoring line, most probably, due to the transient nature of the flow.

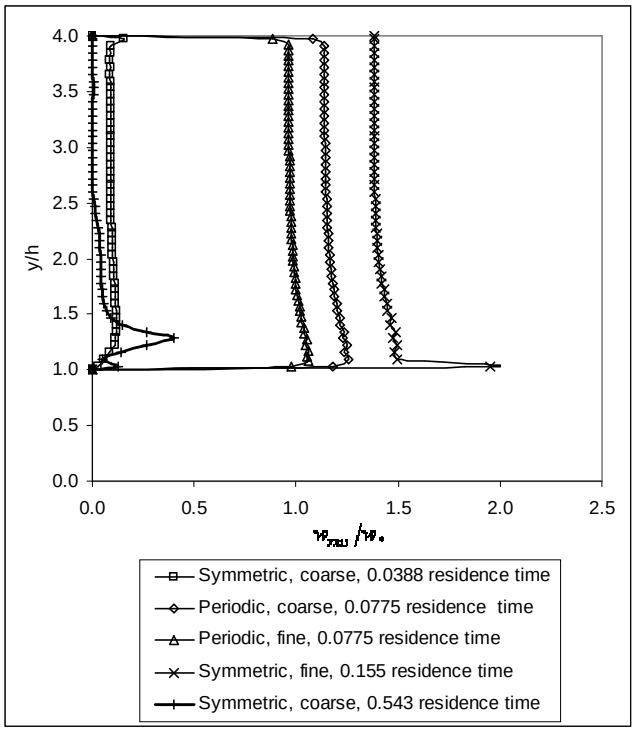

Figure 6.22 Root-mean-square profiles of the resolved velocity component in the streamwise direction on Line A.

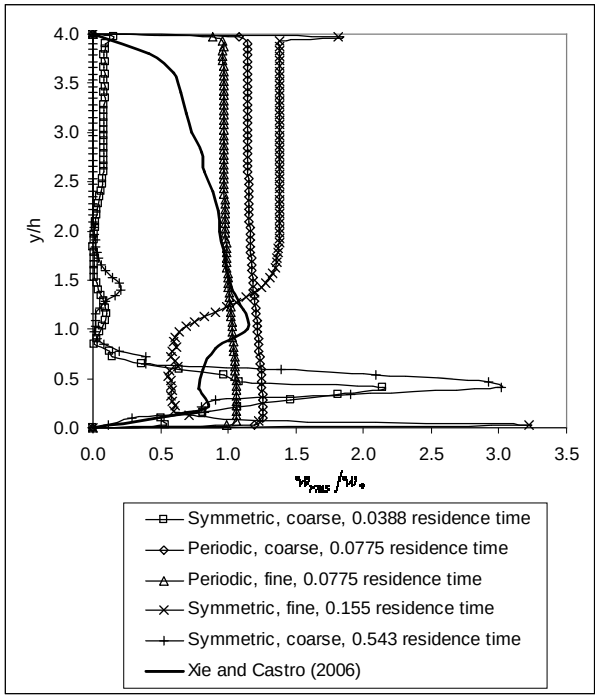

Figure 6.23 Root-mean-square profiles of the resolved velocity component in the streamwise direction on Line B.

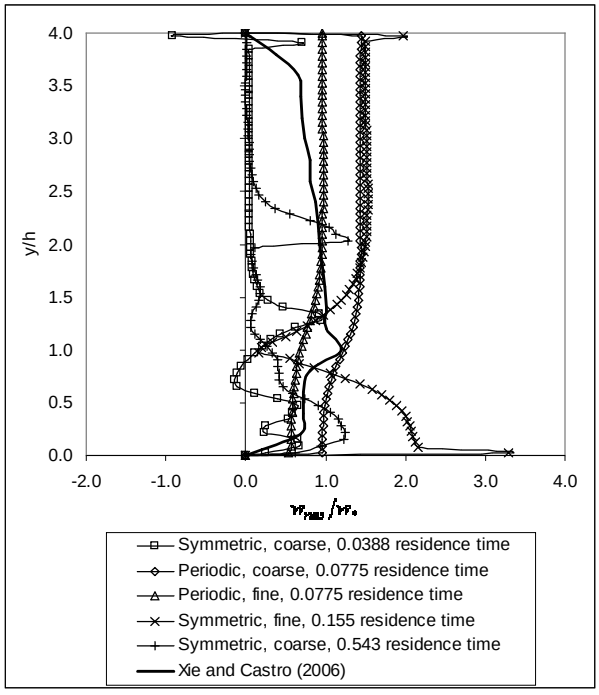

Figure 6.24 Root-mean-square profiles of the resolved velocity component in the streamwise direction on Line C.

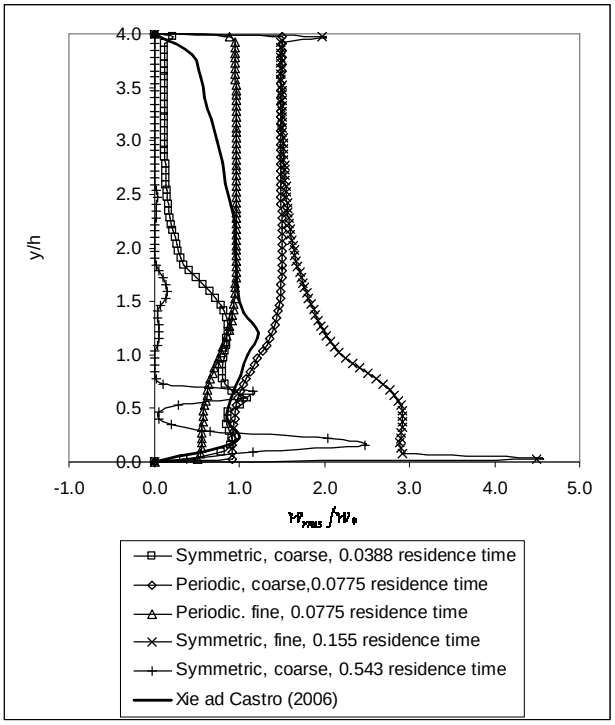

Figure 6.25 Root-mean-square profiles of the resolved velocity component in the streamwise direction on Line D.

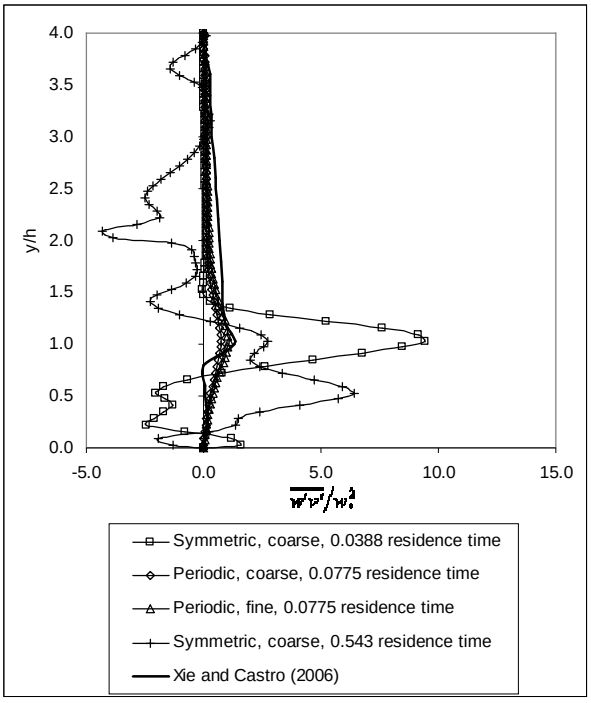

Figure 6.26 $\overline{w'v'}$ stress profiles on Line A.

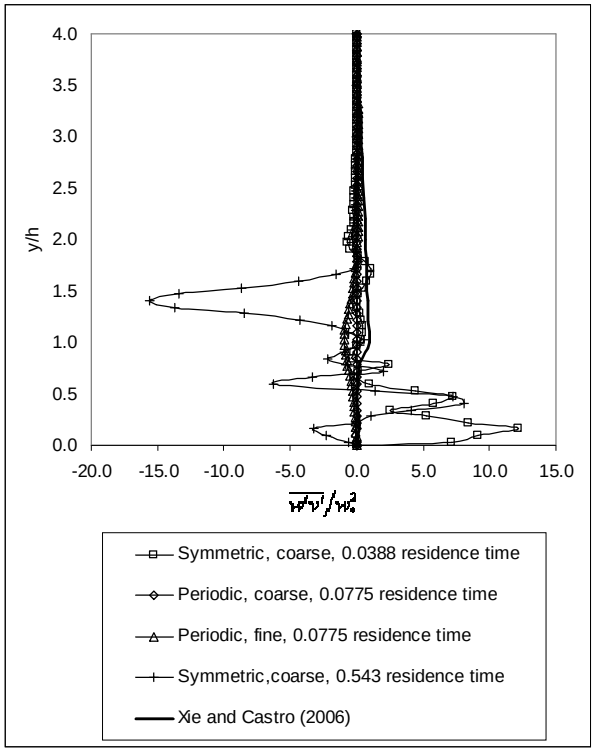

Figure 6.27 $\overline{w'v'}$ stress profiles on Line B.

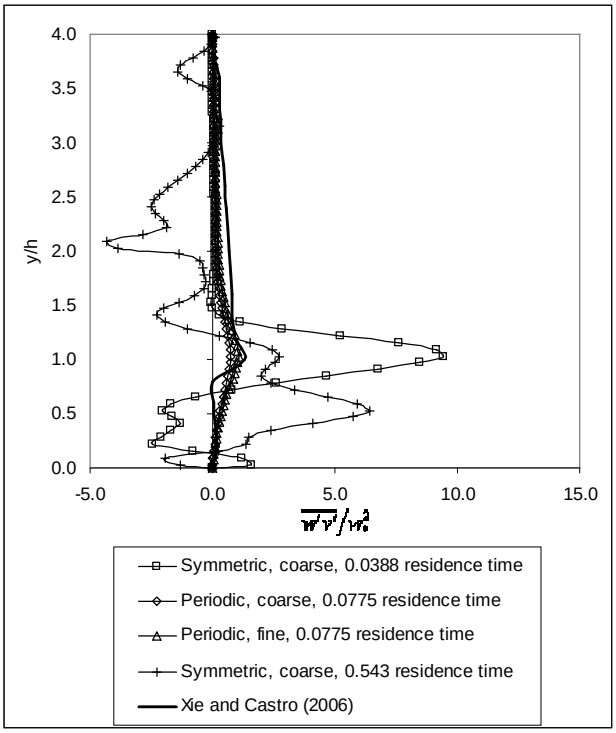

Figure 6.28 $\overline{w'v'}$ stress profiles on Line C.

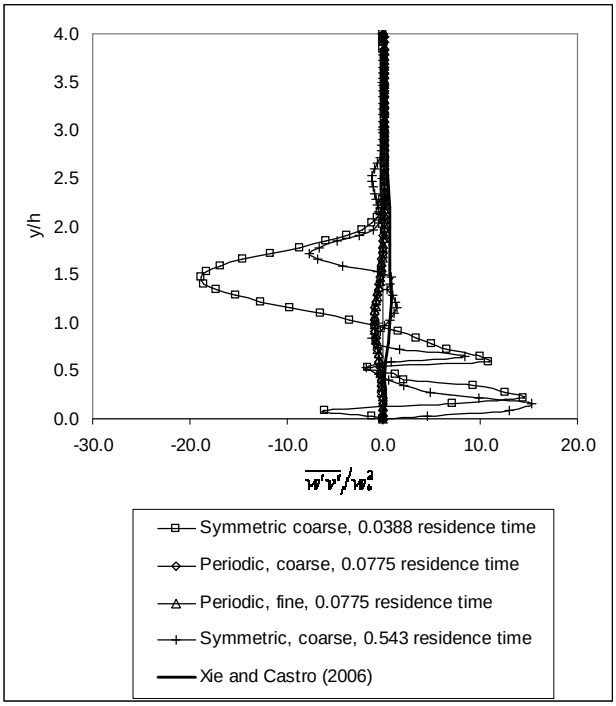

Figure 6.29 $\overline{w'v'}$ stress profiles on Line D.

The turbulence kinetic energy spectrum shown in Figure 6.30 for the case with symmetry boundaries up to 1,000 time steps does not give a clear cut figure for the range of frequencies over which the inertial subrange resides. This is due to the relatively short time period over which recording of the time series data of turbulence kinetic energy occurred and the flow being in a transient mode.

It can be seen from Figure 6.30 that the increase in energy levels from 1,000 time steps to 7,000 time steps was due to the build up of the flow from a quiescent state. Above a frequency of 100Hz, the slope can be seen to be steeper than the -5/3 slope of Kolmogorov which marks the region of dissipating range eddies. It is not possible to plot the spectrum for values of frequencies lower than 4Hz since only 2,500 time series data points were available. The presence of the inertial subrange residing in the frequency range of approximately 4Hz<f<50Hz where f is the frequency of fluctuations due to turbulence, can be seen from Figure 6.30. The level of energy agrees well with that of Xie and Castro (2006) though the frequencies are shifted by approximately +40Hz. Comparing the computed data with equivalent results of Xie and Castro (2006), the

computed frequency ranges start at a value of about an order of magnitude higher than the minimum frequency at which the inertial subrange of the reference plot starts.

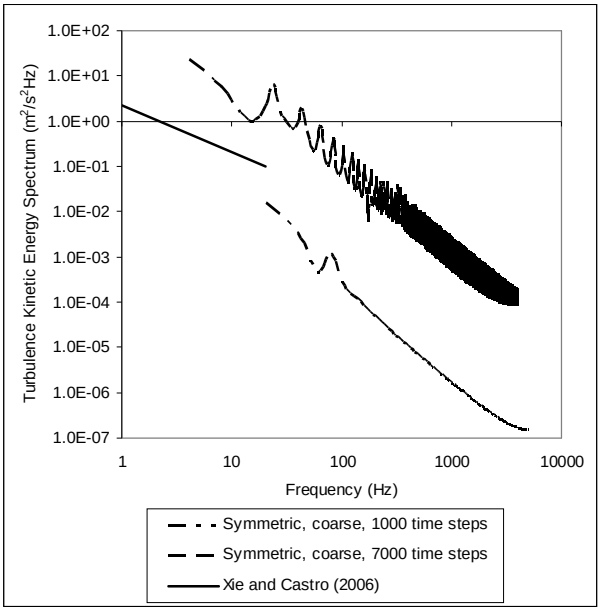

Figure 6.30 Turbulence kinetic energy spectrums at the monitoring point.

6.4 Closure

This chapter has described the application of the method of artificial turbulence to a flow over an array of wall mounted obstacles. The instantaneous velocity vector fields on planes at various locations in the domain have been plotted. The statistical properties have been compared to the reference data and in some instances, good agreement with the reference data were obtained. Even when profiles from computations do not match those of the reference data closely, general trends were reproduced in many instances. In addition, the turbulence kinetic energy spectrum plot gave good agreement with the reference data.

CHAPTER 7

Conclusions

Central to the work reported here is, the parallel, incompressible Navier-Stokes solver for the simulation of large eddies on unstructured Cartesian mesh by employing the second-order in time Adams-Bashforth Crank-Nicolson method for time-integration. To get to this stage, a step by step approach in code development, starting with a simpler code was carried out, in line with the objective stated earlier in Chapter 1. This is described in more detail below.

7.1 Objective

The objective of this study stated again here was, firstly, to create a properly functioning parallel unstructured flow solver to solve turbulent flows of engineering interest on orthogonal Cartesian meshes using the LES approach; secondly, to investigate the performance of different synthetic turbulence generation methods applied at the inlet.

It can be claimed that the first objective has mainly been achieved as can be seen from results of simulations in the three earlier chapters. Results from different synthetic turbulence generators indicate that the methods of artificial turbulence and the hybrid method of particle-spectrum are able to produce good turbulence statistics downstream of the inlet.

7.2 Achievements

Since no existing code with the required features was available to the author at the beginning of this project, the first step towards obtaining the flow solver was the construction of a parallel finite volume Poisson solver designed for an unstructured Cartesian mesh; the results of which were validated by comparing them with existing codes. The data structure for the unstructured grid revolved around the list of faces of cells where the fluxes were computed. The use of Message Passing Interface in combination with the Parallel Iterative Method linear algebraic equation solver managed to produce a satisfactory speed-up of the Poisson solver. Further studies can be conducted to find an optimum pre-conditioner for the coefficient matrix which was not carried out in this study due to time constraints. Another interesting future study can be the division of the coefficient matrix into sub-blocks to fit the cache size of the processor, which may reduce the processing time by increasing the number of cache hits.

The next step taken by the researcher was the formation of a sequential, finite volume, structured Cartesian hexahedral mesh, and incompressible, second-order in time Adams-Bashforth Crank-Nicolson flow solver, to compute a two-dimensional, laminar, driven cavity, flow problem. The time integration to the steady-state level went smoothly with no numerical instabilities implying that the implementation of numerical schemes have been carried out correctly. The order of accuracy with respect to space and time was checked using four grids and three time step sizes. The spatial order of accuracy approached was that of a second order scheme, but this simultaneously did require a reduction in the time step size. The temporal order of accuracy would have required a further reduction in cell size but this was not carried out since it could have been too costly to run such a case sequentially.

Using the unstructured Poisson solver developed earlier as a starting point and implementing the same numerical schemes as in the case of the structured Adams-Bashforth Crank-Nicolson, the unstructured version of the flow solver was built. The unstructured flow solver was validated by comparing the instantaneous velocity profiles from four grids with published data using the laminar, driven cavity flow as a test case. In

general, results agree reasonably well with the published data when the finest of the three meshes is used**.** The speed-up obtained with up to sixteen processors was about twelve. It is understood that to improve the speed-up factor, the serial fraction of the code must be reduced and one way to achieve this is to increase the number of cells used which is essentially Amdahl's law in action.

The first turbulent test case studied was a three-dimensional driven cavity flow at a bulk Reynolds number of 10,000. Three mesh sizes were used to give an idea on the appropriate mesh size to give good approximation to experimental data.

In order to apply LES to more challenging and complicated geometries, periodic boundaries frequently used in simple geometries (e.g. in channel flows), need to make way for inlet and outlet boundaries. To reduce the length in the streamwise direction necessary for turbulence to develop to a certain level or to maintain turbulence at the specified level throughout the entire length of the domain and period of the simulation, an effective turbulence generator at the inlet must be selected. Upon realising this, a literature review of current turbulence generation methods was carried out.

Based on the findings from this review, four test cases were simulated on a duct with square cross-section geometry at an aspect ratio of ten. For the first test case, a method of random perturbation was implemented. A new hybrid particle-wave method was equipped to the second test case. This method assigns turbulent fluctuations in the streamwise direction by superimposing a number of sinusoidal waves on the mean flow; in the directions parallel to the inlet plane the method of vortex particle was used. The third case was coupled with the method of artificial turbulence, which basically yields correlated (in time and space) fluctuations of velocity components by filtering a random fluctuating field (in the x, y and z-directions) residing in a three-dimensional domain with the filter coefficients, obtained via a presumed correlation function.

Two additional cases were also carried out to gain more knowledge on the properties of the flow and turbulence for the square duct geometry. The first one made use of a longer

aspect ratio square duct which was set to twenty or double that of the first four cases, mentioned above. The changes in the flow structure in the extended section of the duct were studied using this case. The second additional case uses a refined uniform mesh of 56x56 in the *x* and *y*-directions but with the aspect ratio reduced to four. A third-order accurate upwind scheme was used instead of the hybrid scheme but this was found to be unstable and consequently the original scheme was used again. The sensitivity of the results to the grid size and spatial differencing scheme was studied using data from this case.

The main conclusions from this study can be stated as follows:

- The main features of the flow such as the vortices forming the secondary flow were produced by all the methods of turbulence generation studied. Differences such as the form and location of these vortices with respect to the different methods of turbulence generation used are noticeable, when the flow is still in its transient stage.

- The mean and turbulence statistics profiles succeeded in highlighting the difficulties encountered in performing LES on the square duct geometry with regards to the mesh and spatial discretisation scheme used in this study. At t=2.5s, the mean velocity profiles from the random perturbation method departed furthest from the reference values compared to other methods while the mean velocity profiles at t=7.0s gave no indication that a turbulence generation method has an advantage over another, since the differences are miniscule.

- The method of artificial turbulence gave the highest degree of two point correlation as the flow approached the steady-state condition. The turbulence kinetic energy spectrum plots strongly favoured the artificial turbulence generation method again in terms of the energy levels produced and also the existence of the inertial subrange.

- Another important finding is the deterioration in the level of turbulence kinetic energy at the monitoring points with respect to time (as the simulation progresses) and space

(moving downstream in the direction of the flow). The artificial turbulence method is least affected by this phenomena compared to the other methods. This method can be improved further by reducing the length scale when filtering in the near wall region to reflect the decrease in the length scale of turbulence when the wall is approached.

To summarise, the main achievements of this study are listed below:

- A fairly efficient message passing routine has been successfully developed resulting in a satisfactory speed-up of the parallel flow solver.

- The flow solver behaved well in terms of the spatial and temporal order of accuracy, grid converging results, magnitude of residual error and turbulence statistics.

- Three different methods of synthetic turbulence generation have been studied; a detailed study of the performance of these methods was carried out. The advantages and shortcomings of each method were identified.

- A hybrid particle-spectrum method for the generation of synthetic turbulence was devised and developed. Results produced by this method are quite favourable and comparable to the method of artificial turbulence of Klein, Sadiki and Janicka (2003).

- The method of artificial turbulence was applied for the first time to the inlet of the flow in a channel with obstructions avoiding the more frequently used periodic boundaries in the streamwise direction. The final test case gave evidence that the flow solver is capable of handling a case with true unstructured grid.

7.3 Future Directions

In the near term, tasks that will be carried out to improve the code and investigate alternative methods to handle geometry, flow and communication are listed as follows:

- Periodic boundaries for the flow with obstructions will be used to replace the

symmetrical boundaries once the flow obtained in Chapter 6 has settled down. Due to the unsymmetrical nature of the instantaneous flow field, periodic boundaries are considered more appropriate than symmetrical ones.

- Anisotropic cells close to the walls will be constructed for the driven cavity flow and square duct cases. This will enable proper integration to the wall to be carried out, allowing a better prediction of turbulence statistics. This will require minor modifications to the flow solver to handle the varying cell edge lengths. Due to time constraints, this was not carried out in the present study and is treated as a future work on the code. A natural extension to this is the utilisation of zonal mesh refinement which becomes handy when dealing with complex geometries. It is relevant to mention here that by applying a coupling method based on the reconstruction of ghost cell values, Quéméré, Sagaut and Couailler (2001) treated the issue of discontinuous characteristic length and the non-conservative transfer of fluxes at the interface of two domains having different resolutions. The method was applied to solve a subsonic compressible channel flow.

- The cyclic message passing routine described in Chapter 3 will be compared to a simplified message passing (resulting from manual partitioning of meshes as exemplified in Chapter 6), also will be carried out, quantification, in terms of wall clock time requirements will be carried out.

- Further work can be carried out on the enhanced vortex particle method to correlate the velocity component in the streamwise direction to that perpendicular to it. An obvious way to do this is to vary the amplitude of fluctuations of the waves in proportion to the magnitude of the velocity on the inlet plane. This will most likely improve this method since this modification results in a physically more realistic secondary flow field.

- Another interesting near term future work that can be carried out on the synthetic turbulence generators is to vary the distribution of turbulence kinetic energy level

(with respect to the x and y-coordinates) so that the physical level of turbulence intensity within the turbulent boundary layer can be imitated for the case of square duct (with a finer mesh than previously used to properly resolve the boundary layer). For the enhanced vortex particle case, this can be carried out by spatially varying the amplitudes of the waves and the length scale in Equation (2.16). For the method of artificial turbulence, the values of the filter support can be varied to achieve the same effect.

Following the completion of the tasks listed above, the intermediate stage involves improvements in the efficiency, accuracy and capability of the code:

- The use of a multigrid solver should improve the efficiency of solving the linear algebraic equations as pointed out by Elman (1996) whose main finding was in favour of the multigrid method based on the fact that the method is twice more efficient than the preconditioned conjugate gradient solver. A multigrid LES flow solver has also been developed by Terracol, Sagaut and Basdevant (2001). In their case, the fluctuating spectrum was splitted into several frequency bands, whereby each band is allocated to a certain computational grid level.

- A more capable turbulence model must be chosen for this type of application and replacing the current (Smagorinsky) subgrid scale turbulence model with a more capable model for instance, the dynamic model, is another important extension to the code, since this will have a significant impact on the accuracy of the prediction of the quantities of turbulence. Studies such as those carried out by Ahn, Choi and Lee (2005) and Germano et al. (1991) are useful for this purpose. Basically, the dynamic model makes use of a test filter to resolve the largest scale of motion and by comparing the subgrid scale stresses from this filter to those of the cut-off filter, the value of the model coefficient is then modified in space and time. Techniques of stabilisation, in order to overcome the antidissipative behaviour of the dynamic model have been proposed by, for example, Ghosal et al. (1995).

- The method of immersed boundary described by Mittal and Iaccarino (2005) which modifies the governing conservation equations by introducing source terms to take into account boundaries that do not coincide with cell faces is a convenient way to handle complex geometries without having to resort to the tedious and complicated issue of embedding the geometrical information of the grid into the discretisation.

- The issue of numerical diffusion as a result of using a low-order upwind scheme in Chapter 5 necessitates the use of higher order schemes such as a second-order accurate in space scheme which satisfies Total Variation Diminishing conditions (see for example, Hirsch (1988)) avoiding the instability issue of central schemes when the Peclet number is high and striking a balance between communication cost and the accuracy of result.

With these improvements, the LES code can be used in a more meaningful manner to help design and analyse engineering artefacts:

- The computation of flow with obstructions described in Chapter 6 can be continued. The use of zonal mesh refinement will significantly increase the accuracy of the average flow field as well as the values of turbulence statistics. Future work can include more complicated physics such as heat transfer, as it is carried out by Murata and Mochizuki (2001).

- It is possible to compute fluid flow around geometries related to small scale aircraft such as unmanned air vehicles which has a smaller Reynolds number compared to a 900 seat passenger aircraft, for instance. This will have a more relaxed requirement on the computing resources, enabling a full LES computation to be performed on the domain avoiding the issues involved in Detached Eddy Simulations.

References

Addad, Y., Laurence, D., Talotte, C. and Jacob, M. C. (2003), "Large Eddy Simulation of a Forward-Backward Facing Step for Acoustic Source Identification," *International Journal of Heat and Fluid Flow*, Vol. 24, pp. 562-571.

Afgan, I., Moulinec, C., Prosser, R., and Laurence, D. (2007), "Large Eddy Simulation of Turbulent Flow for Wall Mounted Cantilever Cylinders of Aspect Ratio 6 and 10," *International Journal of Heat and Fluid Flow*, Vol. 28, No.4, pp. 561-574.

Ahn, J., Choi, H. and Lee, J. S. (2005), "Large Eddy Simulation of Flow and Heat Transfer in a Channel Roughened by Square or Semicircle Ribs," *Journal of Turbomachinery*, Vol. 127, No. 2, pp. 263-269.

Becker, D. (2006), "Parallel Unstructured Solvers for Linear Partial Differential Equations," PhD Thesis, Cranfield University, United Kingdom.

Benhamadouch, S., Mahesh, K. and Constantinescu, G. (2002), "Colocated Finite-Volume Schemes for Large-Eddy Simulation on Unstructured Meshes," Proceedings of the Summer Program 2002, Center for Turbulence Research, Stanford University, pp. 143-154.

Berglund, M. and Fureby, C. (2007), "LES of Supersonic Combustion in a Scramjet Engine Model," Proceedings of the Combustion Institute, Vol. 31, No.2, pp. 2497-2504.

Bijl, H., Carpenter, M. H. and Vatsa, V. N. (2001), "Time Integration Schemes for the Unsteady Navier-Stokes Equations," *AIAA Paper* 2001-2612, Anaheim, California, USA.

Billson, M., Eriksson, L. -E. and Davidson, L. (2003), "Jet Noise Prediction Using Stochastic Turbulence Modeling," *AIAA Paper 2003-3282*, Hilton Head, South Carolina,

USA.

Bouffanais, R., Deville, M. O., Fischer, P. F., Leriche, E. and Weill, D. (2006), "Large-Eddy Simulation of the Lid-Driven Cavity Flow by the Spectral Element Method," *Journal of Scientific Computing*, Vol. 27, Nos. 1-3, pp. 151-162.

Bracewell, R. N. (1965), *The Fourier Transform and its Application*, McGraw-Hill, New York, NY.

Brigham, E. O. (1974), *The Fast Fourier Transform*, Prentice-Hall, New Jersey, USA.

Britter, R. E. and Hanna, S. R. (2003), "Flow and Dispersion in Urban Areas," *Annual Review of Fluid Mechanics*, Vol. 35, pp. 469-496.

Camarri, S., Salvetti, M. V., Koobus, B. and Dervieux, A. (2004), "A Low-Diffusion MUSCL Scheme for LES on Unstructured Grids," *Computers and Fluids*, Vol. 33, No. 9, pp. 1101-1129.

Cannon, S. M., Adumitroaie, V., McDaniel, K. S., Zuo, B. and Smith, C. E. (2004), "LES Software for the Design of Low Emission Combustion Systems," *DOE OSTI Report* FC26-00NT40975-06, Pittsburgh, Pennsylvania, USA.

Chalasani, S., Luke, E. A., Senguttuvan, V. A. and Thompson, D. S. (2005), "Assessing Generalized Mesh Quality via CFD Solution Validation," *AIAA Paper 2005-687*, Reno, Nevada, USA.

Chalot, F., Levasseur, V., Mallet, M., Petit, G. and Reau, N. (2007), "LES and DES Simulations of Aircraft Design," *AIAA Paper* 2007-723, Reno, Nevada, USA.

Chang, K., Constantinescu, G. and Park, S. –O. (2006), "Analysis of the Flow and Mass Transfer Processes for the Incompressible Flow past an Open Cavity with a Laminar and

a Fully Turbulent Incoming Boundary Layer," *Journal of Fluid Mechanics*, Vol. 561, pp. 113-145.

Cheng, G., Koomullil, R. and Noack, R. (2005), "A Library Based Overset Capability Developments for Density- and Pressure-Based Flow Solvers," *AIAA Paper* 2005-5119, Toronto, Ontario, Canada.

Chlond, A. (1998), "Large-Eddy Simulation of Contrails," *Journal of Atmospheric Sciences*, Vol. 55, pp. 796-819.

Choi, H. and Moin, P. (1994), "Effects of Computational Time Step on Numerical Solutions of Turbulent Flow," *Journal of Computational Physics*, Vol. 113, pp. 1-4.

Cottet, G. -H. and Koumoutsakos, P. (2000), *Vortex Methods: Theory and Practise*, Cambridge University Press, Cambridge, United Kingdom.

da Cunha, R. D. and Hopkins, T. (1994), "The Parallel Iterative Methods (PIM) Package for the Solution of Systems of Linear Equations on Parallel Computers", *Technical Report* 19-94*, Computing Laboratory, University of Kent, Canterbury, United Kingdom.

Davidson, L. (2005), "Hybrid LES-RANS: Inlet Boundary Conditions," 3rd National Conference on Computational Mechanics, Trondheim, Norway.

Davis, K., Hoisie, A., Johnson, G., Kerbyson, D. J., Lang, M., Pakin, S. and Petrini, F. (2004), "A Performance and Scalability Analysis of the BlueGene/L Architecture," Proceedings of the 2004 ACM/IEEE Conference on Supercomputing, Pittsburgh, Pennsylvania, USA.

Deardorff, J. W. (1970), "A Numerical Study of Three-Dimensional Turbulent Channel Flow at Large Reynolds Numbers," *Journal of Fluid Mechanics*, Vol. 41, No. 2, pp. 453-480.

di Mare, L., Klein, M., Jones, W. P. and Janicka, J. (2006), "Synthetic Turbulence Inflow Conditions for Large-Eddy Simulation," *Physics of Fluids*, Vol. 18, pp. 1-11.

Ding, C. and He, Y. (2001), "A Ghost Cell Expansion Method for Reducing Communications in Solving PDE Problems," Proceedings of Supercomputing 2001, Nov 2001.

Dris, A. and Johnson, M. W. (2005), "Transition on Concave Surfaces," *Journal of Turbomachinery*, Vol. 127, No. 3, pp. 507-511.

Dubief, F., Naji, S. Lewis, M. and Mendonça, F. (2005), "Prediction of Aeroacoustic Noise in Automotive Centrifugal Fans: Validation of CFD and Acoustic Simulation Techniques," *AIAA Paper 2005-2921*, Monterey, California , USA.

Duff, I. S., Grimes, R. G. and Lewis, J. G. (1992) "User's Guide for the Harwell-Boeing Collection (Release I)," *Technical Report TR/PA/92/86*, CERFACS, Toulouse, France.

Elman, H. C. (1996), "Multigrid and Krylov Subspace Methods for the Discrete Stokes Equations," *International Journal for Numerical Methods in Fluids*, Vol. 22, No. 8, pp. 755-770.

Emmerich, S. J. and McGrattan, K. B. (1998), "Application of a Large Eddy Simulation Model to Study Room Airflow," *ASHRAE Transactions*, Vol. 104, No.1, pp. 1-9.

Erturk, E., Corke, T. C. and Gökçöl, C. (2005), "Numerical Solutions of 2-D Steady Incompressible Driven Cavity Flows at High Reynolds Numbers," *International Journal for Numerical Methods in Fluids*, Vol. 48, pp. 747-774.

Ferziger, J. H. and Peric, M. (2002), *Computational Methods for Fluid Dynamics*. *Third Edition*. Springer, Berlin, Germany.

Fröhlich, J. and Rodi, W. (2002), "Introduction to Large-Eddy Simulation of Turbulent Flows," Closure Strategies for Turbulent and Transitional Flows, Vol. 1, No. 8, pp. 197-224, Cambridge, United Kingdom.

Fröhlich, J., Rodi, W., Kessler, P., Parpais, S., Bertoglio, J. P. and Laurence, D. (1998), "Large Eddy Simulation of Flow around Circular Cylinders on Structured and Unstructured Grids," *Notes on Numerical Fluid Mechanics*, Vol. 66, pp. 319-338.

Gary, J., McCormick, S. and Sweet, R. (1983), "Successive Overrelaxation, Multigrid and Preconditioned Conjugate Gradients Algorithms for Solving a Diffusion Problem on a Vector Computer," *Applied Mathematics and Computation*, Vol. 13, pp. 285-309.

Gavrilakis, S. (1992), "Numerical Simulation of Low-Reynolds-Number Turbulent Flow through a Straight Square Duct," *Journal of Fluid Mechanics*, Vol. 244, pp. 101-129.

Geist, G. A., Kohl, J. A. and Papadopoulos, P. M. (1996), "PVM and MPI: A Comparison of Features," *Calculateurs Paralleles* , Vol. 8, No. 2, pp. 137-150.

Germano, M., Piomelli, U., Moin, P. and Cabot, W. H. (1991), "A Dynamic Subgrid-Scale Eddy Viscosity Model," *Physics of Fluids A*, Vol. 3, No. 7, pp. 1760-1765.

Ghosal, S., Lund, T. S., Moin, P. and Akselvoll, K. (1995), "A Dynamic Localization Model for Large-Eddy Simulation of Turbulent Flows," *Journal of Fluid Mechanics*, Vol. 286, pp. 229-255.

Glaze, D. J. and Frankel, S. H. (2003), "Stochastic Inlet Conditions for Large-Eddy Simulation of a Fully Turbulent Jet," *AIAA Journal*, Vol. 41, No. 6, pp. 1064-1073.

Golub, G. H. and Van Loan, C. F. (1996), *Matrix Computations*, *Third Edition*, Johns Hopkins University Press, Baltimore, Maryland, USA.

Gosman, A. D. (1999), "Developments in CFD for Industrial and Environmental Applications in Wind Engineering," *Journal of Wind Engineering and Industrial Aerodynamics*, Vol. 81, pp. 21-39.

Gropp, W., Lusk, E. and Skjellum, A. (1999), *Using MPI*, *Portable Parallel Programming with the Message-Passing Interface*, *Second Edition*, The MIT Press, Cambridge, MA.

Haworth, D. C. and Jansen, K. (2000), "Large Eddy Simulation on Unstructured Deforming Meshes: Towards Reciprocating IC Engines," *Computers and Fluids*, Vol. 29, pp. 493-524.

Heise, B. and Jung, M. (1997), "Parallel Solvers for Nonlinear Elliptic Problems Based on Domain Decomposition Ideas," *Parallel Computing*, Vol. 22, pp. 1527-1544.

Hendrickson, B., Kolda, T. G. (2000), "Graph Partitioning Models for Parallel Computing," *Parallel Computing*, Vol. 26, No. 12, pp. 1519-1534.

Hirsch, C. H. (1988), *Numerical Computation of Internal and External Flows*, *Volume 1*, Fundamentals of Numerical Discretization, John Wiley, Chichester, England.

Hirsch, C. H. (1990), *Numerical Computation of Internal and External Flows*, *Volume 2*, Computational Methods for Inviscid and Viscous Flow, John Wiley, Chichester, England.

Hinze, J. O. (1975), *Turbulence*, McGraw-Hill, New York, USA.

Hostikka, S. and McGrattan, K. B. (2001), "Large Eddy Simulation of Wood Combustion," International Interflam Conference, 9th Proceedings, Vol. 1, Edinburgh, Scotland.

Huser, A. and Biringen, S. (1993), “Direct Numerical Simulation of Turbulent Flow in a Square Duct,” *Journal of Fluid Mechanics*, Vol. 257, No. 1, pp. 65-95.

Jarrin, N., Benhamadouche, S. and Laurence, D. (2005), “Inlet Conditions for Large-Eddy Simulation using a New Vortex Method,” The Fourth International Symposium on Turbulence and Shear Flow Phenomena, Williamsburg, Virginia, USA.

Jasak, H., Weller, H. G. and Nordin, N. (2004), "In-Cylinder CFD Simulation Using a C++ Object Oriented Toolkit," *SAE Technical Paper* 2004-01-0110, Detroit, Michigan, USA.

Jones, W. P. and Launder, B. E. (1972), “The Prediction of Laminarization with a Two-Equation Model of Turbulence,” *International Journal of Heat and Mass Transfer*, Vol. 15, pp. 301-314.

Jost, G., Jin, H., an Mey, D. and Hatay, F. H. (2003), “Comparing the OpenMP, MPI, and Hybrid Programming Paradigm on an SMP Cluster,” *NAS Technical Reports*, NAS-03-019, NASA Ames, Moffet Field, California, USA.

Kamatsuchi, T. (2007), "Turbulent Flow Simulation around Complex Geometries with Cartesian Grid Method," *AIAA Paper* 2007-1459, Reno, Nevada, USA.

Karypis, G. and Kumar, V. (1998), “METIS – A Software Package for Partitioning Unstructured Graphs, Partitioning Meshes, and Computing Fill-Reducing Orderings of Sparse Matrices. Version 4.0,” Department of Computer Science/Army HPC Research Centre, University of Minnesota, Minneapolis, Minnesota, USA.

Kempf, A., Klein, M. and Janicka, J. (2005), “Efficient Generation of Initial and Inflow Conditions for Transient Turbulent Flows in Arbitrary Geometries,” *Flow, Turbulence and Combustion*, Vol. 74, No. 1, pp. 67-84.

Kim, J. and Moin, P. (1982), “Numerical Investigation of Turbulent Channel Flow,” *Journal of Fluid Mechanics*, Vol. 118, pp. 341-377.

Kim, J. and Moin, P. (1985), “Application of a Fractional Step Method to Incompressible Navier-Stokes Equations” *Journal of Computational Physics*, Vol. 59, pp. 308-323.

Kim, S. -E. (2004), "Large Eddy Simulation Using an Unstructured Mesh Based Finite-Volume Solver," *AIAA Paper* 2004-2548, Portland, Oregon, USA.

Klein, M., Sadiki, A. and Janicka, J. (2003), “A Digital Filter Based Generation of Inflow Data for Spatially Developing Direct Numerical or Large Eddy Simulations,” *Journal of Computational Physics*, Vol. 186, pp. 652-665.

Kobayashi, M. and Maekawa, H. (1995), “Turbulent Flow Accompanied by Taylor-Goertler Vortices in a Two-Dimensional Curved Channel,” *Flow Measurement and Instrumentation*, Vol. 6, No. 2, pp. 93-100.

Kohama, Y. P. (2000), “Three-Dimensional Boundary Layer Transition Study,” *Current Science*, Vol. 79, No. 6, pp. 800-807.

Kolmogorov, A. N. (1991), "The Local Structure of Turbulence in Incompressible Viscous Fluid for Very Large Reynolds Numbers," Proceedings of the Royal Society of London, Series A: Mathematical and Physical Sciences, Vol. 434, No. 1890, pp. 9-13, Republished in English.

Koseff, J. R. and Street, R. L. (1984), “Visualization Studies of a Shear Driven Three-Dimensional Recalculating Flow,” *Journal of Fluids Engineering*, Vol. 106, pp. 21-29.

Krasny, R. (1986a), “A Study of Singularity Formation in a Vortex Sheet by the Point-Vortex Approximation,” *Journal of Fluid Mechanics*, Vol. 167, pp. 65-93.

Krasny, R. (1986b), "Desingularization of Periodic Vortex Sheet Roll-Up," *Journal of Computational Physics*, Vol. 65, pp. 292-313.

Landau, L. D. and Lifshitz, E. M. (1987), *Fluid Mechanics. Second Edition*. Pergamon Press, New York, USA.

Larchevêque, L., Sagaut, P., Mary, I. and Labbé, O. (2003), "Large-Eddy Simulation of a Compressible Flow past a Deep Cavity," *Physics of Fluids*, Vol. 15, No. 1, pp. 193-210.

Launder, B. E. and Spalding, D. B. (1974), "The Numerical Computation of Turbulent Flows," *Computer Methods in Applied Mechanics and Engineering*. Vol. *3*, pp. 269-289.

Le, H., Moin, P. and Kim, J. (1994), "Direct Numerical Simulation of Turbulent Flow over a Backward-Facing Step," *Journal of Fluid Mechanics*, Vol. 330, pp. 349-374.

Lê, T. H., Troff, B., Sagaut, P., Dang-Tran, K. and Ta Phuoc, L. (1997), "PEGASE: A Navier-Stokes Solver for Direct Numerical Simulation of Incompressible Flows," *International Journal for Numerical Methods in Fluids*, Vol. 24, No. 9, pp. 833-861.

LeBeau, R. P., Chen, H., Kristipati, P., Gupta, S. and Huang, P. G. (2005), "Joint Performance Evaluation and Optimization of Two CFD Codes on Commodity Clusters," 43rd AIAA Aerospace Sciences Meeting and Exhibit, AIAA-2005-1380, Reno, Nevada, USA.

Lee, S., Lele, K. and Moin, P. (1992), "Simulation of Spatially Evolving Turbulence and the Applicability of Taylor's Hypothesis in Compressible Flow," *Physics of Fluids A*, Vol. 4, No. 7, pp. 1521-1530.

Lenormand, E., Sagaut, P. and Ta Phuoc, L. (2000), "Large Eddy Simulation of Subsonic and Supersonic Channel Flow at Moderate Reynolds Number," *International Journal for Numerical Methods in Fluids*, Vol. 32, No. 4. pp. 369-406.

Leonard, S., Terracol, M. and Sagaut, P. (2007), "Commutation Error in LES with Time-Dependent Filter Width," *Computers and Fluids*, Vol. 36, pp. 513-519.

Leriche, E. and Gavrilakis, S. (2000), "Direct Numerical Simulation of the Flow in a Lid-Driven Cubical Cavity," *Physics of Fluids*, Vol. 12 , No. 6, pp.1363-1376.

Lilly, D. K. (1967), "The Representation of Small-Scale Turbulence in Numerical Simulations," Proceedings of the IBM Scientific Computing Symposium on Environmental Science, pp. 195-209.

Liu, J., Chandrasekaran, B., Wu, J., Jiang, W., Kini, S., Yu, W., Buntinas, D., Wyckoff, P. and Panda, D. K. (2003), "Performance Comparison of MPI Implementations over Infiniband, Myrinet and Quadrics," Proceedings of the ACM/IEEE SC2003 Conference, Phoenix, Arizona, USA.

Liu, K. and Pletcher, R. H. (2006), "Inflow Conditions for the Large Eddy Simulation of Turbulent Boundary Layers: A Dynamic Recycling Procedure," *Journal of Computational Physics*, Vol. 219, pp. 1-6.

Lund, T. S., Wu, X. and Squires, K. D. (1998), "Generation of Turbulent Inflow Data for Spatially-Developing Boundary Layer Simulations," *Journal of Computational Physics*, Vol. 140, pp. 233-258.

Manoha, E., Trauff, B. and Sagaut, P. (2000), "Trailing-Edge Noise Prediction Using Large-Eddy Simulation and Acoustic Analogy," *AIAA Journal*, Vol. 8, No. 4, pp. 575-583.

Marsden, A.L., Vasilyev, O.V., and Moin, P. (2002), "Construction of Commutative Filters for LES on Unstructured Meshes," *Journal of Computational Physics*, Vol. 175, pp. 584-603.

Martinelli, L., Jameson, A. and Grasso, F. (1986), “A Multigrid Method for the Navier-Stokes Equations,” *AIAA Paper* 86-0208, Reno, Nevada, USA.

Mary, I. and Sagaut, P. (2002), "Large Eddy Simulation of Flow around an Airfoil Near Stall," *AIAA Journal*, Vol. 40, No. 6, pp. 1139-1146.

Mathey, F., Cokljat, D., Bertoglio, J.P. and Sergent, E. (2003), “Specification of LES Inlet Boundary Condition Using Vortex Method,” Turbulence, Heat and Mass Transfer 4, Antalya, Turkey.

McMullan, W. A., Gao, S. and Coats, C. M. (2007), "A Comparative Study of Inflow Conditions for Two- and Three-Dimensional Spatially Developing Mixing Layers using Large Eddy Simulation," *International Journal for Numerical Methods in Fluids*, Vol. 55, No. 6. pp. 589-610.

Meyers, J. and Sagaut, P. (2006), "On the Model Coefficient for the Standard and the Variational Multi-Scale Smagorinsky Model," *Journal of Fluid Mechanics*, Vol. 569, pp. 287-319.

Migeon, C., Texier, A. and Pineau, G. (2000), “Effects of Lid-Driven Cavity Shape on the Flow Establishment Phase,” *Journal of Fluids and Structures*, Vol. 14, pp. 469-488.

Miller, J. H. H. (1971), “On the Location of Zeros of Certain Classes of Polynomials with Applications to Numerical Analysis,” *The Journal of the Institute of Mathematics and Its Applications*, Vol. 8, pp. 397-406.

Mittal, R. and Iaccarino, G. (2005), "Immersed Boundary Methods," *Annual Review of Fluid Mechanics*, Vol. 37, pp. 239-261.

Mittal, R., Simmons, S. P. and Udaykumar, H. S. (2001), "Application for Large-Eddy Simulation to the Study of Pulsatile Flow in a Modeled Arterial Stenosis," *Journal of Biomechanical Engineering*, Vol. 123, pp. 325-332.

Mohamad Badry, A. B. (2004), *First Year Review Report*, School of Engineering, Cranfield University, Cranfield, Bedfordshire, United Kingdom.

Morton, S. A., Tomaro, R. F. and Noack, R. W. (2006), "An Overset Unstructured Grid Methodology Applied to a C-130 with a Cargo Pallet and Extraction Parachute," *AIAA Paper* 2006-461, Reno, Nevada, USA.

Murata, A. and Mochizuki, S. (2001), "Large Eddy Simulation of Turbulent Heat Transfer in an Orthogonally Rotating Square Duct with Angled Rib Turbulators," *Journal of Heat Transfer*, Vol. 123, No. 5, pp. 858-867.

Nikishova, O. D. and Gorbatyuk, N. A. (1991), "Development of Taylor-Görtler Vortices in the Boundary Layer of a Surface Moving Curvilinearly in the Presence of Polymer Additives," *Journal of Engineering Physics*, Vol. 60, pp. 327.

Okong'o, N. and Knight, D. D. (1998), "Accurate Three-Dimensional Unsteady Flow Simulation Using Unstructured Grids," *AIAA Paper* 98-0787, Reno, Nevada, USA.

Oppenheim, A. E., Willsky, A. S. and Young, I. T. (1983), *Signals and Systems*, Prentice-Hall International, London, United Kingdom.

Pacheco, P. S. (1997), *Parallel Programming with MPI*, Morgan Kaufmann, San Francisco, California, USA.

Parikh, P. (2001), "Application of a Scalable, Parallel, Unstructured-Grid-Based Navier-Stokes Solver," *AIAA Paper* 2001-2584, Anaheim, California, USA.

Park, T. S. (2006), “Effects of Time-Integration Method in a Large-Eddy Simulation using the PISO Algorithm: Part I – Flow Field,” *Numerical Heat Transfer*, Part A, Vol. 50, No. 3, pp. 249-245.

Pellegrini, F. and Roman, J. (1996), “Experimental Analysis of the Dual Recursive Bipartitioning Algorithm for Static Mapping,” *LaBRI Research Report* 1038-96, Université Bordeaux I, Talence, France.

Pettersson Reif B. A. and Andersson H. I. (2002), “Prediction of Turbulence-Generated Secondary Mean Flow in a Square Duct,” *Flow, Turbulence and Combustion*, Vol. 68, No. 1, pp. 41-61.

Peyret, R. and Taylor, T. D. (1983), *Computational Methods for Fluid Flow*, Springer-Verlag, New York, USA.

Piomelli, U., Scotti, A. and Balaras, E. (2001), “Large-Eddy Simulations of Turbulent Flows, from Desktop to Supercomputer,” Proceedings of the VECPAR2000, Porto, Portugal.

Prasad, A. K. and Koseff, J. R. (1989), “Reynolds Number and End-Wall Effects on a Lid-Driven Cavity Flow,” *Physics of Fluids A*, Vol. 1, No. 2, pp. 208-218.

Quéméré, P. and Sagaut, P. (2002), "Zonal Multi-Domain RANS/LES Simulations of Turbulent Flows," *International Journal for Numerical Methods in Fluids*, Vol. 40, No. 7, pp. 903-925.

Quéméré, P., Sagaut, P. and Couailler, V. (2001), "A New Multi-Domain/Multi Resolution Method for Large-Eddy Simulation," *International Journal for Numerical Methods in Fluids*, Vol. 36, No. 4, pp. 391-416.

Raverdy, B., Mary, I., Sagaut, P. and Liamis, N. (2003), "High-Resolution Large-Eddy

Simulation of Flow around Low-Pressure Turbine Blade," *AIAA Journal*, Vol. 41, No. 3, pp. 390-397.

Rehm, R. G., McGrattan, K. B., Baum, H. R. and Simiu, E., (1999), "An Efficient Large Eddy Simulation Algorithm for Computational Wind Engineering: Application to Surface Pressure Computations on a Single Building," *NISTIR* 6371, National Institute of Standards and Technology, Gaithersburg, Maryland, USA.

Rembold, B. (2003), "Direct and Large-Eddy Simulation of Compressible Rectangular Jet Flow," PhD Thesis, Swiss Federal Institute of Technology, Zürich, Switzerland.

Rodgers, P. and Eveloy, V. (2003), "Prediction of Microelectronics Thermal Behavior in Electronic Equipment: Status, Challenges and Future Requirements," Fourth Thermal & Mechanical Simulation and Experiments in Micro-electronics and Microsystems Conference (EuroSimE), Aix-en-Provence, France.

Roknaldin, F. and Panigrahy, A. (2004), "Board Level Thermal Analysis via Large Eddy Simulation (LES) Tool," Ninth Intersociety Conference on Thermal and Thermomechanical Phenomena in Electronic Systems, Las Vegas, Nevada, USA.

Rollet-Miet, P., Laurence, D. and Ferziger, J. (1999), "LES and RANS of Turbulent Flow in Tube Bundles," *International Journal of Heat and Fluid Flow*, Vol. 20, pp 241-254.

Sagaut, P. (2001), *Large Eddy Simulation for Incompressible Flows*. Springer-Verlag Berlin Heidelberg, Germany.

Sagaut, P., Comte, P. and Ducross, F. (2000), "Filtered Subgrid-Scale Models," *Physics of Fluids*, Vol. 12, No. 1, pp. 233-236.

Sagaut, P., Garnier, E., Tromeur, E., Larchevêque, L. and Labourasse, E. (2003), "Turbulent Inflow Conditions for LES of Supersonic and Subsonic Wall Bounded

Flows," *AIAA Paper* 2003-68, Reno, Nevada, USA.

Sagaut, P. and Grohens, R. (1999), "Discrete Filters for Large Eddy Simulation," *International Journal for Numerical Methods in Fluids*, Vol. 31, No. 8. pp. 1195-1220.

Sergent, A., Joubert, P. and Le Quéré, P. (2003), "Development of a Local Subgrid Diffusivity Model for Large-Eddy Simulation of Buoyancy-Driven Flows: Application to a Square Differentially Heated Cavity," *Numerical Heat Transfer*, Part A, Vol. 44, pp. 789-910.

Shewchuk, J. R. (1994), *An Introduction to the Conjugate Gradient Method Without the Agonizing Pain*, School of Computer Science, Carnegie Mellon University, Pittsburgh, Pennsylvania, USA.

Simons, T. A. and Pletcher, R. H. (1998), "Large Eddy Simulation of Turbulent Flows Using Unstructured Grids," *AIAA Paper* 98-3314, Reno, Nevada, USA.

Smagorinsky, J. (1963), "General Circulation Experiments with the Primitive Equations I. The Basic Experiment," *Monthly Weather Review*, Vol. 91, pp. 99-164.

Smirnov, A., Shi, S. and Celik, I. (2001), "Random Flow Generation Technique for Large Eddy Simulations and Particle-Dynamics Modeling," *Journal of Fluid Engineering*, Vol. 123, No. 2, pp. 359-371.

Squires, K. D. (2004), "Detached-Eddy Simulation: Current Status and Perspectives," in Direct and Large-Eddy Simulation V, R. Friedrich, B. J. Geurts and O. Metais, editors, Kluwer Academic Publishers, Dordrecht, Netherlands, pp. 465-480.

Stoesser, T., Mathey, F., Fröhlich, J. and Rodi, W. (2003), "LES of Flow over Multiple Cubes," ERCOFTAC Bulletin, No. 56.

Strohmaier, E. (2005), “20 Years Supercomputer Market Analysis,” International Supercomputer Conference 2005, Heidelberg, Germany.

Taiji, M., Narumi, T., Yousuke, Ohno., Futatsugi, N., Suenaga, A., Takada, N. and Konagaya, A. (2003), “Protein Explorer: A Petaflops Special-Purpose Computer System for Molecular Dynamics Simulation,” Proceedings of the ACM/IEEE SC2003 Conference, Phoenix, Arizona, USA.

Terracol, M., Sagaut, P. and Basdevant, C. (2001), "A Multilevel Algorithm for Large-Eddy Simulation of Turbulent Compressible Flow Source," *Journal of Computational Physics*, Vol. 167, No. 2, pp. 439-474.

Trefethen, L. N. and Bau III, D. (1997), *Numerical Linear Algebra*, Society for Industrial and Applied Mathematics, Pennsylvania, USA.

Trottenberg, U., Oosterlee, C. W. and Schuller, A. (2001), *Multigrid*, Academic Press, San Diego, California, USA.

Tutar, M., Celik, I. and Yavuz, I. (2007), "Modeling of Effect of Inflow Turbulence Data on Large Eddy Simulation of Circular Cylinder Flows," *Transactions of the ASME*, Vol. 129, pp. 780-790.

Uchiyama, T. (1998), “Accuracy of Large Eddy Simulation for Turbulent Flow by the Finite Element Method,” Proceedings of the Institution of Mechanical Engineers, Vol 212, Part C, pp. 643-650.

van Driest, E. R. (1956), "On Turbulent Flow Near a Wall," *Journal of Aeronautical Sciences*, Vol. 23, pp. 1007-1011.

Walshaw, C., Cross M. and Everett, M. G. (1997), "Parallel Dynamic Graph Partitioning for Adaptive Unstructured Meshes," *Journal of Parallel and Distributed Computing*, Vol. 47, Part 2, pp.102-108.

Wang, B., Zhang, H. Q. and Wang, X. L. (2006), "Large Eddy Simulation of Particle Response to Turbulence along its Trajectory in a Backward-Facing Step Turbulent Flow," *International Journal of Heat and Mass Transfer*, Vol. 49, pp. 415-420.

Wang, H. P., Olson, S. J., Goldstein, R. J. and Eckert, E. R. G. (1997), "Flow Visualization in a Linear Turbine Cascade of High Performance Turbine Blades," *Journal of Turbomachinery*, Vol. 119, No. 1, pp. 1-8, 1997.

Wang, M. and Moin, P. (2000), "Computation of Trailing-Edge Flow and Noise Using Large-Eddy Simulation," *AIAA Journal*, Vol. 38, No. 12, pp. 2201-2209.

Wang, X., Jiang, J. and Zhang, Y. (2005), "Large Eddy Simulation of Air Flows in a Forced Ventilated Room," *ASAE Paper* 054021, Tampa, Florida, USA.

Wang,. Z. J., Chi, X. K., Shih, T. and Bons, J. (2004), "Direct Simulation of Surface Roughness Effects with RANS and DES Approaches on Viscous Adaptive Cartesian Grids," *AIAA Paper* 2004-2420, Portland, Oregon, USA.

Wesseling, P. (1995), "A Method to Obtain von Neumann Stability Conditions for the Convection-Diffusion Problem," Proceedings of the ICFD Conference on Numerical Methods in Fluid Dynamics, Oxford, United Kingdom.

Wilcox, D. C. (2002), *Turbulence Modeling for CFD*, Second Edition, DCW Industries, La Cañada, California, USA.

Worthy, J. (2003), "Large Eddy Simulation of Buoyant Plumes," PhD Thesis, Cranfield University, United Kingdom.

Xie, Y. and Castro, I. P. (2006) “LES and RANS for Turbulent Flow over Arrays of Wall-Mounted Obstacles,” *Flow, Turbulence and Combustion*, Vol. 76, No. 3, pp. 291-312.

Yuan, Q., Vanka, S. P. and Thomas, B. G. (2001), "Large Eddy Simulations of Turbulent Flow and Inclusion Transport in Continuous Casting of Steel", Proceedings of 2nd International Symposium on Turbulent and Shear Flow Phenomena, Vol. 2, Royal Institute of Technology (KTH), Stockholm, Sweden.

Zhao, X., Richard, P. G., Zhang, S. J., Liu, J. and Chen, Y. –S. (2003), “Parallel Computing Strategy for Solution Adaptive, Multi-Grid Unstructured Flow Solver,” *AIAA Paper* 2003-955, Reno, Nevada, USA.